multi-scale attenuation and dispersion in transmission seismic data

Multi-scale attenuation and dispersion in seismic transmission data

Proefschrift

ter verkrijging van de graad van doctor
aan de Technische Universiteit Delft,
op gezag van de Rector Magnificus Prof.dr.ir. J.T. Fokkema,
voorzitter van het College voor Promoties,
in het openbaar te verdedigen
op donderdag 19 oktober 2006 om 12.30 uur

door

Nikoletta FILIPPIDOU

master of Science in Seismology-Geophysics

National and Kapodestrian University of Athens
geboren te Krefeld, Duitsland

Dit proefschrift is goedgekeurd door de promotor:

Prof.dr.ir. J.T. Fokkema

Toegevoegd promotor: Dr. ir. G. G. Drijkoningen

Samenstelling promotiecommissie:

Rector Magnificus	voorzitter
Prof.dr.ir. J.T. Fokkema	Technische Universiteit Delft, promotor
Dr. ir. G.G Drijkoningen	Technische Universiteit Delft, toegevoegd promotor
Prof.dr. S. B. Kroonenberg	Technische Universiteit Delft
Prof.dr.ir. C.P.A. Wapenaar	Technische Universiteit Delft
Prof.dr. M. Landrø	Norges Teknisk Naturvitenskapelige Universitet, Trondheim, Noorwegen
Dr. A Tzanis	National and Kapodestrian University of Athens, Griekenland

Dr. ir. E. Slob heeft als begeleider in belangrijke mate aan de totstandkoming van het proefschrift bijgedragen.

ISBN-10: 90-9021167-5
ISBN-13: 978-90-9021167-1

Support

The research reported in this thesis has been financially supported by the Netherlands Research Center of Integrated Solid Earh Sciences.

Cover: Private photo collection, shot on location, Pireas, Greece, 2006

Printed by Ipskamp in the Netherlands

to my mother and my father,

Contents

Summary

Resolution decreases with depth in seismic images. One of the main causes is the attenuation of the seismic waves. Transmission losses may occur due to intrinsic properties of the rock (grain-to-grain interaction, fluid movement etc) or due to scattering in thin layers. Through the Kramers-Kronig relations due to causality, attenuation is linked to dispersion, which is the time-delay that occurs due to internal multiples arriving at short times after the direct arrival. It is fundamental that we understand the wave attenuation and dispersion in order to improve our view of the subsurface. In this thesis, a methodology facilitating this understanding as a function of scale is suggested. The scaling issue rises because there is a discrepancy between the scale of observation and the scale of heterogeneities in the earth. Therefore, different experiments capture different medium volumes from which effective values of the properties are measured. The wavelet transform method can elucidate the addressed scale among different experiments.

We consider the effective attenuation to be estimated directly from the seismic experiments (in this case P-wave Vertical Seismic Profile, VSP). This is estimated using the modified spectral ratio method which allows for frequency-dependent attenuation. In order to estimate the attenuation due to internal multiples, i.e., scattering attenuation, we assume a 1D non-dissipative finely-layered medium, constructed from ultrasonic laboratory velocity and density measurements (MST) on cores from the same borehole where the VSP experiment was conducted. For every scale the transmission impulse response is then calculated from full waveform synthetic seismograms and scattering (or Q_{sc}) and dispersion are derived. A new model is proposed that can accurately represent the complicated transmission response at every scale, and this new model is used to determine attenuation and dispersion. The VSP represent the largest scale experiment, while the MST measurements the finest. To facilitate comparison, we use a scaling

method relying on the wavelet transform technique. The wavelet transform is used in order to regularize and upscale the fine-scale information derived from the laboratory measurements at different scales. In this way, the MST information is upscaled to the VSP scale. We estimate the intrinsic attenuation using a cumulative scheme between the attenuation due to scattering and intrinsic attenuation.

We performed a multitude of seismic transmission and reflection seismic experiments in two Natural Laboratories, that provided both the complexity of the natural features and the controlled conditions required. The two Laboratories have fundamental geological differences. The first, located in France (Boulogne), is an Upper Jurassic siliciclastic sequence and the second is a Miocene carbonate reef platform, situated in Spain (Mallorca). In this thesis we use mainly the data from transmission measurements to estimate attenuation and dispersion. The recorded signals in the VSP experiments between the two sites differ in the frequency content. Higher effective and attenuation is observed in Mallorca than in Boulogne. This is attributed to the intrinsic properties of the rock and to high scattering due to the large primary and secondary porosity observed on cores and thin sections. Full waveform synthetic seismogram on impedance logs constructed from the laboratory measurements confirm this by showing higher expected scattering for Mallorca than for Boulogne. The new model is used to approximate the attenuation and dispersion due to scattering at the scale of the VSP.

We show how scattering occurs from compartmentalization of the seismic energy at impedance contrasts. Internal multiple lead to interference that may result in bands of very low transmission (also known as spectral gaps) embedded in bands of higher transmission in a specific regularity. Such transmission responses are typical for e.g. periodic media. Detailed study on the sequence and distribution of these bands can explain the statistical distribution of the media properties. In the case of acoustic media the properties are density and velocity. Such studies and analyses are not common in geosciences, due to the complex statistics and perturbations of geological sequences that deviate from strict periodicity or other partially periodic structures. However, they are

common in fields like optics and experimental biology, and we discuss how we could borrow some know-how to elucidate geophysical experiments.

In the appendix section, we describe numerical experiments performed on discrete particle lattices involving grain-to-grain interaction and attenuation due to intergranular friction. It is shown that increase of friction has a non-linear effect in the amplitude of a wave.

Samenvatting

In seismisch beelden van de ondergrond neemt de resolutie af met diepte. Een van de belangrijkste redenen hiervoor is de demping van het seismische golfveld. Transmissieverliezen kunnen veroorzaakt worden door de intrinsieke eigenschappen van het gesteente (interactie tussen de korrels, vloeistofstroming, enz.) of door verstrooiing door fijngelaagdheid . Op grond van causaliteit wordt demping, via de Kramers-Kronig relaties, gekoppeld aan dispersie. Dispersie is het tijdsverschil dat ontstaat door de aankomst van intern-gereflecteerde aankomsten ("multiples") die volgen op korte tijden na de directe aankomst. Om onze blik op de ondergrond te verbeteren is het van fundamenteel belang dat we demping en dispersie van het golfveld begrijpen. In dit proefschrift wordt een methode gesuggereerd om dit begrip, als functie van schaal, te verwezenlijken. De schaal is van belang omdat er een discrepantie bestaat tussen de schaal van observatie en de schaal van ongelijkmatigheden in de aarde. Daarom vangen verschillende experimenten verschillende mediumvolumes waaruit effectieve waarden van de eigenschappen gemeten worden. De wavelet-transformatiemethode kan de aan verschillende methodes toegewezen schaal verklaren.

Wij gaan ervan uit dat de effectieve demping direct uit een seismisch experiment geschat wordt (in dit geval uit een compressiegolf Vertikaal Seismisch Profiel (VSP) experiment). De schatting wordt gedaan met de gemodificeerde spectrale ratio methode die frequentie-afhankelijke demping toestaat. Om de demping ten gevolge van interne reflecties, of wel verstrooiingsdemping, te schatten gaan we uit van een 1D fijngelaagd medium zonder dispersie. Dit medium wordt geconstrueerd uit ultrasonische metingen van de golfsnelheid en dichtheid (MST) op kernen uit hetzelfde boorgat waar het VSP experiment is uitgevoerd. Vervolgens wordt voor elke schaal de transmissie

impulsrespons uitgerekend met behulp van synthetische seismogrammen van het volledige golfveld en hieruit worden verstrooiing (of Q_{sc}) en dispersie afgeleid. Een nieuw model wordt voorgesteld dat het gecompliceerde transmissierespons op elke schaal accuraat kan representeren. Dit nieuwe model wordt gebruikt om demping en dispersie te bepalen. De VSP representeert het experiment van de grootste schaal, terwijl MST het kleinste schaalexperiment representeert. Om een vergelijking mogelijk te maken, gebruiken we een schaalmethode die gebaseerd is op de wavelet-transformatietechniek. Deze wavelet transformatie wordt gebruikt om de fijnschalige informatie verkregen uit de labexperimenten van verschillende schalen te regulariseren en op te schalen. Op deze wijze wordt de MST informatie opgeschaald naar de VSP schaal. We schatten de intrinsieke demping door uit te gaan van een cumulatief schema van de demping als gevolg van verstrooiing en de intrinsieke demping.

We hebben een veelvoud van seismische transmissie- en reflectie-experimenten uitgevoerd in twee natuurlijke laboratoria, welke zowel de complexiteit van de natuurlijke eigenschappen als de benodigde gecontroleerde eigenschappen verschaften. De twee laboratoria spreiden belangrijke geologische verschillen tentoon. De eerste, gelegen in Frankrijk (Boulogne), is een siliclastische formatie uit het Laat-Jura. De tweede is een carbonaat platformrif uit het Mioceen, gelegen in Spanje (Mallorca). In dit proefschrift gebruiken we voornamelijk de data van transmissie metingen om de demping en dispersie te schatten. Bij de twee verschillende locaties verschillen de geregistreerde frequentiebanden van de VSP-experimenten. In Mallorca wordt een hogere effectieve demping waargenomen dan in Boulogne. Dit wordt toegeschreven aan de intrinsieke eigenschappen van het gesteente en aan een grote mate van verstrooiing ten gevolge van een hoge primaire en secondaire porositeit, zoals waargenomen in de kernen en slijpplaatjes. Synthetische seismogrammen van het volledige golfveld, welke gemaakt zijn met behulp van impedantie logs van laboratorium metingen van de gesteentes, tonen een grotere mate van verstrooiing bij het gesteente van Mallorca dan dat van Boulogne en

bevestigen daarmee de eerdere bevinding. Het nieuwe model wordt gebruikt om de demping en dispersie door verstrooiing, op de schaal van een VSP meting, te schatten.

We laten zien hoe verstrooiing ontstaat door een opdeling van de seismische energie bij impedantiecontrasten. Interne reflecties leiden tot interferentie, hetgeen kan leiden tot frequentiebanden met zeer lage transmissie (ook bekend als spectrale gaten) ingebed tussen banden met een hoge transmissie, in een bepaalde regelmatigheid. Dergelijke transmissieresponsies zijn karakteristiek voor bijvoorbeeld periodieke media. Een gedetailleerde studie van de opeenvolging en verdeling van deze frequentiebanden kan de statistische verdelingen van de media-eigenschappen verklaren. In het geval van akoestische media zijn de relevante eigenschappen dichtheid en golfsnelheid. Zulke studies en analyses zijn niet gebruikelijk in aardwetenschappen, vanwege de gecompliceerde verdelingen en verstoringen in geologische formaties die afwijken van strikte periodiciteit of andere gedeeltelijk periodieke structuren. In andere disciplines echter, zoals in de optica en experimentele biologie, zijn deze studies en analyses wel gebruikelijk. Wij behandelen hoe we iets van deze kennis kunnen lenen om geofysische experimenten te verklaren.

In de appendices beschrijven we numerieke experimenten uitgevoerd op roosters van discrete deeltjes met betrekking op interactie tussen korrels en demping ten gevolge van intergranulaire wrijving. Het wordt aangetoond dat een toename van de frictie een niet-lineair effect heeft op de amplitude van een golf.

The unexplored life is not worth living.
Socrates

Chapter 1

Introduction

1.1. Introduction

Imagine a cave hosting prisoners chained since childhood. Not only are their limbs immobilized but their heads are also chained so that their eyes are fixed on a wall. Behind the prisoners there is a fire burning. Between the fire and the prisoners is a stage, along which shapes of various animals, plants and other objects are carried. The shapes cast their shadow on the wall where the prisoners look. When one of the shape-carriers speaks, the prisoners hear the voice. They conclude that the voice comes from the shadows. The prisoners name the shape of the shadows as the pass by. For them, the shadows is their reality, for this is the only thing they know. Suppose a prisoner is released, stands up and turns around. His eyes would be blinded by the firelight and the shapes passing would appear less real than their shadows. Suppose even that he is urged out of the cave into the sunlight. He does not want to leave the cave but is forced to. At first, his eyes would be so blinded that he would not be able to see anything. As the time passes, his eyes would get used to the light and he would start distinguishing the shapes he sees. In time, he would learn to perceive the objects as reality. The last object he would be able to see is the sun, which in time, he would learn to see as that object which provides the seasons and the courses of the year, presides over all things in the visible region and is in some way the cause of all these things that he has seen.

The above is a summary of a story known as *The Allegory of the Cave*[1]. It presents, in

[1] The *Allegory of the Cave* is a lengthy dialog on the nature of justice between Socrates and Glaucon. It can be found in Book VII of Plato's best-known work, *The Republic.*

brief form, some of Plato's major philosophical assumptions: his belief that the world revealed by our senses is not the real world but only a poor copy of it.

In "The Republic", Plato sums up his views in an image of ignorant humanity, trapped in the depths and not even aware of its own limited perspective. The rare individual escapes the limitations of that cave and, through a long, tortuous intellectual journey, discovers a higher realm, a true reality. This could also describe, quite accurately, the journey of a geoscientist who is in constant search for the most representative model of the subsurface. In order to build a high-resolution description, we need to combine different types of information. They can be largely classified as static or dynamic. Static data consist of time-invariant information. Geology could be considered as a relatively static observation. Dynamic data are time-varying quantities and may include surface seismic experiments, vertical seismic profiles, sonic and ultrasonic measurements. Metaphorically speaking, our seismic experiments are the shadows cast by the geological forms.

Reconciling static and dynamic data from the subsurface is essential. It is important that our models contain the small-scale property variations observed in well logs or laboratory measurements, while reproducing the large-scale composition in seismic data. However, models constructed from static data, usually do not match the dynamic data. There is no uniform description. Therefore, the experiment itself affects significantly the way we look at the medium. For example, a typical surface seismic experiment will not “see” the squirt flow which is excited in ultrasonic measurements. Hence the model needs to be conditioned to the dynamic data. Conditioning is equivalent to investigating the behaviour of the medium when observed at different scales.

The term scaling or scale analysis can have several meanings. In this work, scaling is defined as the process determining the interdependency of temporal and spatial properties observed in different dimensions in a physical system. Apart from establishing the quantitative relation between those properties, a physical reasoning is needed to explain and possibly predict this scaling behaviour. A proper scaling should reflect the physical processes taking place during the phenomenon under study [*Lhomme* (2005)].

1.2. The concept of scales

The concept of scales is primarily a matter of establishing a common ground of communication and observation. But, why are scales all so important? Because scales are extensively omnipresent; they are the essence and beauty of life. Failing to understand them means failure to communicate the different aspects of the world each one of us –scientists or not, geophysicists or not– perceives.

The most striking and ground-breaking concepts on scales were introduced in the talk "There is Plenty of Room at the Bottom", given by Richard Feynman at a meeting at Caltech (1959) [*Feynman* (2001)]. He described a process by which individual atoms and molecules could be manipulated in such a way that precise tools could be developed and operated in a needed, very small scale. Feynman did not use the word nano-scale or nanotechnology; the latter term was introduced 15 years later [*Taniguchi* (1974)]. Feynman was inadvertently bridging the concept of **scale of observation** and the **scale of heterogeneity**[2], while describing the scaling issues that would arise from a change in the magnitude of the physical phenomena. For instance, gravity would become less important compared to surface tension and van der Waals attraction, if one goes to finer scales. The scale of observation has to be finer in order to observe the atom-composed tools, and the scale of heterogeneities at the finest scale of observation would refer to atoms or molecules. Technological advances allow scientists to extend the range of the scale of observation, which is linked to resolution, while the scale of heterogeneity is an intrinsic natural property.

Hence, scale is woven in the very fabric of the universe and everything around us is scale-dependent. Scales are inherent in Heisenberg's Uncertainty Principle[3]; the finer one measures the particle position, by viewing it in increasingly smaller scale, the more uncertain its momentum becomes. Scales differentiate an intricate musical part from simplistic rhythms. They make a photographic camera with powerful zoom more desired than one without. Scales

[2] Heterogeneity can be loosely defined as spatial variations in the natural properties of the medium.
[3] A quantum mechanical principal due to Werner Heisenberg (1927). In its most common form it states that it is not possible to simultaneously determine the position and momentum of a particle; the better the position is known, the less well the momentum is known (and vice versa). The uncertainty principle does not just apply to position and momentum of a particle. In its general form, it applies to every pair of conjugate variables. Such an example is time and frequency in a sound wave: the frequency content cannot be determined over one time sample, more time samples are necessary. That means we lose accuracy in time. In other words, we cannot have both a precise time (as in a short pulse) and a precise frequency as in a continuous pure tone.

are responsible for satellite failures and for discrepancies between theoretical models and laboratory measurements, due to scale dependent overlooked detail and assumptions. In our geoscience-world, scales are important because earth has heterogeneities that we are trying to characterize at all levels in space and time. And last –but not least– scales are important to geophysicists because with the wave propagation experiments we do nothing but averaging smaller than the wavelength heterogeneities. Hence, scales unwittingly feed the human mind and life, and although many would not be able to quantify the concept, not a single person would ignore the effect they may have.

Scale in that respect, can be debated upon as an intriguing philosophical subject that, unfortunately, will not be fully addressed in this thesis. What will be address –to what extent is discussed in the last chapter– is the effect scale has in some of the fundamental issues regarding wave propagation: dispersion and attenuation. Dispersion refers to the dependence of phase velocity on frequency. This can lead to a change in the shape of a time-localised pulse as it propagates through a dispersive medium. Dispersion is attributed to an intricate interference mechanism introduced by the medium's heterogeneities. On the other hand, attenuation causes decreased resolution of seismic image with depth and transmission losses induce variations in amplitudes with offset [*Ursin and Toverud* (2002)]. Therefore, it is important to understand such wave propagation phenomena so that they can be corrected for seismic imaging.

The fact that attenuation and dispersion were related was recognized by Kramers and Kronig [*Landau and Lifschitz* (1984)], who showed that as a consequence of causality and linearity, the real part of the electromagnetic index of refraction (i.e., $c_0/c_P\,(\omega)$, the ratio of the speed of light to phase velocity) could be related to the Hilbert transform of the imaginary part. The term *Kramers-Kronig relations* now refers to the relations between physical quantities that are fundamentally expressed through Hilbert transforms. In the simplest case, the two quantities may be taken as the real and imaginary parts of a complex function in which each of the pair may be expressed as an integral over the other. The fact that dispersion and attenuation in a medium are not independent of one another, but are related due to causality forms the basis of this thesis.

1.3. Objectives of this thesis

The seismic methods are the most fundamental non-invasive techniques for extracting information about the physical and geological properties of the subsurface. Lack of understanding of the seismic images acquired is a serious impediment in the evaluation and usage of this information. In order to facilitate better understanding of the subsurface different seismic datasets are linked, which are acquired at different scales, including field and laboratory experiments. The main underlying objective of this study is to investigate and quantify the attenuation and dispersion in transmission seismic measurements and to compare the findings with models constructed from laboratory measurements. The complexity of the natural features does not allow for an accurate representation in an artificial laboratory. Similarly, when interested in developing a methodology, a controlled environment is necessary. Natural Laboratories provide both the complexity of the natural features and the controlled conditions required for the development of new field-experiment techniques.

Two Natural Laboratories amounting to two different outcrops were chosen mainly for their fundamental geological difference. The first site, Boulogne, is a typical Late Jurassic consolidated to partly consolidated siliciclastic sequence, dominated by shale and mudstone with few alterations of sandstones and limestones. The second site, Cap Blanc in Mallorca, is an analogue of a carbonate hydrocarbon reservoir. It is a Miocene coral reef, with a distinctive upper layer of well organized compacted aeolian sediments, resting upon a thin layer of lagoonal sediments and then on a reef platform of chaotic internal structure.

This research addresses the issue of investigating and acquiring the right link between different types of geophysical, petrophysical and geological datasets and suggests a methodology for integrating this information in terms of attenuation and dispersion. It is expected that the links between measurements at different scales are distinctive of the geological setup of the field.

1.4. Structure of this thesis

This thesis is divided into six chapters (Figure 1.1). Chapter 2 gives an insight in the effects of scale and the control they exert on acoustic properties. Chapter 3 includes the theoretical background and the tools that will be used in order to achieve the goals of this

research. The concepts of wave propagation in layered media, regularization of velocities and attenuation and dispersion are presented and discussed. For illustration purposes a simple synthetic model is used. An average effective media is suggested, that approximated the transmission response and is used on the real data for attenuation and dispersion approximation. Chapter 3 is related to Appendix A, where the convention of Fourier transform, the definition of Hilbert transform and details about the wavelet transform are given. Chapter 4 is related to the experiments performed in the first Natural Laboratory. A brief description of the acquisition of the transmission measurements and the geology of the area is presented. The link between the different measurements acquired is explained and conclusions for the nature of the measurements are drawn. Effective attenuation is estimated from the VSP data, and attenuation due to internal multiples is estimated by modelling. For the model we use ultrasonic measurements from cores. Chapter 4 is related to Appendix B, where a discrete particle model (Lattice Solid Model or LSM) is presented. This is work was done in cooperation with the University of Queensland, Australia, and is an attempt to study attenuation due to internal friction. Chapter 5 explains the experiments performed on the second Natural Laboratory. Similarly to the first, acquisition and processing of the transmission data is discussed and the key information is identified. Effective attenuation and attenuation due to scattering are also studied. Chapter 6 is a synthesis of results and observations from Chapters 4 and 5. It concludes with the essence of this study: an “improved vision” on scales and multi-disciplinarity.

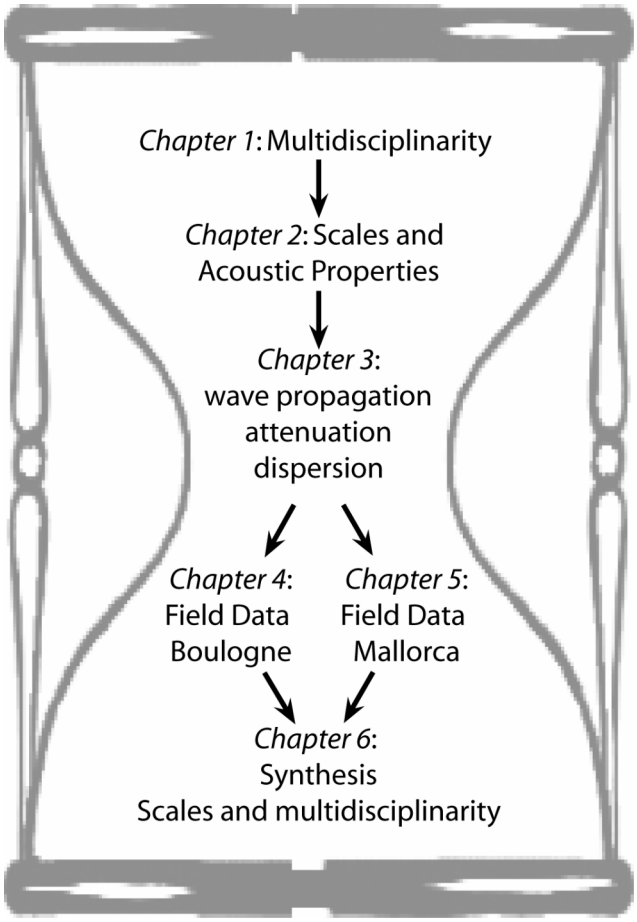

Figure 1.1. Schematic outline of the thesis.

Big fleas have little fleas upon their backs to bite them,
and little fleas have lesser fleas,
and so ad infinitum
Jonathan J. Swift

Chapter 2

Scales at Natural Laboratories

2.1. Introduction

The shared conviction that the stand-alone scientific disciplines are unable or unwilling to address satisfactorily a problem has led to the formation of multidisciplinary groups in both industry and academic environments. Because most participants in such multidisciplinary projects are trained in different disciplines, they endorse diverse perspectives and approaches for solving a problem. The performance of a series of multidisciplinary experiments can lead to a better understanding of the subject under research and shed light to issues that were possibly not anticipated previously. Effects negligible in one discipline may become important in another and an understanding of the origin of such differences can lead to generalising results obtained at various scales [*Wautelet* (2001)].

In this context a common conceptual framework was developed as part of an ISES (Netherlands Research School of Integrated Solid Earth Science) project, the results of which are presented in this thesis. Expertise in reflection seismology, petrophysics and sedimentology was gathered together on two different, relatively small but geometrically well controlled geological objects, the so-called Natural Laboratories.

In exploration geophysics, the seismic method is one of the most powerful, non-invasive approaches for unravelling the subsurface structure. Lithological information extracted from seismic measurements, ranging from in situ seismic sections to laboratory petrophysical studies, can ultimately be compared and linked by the development of an exemplary field laboratory, pertaining to the same geological outcrop.

Seismic measurements at different scales (e.g. surface seismic, vertical seismic profiling, sonic logging, and laboratory measurements) may share a lot of information, but occasionally the observed link is weak. Therefore it is necessary to investigate the relationship between various seismic measurements to explain and enhance the potential of the derived information. The variety of experiments performed concern a wide range of spatial and temporal frequencies, thus observables at different scales are studied and analysed. Consequently, a quantitative integrated approach should be proposed concerning handling information acquired, processed, analysed and interpreted at different scales.

In the following sections the importance of scale of observation and the scale of heterogeneities in the Earth will be discussed. The discussion will involve the effect of scales on acoustic properties of the rocks. In the end, background information of the two Natural Laboratories used in this study will be given.

2.2. Multidisciplinarity and scales

The effort to investigate the combination of a set of phenomena or observations at different scales, to evaluate and parameterise their scale-dependent behaviour -in this study pertaining to geological and geophysical targets- requires a **multidisciplinary** approach. The simple act of juxtaposing several scientific disciplines, without any systematic attempt for integration or combination does not yield optimal results in a study where different types of expertise are necessary. Multidisciplinary teams might teach a survey course, work on a research project, or serve as a presentation or expert panel. Multidisciplinary efforts are often problem centered. The results are frequently confusing because each specialist is speaking her/his language, using her/his particular concepts and focusing on her/his aspect of the problem. This conundrum can be tackled by approaches that involve real interaction across disciplines, though the extent and nature may vary considerably. The grand synthesis aspires to put different disciplines all together, but it has never been successfully accomplished due to the incommensurability of disciplinary structures. Such an approach was not widely applied before 1990 (Figure 2.1), until Daubechies published her pioneering work on wavelets and time-frequency signal localisations [*Daubechies* (1988, (1990)]. She initiated a great deal of

research to look at different scales and accordingly use "translators" to understand and exploit information beyond the direct measurement resolution. According to the science citation index, the usage of the "scale-dependent" term in all listed scientific publications listed saw a sudden rise in 1990 and since then it is of continuously high importance; let alone publications related to scale-dependent concepts without explicitly using the term. For example, Daubechies' two classical publications, mentioned above, have been cited almost 3000 times at the moment of this writing. This emergence of scientific interest and the popularity of the concept of scale is related to an increase in information exchange between various multidisciplinary groups. This has led to scaling of physical properties measured by means of various techniques.

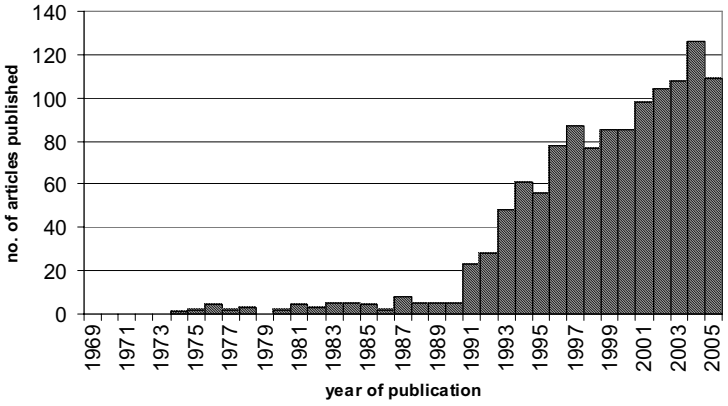

Figure 2.1. Number of scientific publications using the term "scale-dependent" in the last 4 decades. (data from Web of Science, the science citation index, Jan 2006).

The notions of scale in seismic exploration and in particular pertaining to seismic waves will be addressed in the next sections. The main focus will be on describing the concepts of scales of observation and those of geological heterogeneities.

2.3. Scales of observation in typical seismic experiments

Seismic measurements at various scales often exhibit differing results. However, the measured property still pertains to a given medium. Even though linking measurements of different types has become relatively common, especially in the oil industry, the scientific community seems to have reached not yet a good understanding about the cause or the

governing mechanism. For instance, it is well-known that NMO (Normal Move-Out) velocities from surface seismic do not tie well with the velocities obtained from the sonic logs or the laboratory measurements [*Karrenbach* (1995)]. Check shots are often used to stretch the sonic log to the surface-seismic scale. Borehole logs demonstrate that small to intermediate scale variations are not simply random noise. But these cannot be captured as useful information by surface-seismic experiments. Till now, it is difficult to explain these scale-dependent variations. One can assume that seismic velocity does not vary sharply as a function of frequency. Therefore, each measurement is valid in its own frequency range and addresses a specific scale of heterogeneity. Effective medium schemes suggest ways to relate measurements carried out at different scales. This will be discussed in Chapter 3. Overlapping scales can provide additional information. On the other hand non-overlapping measurements exhibit similar information, demonstrating the scale-dependency of phenomena (Figure 2.2). Next, we shall discuss the spatial and temporal distribution of the measurements used in this study.

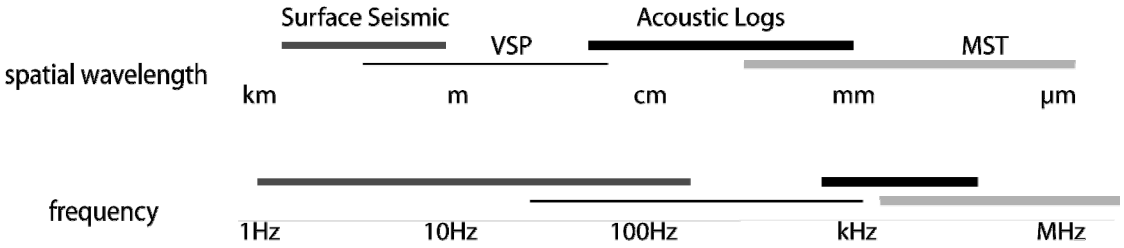

Figure 2.2. Schematic display of different types of seismic measurements with commonly used spatial wavelength and frequency. There can be a fair amount of overlap and a good frequency coverage in the total dataset.

Surface-seismic data can be laterally and vertically dense, but usually with coarse vertical resolution (i.e. in depth or time). VSP data act somewhat in a complementary nature: it has a good depth control, but little to limited lateral information. However, surface seismic and VSP both represent averages over certain intervals. On the other hand, well logs, which usually provide information of seismic velocity, density, porosity and resistivity, have a more accurate and finer vertical resolution but they represent a horizontally limited portion of the formation and can have limited depth range. Laboratory measurements on cores and rock samples usually have even higher resolution but they describe even smaller parts of the medium. The last two measurements are normally considered to offer “point” measurements,

in the sense that they represent the properties of the medium in scales which are much smaller than the size of the Natural Laboratory. In short, the representative volume is different within every measurement, and this leads to the scale-dependency of the measured properties.

Obviously, the most challenging task would then be to relate the MST (ultrasonic measurements using a Multi-Sensor Track) or the well log with the surface-seismic measurements and the VSP. Numerous earlier works have illustrated the problem that different seismic measurements provide different velocity estimations. It is evident that difference in the scale of experiment leads to quite different results in resolution and value of the observed parameter. Figure 2.3A[1] shows stacking velocity derived from surface seismic data (black line) and RMS velocity derived from a P-wave sonic log (grey line) obtained at the same location [*Karrenbach* (1995)]. Figure 2.3B depicts P-wave RMS velocity estimations, calculated from VSP (black line) and from sonic log (grey line) starting at a depth of 600 m. The velocity profiles showed significant discrepancies between 700-1000 m depth, which introduced the large RMS discrepancy [*Salo and Schuster (1989)*]. Figure 2.3C presents one more example comparing between RMS velocities derived from P-wave sonic log (black line) and the laboratory measurements (grey line), from an Imperial College borehole [*Sams et al. (1997)*]. For these datasets, the authors have attributed the differences in velocity to the presence of fractures and cracks (Figure 2.3A), to traveltime discrepancies due to velocity dispersion (Figure 2.3A and B) or to attenuation due to frequency dependent squirt flow. In all cases, the disagreement of measurements was ascribed to scale/frequency-dependent quantities and heterogeneities.

The types of measurements used in this study and their scales of observation are summarized below:

2.3.1. Surface seismic reflection experiments

Surface-seismic measurements generally cover areas in the range tens of meters to kilometres. For exploration applications the typical scale length is tens/hundreds of meters is

[1] Figure 2.3B and C are interpretation of the author, from adapted plots in the publications mentioned

reasonable. The scale of wavelength is typically in the order of a few meters to several hundreds of meters, while the frequency of the recorded signal is usually in the range of 1-100 Hz. In this research, shallow high-resolution surface seismic experiments were performed, using high-frequency vertical and horizontal portable vibrators [*Ghose et al.* (1998)]. Observed frequencies were in the range of 50-800Hz, yielding wavelengths as small as 2.5 m. The spatial distribution of the receivers ranged between 1.5 and 2.0 m and maximum source offset was up to 60 m.

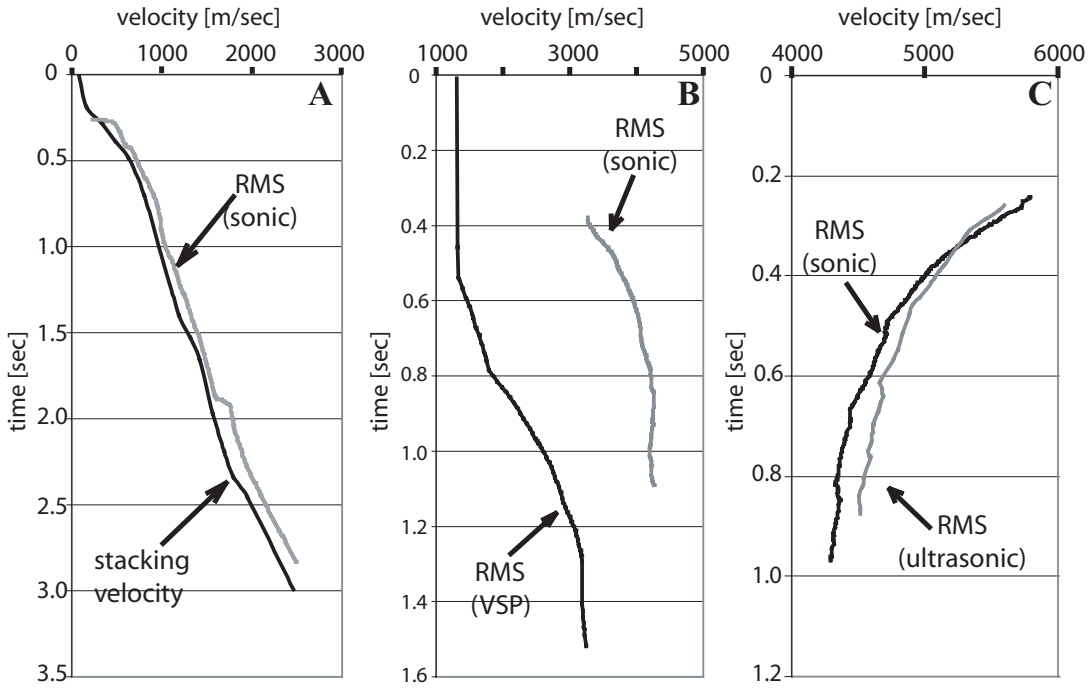

Figure 2.3. A) Example of stacking velocity (black line) obtained from conventional velocity analysis of surface seismic data compared to the RMS velocity (grey line) calculated from the corresponding P-wave sonic log. [*Karrenbach* (1995)] B) Example of P-wave RMS velocities calculated from VSP (black line) and from sonic log (grey line) Log starts at a depth of 600m. *(adapted from Salo and Schuster (1989))*.C) A comparison between RMS velocities derived from P-wave sonic log (black line) and laboratory measurements (grey line), from the Imperial College borehole (*adapted from Sams et al. (1997)*).

2.3.2. Vertical Seismic Profile (VSP)

Vertical Seismic Profile (VSP) experiments can show a large spatial and temporal overlap with surface seismics (although in a vertical sense); nevertheless, the spatial scale typically ranges from meters down to decimetres. This includes reversed VSPs and cross-well measurements. Cross-well measurements often have higher frequencies. Depending on the

type of source (surface or borehole type), the time and frequency scale in VSPs ranges from surface seismic to sonic log values.

In this study, the same surface seismic sources (portable horizontal and vertical vibrators) as for the surface-seismic experiments were used in VSP experiments, with source frequency comparable in range with the surface seismic. At times, a higher spatial frequency could be achieved for the VSP experiments compared to surface seismic experiments, due to the smaller sampling in VSP. The tool had 8 groups of 3-component geophones, each group spaced by 2 m. It was lowered in the borehole 25 cm after each shot, in a near zero-offset VSP geometry.

2.3.3. Acoustic Well Logs

In case of acoustic well logs (sonic logs), there can be spatial overlaps with VSP measurements. Overlaps with the surface seismic experiments are more limited, with few exceptions in very high frequency shallow experiments. The main overlap is with laboratory ultrasonic measurements, especially in the spatial coverage. In this project, acoustic wireline logs were acquired. The source frequencies usually ranged from 7 to 25 kHz (sonic frequencies), and the four receivers were 1 ft apart on the tool. Measurements are usually made every 10cm and transit times are picked manually, or automatically using a semblance algorithm.

2.3.4. Ultrasonic measurements

In this study, ultrasonic measurements (MST) were performed on whole cores, using a pulse centred on a frequency of 320 kHz for this study. By definition, ultrasonic measurements range from 20 kHz to MHz. Spatial interval used in the experiments described in this thesis is at the order of 1 cm. In this research, we consider MST logs as being the finest in scales (both spatially and temporally).

2.4. Scales of heterogeneities

It is widely recognized that natural heterogeneity can typically have multiple scales of variability [*Bourbier et al.), Schön* (1996), *Lu et al.* (2002)]. It is present in most, if not all, physical properties of both the sedimentary cover as well as the crystalline crust [*Goff and Holliger* (2003)]. The intrinsic heterogeneities of a medium are averaged in the characteristic resolution of measurements. This yields apparent properties that are related to the actual properties (Figure 2.4). The effective properties of natural rocks depend on the volumetric fractions of the rock and the properties of the constituents (minerals, pore content, etc.) [*Schön* (1996)]. Clearly, heterogeneity, which depends on scale, is the norm. The opposite, homogeneity, is an exception [*Marsan and Bean* (1999)].

The scale-dependency of the heterogeneities in the various fields of geosciences, has been assessed by various authors. It is now accepted that the phenomena that occur in the field-scale in porous media are scale-dependent. Flow and transport [*Murphy et al.* (1986), *Pachepsky et al.* (2000), *Liu and Bodvarsson* (2003)], resistivity [*Jones* (1995)], permeability [*Neuman* (1994), *Hyun et al.* (2002), *Lake and Srinivasan* (2004), *Odling et al.* (2004)], hydraulic conductivity and dispersivity [*Neuman* (1990), *Winter and Tartakovsky* (2001), *Neuman and Di Federico* (2003), *Nastev et al.* (2004), *Su et al.* (2005)], porosity [*Zhang et al.* (2000), *Sahimi and Tajer* (2005)], and acoustic velocities [*Sams et al.* (1997), *Goudswaard and Wapenaar* (2001), *Herrmann* (2001), *Ghose and Goudswaard* (2004)] are scale-dependent.

In the following section we will focus our attention on the scale-dependent heterogeneities and properties that have significant effect on the acoustic properties [*Braaksma* (2005)].

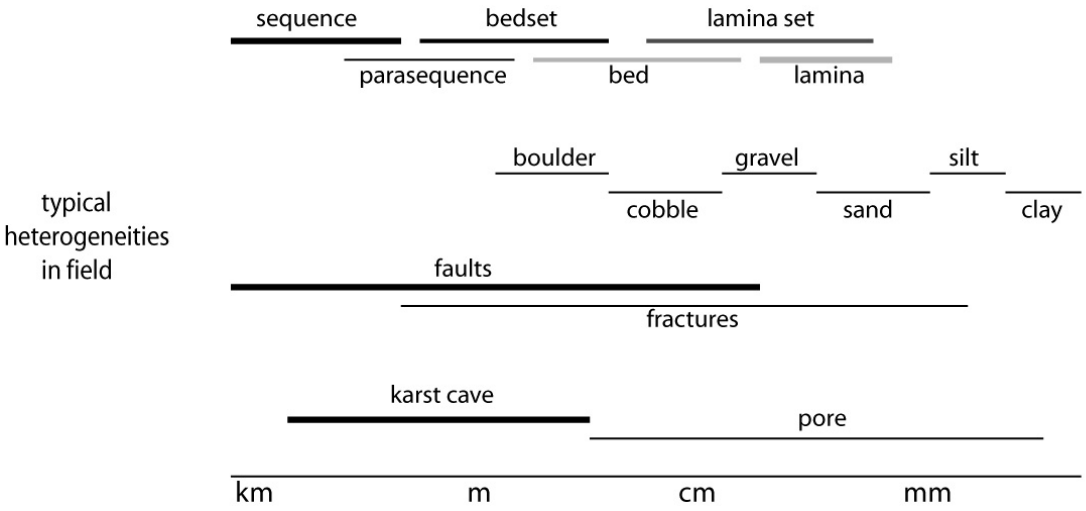

Figure 2.4. Examples of scale-dependent heterogeneities affecting various measurements in geology, including stratigraphic units in hierarchy [*Campbell* (1967), grain size, faults and fractures, and voids in rock formations (from karsts to pores). Strict definitions exist only for grain size. Rock properties and seismic measurements are sensitive to all the above, and thus are scale–dependent over the entire range.

2.4.1. Scale-dependent properties controlling acoustic velocities

As discussed previously, acoustic velocities are controlled by scale-dependent properties. Pore space properties, such as porosity [*Klimentos and McCann* (1990)], pore shape, mineralogical composition of the matrix, consolidation and cementation of the rock matrix, pressure and temperature are the main determinants. They may yield different values for acoustic velocities depending on the component volume fraction. In the following paragraphs, each of these properties in relation to seismic properties is briefly discussed.

POROSITY AND GRAIN SIZE

Porosity is the primary controlling factor for the acoustic velocity variations, along with density. Velocity, in general, decreases with increasing porosity [*Hearst and Nelson* (1985), *Bourbier et al.* (1986), *Schön* (1996)]. However, velocity dependence on porosity is not always that straightforward (Figure 2.5). Velocity correlates well with grain size in granites, but for sedimentary rocks, the effect is more complicated [*Schön* (1996)]. This is because the smaller-size grains tend to be transported easily and fill up the pore spaces. Velocity is, therefore, also a function of grain-size distribution in a complex way. The correlation is better

between velocity and grain size: velocity decreases with increasing grain-size [*Morgan* (1969)].

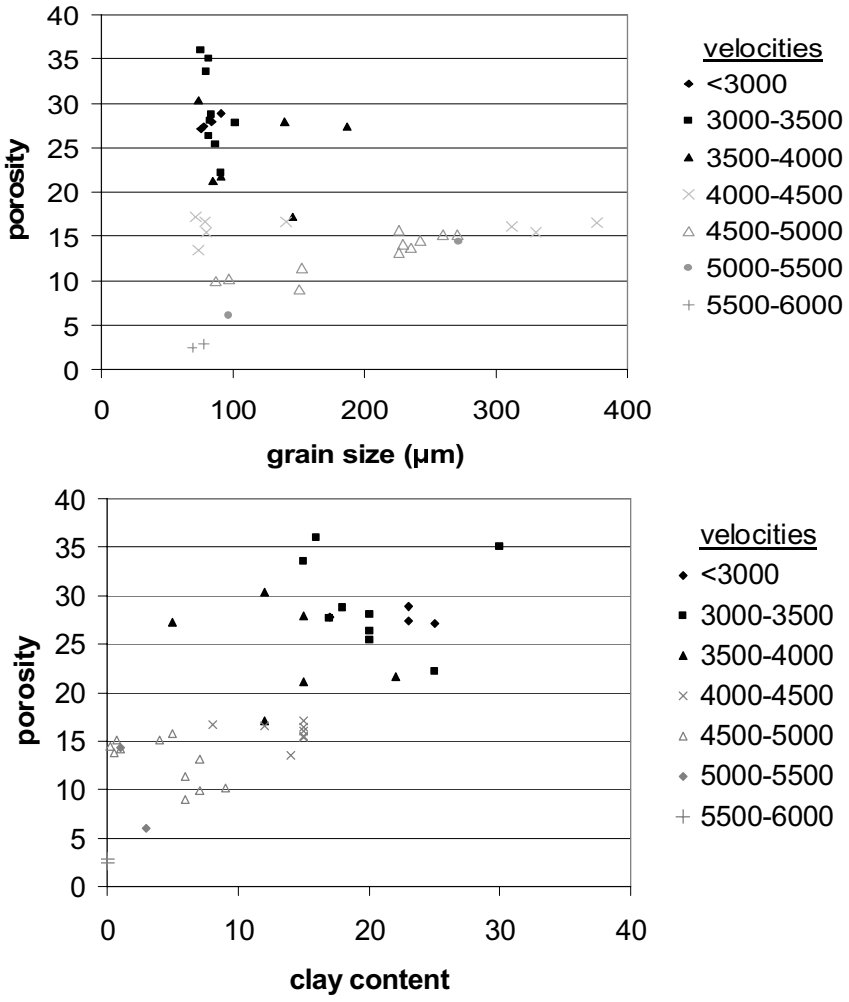

Figure 2.5. Median grain size (top) and clay content (bottom) plotted against porosity for various velocities in sandstones [*adapted from Klimentos and McCann* (1990)]. Median grain size is not really characteristic for the velocity-porosity relationship, while clay content has a more conspicuous effect.

PORE FLUIDS

Even though velocity in clay-bearing sandstones and in shales seems to be independent of the pore-fluid content (unless gas is present), velocity in clean limestones tend to be affected by the pore-fluid velocity. Another important factor is the fluid saturation. This is the case for both field and lab measurements. Many studies have demonstrated that the spatial

distribution of fluid components [*Gregory* (1976)] and fluid mixes [*Kopf* (1977), *Bacri and Salin* (1986), *Cadoret et al.* (1992)] influences fundamentally the P-wave velocity.

MINERALOGICAL COMPOSITION

Another important factor influencing the acoustic velocity in sedimentary rocks is the clay content. Clay significantly reduces the acoustic velocity and increases the pressure-dependence. The influence of the presence of clay depends obviously on the degree of water saturation. Field results from sonic log data [*Castagna et al.* (1985)] suggest that velocity has a linear dependence on both porosity and clay content. The effects of clay strongly depend on its distribution and configuration in the rock frame. Braaksma (2005) demonstrated meticulously the effect of clay content and carbonate content on the measured acoustic velocity from plugs and cores from the outcrop of Boulogne. He found that clay and carbonate content have opposite and overlapping effects of velocity. This result agrees with findings from *Klimentos and McCann* (1990) (Figure 2.5).

CONSOLIDATION

Unconsolidated sediments generally follow the same qualitative trends as their consolidated counterparts. However, cohesion becomes important for consolidated sediments as clays. Physiochemical phenomena and friction are significant for unconsolidated sediments as they highly affect the acoustic properties of the medium. The effects of grain boundary and the capillary tension are also important. In unconsolidated sediments, for example, water saturation plays a fundamental role for a constant porosity [*Ghose and Slob* (2006)]; the P-wave velocity increases abruptly when the water saturation exceeds 80-85% [*Murphy et al.* (1993)]. The effect of clay content is similar; however, the velocity decreases as a result of the low stiffness of clay-water aggregates in the sediment. P-wave velocity in unconsolidated sediments is frame-determined in the dry state, but follows the pore-fluid velocity when saturated.

CEMENTATION - DIAGENESIS

The presence of carbonate cement results in high variations in the acoustic properties, in contrast to the low variation in case of clay-dominated sediments. *Braaksma et al.* (2003) compared the velocity-porosity dependence (for non-carbonate sediments) with results from

Vernik and Nur [*Vernik and Nur* (1992)] and attributed the difference in trends (non-linear versus linear) to difference in compaction and history of diagenesis.

PRESSURE/DEPTH

Overburden and static pressure is another significant factor affecting velocity. Acoustic velocity increases non-linearly (with a decreasing gradient) with increasing pressure, especially when the measured rock sample is water saturated. The effect has been attributed to crack and fracture closing with increasing pressure; the latter plays an important role in carbonates. The shape of the grain also affects the dependence of acoustic properties on pressure. Apparently, more angular shaped grains allow higher contact region than more rounded ones. Rocks with clay/shale exhibit stronger dependence on pressure in comparison with pore-free rocks (i.e. salt, anhydrite). Elastic hysteresis has also been observed; inelastic deformation contributes to this non-linearity. Compressional and shear velocities increase at different rates with increasing pressure [*Schön* (1996)].

TEMPERATURE

Generally, the effect of temperature is small compared to porosity and saturation. Generally a small decrease of velocity is noted with an increase in temperature [*Schön* (1996)]. However, for heavy oil and steam injection processes, time lapse seismic has shown that the temperature effect is the dominant effect.

In conclusion, the complex nature of the influence of different factors, like porosity, pore structure and other physical-chemical properties, makes it difficult to determine any general description and explanation for the scale-dependent acoustic properties. It is, therefore, important that well-defined and controlled Natural Laboratories are used to integrate a plethora of scales of observations and heterogeneities. The efforts to unravel the spatial variability of the heterogeneities should incorporate a multitude of scales [*Painter* (1995, (1996)]. As far as sedimentary rocks are concerned, several authors have considered a wide range of physical measurements. Despite the differences in techniques of measurement and data analysis, all studies depict power law behaviour between the range of scales which is bounded by the resolution of the measurements (Figure 2.2) and the finite size of the

heterogeneity (Figure 2.4). It is thus expected that the discrimination of the exact scaling behaviour is geology or site-specific.

2.5. Acoustic Scales in Natural Laboratories

In the current project, a multidisciplinary group was formed comprising geologists, petrophysicists and geophysicists. These disciplines operate at different scales to observe and evaluate a given physical system. Seismic field experiments and lab measurements also have differing scales. However, it is striking that we still can find remarkable similarities [*Poggiagliolmi and Allred* (1994), *Ziolkowski et al.* (1998)]. Experimental data from two Natural Laboratories have been investigated in this research in terms of seismic velocity variations and seismic wave attenuation and dispersion. Both these outcrops exhibit heterogeneities at different scales and an extended set of geological, petrophysical and geophysical observations was performed.

As mentioned above, heterogeneities in outcrops are, without exception, distributed over a wide spectrum of scales. In order to facilitate the bridging of the entire range of geological, petrophysical and geophysical parameters in a so-called Natural Laboratory, careful selection of the test sites is important. Even though geological analogues are often used to better describe and understand the subsurface imagery, outcrops at the scale and proximity of the seismic measurements are rare [*Braaksma* (2005)].

The first ISES Natural Laboratory is located on the English Channel coast of the northern France. We shall call it the “Boulogne” site. Experiments at this site took place both on land and offshore. The area is a typical Upper Jurassic siliciclastic sequence, characteristic of the North Sea, with relatively simple geological architecture of horizontal to sub-horizontal parallel alternating beds of shale, sandstone and limestone. An excellent fresh cliff exposure of few kilometres of lateral extent is present. The shoreline along this cliff provided a good opportunity for a high-resolution shallow 3D surface-seismic experiment. The beach level represents the equivalent subsurface for the data acquired on the cliff. Marine seismic sections were acquired further offshore. Two boreholes, one of them drilled in the centre of the onshore 3D seismic spread, provided the petrophysical, geophysical and sedimentological tie

between seismic data and fresh cliff. A series of VSP, sonic, core and rock sample measurements, both in situ and on samples in the laboratory, were performed in and from this borehole.

The experiments at the Boulogne site were followed by a scouting tour around Europe. Many sites were evaluated for the feasibility of similar multidisciplinary sets of experiments. Advancing to a more complex geological situation with lateral facies change, a relatively low-relief (100-150m) prograding Miocene coralgal reef sequence on the island of Mallorca, Spain, was selected as the second Natural Laboratory. This carbonate sequence is frequently used for many reservoir analogues for hydrocarbon exploration. Similar to the Boulogne site, an exceptional fresh cliff exposure was available. From this site, rock samples were collected and analyzed in the laboratory. Offshore sparker lines and land 3D seismic experiments were performed. They constitute the larger scale of observations. In the middle of the seismic spread two boreholes were drilled. They provided valuable cores. VSP and ultrasonic measurements were also carried out.

These two datasets are unique, considering the full coverage of scales and frequencies for all the parameters involved. There is a remarkable overlap in the scales of the observations and heterogeneities, offering the continuity necessary to address and link them. In these Natural Laboratories, in the frame of integrated geosciences, one may start observations from mineralogical components (for example calcite or clay under electron microscope or in thin sections) in the order of μm to cm, to grain distribution and lithofacies in the centimetre scale core plugs drilled along a measured section on the cliff faces, to cores and slabs from the project-specific drilled boreholes (of maximum depth less than 150m), and ultimately to continuous observations directly on the cliff face.

Figure 2.6 provides an example of the different scales of heterogeneities observed at different rock samples. A-B are cores and thin sections from the Mallorca Natural Laboratory. C is a SEM image that could also be found in rocks as shown in A and B. Noteworthy are also the on-going studies on defining the scale-dependency of porosity (Figure 2.7).

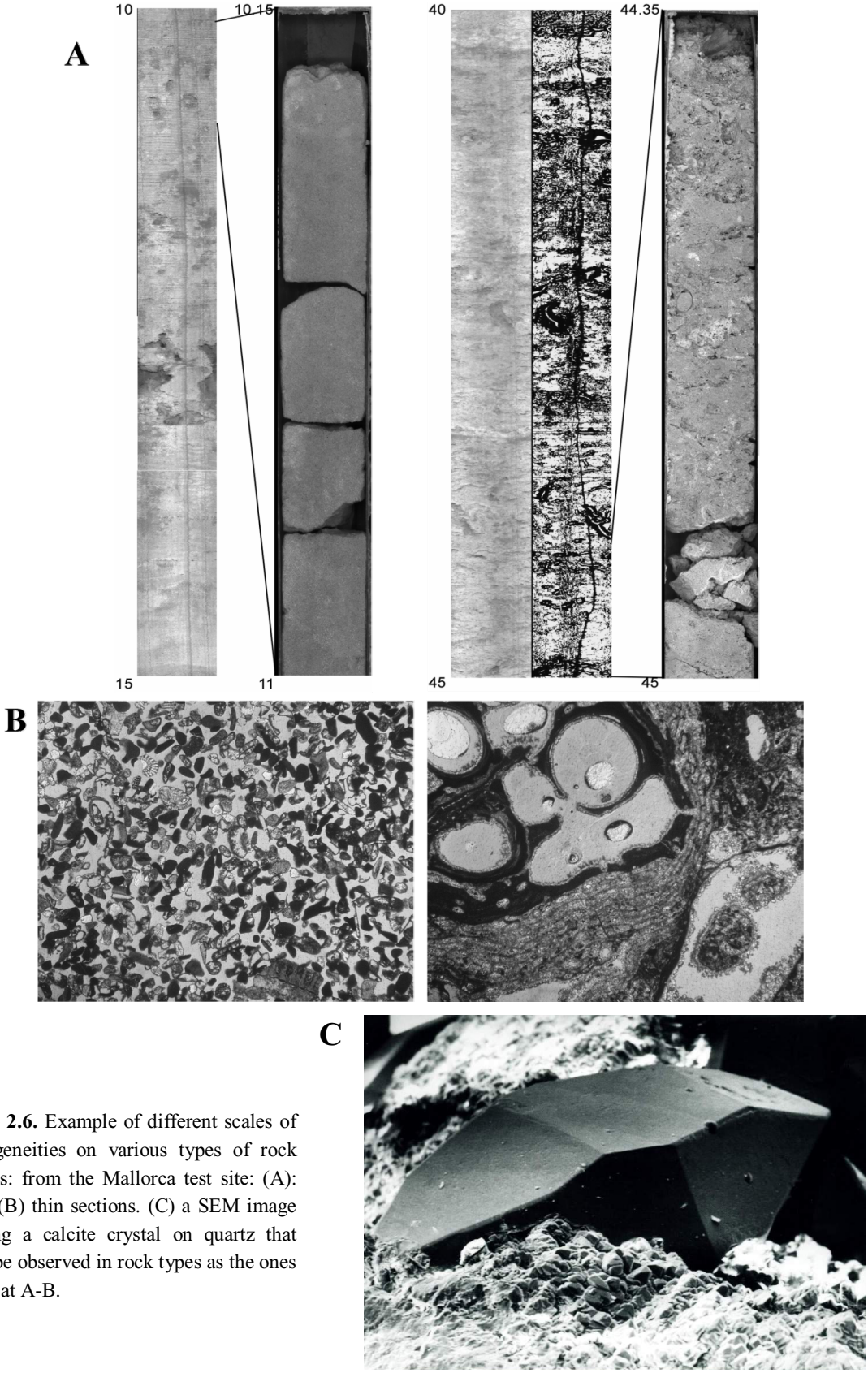

Figure 2.6. Example of different scales of heterogeneities on various types of rock samples: from the Mallorca test site: (A): cores, (B) thin sections. (C) a SEM image showing a calcite crystal on quartz that could be observed in rock types as the ones shown at A-B.

Digital photos from the cliff are taken and primary and secondary porosity are determined in situ [*Verwer* (2004)]. At a later stage these results are compared against laboratory observations on the cores and thin sections.

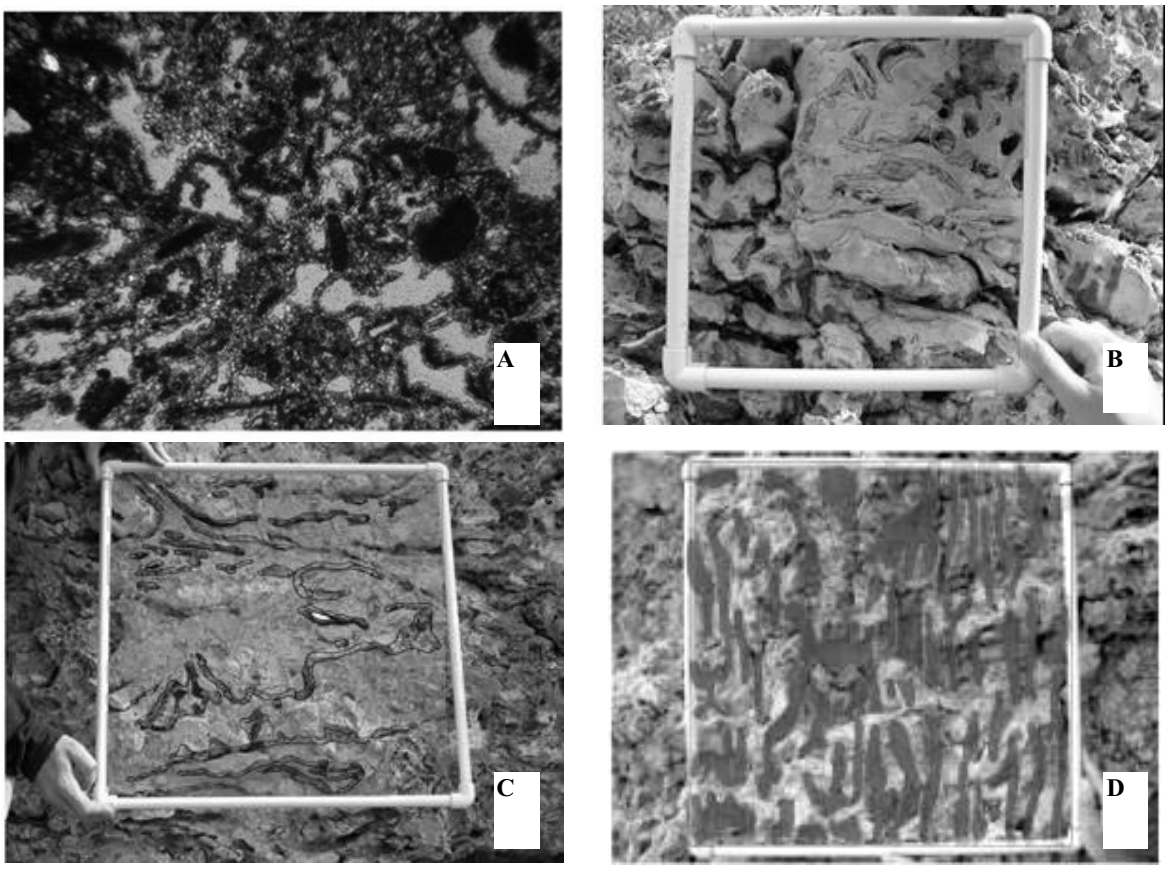

Figure 2.7. Mapping micro- (A), meso- (B), and macro- (C and D) porosity, using thin sections and in situ observations (25cm (B) and 50cm (C and D) square frames) on the cliff exposure in Mallorca [*Verwer* (2004)].

2.6. Multi-scale analysis using wavelet transforms

It was discussed previously that different measurement techniques carried out at different scales are sensitive to different properties of the Earth's subsurface. High-resolution geophysical experiments, constituting the main theme of this research, are performed at the Earth's surface or in a borehole using frequencies, up to 1500 Hz. These experiments offer a spatial resolution of typically less than 2 m. This resolution, inconceivable for common hydrocarbon geophysical exploration from the surface, is still far from the resolution achieved by borehole sonic measurements or laboratory ultrasonic experiments. Matching geological

boundaries appearing as reflections in seismic data to the equivalent changes in sonic and ultrasonic velocities measured in a well and on cores or rock samples is a difficult problem.

In this research the wavelet transform is used as a main tool to bring different datasets together in terms of velocity variations and seismic wave attenuation and dispersion. Wavelet transform has been applied earlier to analyze properties of locally varying signals [*Mallat* (1989), *Herrmann* (1997), *Wapenaar et al.* (2005)]. Once the scale-dependency of velocity is established, conclusions can be drawn about the wave propagation in varying scales. The other focus of our research is the attenuation and dispersion properties in a heterogeneous medium with a specific velocity profile. Shifting from the effect of porosity, we model seismic attenuation as a function of layering in the subsurface. The theoretical concepts and implications, assumptions and limitations, and the results of applications to real data are presented in the following chapters of this thesis.

He who loves practice without theory is like the sailor
who boards ship without a rudder and compass and never knows where he may cast.
Leonardo da Vinci

Chapter 3

Wave propagation, attenuation and dispersion at different scales

3.1. Introduction

The concept of scales in measurements has been explained in Chapter 2. Different results for the same properties (i.e. velocity, density etc) are obtained at different scales of measurements. Ultrasonic (laboratory) measurements and sonic logs are typically used for analysis and model building in reservoir engineering and geophysical projects. The velocities obtained from these measurements can fluctuate greatly. A question that arises is if these measurements (ultrasonic and sonic) can be used for an accurate response of a medium in comparison with the VSP or eventually, surface seismic measurements. The response of a medium depends on the effective volume measured. Differences arise due to different spatial interval or different wave-frequencies used. One should not attempt a direct comparison even though they are all measurements of the "same" medium and there is an excellent control of depth positioning. The underlying assumption and measurement conditions should be taken care of before a comparison is made between measurements at different scales.

The data used in this thesis mainly consist of ultrasonic measurements (MST) on cores in the laboratory and vertical seismic profiling (VSP). The laboratory ultrasonic measurements represent the finest in scale and highest in frequency in the whole dataset. The VSP is the coarsest-scale measurement. The two measurements differ substantially

both in the frequency range of the recorded signal and in spatial interval (effective volume).

In the following chapters we consider acoustic wave propagation. Transmission of acoustic energy depends on the acoustic properties, which are scale dependent. The attenuation and dispersion that a wave suffers during its propagation are as a consequence scale dependent. Dispersion and attenuation are linked because of the principle of causality [*Kronig* (1926), *Kramers* (1956)]. Theories exist that investigate media solely based on arrival times of the transmitted waves. In those cases, dispersion and hence attenuation, are ignored. In this research we consider arrival time, amplitude and phase. In the following sections, we shall discuss some theoretical concepts that describe transmission in 1D finely layered acoustic media. First, we shall investigate the direct arrival time issues. Secondly, dispersion and attenuation will be discussed. Thirdly, a differential effective medium model will be proposed in order to approximate attenuation and dispersion. To illustrate the application of this concept, a fractal model will be proposed and used as a reference.

3.1.1. Attenuation and dispersion

The phenomenon of attenuation is rather complex. While the transmission and reflection parts of the wave propagation are generally well understood, anelasticity and dissipation are not. Various mechanisms have been proposed and each may have a certain importance under certain physical conditions. These mechanisms cover:

- matrix anelasticity, including frictional dissipation owing to relative motions at grain boundaries and cracks [*Walsh* (1966)],
- attenuation attributed to fluid flow, including relaxation owing to shear motion at pore-fluid boundaries [*Walsh* (1968), *Walsh* (1969), *Solomon* (1973)],
- dissipation in a fully saturated rock because of relative motion of the frame with respect to fluid inclusions [*Biot* (1956a, 1956b), *Stoll and Bryan* (1970)],
- shearing “flow” of the fluid layer [*Riesz* (1981)],
- “squirt” phenomena [*O'Connell and Budiansky* (1977), *Mavko and Nur* (1979)],
- partial saturation effects such as gas-pocket squeezing [*White et al.* (1976), *Mavko* (1979)],

- enhanced inter-crack flow , stress-induced diffusion of absorbed volatiles [*Tittmann et al.* (1980)],
- energy absorption in systems undergoing phase changes [*Spetzler and Anderson* (1968)],
- a large category of geometrical effects including scattering of small pores [*Kuster and Toksöz* (1974)],
- scattering due to large irregularities and selective reflection from thin beds [*O'Doherty and Anstey* (1970)].

All these theories agree, explicitly or implicitly, that attenuation, dispersion and effective velocity, are related to the inherent frequency-dependency of the rock-response. Rock properties are scale-dependent and the response of the rock is also frequency dependent. Instead of considering a specific mechanism, attenuation in elastic solids has often been described by empirical formulations. In such a description, the elastic moduli become complex function of frequency. This results in complex propagation velocity, which as explained in *Aki and Richards* (1980), gives rise to wave dispersion and attenuation. To preserve causality of a propagating wavelet, these phenomena must be related via the Hilbert transform [Aki and Richards, 1980]. Ursin and Toverud (2002) have compiled and compared algebraically and numerically eight different models involving complex velocity: the Kolsky-Futterman model, the power-law model, Kjartansson's model, Müller's model, Azimi's second and third model, the Cole-Cole model, and the standard linear-solid model. The model that is most commonly used in seismology and seismic data processing is the Kolsky-Futterman (KF) model [*Kolsky* (1956), *Futterman* (1962)] wherein the attenuation coefficient is proportional to frequency. A constant Q model [*Kjartansson* (1979)] is also frequently used. Constant Q alone is not in conflict with causality if the phase velocity is allowed to converge to zero in the long wavelength limit. The standard linear solid (SLS) model is preferred in finite-difference algorithms because it gives additional differential equations that can be approximated by finite differences [*Causse and Ursin* (2000)]. They found that "*by selecting proper parameters, all models, except the standard linear-solid model, show behavior similar to that of the Kolsky-Futterman model. The SLS model behaves differently from the other models as the frequency goes to zero or infinity"*. Broadband measurement data is needed to select a specific model for a given seismic experiment.

Attenuation is usually described in terms of the attenuation coefficient, α [m^{-1}] which is the exponential decay constant of the amplitude of a plane wave travelling in a homogeneous medium, the quality factor Q and it's inverse Q^{-1} [*Johnston and Toksöz* (1981)]. These quantities are related as:

$$\frac{1}{Q} = \frac{\alpha c}{\pi f}, \tag{3.1}$$

where c is the velocity and f is the frequency. As an intrinsic property of the rock, Q is a ratio of stored energy to dissipated energy. When estimating Q from surface seismic or VSP measurements, one usually obtains the effective quality factor (Q_{eff}). The quantity Q_{eff} represents the combined effect of a)apparent attenuation (Q_{sc}) which is a redistribution of energy due to transmission, reflection and further fragmentation of the wavefield due to internal scattering, such as multiples, and b) the intrinsic attenuation (Q_{int}) or absorption of energy, which is indicative of lithology, fluids and there interaction.

In the quest for the intrinsic quality factor, Q_{int}, one can measure Q_{eff} from the seismic data, surface seismic or VSPs. In order to correctly estimate the absorption of energy during wave propagation, one should use reflection and transmission measurements with accurate amplitude information. Given the conservation of energy, the energy that is not reflected should be transmitted. The energy deficit estimated form the total of the measured reflected and transmitted energy would yield the absorbed energy. However, such field experiments are until now impossible. Therefore, various models and techniques are used to obtain information about the attenuation. This study uses VSP data, because VSP data is comparable to log data, both being transmission measurements. Apparent attenuation due to scattering is modelled using the highest spatially sampled measurement available to us, i.e. MST logs. In this way, we can estimate the scattering effects due to wave propagation through a finely layered medium, assuming no intrinsic losses. This idea forms the basis of a "stratigraphic filter" [*O'Doherty and Anstey* (1970), *Banik et al.* (1985)]. Simply stated, the way a wave propagates through a stack of layers is described as a convolution of the wave with the acoustic properties of the medium.

In order to use this idea, we have to make certain assumptions. First, the Q_{eff} is assumed to be controlled by transmission and reflection from above and below a receiver in the borehole. That means that we assume no isolated transmission signal. Secondly,

when employing the VSP as a "reference" measurement the wavelengths are assumed to be much larger than the thickness of the layers as seen by the core logger (MST) at 320 kHz. These assumptions are reasonable. MST has much denser interval sampling; it quantifies layers as thin as 0.5-1 cm. VSP measurements, on the other hand, do not resolve such fine layering. They yield an "average" effect within the resolution of the measurement. The scattering estimates obtained from the high resolution MST data cannot be linked to those estimates obtained from the VSP data. One needs to apply some scaling before such link between the two estimates is made. Without such scaling MST data can lead to high apparent attenuation due to the high number of impedance fluctuations (large number of fine layers). This would, in turn, lead to an underestimation of the Q_{int} (overestimation of the $1/Q_{int}$). If we use the VSP-derived velocity profile to calculate the scattering effects, the interpreted "layers" would be thicker than these derived from the MST, and consequently the scattering effect would be underestimated (overestimation of Q_{int}).

A compromise is required in order to maintain the detailed information provided by the fine-scale MST measurement, but at the same time to bridge the gap between MST and VSP. If we assume that the MST is an almost continuous representation of the medium, thus more accurate, then we can assign more weight to MST data than to VSP data. Various theories exist on wave propagation through effective representations of layered media. When considering only arrival time issues, averaging techniques return average velocities. Propagation times are bounded by two extremes: the short- and the long-wavelength values. In order to bridge these two extremes, we use the composite averaging method [*Sams and Williamson* (1994), *Rio et al.* (1996)]. The composite method averages the velocity profile. In this way the velocity change at different scales can be investigated. The averaging of the velocity profiles is achieved by means of the wavelet transform, to be explained later in this chapter. The above averaging techniques can be used to calculate the arrival time of the direct transmitted wave. We start with a discussion of the composite method because it offers insight on the averaging effect of a finely layered medium. The composite method approximates the time delay as determined most correctly by full waveform synthetic seismogram.

3.2. Time delay from different averaging schemes

The assumption that the earth can be simulated by a stack of layers has led to the development of various approximate theories. In particular, depending on the thickness, d [m], of a layer compared to the wavelength, λ [m], of the propagating wave, some theories suggest macro-model properties (such as averaged velocities) while others accept fine-layer information. The ratio λ/d distinguishes these two approaches. In the short-wavelength limit $\lambda<<d$; this is called "ray theory" (or RT). In the long-wavelength limit $\lambda>>d$; this is known as "effective medium theory" (or EMT). Note that these two theories are primarily referring to average values of effective velocity of a layered medium, without considering the effect on the amplitude of a propagating wave.

3.2.1. Short wavelength limit ($\lambda<<d$): Ray theory

In this limit, the average P-wave velocity, $c_{P_{RT}}$ [m/sec], for plane waves propagating perpendicular to N layers is given by:

$$\frac{1}{c_{P_{RT}}} = \sum_{n=1}^{N} \frac{g_n}{c_{Pn}} = \left\langle \frac{1}{c_P} \right\rangle, \text{ with } \sum_{n=1}^{N} g_n = 1, \tag{3.2}$$

where g_n is the volume fraction and c_{Pn} is the exact P-wave velocity of the individual layer. The symbol <.> denotes the averaging of the property between the bracket. The velocity can also be expressed in terms of compressibility, κ, and mass density, ρ [kg/m^3], as:

$$\frac{1}{c_{P_{RT}}} = \left\langle \sqrt{\rho\kappa} \right\rangle, \tag{3.3}$$

3.2.2. Long wavelength limit ($\lambda>>d$): Effective medium theory

In this case, some internal multiples will arrive shortly after the direct arrival, thus potentially interfering with the main lobe of the primary arrival, resulting in amplitude change and extra time delay. The wavelet will become dispersed and attenuated. From time delay alone, the average velocity can be determined. When the velocity is calculated using the effective medium theory, the extra time-delay due to the interference of the later

arrivals is taken care of. This is done through averaging of the compressibility, κ [m^2sec/kg] [*Levin* (1979), *Mavko and Mukerji* (1998)]:

$$\kappa_{\mathrm{EMT}} = \sum_{n=1}^{N} g_n \kappa_n = \langle \kappa \rangle, \text{ or} \tag{3.4}$$

$$\frac{1}{\rho_{\mathrm{EMT}} c_{P_{\mathrm{EMT}}}^2} = \sum_{n=1}^{N} \frac{g_n}{\rho_n c_{P_n}^2} = \left\langle \frac{1}{\rho c_P^2} \right\rangle, \tag{3.5}$$

$$\text{with } \rho_{\mathrm{EMT}} = \sum_{n=1}^{N} g_n \rho_n = \langle \rho \rangle. \tag{3.6}$$

The average P-wave velocity, $c_{P_{\mathrm{EMT}}}$, estimated from the effective medium theory, is lower than the ray theory velocity, $c_{P_{RT}}$, due to the weighted average of the compressibility.

It is important to note the fundamental difference between the short-wavelength limit and its long-wavelength counterpart: in short-wavelength limit the multiple-scattered reflections will not interfere with the primary wave, due to the $\lambda << d$ regime. That means that the shape of the wavelet of the first arrival will not be altered by following events. Therefore, it will not be dispersive and no extra phase/time delay[1] will occur due to layering. The amplitude of the direct wave will depend on the impedance contrasts through primary propagation. However, dispersion and attenuation will occur at $\lambda >> d$ regime.

3.2.3. Numerical and Laboratory experiments

The transition between these two theories is of particular interest, because laboratory and numerical models have shown that none of the theories predicts perfectly the traveltimes [*Marion et al.* (1994), *Mukerji et al.* (1995), *Rio et al.* (1996)]. The velocities differ from one theory to the other depending on the ratio λ/d, which is directly related to the scale of heterogeneities (in a non-linear fashion). We shall discuss next several physical experiments which investigate wave propagation through a stack of layers,

[1] Phase delay, dispersion and time delay are all terms pertaining to the same phenomenon. We will be using the term "dispersion" in the remaining of the thesis.

studying both stationary and non-stationary artificial samples at core scale in laboratories [*Morgan* (1969), *Mavko et al.* (1979), *Bourbier et al.* (1986), *Mavko and Jizba* (1991), *Cadoret et al.* (1992), *Marion et al.* (1994), *Sams and Williamson* (1994), *Dvorkin et al.* (1995), *Rio et al.* (1996), *Schön* (1996), *Mavko and Mukerji* (1998)]. To determine the effective velocity of the medium, the first break arrival is used [*Dellinger and Vernik* (1994)].

Marion *et al.* (1994) performed laboratory measurements using a periodic stack of layers of plastic and steel disks. A base sequence of thickness (d) made of different combinations of these two materials was prepared and the medium was constructed by repetition of this base sequence. Transmission measurements where performed and the velocity was determined from the first break arrivals. The derived velocity was plotted against the normalised seismic wavelength, λ/d (Figure 3.1(A) – grey points, grey line). The experimental results revealed two regimes, one almost constant high velocity for low λ/d values, and an almost constant low velocity for high λ/d values. These two regimes correspond respectively to the short- and long- wavelength limits. The transition between the two regimes is quite abrupt (around λ/d=10). This transition was found to be independent of the volume fractions of steel or plastic. Marion et al. (1994) went on to calculate numerically this transition, also considering a two-component layered medium. They found that this transition depends on the acoustic parameters of the medium.

Different studies on the transition between ray and effective medium theory for periodically layered media have yielded similar results. The transition occurs in a relatively small interval of λ/d. In a previous publication [*Braaksma et al.* (2006)], the value around which the transition occurs has been determined numerically, using a two-component synthetic medium consisting of sandstone and claystone. The values of c_p and ρ were derived from the lithological information of the field sites used in this study (Figure 3.1(B)). *Braaksma et al.* (2006) investigated the experimental results of Marion et al. (1994), by performing numerical experiments (Figure 3.1 (A) – black points, black line) Here, the transition occurs around λ/d=5, a smaller value than that with the plastic-steel configuration of Marion et al. (1994). Despite the fact that our two field experiment sites are of different geology, the value where the transition occurs was found to be comparable. This is due to the fact that the impedance contrasts of a binary system that described the lithologies was be similar. Worthwhile noting that calculations using the full waveform

synthetic seismograms compare well with the lab experiments of *Marion et al. (1994)* but less well with the results from their numerical experiments [*Braaksma et al.* (2006)]

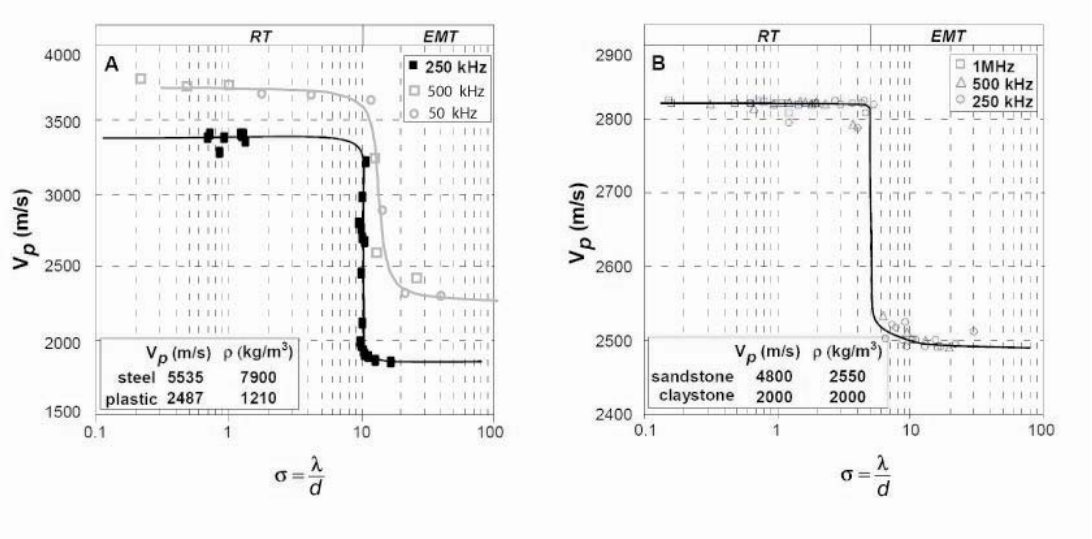

Figure 3.1. Summary of : (A) experimental results (grey points, grey line) of normal incidence propagation through stratified samples of plastic and steel layers (modified after Marion et al. (1994)) and numerical results (black line, *Braaksma et al. (2006)*), and (B) numerical experiment (solid lines) for a typical layered binary system for the Boulogne field, consisting of sandstone (with c_p=4800m/s and ρ=2550kg/m^3) and claystone (c_p=2000m/s and ρ=2000kg/m^3)[*Braaksma et al.*, *(2006)*].

Similar transmission experiments in non-periodic media [*Rio et al.* (1996)] showed that times predicted from ray theory followed closely thick layers of the same material. Following the effective medium predictions, regions with thin layers resulted in an increase in traveltime, hence a decrease in velocity. However, the entire experiment clearly showed that the exact behaviour of the traveltime through such a medium corresponds somewhere between the ray theory and the effective medium theory. Combining the results from these experiments it can be concluded that for the same thickness of layers, small or large velocity fluctuations will cause short or long wavelength behaviour, respectively. A fast approximate method was proposed [*Sams and Williamson* (1994), *Rio et al.* (1996)]. This method gives a good approximation of the first break velocity. This method was also used by *Verhelst* (2000) in order to tie effectively seismic reflection data with well-log data. We use this method to study the change in the average velocity. The average velocity profiles are used to understand how attenuation and dispersion of a propagating wave change in a layered medium. The composite averaging method is described in the following section.

3.2.4. Composite averaging method: middle way between ray and effective medium theories

The experiments discussed above, demonstrate that in layered media none of the two theories (long- and short-wavelength limits) predicts accurately the effective velocity of the medium. For reflections measured from sedimentary rocks the transition from ray to effective medium theory, as explained before, is observed to occur at $\lambda/d=5$ [*Verhelst* (2000), *Braaksma* (2005)]. Verhelst (2000) explained and used the composite method for calculating first-break arrival times. This approach essentially comprises two steps:

1) apply a windowed effective medium theory, and
2) proceed with ray theory for calculating the first arrival time.

The composite method is a fast method for estimating first arrival times, accommodating for both fine-scale and coarse-scale variability. The first step regularizes the small-scale variability. This regularisation allows for implementation of ray theory in the next step. Rio et al. (1996) used a Haar wavelet for the first averaging step. The length of the Haar wavelet was estimated through trial-and-error until the averaged velocities/propagation times matched the laboratory measurements. The composite method was successfully evaluated for a series of synthetic layered media, with Poisson, Gaussian and fractal distributions of velocity and density values. The calculated propagation times with the composite method were in good agreement with the propagating times obtained from full waveform synthetic seismograms.

The application of the first step of the composite method comprises a convolution of the medium properties with a window function. So it is essentially the so-called continuous wavelet transform (see Appendix A). In this thesis we use the Gaussian-function as an analyzing wavelet after *Herrmann* (1997) and *Verhelst* (2000). The subsequent sections will treat the usage of the wavelet transform in the framework of this thesis. Strictly speaking, the Gaussian is not a wavelet because it has a non-zero mean value.

3.2.5. Regularization of a velocity profile

The present work closely follows that of *Herrmann* (1997), *Verhelst* (2000) and *Goudswaard* (2001). The L_1-norm Gaussian function used for the mother wavelet, $\vartheta(z)$, is defined as:

$$\vartheta(z) = \frac{1}{\sigma_z} \exp\left[-\pi \left(\frac{z - z_0}{\sigma_z} \right) \right], \tag{3.7}$$

where σ_z is the scale in depth and z_0 is the depth point around which the Gaussian (Figure 3.2) function is centred. In this thesis, the Gaussian is used for regularization or averaging purpose.

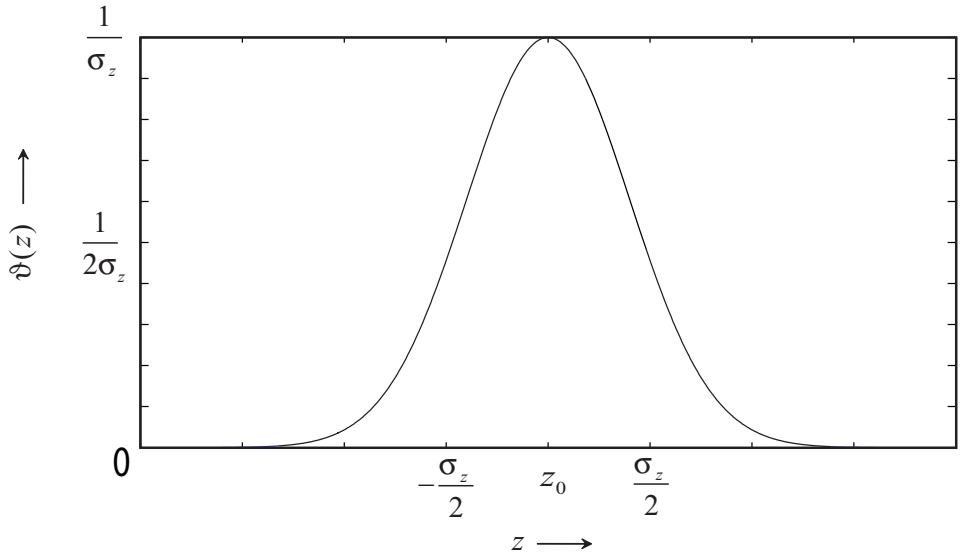

Figure 3.2. The Gaussian function is used as the analysing wavelet for regularizing velocity profiles.

To illustrate the methodology, a synthetic log (Figure 3.3) was created with statistics of fine layering described by a fractal Brownian motion. *Walden and Hosken* (1985) have shown that many well logs exhibit a fractal-like behaviour, i.e. that the power spectrum of the reflection coefficients follows a power law behaviour of the form k_z^a. The synthetic log represents a fine-layered medium of 15000 layers, each of 0.01 m thickness and a= 0.8. A background velocity of 2000 m/sec was chosen. The density ρ has a constant value of 1000 kg/m^3.

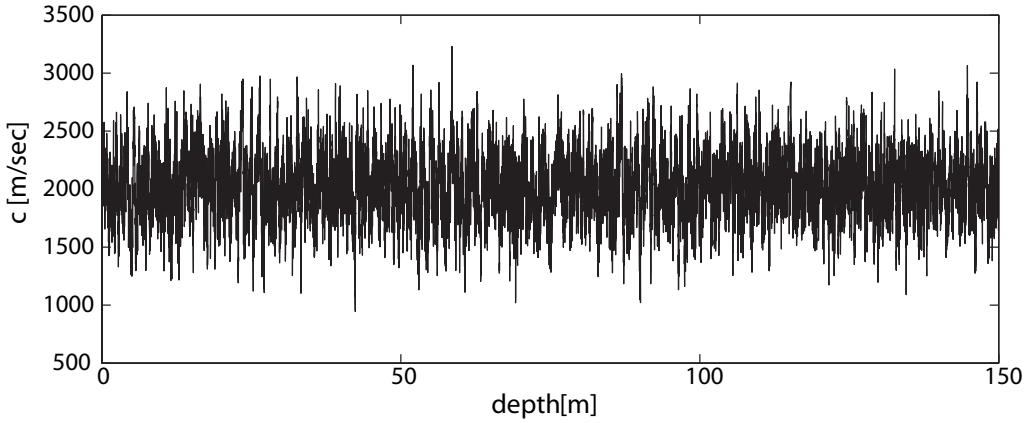

Figure 3.3. Synthetic velocity log. It consists of 15000 layers, each of 1cm thickness. The fractal exponent used is 0.8. The base velocity is 2000m/sec.

The regularized velocity is calculated for different scales. The resulting velocity of the windowed effective medium is given by:

$$\breve{c}(\sigma_z, z) = \sqrt{\frac{1}{\breve{\kappa}(\sigma_z, z)\,\breve{\rho}(\sigma_z, z)}}, \tag{3.8}$$

where $\breve{\kappa}$ and $\breve{\rho}$ are the regularized compressibility and density according to:

$$\breve{\kappa}(\sigma_z, z) = \frac{1}{\sigma_z}\int_{-\infty}^{+\infty} \kappa(z') \exp\left[-\pi\left(\frac{z'-z}{\sigma_z}\right)^2\right] \mathrm{d}z' \text{, or,} \tag{3.9}$$

$$\breve{\kappa}(\sigma_z, z) = \frac{1}{\sigma_z}\int_{-\infty}^{+\infty} \frac{1}{\rho(z')c_P^2(z')} \exp\left[-\pi\left(\frac{z'-z}{\sigma_z}\right)^2\right] \mathrm{d}z', \tag{3.10}$$

$$\text{and } \breve{\rho}(\sigma_z, z) = \frac{1}{\sigma_z}\int_{-\infty}^{+\infty} \rho(z') \exp\left[-\pi\left(\frac{z'-z}{\sigma_z}\right)^2\right] \mathrm{d}z', \tag{3.11}$$

The effect of velocity regularization is shown in Figure 3.4. Velocity fluctuation decreases as the scale becomes coarse. In this way, a smoother medium is generated. The original log (A) and the same log at three different scales (B-D) are shown in Figure 3.4. Panel E represents a look-up table for a nearly-continuous range of scales. The greyscale denotes the velocity values. The regularised velocity profile of small scales (until approximately $\sigma_z = 0.05\,\mathrm{m}$) is very close to the original medium, and as the scale value

increases the velocity log becomes smoother approaching an equivalent averaged medium. Actually for infinite scale, the regularised velocity matches the value predicted by the effective medium theory.

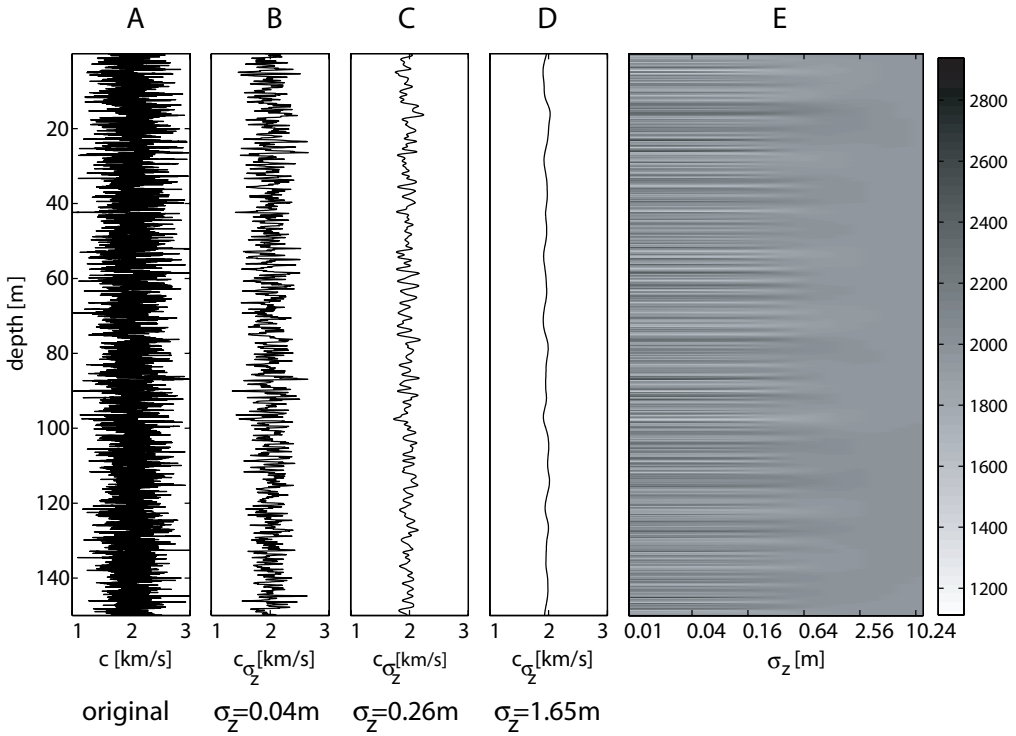

Figure 3.4. Synthetic velocity log (A) of fine-layering described by fractal Brownian motion and the regularised result in three different scales (B-D). The regularised velocity in greyscale for a range of scales, 0.01m-10.24m (E).120 velocity profiles are plotted next to each other. The greyscale denotes velocity values.

At every scale the velocity is regularized according to (3.8). The effect of velocity regularisation can be calculated in terms of the one-way traveltime of the direct arrival, t_P, between two depths z_1 and z_2:

$$t_P\left(z_1, z_2\right) = \int_{z_1}^{z_2} \frac{1}{\left\langle c(z')\right\rangle} \mathrm{d}z' . \tag{3.12}$$

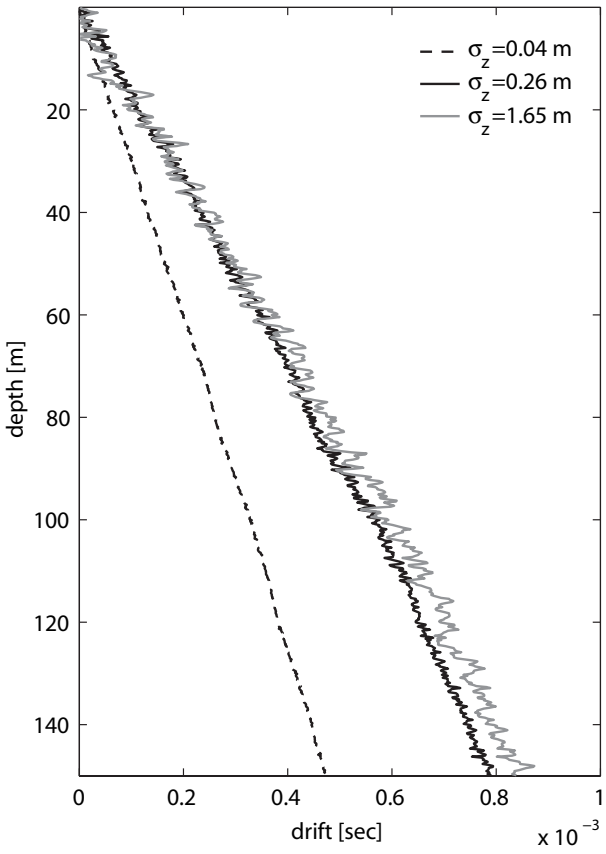

Figure 3.5. Calculated drift for 3 different scales, presented in Figure 3.4.

The quantity *c(z)* represents any type of velocity at any scale σ_z. For the original velocity log the ray theory is used to calculate the traveltime. For the regularised velocities, the one-way traveltime $\breve{t}_P(\sigma_{z,} z_1, z_2)$ with a specific value for σ_z is used:

$$\breve{t}_P\left(\sigma_z, z_1, z_2\right) = \int_{z_1}^{z_2} \frac{1}{\breve{c}(\sigma_z, z')} \mathrm{d}z' . \tag{3.13}$$

The difference in traveltime between of the regularized velocity (3.13) and the velocity from the ray theory (3.12) is called drift:

$$\Delta t_{\sigma_z} = \breve{t}_P(\sigma_{z,} z_1, z_2) - t_P(z_1, z_2), \tag{3.14}$$

The drift of the regularised velocity profiles at certain scales is presented in Figure 3.5. The drift increases with depth (cumulative effect) and with increasing scale. This is due to the fact that the regularized medium approaches the effective medium and hence the

average velocity decreases. The drift fluctuates more with increasing scale. At small scales the averaging effect of the velocity is not that strong. This is because the velocity profiles at small scales are rather similar to the original log. At higher scales the regularised velocity profile is quite smooth, compared to the original log.

The drift is related to the time delay that occurs due to the internal multiples. This will be discussed later on in this chapter. If one could estimate accurately the time delay then a stratigraphic filter could be reconstructed for the specific scale.

3.3. Time delay and amplitude change: Dispersion and attenuation

Until now, we have addressed the issue of the propagation traveltime for the first arrivals only. No further information about the amplitude of the propagating wave can be given or inferred from the above theories. However, in order to use the amplitude, it is of fundamental importance to address the phenomenon of dispersion which is inherently coupled to attenuation. Therefore, the calculation of full waveform seismograms becomes necessary, as these seismograms describe accurately the wave propagation through a layered medium. In order to demonstrate this, we use the reflectivity method [*Redheffer* (1962), *Kennett* (1974)]. Specifically, we use the reflection-to-transmission transform principle [*Wapenaar et al.* (2003)]. In the following sections we discuss how the drift is related to the amplitude of the transmission response of a finely layered 1-D medium. The same finely-layered medium, as used to calculate the synthetic log (Figure 3.3) will be used here. Calculating the full waveform synthetic seismograms, the exact time and the amplitude change, and hence dispersion and attenuation due to the internal scattering, can be calculated.

3.3.1. Vertical propagation through a 1-D finely-layered acoustic medium

A full waveform synthetic seismogram describes the full response of a medium. The internal multiples due to the layering cause velocity dispersion. This can also be described by the so-called stratigraphic filter. Many results have been published so far on this issue, the most well-known being the one from O'Doherty and Anstey (1971). In many studies, assumptions are made about the statistics of the medium. We refrain from doing that. We take a deterministic approach with known values of the acoustic properties of each layer. *Redheffer* (1962), *Kennett* (1974) and *Aki and Richards* (1980) have developed

the reflectivity method for the calculation of the full waveform response. In this study, we use the WRW model [*Berkhout* (1982, (1984),*Wapenaar and Berkhout* (1989)] for acoustic wave fields, and flux-normalized results are presented [*Wapenaar and Grimbergen* (1996)].The notation will closely follow the publications of the DELPHI consortium [e.g., *Wapenaar and Berkhout* (1989), *Wapenaar and Grimbergen* (1996)]. The WRW reflectivity method is based on one-way wave theory. This means that a decomposition of the total wavefield into up-ward and down-ward propagating waves is performed[2]. Downward propagation is described by a propagator W^+ (the + sign denotes the propagation occurring along the positive z-axis, which, in our case, is pointing downwards), and upward propagation is described by W^- (Figure 3.6). The reflection operator transforming the downward propagating wave into an upward reflected propagating one is R^+ and from an upward to a downward reflected wave is R^-. Accordingly we have for transmission: downwards T^+ and upwards T^-. In particular, in the case of 1-D medium, with a plane wave propagating perpendicular to the layering, the propagator W^+ for a medium inter-bedded in two homogeneous lossless half spaces becomes:

$$\begin{aligned} W_g^+(z,z_0,\omega) &= W_p^+(z,z_0,\omega) \\ &+ \int_{z_0}^{z} \mathrm{d}z' \int_{z'}^{z} W_p^+(z,z')R^-(z')W_p^-(z',z'')R^+(z'')W_p^+(z'',z_0)\mathrm{d}z'' \\ &+\ldots, \end{aligned} \tag{3.15}$$

where the W_g^+ is the so-called flux-normalised generalised primary propagator [*Wapenaar and Grimbergen* (1996)] and ω is the angular frequency. The W_g^+-propagator includes the effects of internal multiples. The first term of (3.15) describes the direct propagation, while the added terms describe the first, second etc. order of internal multiples. The quantities $W_p^\pm$ are the so-called primary propagators defined as:

---

[2] The definition of the Fourier transform used in this thesis is given at Appendix A.

$$W_p^+(z_2,z_1,\omega)=\exp\left(-i\omega\frac{1}{c_\infty}\Delta z\right)=\exp\left(-i\omega\left\langle\frac{1}{c_P}\right\rangle\Delta z\right)=\exp\left(-i\omega t_P\right), \tag{3.16}$$

with $i=\sqrt{-1}$, c_∞ is the velocity at infinite frequency, and $<1/c_P>$ denotes the spatially averaged value of slowness over the interval (z_1, z_2) and t_P is the one-way traveltime. $<1/c_p>$ is the slowness averaged using the ray theory limit. The global reflection operators, $R^\pm$, in this 1-D medium for vertical wave propagation are defined as:

$$R^\pm(z)=\pm\frac{1}{2Z^{ac}}\frac{\mathrm{d}Z^{ac}}{\mathrm{d}z}, \tag{3.17}$$

where $Z^{ac}(z)=\rho(z)c_p(z)$ is the acoustic impedance.

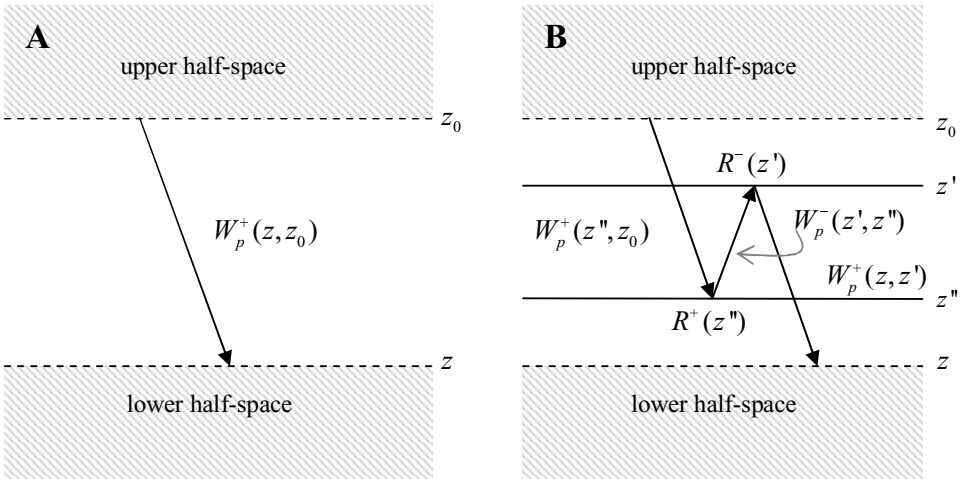

Figure 3.6. A graphical representation of the WRW model and the different terms that are used in (3.15) for a medium embedded in two homogeneous half-spaces: no multiples (A), with multiples (B).

In the rest of this chapter we will focus only on waves propagating vertically, i.e. perpendicularly to the layering [*Wapenaar et al.* (2003)].

For the transmission response $T^+(z_1,z_2,\omega)$ (no free surface multiples are included) of a stack of layers between depth z_1 and z_2, we can specifically write [*Wapenaar et al.* (2003)]:

$$T_0^+(z_2,z_1,\omega) = W_p^+(z_2,z_1,\omega)C(z_2,z_1,\omega), \tag{3.18}$$

where $T_0^+(z_2,z_1,\omega)$ is the transmission response and $C(z_2,z_1,\omega)$ accounts for the coda waves due to multiple scattering caused by the inhomogeneities in the depth interval z_1-z_2. The amplitude of $C(z_1,z_2,\omega)$ can be calculated from the transmission $T^+(z_1,z_2,\omega)$ or the reflection $R^+(z_1,z_2,\omega)$ response, according to:

$$\left\{C(z_2,z_1,\omega)\right\}^* C(z_2,z_1,\omega) = \left\{T_0^+(z_2,z_1,\omega)\right\}^* T_0^+(z_2,z_1,\omega), \tag{3.19}$$

$$\text{or, } \left\{C(z_2,z_1,\omega)\right\}^* C(z_2,z_1,\omega) = 1 - \left\{R_0^+(z_2,z_1,\omega)\right\}^* R_0^+(z_2,z_1,\omega), \tag{3.20}$$

where the asterisk * denotes complex conjugation. The term $C(z_1,z_2,\omega)$ can be written as:

$$C(z_2,z_1,\omega) = \exp\left(-A(\omega)\right), \tag{3.21}$$

with $A(\omega)$ being the Fourier transform of a causal function in the time domain. The real part of $A(\omega)$ is then calculated from:

$$2\Re\left\{A(\omega)\right\} = -\ln\left[\left|T^+(z_1,z_2,\omega)\right|^2\right], \tag{3.22}$$

The imaginary part can be reconstructed from the real part via the Hilbert transform[3]:

$$A(\omega) = \Re\left\{A(\omega)\right\} + \frac{1}{i\pi}\int_{-\infty}^{+\infty}\frac{\Re\left\{A(\omega')\right\}}{\omega-\omega'}\mathrm{d}\omega' \tag{3.23}$$

In this way, $A(\omega)$ is fully determined. The primary propagator contains no information about the amplitude of the wave after it propagates through the medium. It contains the information about the timing of the first arrival according to the short-wavelength limit (the ray theory predicted time). The information about the amplitude, plus the extra time delay ($\tau(\omega)$), expressing dispersion due to the internal multiples, is contained

[3] The definition of the Hilbert transform is given in Appendix A.

in the $C(\omega)$ term. Note that according to (3.26) the imaginary part of $A(\omega)$ describes the dispersion of the propagating wave. The term $\tau(\omega)$ is sometimes referred to as "time delay" or "extra time delay" [*Banik et al.* (1985)] because it has time-units. However, time in the usual context is not a frequency-dependent property. We will be using the term dispersion. We can then investigate the real and imaginary part for $C(\omega)$ or, otherwise, the real and imaginary part of $A(\omega)$:

$$C(\omega) = \exp\left(-i\Im\{A(\omega)\} - \Re\{A(\omega)\}\right), \tag{3.24}$$

Combining (3.24) and the notation from Aki and Richards [p.168, eq. 3, 1980] for the "temporal" seismic quality factor Q, we can write:

$$\exp\left(-A(\omega)\right) = \exp\left(-i\omega\tau(\omega)\right)\exp\left(-\frac{\omega t_P}{2Q(\omega)}\right), \tag{3.25}$$

Combining (3.24) and (3.25) we have:

$$\Im\{A(\omega)\} = \omega\tau(\omega) \rightarrow \tau(\omega) = \frac{\Im\{A(\omega)\}}{\omega}, \tag{3.26}$$

$$\Re\{A(\omega)\} = \frac{\omega t_p}{2Q(\omega)} \rightarrow Q(\omega) = \frac{\omega t_p}{2\Re\{A(\omega)\}}, \tag{3.27}$$

Because the expression for $Q(\omega)$ contains a division by the real part of $A(\omega)$, it might be more convenient for numerical computations to write:

$$\frac{1}{Q(\omega)} = \frac{2\Re\{A(\omega)\}}{\omega t_p}, \tag{3.28}$$

Here we showed how we can reach and estimate frequency dependent $Q(\omega)$ and $\tau(\omega)$. In the following we will assess the transmission response on the regularized velocity profile, that is to say, the transmission response of the original medium scaled at scale σ_z.

3.3.2. Transmission response of a scaled medium

In this section we will investigate the effect of regularizing the velocity in the transmission response, as well as the relation between the drift Δt (3.14) and the delay $\tau(\omega)$.

By using the subscript σ_z we distinguish the terms for the scaled medium from these for the original medium. For a velocity regularized at scale σ_z that corresponds to a regularized medium at the same scale, we can write, using (3.18):

$$T^{+}_{\sigma_z}(\sigma_z, z_2, z_1, \omega) = W^{+}_{p_{\sigma_z}}(\sigma_z, z_2, z_1, \omega) C_{\sigma_z}(\sigma_z, z_2, z_1, \omega), \tag{3.29}$$

From (3.16), the primary propagator, using (3.14), can be written as:

$$W^{+}_{p_{\sigma_z}}(\sigma_z, z_2, z_1, \omega) = \exp\left(-j\omega\breve{t}_P\right) = \exp\left(-j\omega t_P\right)\exp\left(-j\omega\Delta t_{\sigma_z}\right), \tag{3.30}$$

which means that the time of the first break of the direct arrival can be calculated. When the time delay due to the internal multiples is small, the drift compares well with the first break picked from the first arrival of the full waveform synthetic seismogram. However, the drift cannot be directly used to account for the amplitude change of the wave, because it is only an approximation of the first arrival.

The transmission and reflection responses of the original velocity log (Figure 3.7 A) and certain scales (Figure 3.7 B-D) for the synthetic fractal medium were calculated. Figure 3.7 shows the amplitude spectra of the calculated full waveform seismogram for the velocity profiles shown in Figure 3.4. The complementary nature of the transmission and reflection amplitude spectra is evident. Figure 3.7(A) shows the spectra for the original fractal medium (Figure 3.3). Transmission is nearly completely absent in a wide range of frequencies (500-3500Hz). This is a result of destructive interference. It means that in this frequency range no notable transmission is expected. Conversely, all the energy is reflected back. The regions of destructive interference are of particular interest, because they reveal information about the statistics of the medium. They are regularly used in optics and in dielectric structures [*Szipocs et al.* (1994), *Large et al.* (2001), *Yariv and Yeh* (2002)]. In their acoustic analogue they are related to the impedance contrasts and thickness of the layers. Periodic media illustrate the phenomenon possibly better. In periodic media, these spectral gaps appear also periodically in the amplitude spectra. They have been under extensive investigation [*Rozman et al.* (1994), *Erdos et al.* (1997), *Barra and Gaspard* (1999), *Griffiths and Steinke* (2001)]. Large impedance contrasts result in higher interference for the same layer thickness. Small layer thickness will result in high interference for the same impedance contrasts. As the velocity profile is regularised, the

impedance contrasts decrease, thus the interfence patterns change. The frequency range where the spectral gap was observed (Figure 3.7 A) is now rich in peaks (Figure 3.7).

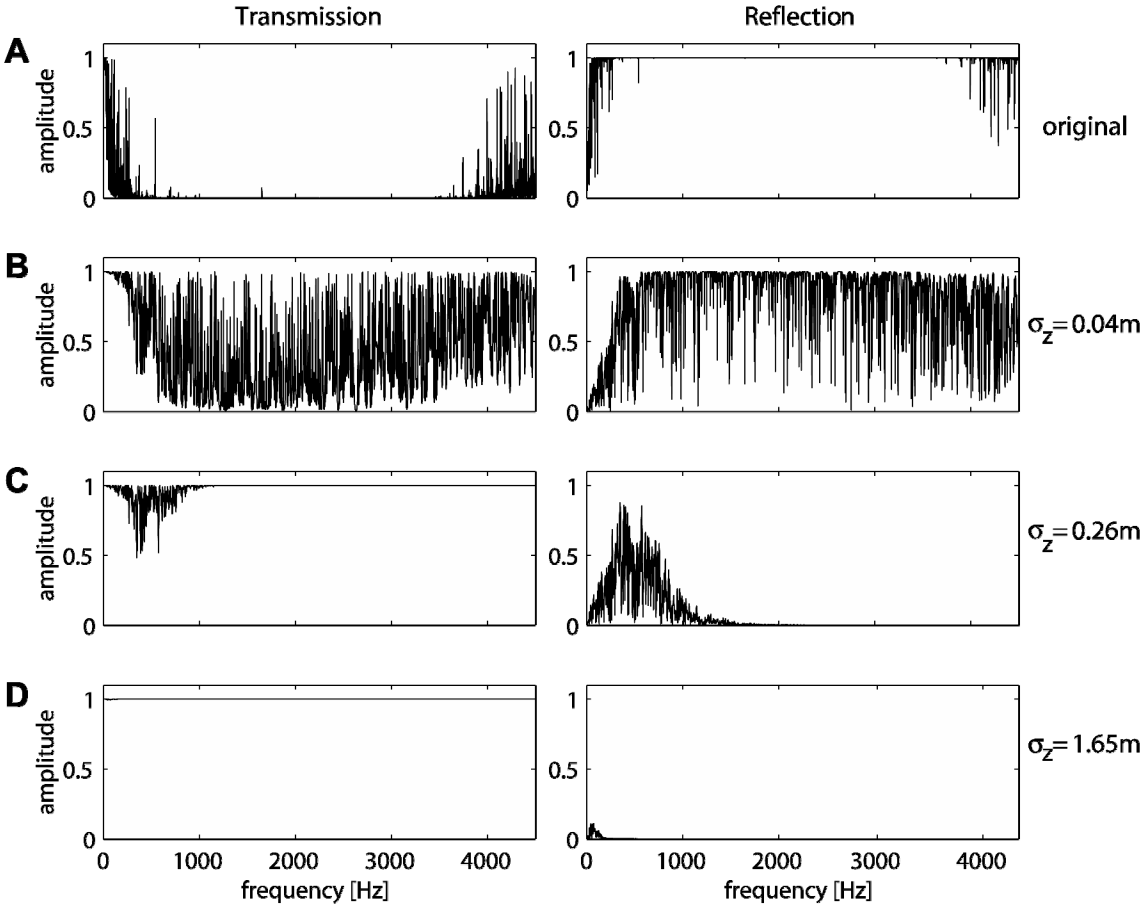

Figure 3.7. Amplitude spectra of transmission (left column) and reflection (right column) response of the fractal medium studied in this chapter. (A) medium at original scale, and (B)-(D) regularised medium averaged to various scales.

It is interesting to investigate the dependence of the coda term $C_{\sigma_z}(\sigma_z, z_2, z_1, \omega)$ on the regularization of the velocity profile, particularly the dispersion term $\tau(\omega)$ and/or the relation between the dispersion and the drift. This relation is important for us, because the ultimate goal is to relate quantitatively the drift to attenuation, and this is essentially relating the drift to the dispersion[4]. It has been demonstrated through numerical experiments that the drift is related to the regularized velocity. The total drift time

[4] The drift is a frequency independent quantity. Therefore it cannot lead to the correct amplitude decay, which involves the coda waves. This has been discussed in the previous paragraphs. A constant time yields a linear phase in the coda term.

increases with increasing scale. At large scales the velocity profile is much smoother, thus the fluctuations are lower. A smoother velocity function will cause less attenuation due to internal multiples as attenuation depends on the local reflectivity fluctuations [*Banik et al.* (1985)]. When attenuation is small, the observed time delay (dispersion) should also be small.

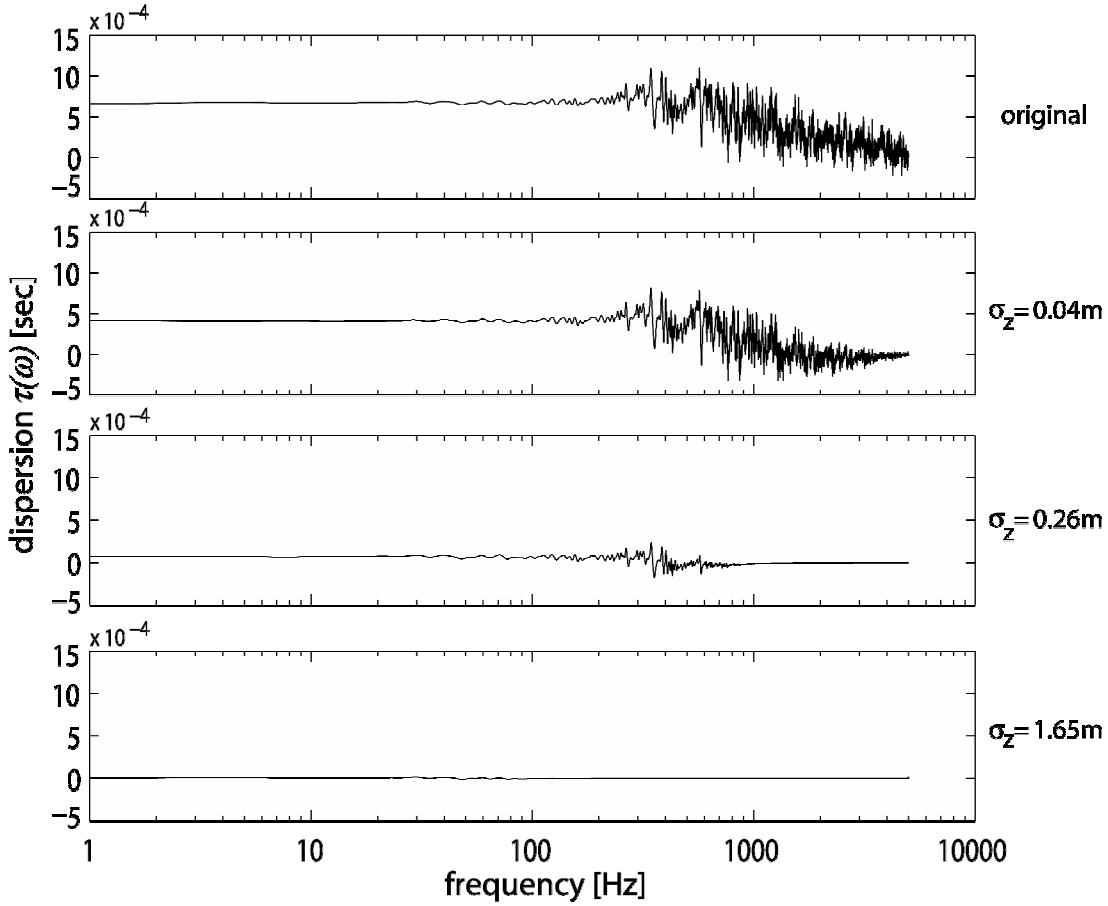

Figure 3.8. The dispersion term $\tau(\omega)$ due to internal multiples as calculated using (3.26) for certain scales. Frequency is plotted here in logarithmic scale.

Using the flux-normalized full waveform reflectivity method, the reflection and transmission responses for the synthetic log were calculated. The coda term was calculated from the transmission response. The dispersion $\tau(\omega)$ (3.26) is plotted against frequency (Figure 3.8). Two regions can be distinguished: constant delay at low frequencies and a rapid decrease at high frequencies. For low frequencies the dispersion delay can be considered frequency independent (Figure 3.9), indicating an almost linear phase change, so a pure time shift in the time domain.

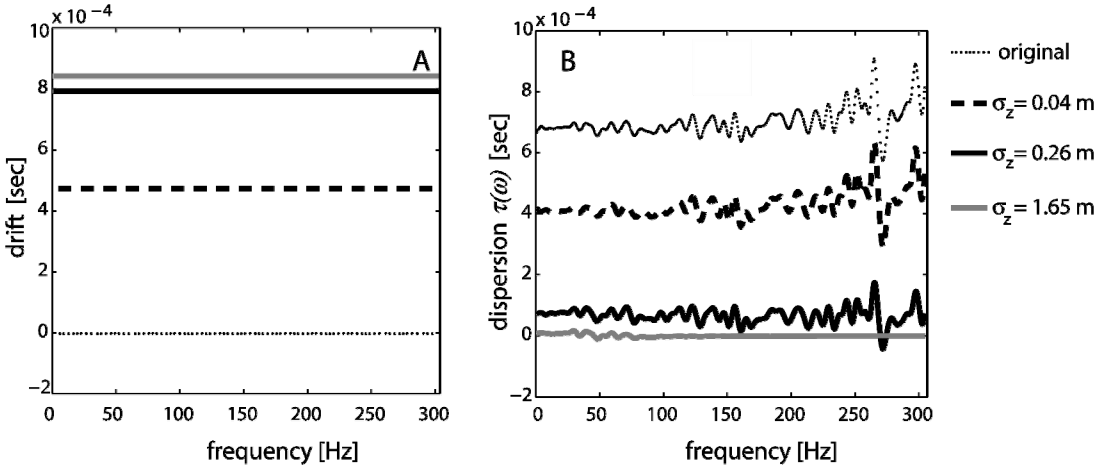

Figure 3.9. A: The drift for the 3 different scales and for the original scale (zero). Unlike the drift, the time delay (B) is frequency dependent. However, at low frequencies the time delay may be considered constant.

The real part of $A(\omega)$ is shown in Figure 3.10 as a function of frequency. It is interesting to distinguish, again, two regions: a linear trend at lower frequencies and a decrease at higher frequencies, for the regularised profiles. The decrease occurs much later for the original profile than for the scaled profiles, which is indicative of the effect of regularization of the velocity profile.

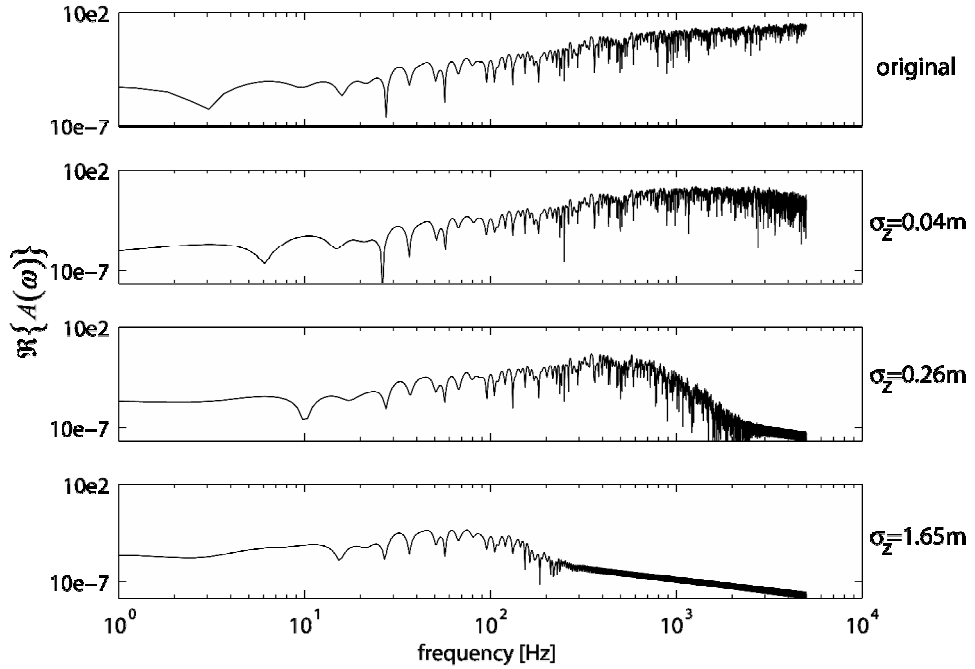

Figure 3.10. $\Re\{A(\omega)\}$ for different scales. Note that both axes are in logarithmic scale.

In an effort to quantify the stratigraphic filter (i.e., the effect of the internal multiples) we present a differential effective medium equivalent to a lossless fine-layered medium.

3.4. A differential effective medium equivalent to finely-layered non-dissipative medium

In this section, a mechanical analogue with damping from classical mechanics is presented that can be used to approximate the argument of coda term $C(z_2, z_1, \omega)$, as described in (3.21), of the transmission response of a planewave propagating perpendicular to the layering of a stratified lossless medium. This is done by using the solution of the differential equation describing the motion of a damped driven harmonic oscillating system.

We have approximated the real and imaginary parts of $A(\omega)$ with y, using the equation:

$$y = i\omega \boldsymbol{a}\left(\frac{1}{\omega_0^2 - \omega^2 + i\boldsymbol{b}\omega}\right), \text{ or,} \tag{3.31}$$

$$y = i\omega \boldsymbol{a}\left[\frac{\omega_0^2 - \omega^2}{(\omega_0^2 - \omega^2)^2 + \boldsymbol{b}^2\omega^2} - i\left(\frac{\boldsymbol{b}\omega}{(\omega_0^2 - \omega^2)^2 + \boldsymbol{b}^2\omega^2}\right)\right], \tag{3.32}$$

with $\boldsymbol{a}$ being the acceleration due to the driving force, $\boldsymbol{b}$ the damping coefficient and ω_0 the resonant frequency of the system. Note that the real and the imaginary parts of the right hand-side of the (3.32) are Hilbert pairs, i.e.:

$$\boldsymbol{a}\frac{\omega_0^2 - \omega^2}{\left(\omega_0^2 - \omega^2\right)^2 + \boldsymbol{b}^2\omega^2} = -\mathcal{H}\left[\boldsymbol{a}\frac{\boldsymbol{b}\omega}{\left(\omega_0^2 - \omega^2\right)^2 + \boldsymbol{b}^2\omega^2}\right], \tag{3.33}$$

We may then write:

$$C(z_1, z_2, \omega) = \exp\left\{-i\omega\boldsymbol{a}\left[\frac{\omega_0^2 - \omega^2}{(\omega_0^2 - \omega^2)^2 + \boldsymbol{b}^2\omega^2} - i\left(\frac{\boldsymbol{b}\omega}{(\omega_0^2 - \omega^2)^2 + \boldsymbol{b}^2\omega^2}\right)\right]\right\}. \tag{3.34}$$

Let us recall now Figure 3.8 and Figure 3.10, and choose e.g. scale $\sigma_z = 0.26\,\mathrm{m}$ to observe the imaginary and real part of *A(ω)* (Figure 3.11). We can approximate the observed trend, by fitting the **real** part with:

$$\Re\left\{A(\omega)\right\}_{fit} = y_{real}(\omega) = \omega\sum_{n=1}^{N}\boldsymbol{a}_n\frac{\boldsymbol{b}_n\omega}{\left(\omega_n^2 - \omega^2\right)^2 + \boldsymbol{b}_n^2\omega^2}, \tag{3.35}$$

and the **imaginary** part accordingly:

$$\Im\left\{A(\omega)\right\} = y_{imag}(\omega) = \omega\sum_{n=1}^{N}\boldsymbol{a}_n\frac{\omega_n^2 - \omega^2}{\left(\omega_n^2 - \omega^2\right)^2 + \boldsymbol{b}_n^2\omega^2}. \tag{3.36}$$

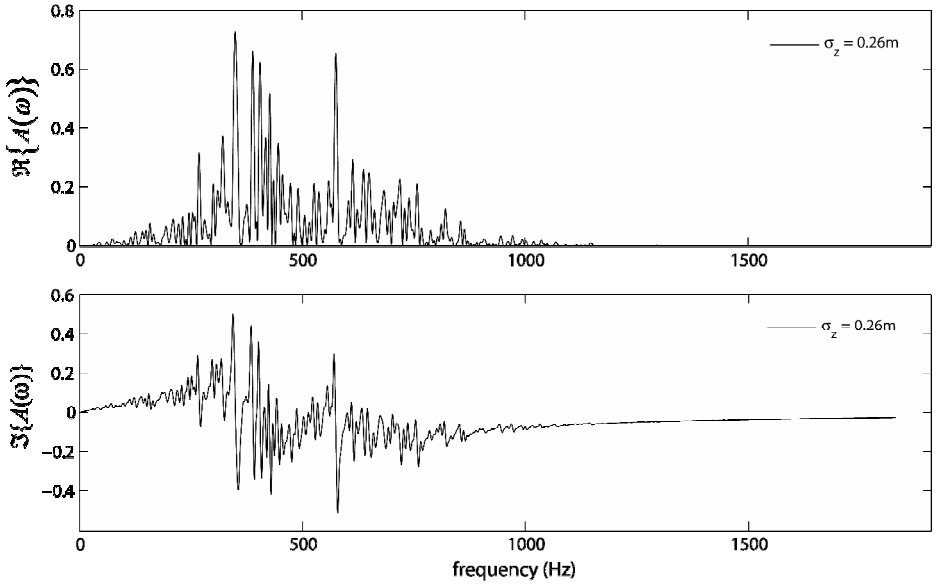

Figure 3.11. Real and imaginary part of the complex *A(ω)* at scale $\sigma_z = 0.26\,\mathrm{m}$.

The values of the coefficients ω_0, $\boldsymbol{a}$ and $\boldsymbol{b}$ that best match the raw data are the ones that minimise the χ^2-value [*Abramowitz and Stegun* (1972)]. The χ^2-value is defined as:

$$\chi^2 = \sum_{i=1}^{r} \left(y - \frac{y_i}{\sigma_i} \right)^2 , \tag{3.37}$$

where y is the fitted value for a given point, y_i is the measured data value for the point and σ_i is the standard deviation for y_i. Various values are tried, in an iterative scheme, for the unknown coefficients. New initial values are used to search for the coefficients that offer the minimum χ^2-value. We use the Levenberg-Marquardt algorithm[5] to minimise χ^2 and determine the coefficients [*Marquardt* (1963), *Levenberg* (1944), *Gill et al.* (1981), *Wikipedia* (2006)]. As χ^2 decreases the fitting improves. The fitting process ends when the rate of decrease of χ^2 drops below a minimum threshold. In order to increase efficiency, we smooth (filter) the input curve. This facilitates making faster initial guesses of the values of the coefficients. The "intermediate" smoothed curve is calculated by employing a binomial (Gaussian) smoothing operation [*Marchand and Marmet* (1983)].

The curves were fitted for one (N=1) and two (N=2) resonant frequencies respectively. Figure 3.12 shows the fitted curves.

Variables	N=1	*N*=2
ω_1	2430	2250
$\boldsymbol{a_1}$	355	250
$\boldsymbol{b_1}$	1526	775
ω_2		3650
$\boldsymbol{a_2}$		120
$\boldsymbol{b_2}$		775

Table 1. Parameters used in (3.35) and (3.36) to fit curves to data as shown Figure 3.12.

Inverting for the transmission coefficient series, $T_0^+(z_2, z_1, \sigma_z = 0.26 \text{ m}, \omega)$, as described by (3.29), can be achieved by constructing the coda term,

[5] The Levenberg-Marquardt fitting is a non-linear least-square fitting.

$C(z_2, z_1, \sigma_z = 0.26 \text{ m}, \omega)$ and then use the calculated direct traveltime for the primary propagator term, $W_p^+(z_2, z_1, \sigma_z = 0.26 \text{ m}, \omega)$. In fact, since the primary propagator is common, only the originally calculated $C(z_2, z_1, \sigma_z = 0.26 \text{ m}, \omega)$ needs to be compared to the inverted ones. The inverted curves are obtained as a result of fitting (Figure 3.13).

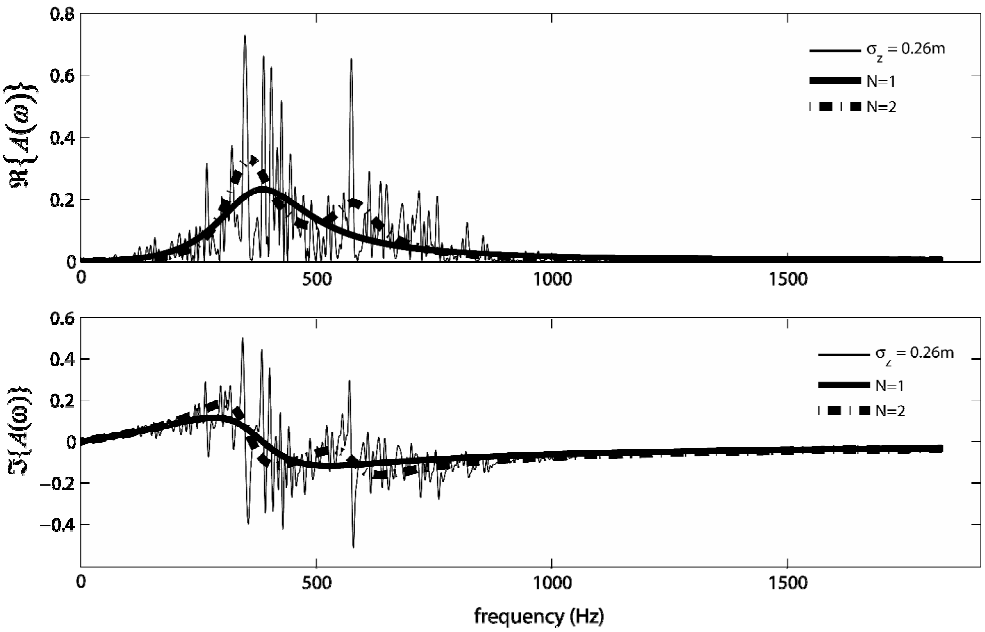

Figure 3.12. Fitting the real and imaginary part of *A(ω)* with one (*N*=1, solid line) and two (*N*=2, dashed line) characteristic frequencies.

It is evident from Figure 3.13 that the approximation, although coarse at first sight, yields good results. The relative amplitude error is less than 0.8% for the first sample. Not only is the amplitude of the first arrival predicted well, but also the subsequent oscillations are reconstructed. Moreover, it is evident that a single term (one characteristic frequency) can actually be sufficient for a good representation and estimation of the attenuation and dispersion.

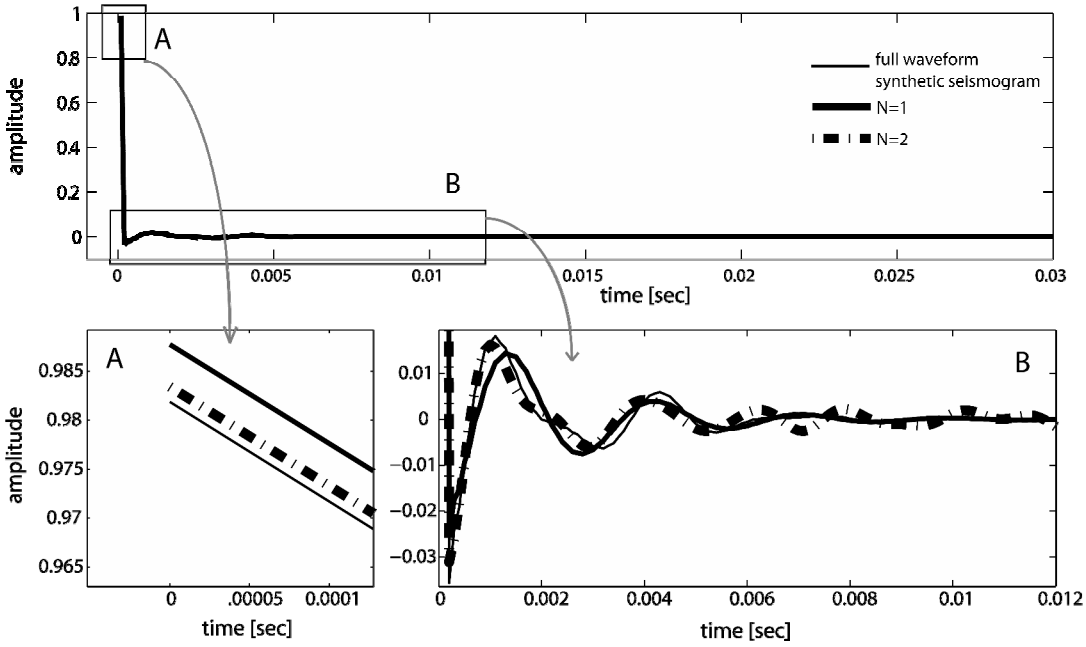

Figure 3.13. Reconstructed coda term ($C(z_2, z_1, \omega)$) in the time domain, using the fitted curves to the fractal model at $\sigma_z = 0.26\,\mathrm{m}$. Zooming in the two marked areas in (A) the first time samples, (B) the first 0.012sec.

To demonstrate the robustness of the proposed differential effective medium, three different realisations of the fractal medium were investigated. For these realisations, we used the same values for the parameters (15000 layers of 1cm thickness, *a*=0.8, base velocity 2000 m/sec) as for the velocity profile shown in the previous sections. The transmission responses and subsequently the *A(ω)* term were calculated. From here on, we will use the term macro-model for the fitting procedure. We use the same values as shown in Table 1 for the macro-model (Figure 3.14). The fitted curves described by the oscillator model are generally good.

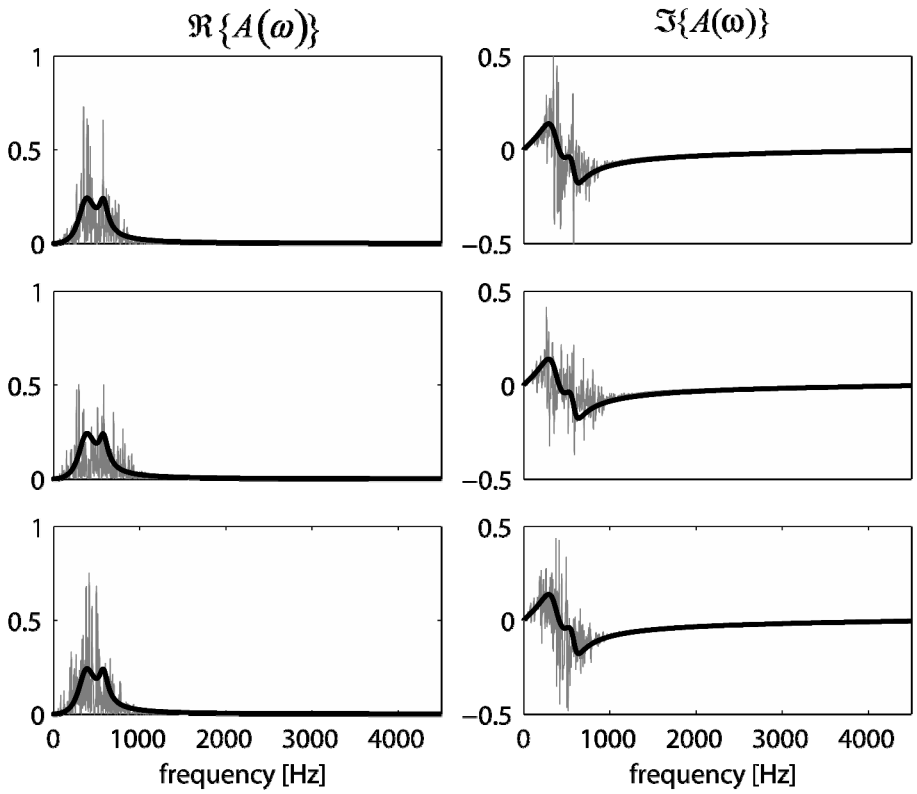

Figure 3.14. Same values for the parameters a, b and ω_0 as in **Table 1**, for N=2, were used to fit 3 different regularized velocity profiles. The velocity profiles are different realizations of the same synthetic fractal model used in the previous sections.

The number and the value of the resonant frequencies used are related to the characteristic frequencies of the *A(ω)* term. Using more than one resonant frequency means a superposition of solutions as described in (3.35) and (3.36). Certain assumptions can be then made for the term a_n in order to describe a mechanical system consisting of more than one harmonic oscillator.

The fact that no more than one resonant frequencies are necessary to fit the real and imaginary part of *A(ω)* as shown is beautifully simple. Naturally, the more resonant frequencies added the better the approximation will be. Adding high-frequency members in the system, the approximation improves in later times. Low-frequency members result in accurate early time amplitude.

3.5. Conclusions

The theory used in this research has been presented in this chapter. We have discussed wave propagation through 1-D finely layered media. Two theories that predict the time of the first arrival of a propagating wave have been considered. These correspond to the long- and short-wavelength limits. It has been shown that none of the above theories predicts accurately the first arrival. An improved method was therefore suggested by *Sams and Williamson* (1994). This composite method rests on both laboratory experiments and numerical results. The method shows that a transition between the ray theory and effective medium theory occurs at a very narrow band of the λ/d ratio. We have used this method to regularize velocity measurements. This allows the velocity, the transmission and the reflection response of the medium to be studied at different scales. However, even though this method yields good estimates of the first-arrival time, it cannot account for the attenuation and dispersion that is caused by internal multiples of the propagating wave.

The reflectivity method is used to calculate the full waveform synthetic seismograms. From the transmission response we can accurately estimate dispersion and attenuation caused by internal multiples in a 1D, finely layered, lossless medium. A combination of the regularization of the velocity and the reflectivity method allows us to model the transmission response at different scales. Hence the dispersion and the attenuation due to scattering could be estimated at different scales.

A differential effective medium is suggested to provide an average for the coda term. The term $A(\omega)$ is described by a simple harmonic oscillator-model. The transmission response of a regularized fractal medium was used to test this model. The number and value of the resonant frequencies involved are related to characteristic frequencies in the spectrum of the transmission/reflection response of the layered medium. Adding more resonant frequencies, that is to say for N>1, results in a better approximation. In the following chapters we use the simplest case; N=1. The parameters $\boldsymbol{a}$, $\boldsymbol{b}$ and ω_0 should be linked with real –elastic or acoustic- medium parameters. In this way, we can use this as a differential effective medium theory with properties directly measured in the field.

Discrete particle models offer the possibility to study heterogeneities at different scales in two- or three- dimensions. We have used the so-called Lattice Solid Model to

study the effects of intra-granular friction on the propagation of wave in a 2D medium (Appendix B). Despite the significant computational cost accurate models can be constructed at any scale to represent dry rocks of any porosity and any velocity/density values. Given the continuous improvement in computational resources such models could become an invaluable tool to model and understand wave propagation at a grain scale. We have used this model to focus on wave propagation in a 2D discrete particle model as a function of frictional losses. In Appendix B, some of our numerical experiments and results presented at various conferences are explained.

In the following two chapters, the concepts described above are applied on real data. Seismic transmission measurements from two geologically different areas will be used. We shall focus on attenuation and dispersion. The effective and the apparent quality factors is estimated, in order to better understand the wave propagation in these two Natural Laboratories.

Before we take to sea, we walk on land. Before we create, we must understand.
Joseph Louis Lagrange

Chapter 4

Scale-dependent attenuation and dispersion in an Upper Jurassic siliciclastic sequence

4.1. Introduction

Sedimentary rocks have been a primary research target due to their commercial importance in hydrocarbon exploration. The siliciclastic sequence studied in this thesis is located in Boulogne, France. It is the age-equivalent of the most important source rock in the North Sea. The outcrop in Boulogne serves as the first integrated Natural Laboratory of our group. In September 2000 a very shallow 3-D seismic survey was performed on a beach just north of Boulogne-sur-Mer in France. Complementary to this experiment, boreholes were drilled and fully cored. VSP experiments were performed at the centre of the 3-D seismic reflection experiment. Rock samples were taken from the exposed fresh cliff.

The multidisciplinary experiments performed in our first Natural Laboratory have multiple objectives. Although not of this thesis, one objective of the 3D surface seismic experiment was to see whether the predicted amplitudes from a tailored survey design could be verified in the 3-D surface seismic dataset (including acquisition foot print) [*Draganov et al.* (2001), *Filippidou et al.* (2001)]. Another objective was to obtain a structural image of the upper 100 m of the subsurface and verify it using a very nearby geological outcrop [*Braaksma et al.* (2005)]. The acquisition and processing of the 3D surface-seismic data were focused on these two objectives. This has produced seismic images with very high resolution. It may be emphasized that prior to this work, 3-D imaging of such shallow targets on land was very uncommon.

The final objective was to achieve a better understanding of the lithological properties that influence or control seismic wave propagation in a siliciclastic sequence. This subject is studied in this thesis in terms of attenuation and dispersion at different scales. Two different types of seismic measurements –vertical seismic profiling and laboratory acoustic core measurements– are integrated.

In this Chapter, we show how we link the high-frequency velocity measurements on cores and the VSP velocity employing the notion of dispersion and attenuation analysis at different scales, as described in Chapter 3. A non-dissipative finely layered medium at the scale of observation of VSP is constructed through a velocity regularization scheme applied to the data of ultrasonic measurements on core. The modelling of the transmission response of a wave propagating through this finely-layered lossless model provides an estimate of the scattering-induced attenuation (Q_{sc}) due to internal multiples. The maximum resolution at the finest scale of observation (acoustic measurements on cores) is 0.01m. Below this limit it is assumed that the layers are homogeneous. Although this assumption is not realistic in a general sense, it is acceptable for the objectives of this thesis. The effective attenuation (Q_{eff}) is determined from the seismic transmission data and subsequently the intrinsic attenuation (*Qint*) is calculated.

4.2. Lithological setting and geological history

The in situ seismic experiments were carried out in the coastal area of northern France near Boulogne-sur-Mer. An overview of the geological history of the area has been described in Braaksma (2005). This area consists of rocks which are age-equivalent of some of the most important offshore marine hydrocarbon source rocks in the North Sea. The sediments were deposited during the Late Jurassic period in the Kimmeridgian (156-150 millions of years ago) and Tithonian (150-144 millions of years ago) stages.

The studied area belongs to the wide, north-west European epicratonic platform [*Cope et al.* (1992)]. During the post-Triassic times this palaeogeographical domain was mainly governed by plate reorganization between the old Caledono-Hercynian orientations and the new Atlantic trends. From the Early Triassic to the Middle Jurassic, the palaeogeography was mainly driven by the southward migration of the Norwegian-Greenland rift and the westward migration of the Tethyan rift. From the Late Jurassic to Palaeocene time it was controlled by

the Atlantic regime and the northward propagation of the North Atlantic rift [*Ziegler and Hoorn* (1989)]. This plate reorganization, occurring by Late Jurassic time, gave rise to doming, subsidence and break up in the adjacent North Sea. The Late Jurassic sections of the North Atlantic margins are marked at their base by either one or two major unconformities, one at the base of The Lower Oxfordian and one in the lowermost part of the Tithonian. These deposits are sharply truncated by the Early Aptian unconformity, which reflects fundamental changes in the oceanic circulation pathways throughout the entire North Atlantic margins [*Tankard and Balkwill* (1989)]. The Jura-sequence in the Boulonnais is characterized by an alternation of clay-rich and sandy formations. The clay-rich formations were deposited below wave base in a low-energy environment. The sandy formations, on the contrary, were deposited near the beach, in a high-energy environment. These different environments resulted in several coarsening-upward sequences. Three clay-to-sand sequences can be distinguished (Figure 4.1); Argiles du Moulin Wibert - Grès de Châtillon, Argiles de Châtillon, Grès de la Crèche and Argiles de la Crèche, and Grès des Oies. These sequences can be seen as sedimentation cycles starting at a few tens of meters depth and building up to the sea-level (beach level).

The sediment deposition is interpreted as part of a homoclinal ramp. The depositional environment distribution on a homoclinal ramp profile [*Burchette and Wright* (1992)] is controlled by the palaeobathymetry and carbonate productivity. No information on the maximum overburden of the Upper Jurassic interval is available from the literature. It is estimated from reconstruction of the regional geology that the overlying sediment package may have reached a thickness of no more than 500 m [*Albani et al.* (1993)]. As a result, most of the sandy and shaly formations are not well compacted.

The vertical alternation and lateral “layer-cake” continuity are, respectively, attributed to relative sea-level changes and deposition on a very low-angle depositional ramp. The depositional signature is reflected in the textural and mineralogical composition, which in turn affects the acoustic response. The detailed petrophysical analysis of borehole data, plug samples drilled from the freshly weathered cliff face along with quantification of the textural and mineralogical properties of the same samples, supplies high quality data for comparison with the published velocity information. In addition, this dataset provides a direct link between acoustic properties and the depositional system.

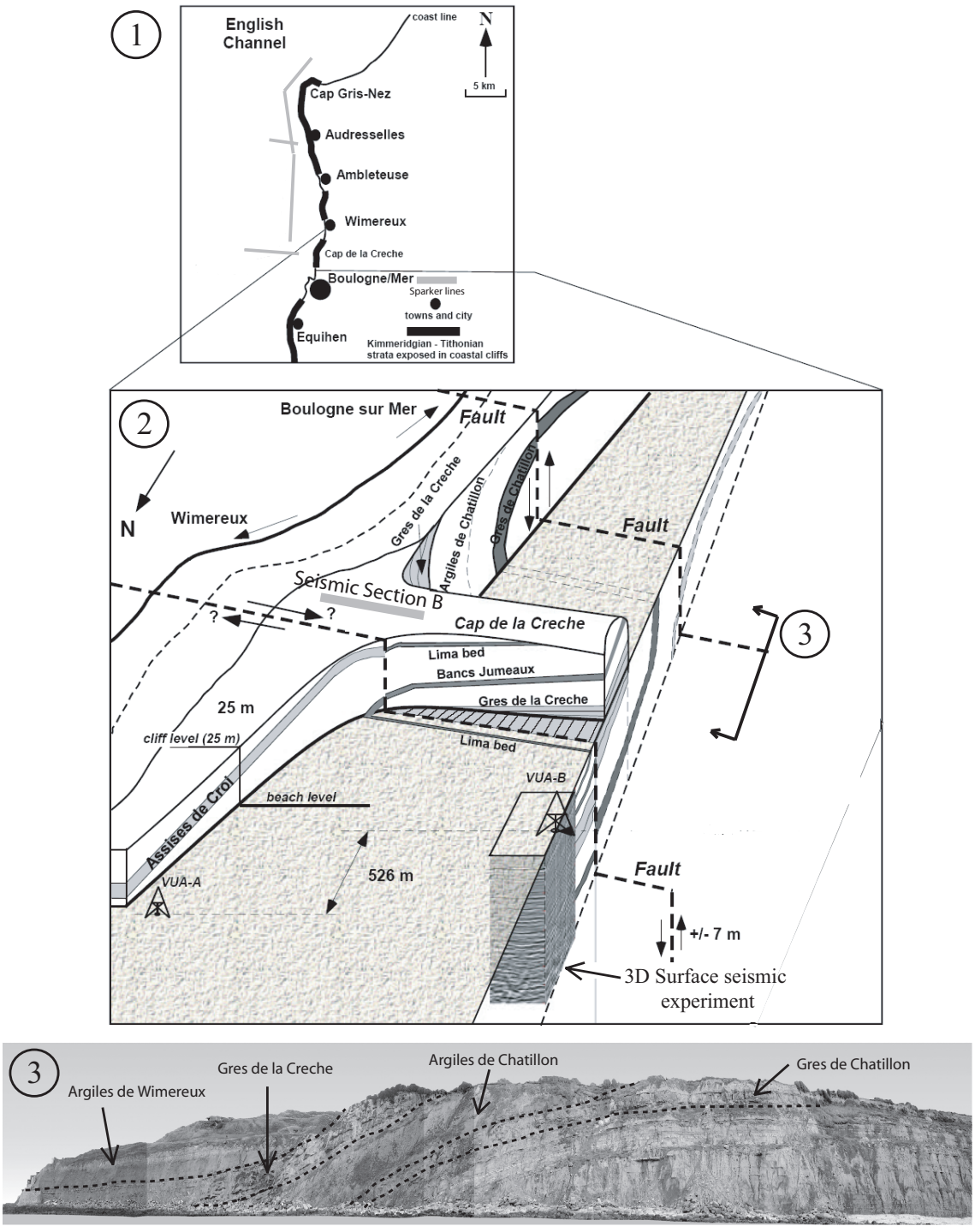

Figure 4.1. The Boulonnais Natural Laboratory: Location of the site (1); schematic NNW view (2) of the Upper Jurassic monoclinal structure folded strata. Indicated is the location of the offshore experiments (1), the seismic section on the cliff and the 3D surface seismic survey (2) that was performed at the beach level. In the middle of the 3D setup, borehole VUA-B was drilled. A second borehole (VUA-A) was drilled a few hundreds of meters further [*Braaksma et al. (2006)*]. (3): The southern part of the exposed cliff with interpretation of the formations.

4.3. Seismic Setting

In the previous section the geological setting has been given, but the seismic setting is as important. The borehole measurements that will be discussed in the next sections, are only describing the seismic along the borehole, i.e., only in one dimension. A crucial question is whether an analysis in the borehole is representative for other parts of the formations, i.e., lateral continuity. This means that other (seismic) data are necessary to illustrate this. As part of the project from ISES, some surface-seismic campaigns have been carried out, culminating in a unique high-resolution 3-D dataset. The results of the surface-seismic, with its characteristics, are discussed in this section.

The first shallow seismic sections from the area were obtained offshore using sparker as a seismic source. Such a source often gives high-resolution images to some tens of meters deep but then deteriorates or gets masked by multiple reflections within the sea layer. The seismic image for the Boulonnais area is shown in Figure 4.2, obtained from *Mahieux et al.* (1988), *Mahieux et al.* (1999) and *Proust et al.* (2001). It can be seen that the reflectivity is high and a high lateral continuity exists.

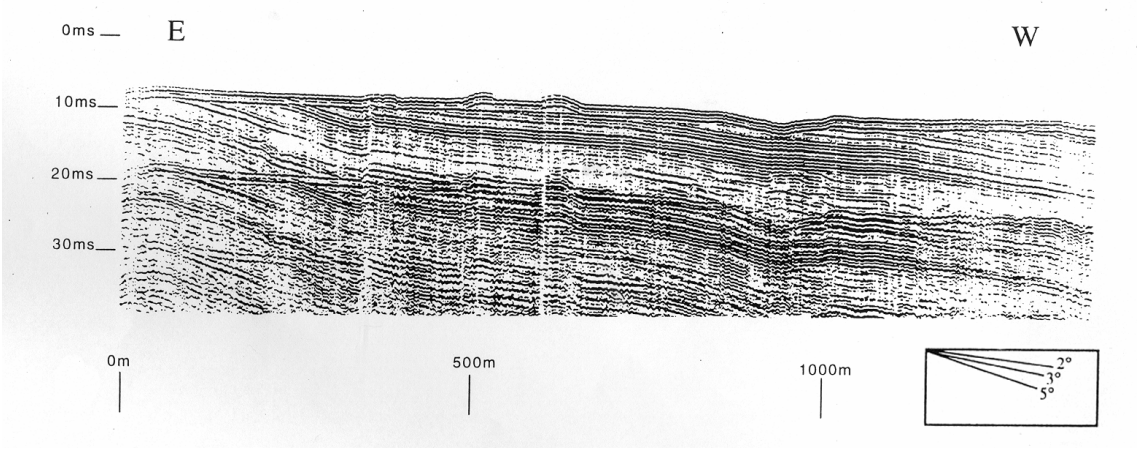

Figure 4.2. One of the seismic sections obtained from the offshore sparker survey, located off Wimereux .

The next seismic results were obtained on-shore, on top of the cliff (see location on Figure 4.1-2). The results are given in Figure 4.3. The image is of poor quality. The main reasons probably being that weathering has taken place which has resulted in a top-soil layer, and that the soils/rocks are tens of meters above the water-table so that the rocks have mainly air in their pores damping the seismic signal.

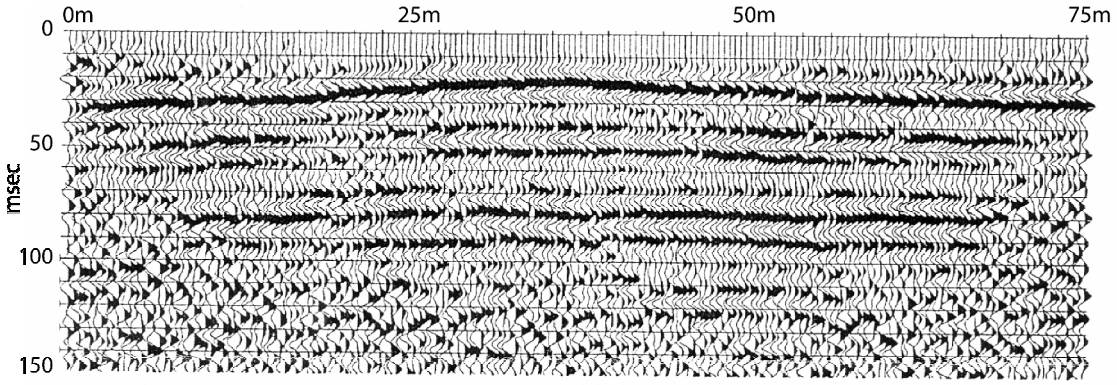

Figure 4.3. Seismic section obtained on top of the cliff near Wimereux (Cap Gris Nez).

Since the idea of our project was to obtain seismic sections right near or above the rocks that were to be studied in the cliff face, none of the above results sufficed. Therefore it was decided to shoot the seismic on the beach in the inter-tidal zone (Figure 4.4). The outcropping rocks have a small dip towards the north so the seismic could be compared to rocks seen on the cliff face somewhat more to the south. Seismically, the great advantage of shooting on the beach is that the effect of the weathering layer on top of the cliff could be avoided and the rocks below the beach would be fully water-saturated, thereby avoiding the air/gas problem in the wave propagation. The beach itself consists of mostly 5 m beach sand, deposited on top of the Jurassic rock succession.

Initial seismic tests on the beach showed superb P-wave reflectivity for the vertical-component data. This was already well visible on the raw records. For the data acquisition, a vertical portable vibrator (Figure 4.5) was used as source [*Ghose et al.* (1998)], and the vertical component of the wavefield was recorded. For the reflections, a dominant frequency of some 650 Hz was obtained. In the initial tests, the full elastic wavefields were recorded, i.e., three components for the source and three components for the receivers. After careful analysis, it turned out that shear-wave reflectivity was not possible to obtain since the records were swamped with surface waves. The sand layer on the beach has a very large contrast with the underlying rocks, specifically in shear-wave velocities, so that the shear-wave energy gets trapped in the sand layer. Therefore, further experiments on obtaining shear-wave reflectivity were abandoned.

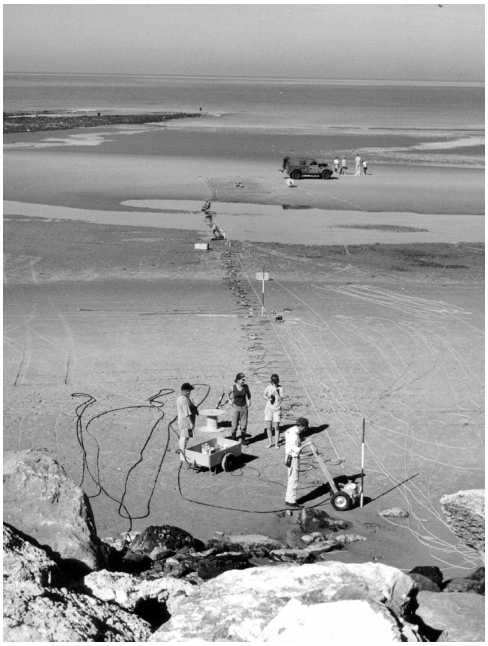

Figure 4.4. Setting up the equipment for the 3D surface seismic experiment in the intertidal zone on the beach, just off Wimereux.

Figure 4.5. A portable vertical vibrator was used seismic source for both the 3D surface seismic and the VSP experiment.

Based on these tests, it was decided to conduct a 3D seismic survey, using vertical-component sources and receivers only, thereby focusing on P-wave reflectivity. The survey was designed such that the so-called acquisition footprint would be minimized, in our case theoretically to a level below 5% [*Volker,* (2002)]. The geometry resembled a marine geometry since an orthogonal geometry was not possible on the beach. It differs from the marine case in the respect that the receivers were placed on both sides of the source, and that the receivers remained at a fixed position for a while. Although the records showed good reflectivity throughout the survey, the amplitudes turned out to be very variable such that effects of an "acquisition footprint" could not be shown in the data [*Filippidou*, (2001)]. The sand layer on top of the rock and the rock surface beneath it, did not allow an accurate amplitude analysis, not only because of it just being there but also because the tide changed the properties of the sand during the acquisition itself. Still, structurally, the obtained image after processing looks very good on account of its resolution, as shown in Figure 4.6. In this figure a 3D post-stack migration seismic section is shown; the data is taken from the seismic cube shown in Figure 4.1.

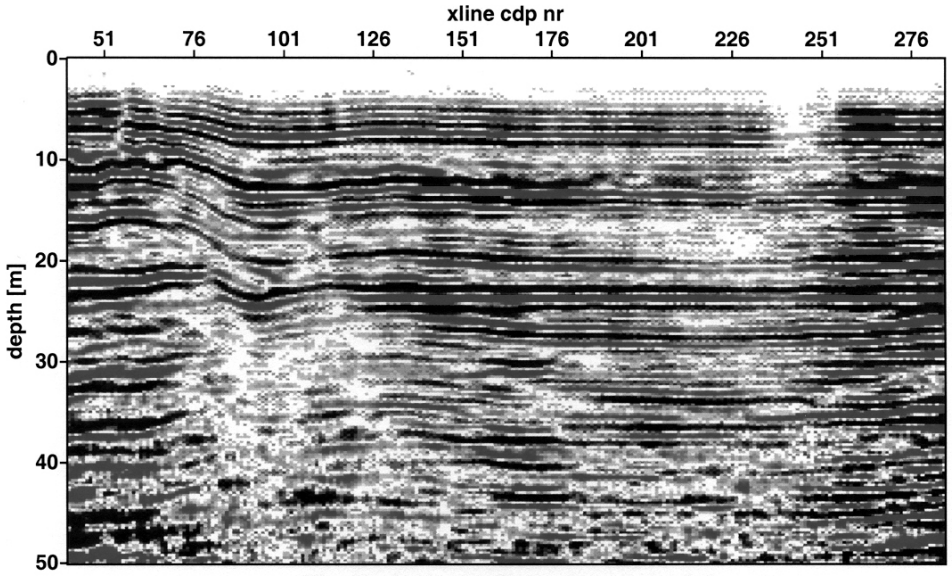

Figure 4.6. Seismic section from 3D seismic survey on beach south of Wimereux (intertidal area).

From Figure 4.6 it is evident that the layering is very continuous in this area, both in-line as well as cross-line. There is some slight folding (or nearly a fault) of the rocks towards the left (South) of the survey area, after which the rocks are again laterally continuous. So based on these data it is expected that the results, obtained from the borehole, will be valid laterally as well.

4.4. Estimation of effective attenuation from VSP Data

The beauty of a VSP experiment lies in the fact that measurements are performed at controlled depths. Therefore no ambiguity in a time-to-depth conversion is involved in the processing scheme. The observed frequencies in the VSP experiment are comparable to those in the surface seismic reflection experiment. The interval velocity profile obtained from a VSP is routinely used for migration schemes of surface seismic data. Opposite to the laboratory core measurements, the rocks of interest are explored in undisturbed state, thus providing measurements of physical properties in situ. When valid estimates of dissipation are derived from VPSs, they provide the basis with which dissipation estimates derived from reflection data and core measurements can be compared [*Spencer et al.* (1982)].

In the last two decades, several authors have used VSP data to obtain in-situ attenuation estimates at specific depth ranges in the subsurface [*Hauge* (1981), *Stainsby and*

Worthington (1985), *Portsmouth et al.* (1993), *Amundsen and Mittet* (1994), *Haase and Stewart* (2004)]. However, attenuation studies through shallow (<100m) VSP experiments are not very common. In many cases, the resolution is not good enough to provide the needed information.

At our site in Boulogne, due to the limited vertical extent of the formations, distinct Q factors for each characteristic formation could not be estimated with sufficient accuracy. Therefore, we have derived an average Q using an adapted spectral ratio method.

4.4.1. Acquisition and processing of VSP data

In September 2001, we designed and acquired a P-wave VSP dataset at one of the boreholes (VUA-B) drilled at Boulogne-sur-Mer (Figure 4.1). The goal was to obtain a reliable velocity profile to be used in imaging. Surface seismic revealed little lateral variation of the formations. Consequently, the horizontal to sub-horizontal layers of the formations are shown to be consistent and laterally invariable at the location of the well. That implies that properties derived from core measurements, borehole logs and VSPs can be representative beyond their point-measurement nature.

Because our early VSP experiments with small source offsets have provided poor quality data, we chose 8m offset. The down-hole seismic receiver used was a 6-level tool, each level housing a 3-component geophone and one hydrophone. The distance between two levels was 2 m. The geophones were clamped to the borehole wall with an air-filled hose. The exact positioning of the tool was sometimes affected by slight upward creeping of the tool, resulting in irregular depth sampling. In this study only the vertical component data are used. The seismic source was a portable vertical vibrator. The same source was used for the 3D surface-seismic data acquisition in September 2000. This vibrator can emit a well-controlled and broad-band seismic signal. For the VSP experiment, a linear sweep with frequency ranging from 50 to 600 Hz was used. Therefore the source signal overlapped with that of the surface-seismic experiment. The exact ground force at the surface was monitored and used for deconvolution to correct for source coupling and source strength variations. Four sweeps of 3500 msec length were stacked for each depth of measurement to enhance the signal-to-noise ratio. The depth sampling interval was 0.25 m. Typical vertical component raw recorded

traces from two different shots for depths 24-34m (left) and 66.20-76.20m (right) are shown in Figure 4.7. Receiver spacing is 2m.

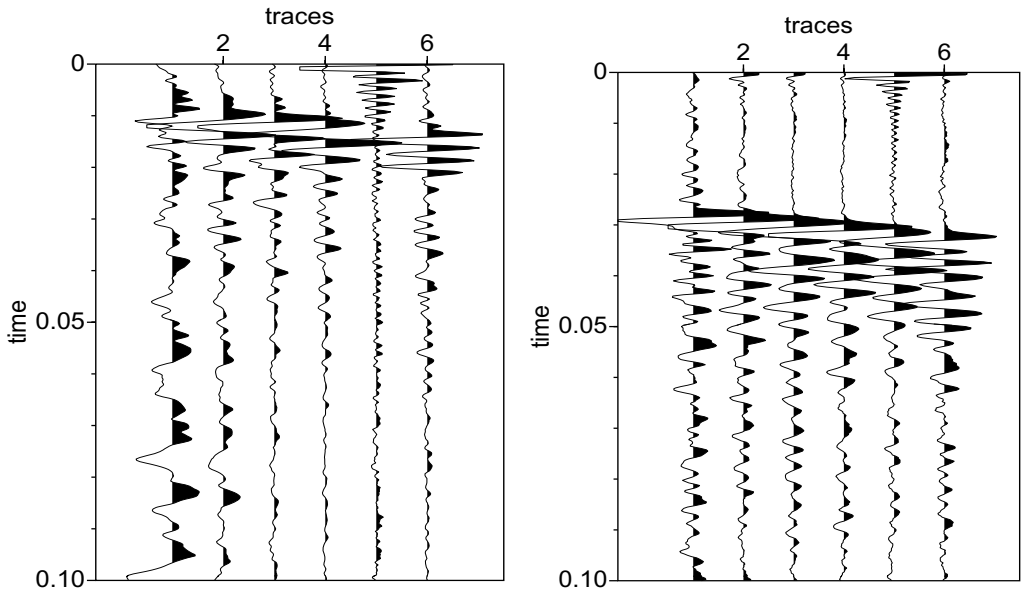

Figure 4.7. Typical vertical component raw recorded traces from two different shots for depths 24-34m (left) and 66.20-76.20m (right). Receiver spacing is 2m.

A standard processing scheme was used for the VSP data. The depth positions were calculated and applied to the data. Noisy traces and duplicates were zeroed. Normal move-out correction was applied using an average velocity of 2000 m/sec. This velocity was obtained from the surface-seismic data. Time statics were applied. The upgoing wave was separated from the down-going wavefield using a median filter. A simple depth factor was used to correct for the geometrical spreading. Interval velocity was determined using the time of the maximum of the envelope of the first arrival (Figure 4.8). The first 15 m data were of poor quality mainly due to near-surface effects, and therefore were not used for velocity or amplitude studies. Even though the quality of the data was reasonable, not many clear reflections could be discerned. This result differs from our observations in the surface seismic experiment. The most prominent reflection comes from below the last sampled depth (78m). For migration of the surface-seismic data a velocity profile was created using the time of the envelope of the first arrival. In order to estimate Q_{eff}, the first arrival is windowed and careful tapering was applied around that time window.

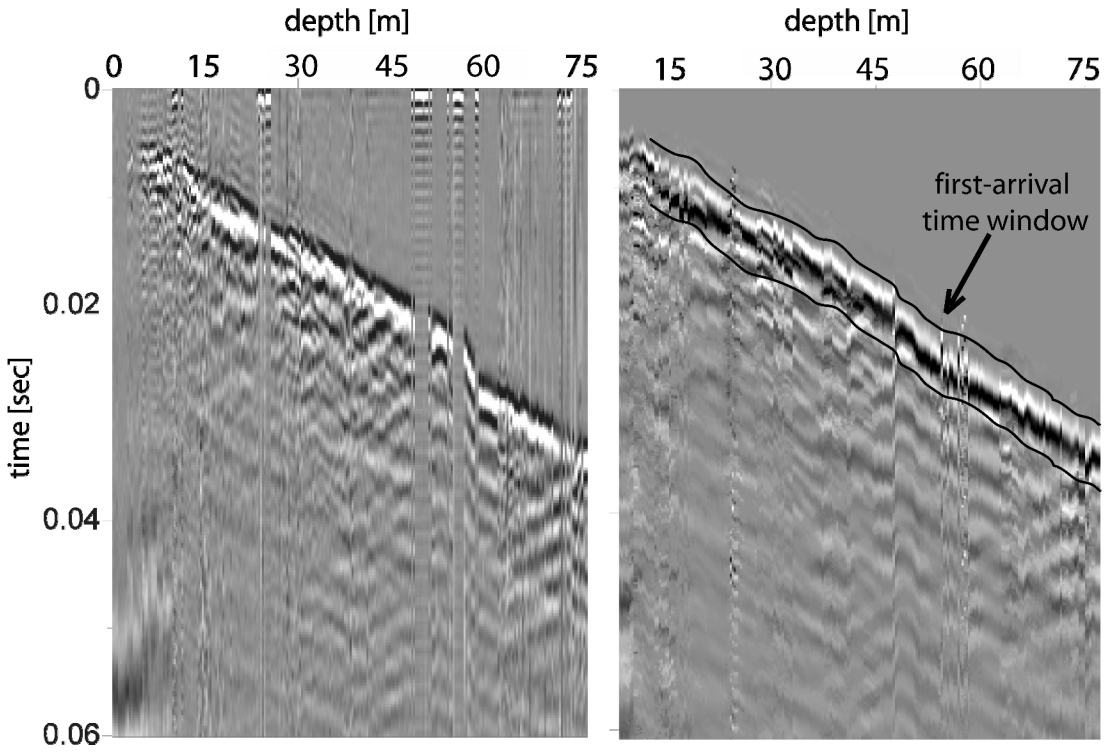

Figure 4.8. Raw (left) and processed (right) VSP data. The prominent first arrival is windowed for further attenuation analysis using the spectral ratio method.

4.4.2. Field data: resolution and S/N issues

Ambient noise, variations in source, interference with upgoing waves, coupling of the geophones with the borehole wall, presence of internal multiples, near-surface noise (e.g. ground roll), were some of the factors that offset the spectral amplitude of the recorded signal. During data acquisition, we were conscious of these problems and made efforts to achieve the highest possible quality data. Next, we shall discuss on some of the aforementioned factors, and the measures we took to address these problems.

Variations in source wavelet

During the VSP experiment, the source was placed always at the same position. The repeatability was good. The source was monitored for each shot separately by the accelerometers placed on it. The ground-force was reconstructed and used for deconvolution. In case of deliberate source amplitude amplification for the measurements at greater depths,

the amplitudes have been corrected during processing using the field notes. The effective source wavelet after processing remained nearly unchanged for the entire VSP dataset.

Interference due to up-going waves

Downgoing waves are distorted by upgoing waves generated by reflectors below the geophone position. There are two common approaches for separation of upgoing and down-going wave-fields: f-k filtering and median filtering. These filters are applied after shifting the first arrivals at all depths to a common time level. We removed the upgoing from the downgoing events, but this did not significantly enhance the resolution of the first arrival pulse.

Geophone coupling and coupling of borehole casing to the formation

One of the challenges in VSP surveys, is to monitor, quantify and model the receiver/tool coupling in a borehole for given borehole conditions. The coupling quality very important, since the method used for attenuation estimation depends heavily on the small changes of the shape of the measured pulse. This VSP experiment was performed in a cased borehole, thus geophone coupling issues are negligible. Unfortunately, the coupling of the casing to the formation remained unknown.

4.4.3. Method of estimation of the quality factor Q_{eff}

There are a number of ways to estimate the seismic quality factor (Q_{eff}) from VSP experiments. A comparison of different computational methods for the determination of Q_{eff} from VSP data was presented in the paper by *Tonn* (1991). The most widely used techniques are variations of the spectral ratio method. For our research, an improved version of the spectral-ratio method was used as proposed by *Jeng et al.* (1999). In this approach, the estimated Q_{eff} is assumed to be frequency dependent. The amplitude ratios are then plotted against the arrival-time difference at any two receivers for a particular frequency. The amplitude spectra S_1 and S_2 recorded at two different depths (z_1 and z_2) are compared, giving:

$$\ln \frac{S(f,z_1)}{S(f,z_2)} = \xi + \frac{\pi f}{Q_{eff}} \frac{(z_2 - z_1)}{c_p}, \text{ or} \tag{4.1}$$

$$\ln \frac{S(f, z_1)}{S(f, z_2)} = \xi + \frac{\pi f}{Q_{eff}}(t_2 - t_1), \tag{4.2}$$

where ξ is a constant that may include the effect of the geometric divergence and the source and receiver functions, z_1, t_1 and z_2, t_2 are depth and first-arrival traveltime at the two receivers and f is the frequency. The left-hand side of equation (4.2) is obtained from the processed VSP data. Assuming that Q_{eff} is frequency-dependent, $\ln\left(S(f, z_1)/S(f, z_2)\right)$ is plotted against the arrival time difference $\Delta t = t_2 - t_1$ between two receivers. The slope $S_{eff}(\omega)$ per frequency can be found by linear regression and is related to the effective quality factor Q_{eff} by

$$S_{eff} = \frac{\pi f}{Q_{eff}}, \tag{4.3}$$

$$\text{hence } \frac{1}{Q_{eff}} = \frac{S_{eff}}{\pi f}. \tag{4.4}$$

A large number of traveltime pairs throughout the whole depth range of the VSP experiment are calculated for the same frequency. Subsequently the Q_{eff} of a particular frequency is calculated.

It has already been established that apparent attenuation due to scattering is frequency-dependent (Chapter 3). Laboratory studies indicate that Q_{eff} is also frequency-dependent, for example for fluid saturated rocks [*White et al.* (1976), *O'Connell and Budiansky* (1977), *Johnston et al.* (1979)]. It has been shown that apparent attenuation depends on frequency in a complicated way. We therefore consider the *Jeng et al.* (1999) model most appropriate for this study.

4.4.4. Analysis and results

The first arrival of the VSP under study has been windowed and tapered. The taper length was varied depending on the length of the first arrival window to minimise any bias. Ambient noise was relatively low, so only the first arrival was used, instead of including the coda. Windowing of the first arrivals yields a smoother version of the amplitude spectrum (Figure 4.9).

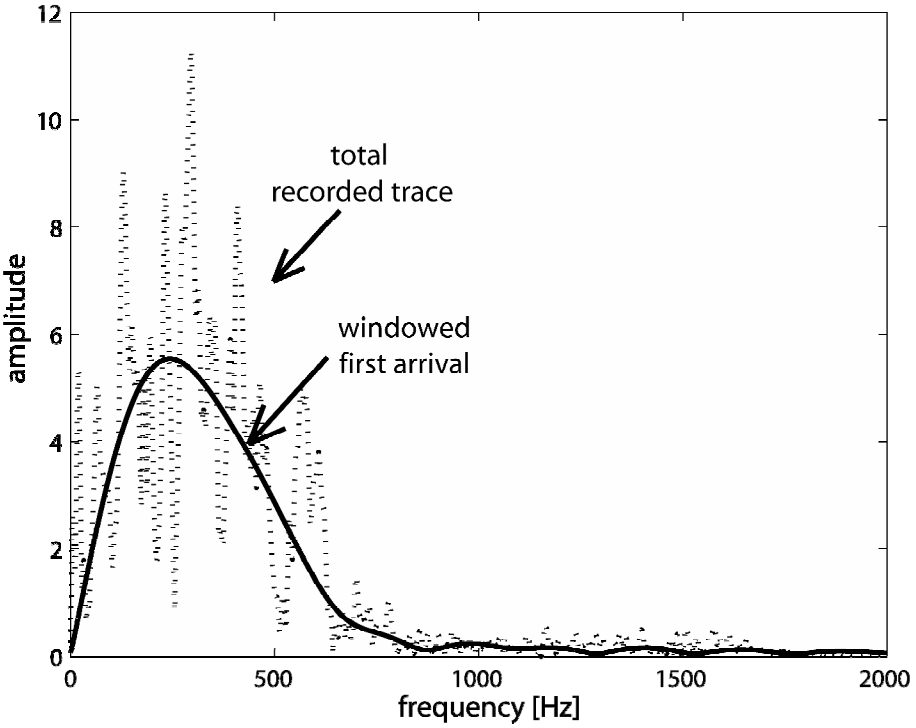

Figure 4.9. Typical example of amplitude spectra of full trace (dotted) and windowed first arrival (solid) for recorded signal at depth 55.75m.

The amplitude spectra of the first arrival at all depths were determined in order to investigate the lithology-sensitivity of Q_{eff}. It is clear that many geological and lithological boundaries can be identified in the frequency domain. A direct comparison of a look-up table depicting the amplitude spectra of the first arrival recorded in the VSP experiment as a function of depth versus frequency with the interpreted key surfaces and the system tracks obtained from core interpretation reveals impressive similarities (Figure 4.10). The changes of amplitude spectra with depth show good agreement with the changes in grain-size, indicating sequence boundaries (SB), regressive surfaces of marine erosion (RSE), or transgressive surfaces of marine erosion (TSE). In some cases, unexpected increase in both the spectral amplitude and frequency content, results from the "leaky modes" that some times exist in the window of the first arrival [*Jeng et al.* (1999)]. Such events are not distinguishable in the time domain. However, they are indicative of lithology (in particular grain-size) changes. It has not been possible to identify so distinctive changes in lithology from the processed VSP in the

time domain. Apparently, interpretation of amplitude spectrum is more sensitive to sequence boundaries than direct interpretation of the time-depth traces.

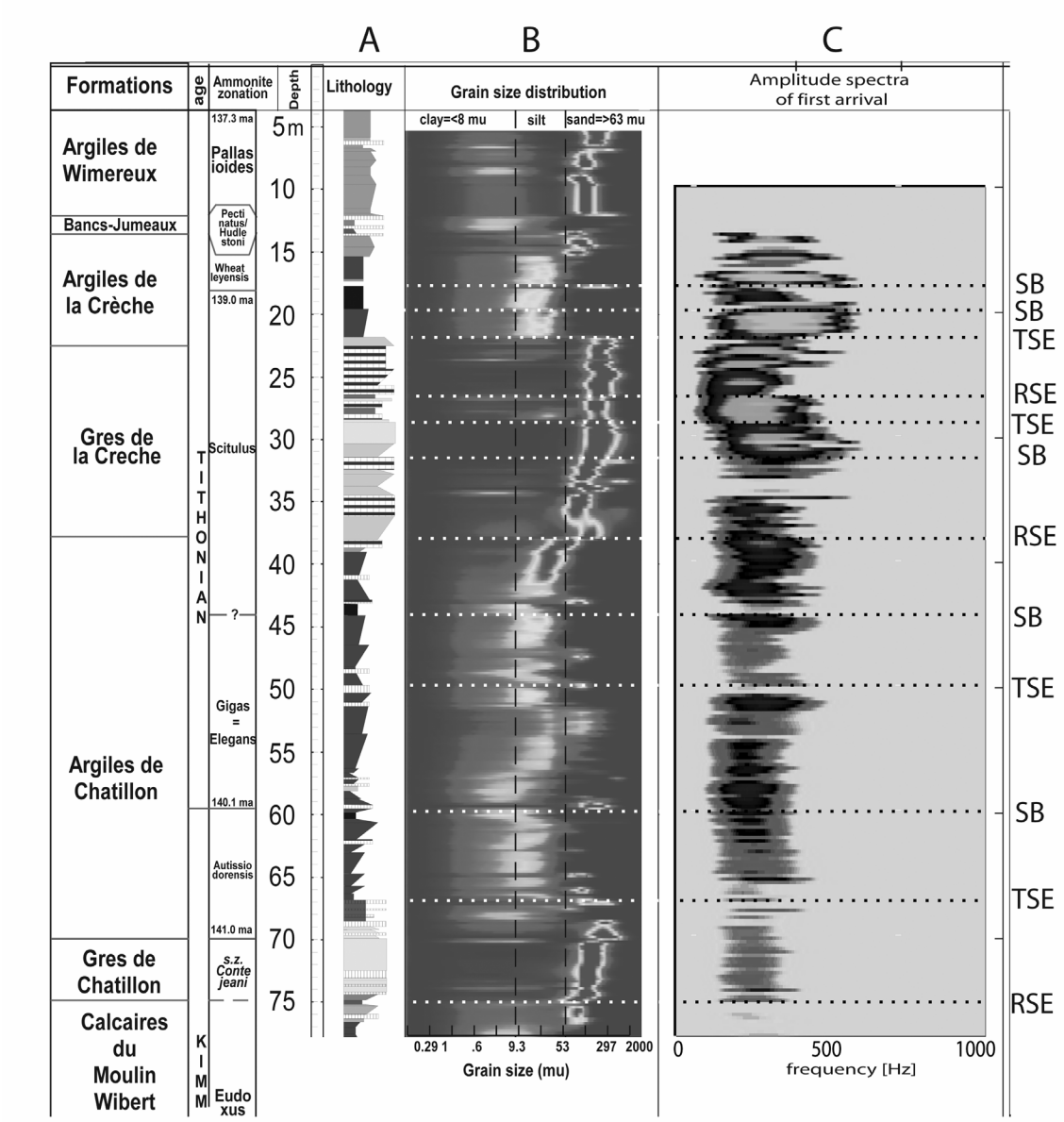

Figure 4.10. Comparison of the grain-size, the amplitude spectra of the windowed first arrival and stratigraphical boundaries. Changes in the spectra coincide with characteristic lithology changes expressed as sequence boundaries (SB), and regressive (RSE) or transgressive surfaces of marine erosion. Smaller changes are related to local marine flooding surfaces, maximum flooding surfaces and downlap surfaces.

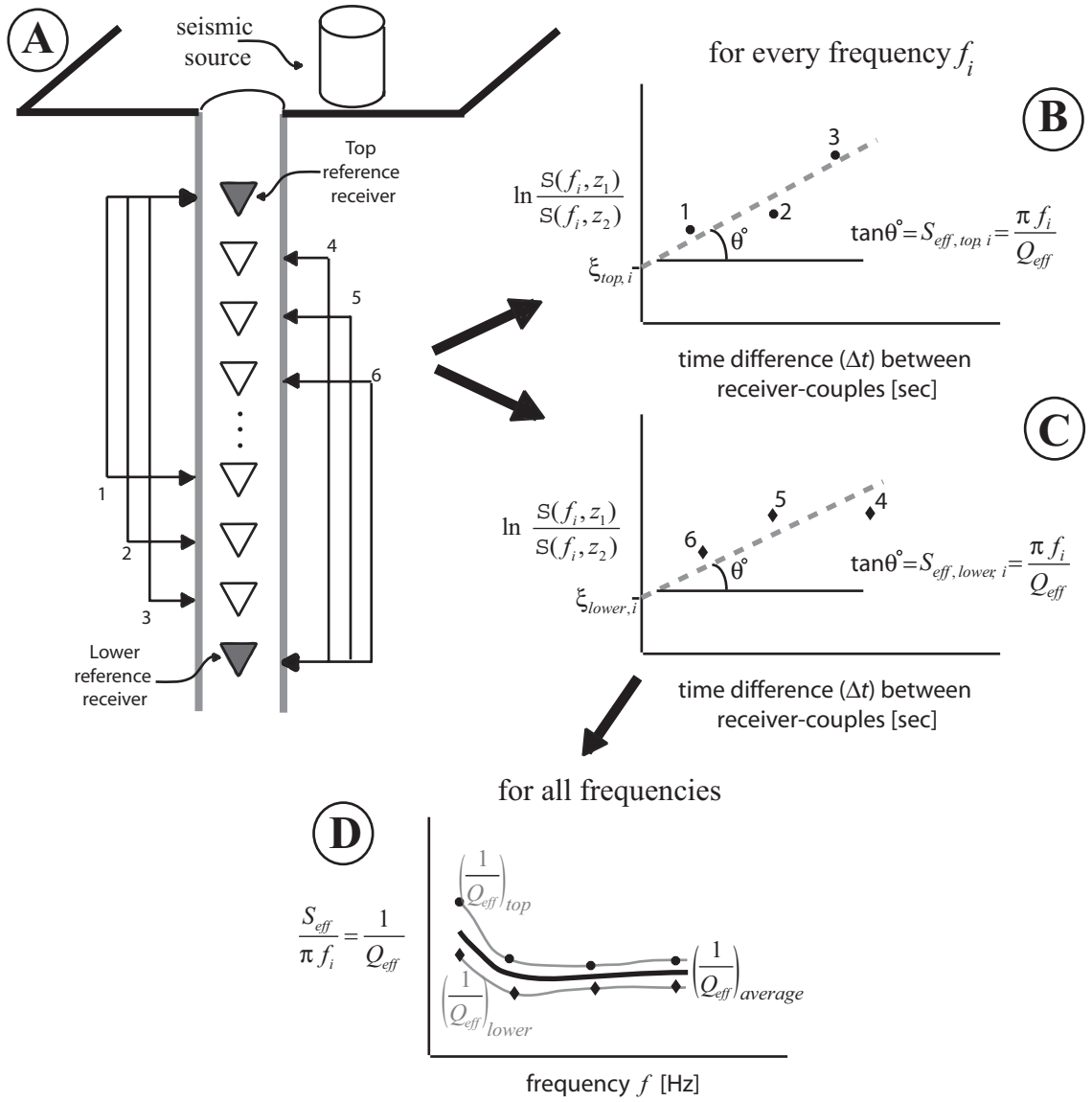

Figure 4.11. Schematic representation of the spectral ratio method used: A) The receiver pairing technique. B-C) Spectral ratio with reference the top (B) and the lower (C) receiver are plotted versus separation time Δt for every frequency within the frequency range of interest. The slope is calculated with a least square linear fit for every frequency and the $1/Q_{eff}$ curve versus frequency can be plotted (D).

In order to obtain Q_{eff} estimates with low measurement error we need to take as many non-redundant receiver pairs as possible. When we fix one receiver in a VSP with n receivers, $(n-1)$ non-redundant pairs can be formed. A reliable Q_{eff} is obtained when the spectral ratio slope calculated from the different spectral ratios is large compared to the variability. That means that we would like to maximise the distances Δz or the traveltimes Δt. Therefore, we chose the pairs with the top receiver paired with the receivers from the

lower half, and the bottom receiver with the receivers from the top half (Figure 4.11A). Since our interest is focused on retrieving a reliable estimate of Q_{eff}, we did not separate the VSP recording further into different layers. The depth range used was from 15 to 78 m. The initial depth was chosen as 15m based on criteria pertaining to data quality and signal contamination due to near-surface effects.

Two Q_{eff} versus frequency curves were constructed in this way using the top and lower receivers as reference (Figure 4.11). The source signal was 50 to 600Hz. The frequency range 50-100Hz was not used due to the presence of low-frequency ambient noise. The frequency range used for the spectral ratio analysis was 100-600Hz. For frequencies higher than 600Hz, there is actually no useful information contained in the first arrival.

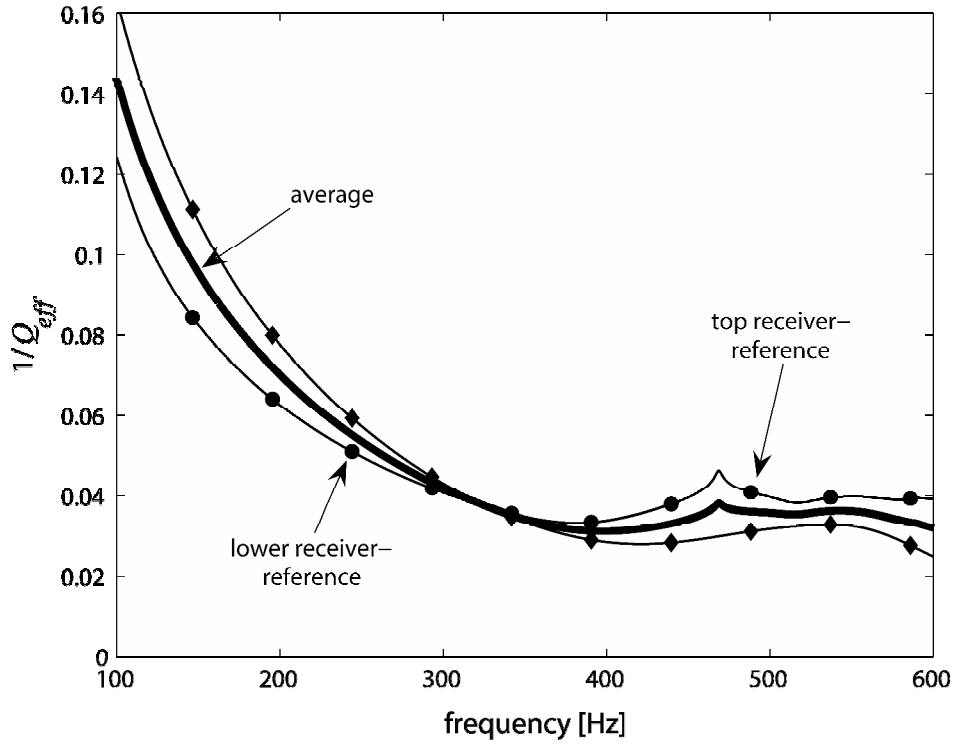

Figure 4.12. Q_{eff} versus frequency, as calculated from the process described.

The close agreement of the two Q_{eff} profiles shown in Figure 4.12 suggests that the estimated attenuation is fairly consistent between the deeper and the shallower receivers. The unstable Q value, for frequencies 400-600Hz may result from wobbly spectral ratio values. *Jeng et al.* (1999) explained such behaviour as to be due to nodes associated with the leaky modes. Other authors also observed this phenomenon and attributed the increase of spectral

amplitude with source-receiver offset to a significant energy contribution from the P-wave leaky modes [*Paillet and Cheng* (1986)].

4.5. Estimation of apparent attenuation, Q_{sc}, and dispersion

To this point, it is clear that attenuation due to scattering cannot be quantified unless a proper model is used. Attenuation remains an elusive seismic property that is hard to measure. In the last several decades, a number of researchers have used synthetic seismograms including all multiples constructed from sonic and density logs in order to estimate attenuation due to scattering. Interestingly enough, when the spatial sampling of the information from the sonic logs is very fine (e.g. in the Boulogne dataset core velocity and density is measured every 1 cm) the direct primary arrival is completely attenuated due to the impedance contrasts. What remains is the energy of the multiples coming at later times as a single energy package. In other words, *"transmission losses reduce the primary to nothing and the advancing wavelet is entirely multiple energy"* [*Banik et al.,*(1985)]. Even more complicated would be the case of including in such modeling the multiples coming from below the receiver position. In such a situation, the O'Doherty-Anstey description [*O'Doherty,* (1971)] of stratigraphic filtering due to thin layers will not hold. For this reason, the model used in this research to describe the intra-bed scattering is derived using the finest scale information (in this dataset the core measurement). We assume this information to be embedded in two homogeneous half-spaces with velocity equal to the first and last sample respectively and scaled to the VSP spatial sampling, as explained in Chapter 3.

Acoustic velocity and wet bulk density were measured every 1 cm using a Multi-Sensor Core logger (GeoTek MST) on a nearly continuous core recovered from the borehole. The same borehole was used for VSP. In the MST, a source crystal is excited by a fast-rise time pulse, which is then recorded by a receiving crystal. By automatically picking the one-way travel time of the acoustic wave along the sample axis and dividing it by the core thickness, the acoustic velocity is obtained. The centre frequency of the pulse used was 320 kHz and measurements were performed under ambient pressure. The precision of the measured velocities is estimated to be approximately 5% [*Braaksma et al.* (2005)].

4.5.1. Transmission, apparent attenuation and dispersion at different scales

The MST velocity log has been regularised for different scales using wavelet transform with the Gaussian as analysing wavelet, following the procedure described in Chapter 3. The result is shown in Figure 4.13. Evidently, the velocity log used here is much smoother than the fractal model used in Chapter 3. Therefore, the velocity values reache the effective-medium average velocity at smaller scales than for the fractal model.

The full-waveform transmission and reflection responses were calculated using the regularised velocity logs for every scale. The regularised density logs were also used in the calculation. The regularised velocity at various scales is shown in Figure 4.13. Using the regularised velocity and density logs, regularised local impedance logs were created.

The medium used for modelling is embedded in two half spaces and there are neither upward reflections coming from below the last receiver nor downward reflections above the first receiver. The assumption that there are no more layers below the last receiver is as valid/invalid as artificially extending the velocity and density information using an assumed distribution (fractal, Poisson etc).

The regularization of velocity affects the higher frequencies. That is a direct consequence of the observation that a smoother medium can be accurately represented by thicker layers, with locally averaged velocity, thus approaching the short-wavelength limit. In general, the large-scale variability (corresponding to low frequencies) is not affected significantly except for really large scales. As the impedance contrasts in the medium decrease, the high-frequency variability decreases facilitating wave transmission. Complementary to this, as the scale increases, there are fewer contrasts to cause reflections.

The goal of our numerical modelling efforts is to obtain an estimate of apparent attenuation which is solely due to internal multiples. The internal multiples occur at different scales. Following dispersion and attenuation analyses explained in Chapter 3, the coda term is constructed from the transmission response and is separated in real and imaginary part. According to the Kramers-Kronig relationship these real and imaginary parts are Hilbert pairs

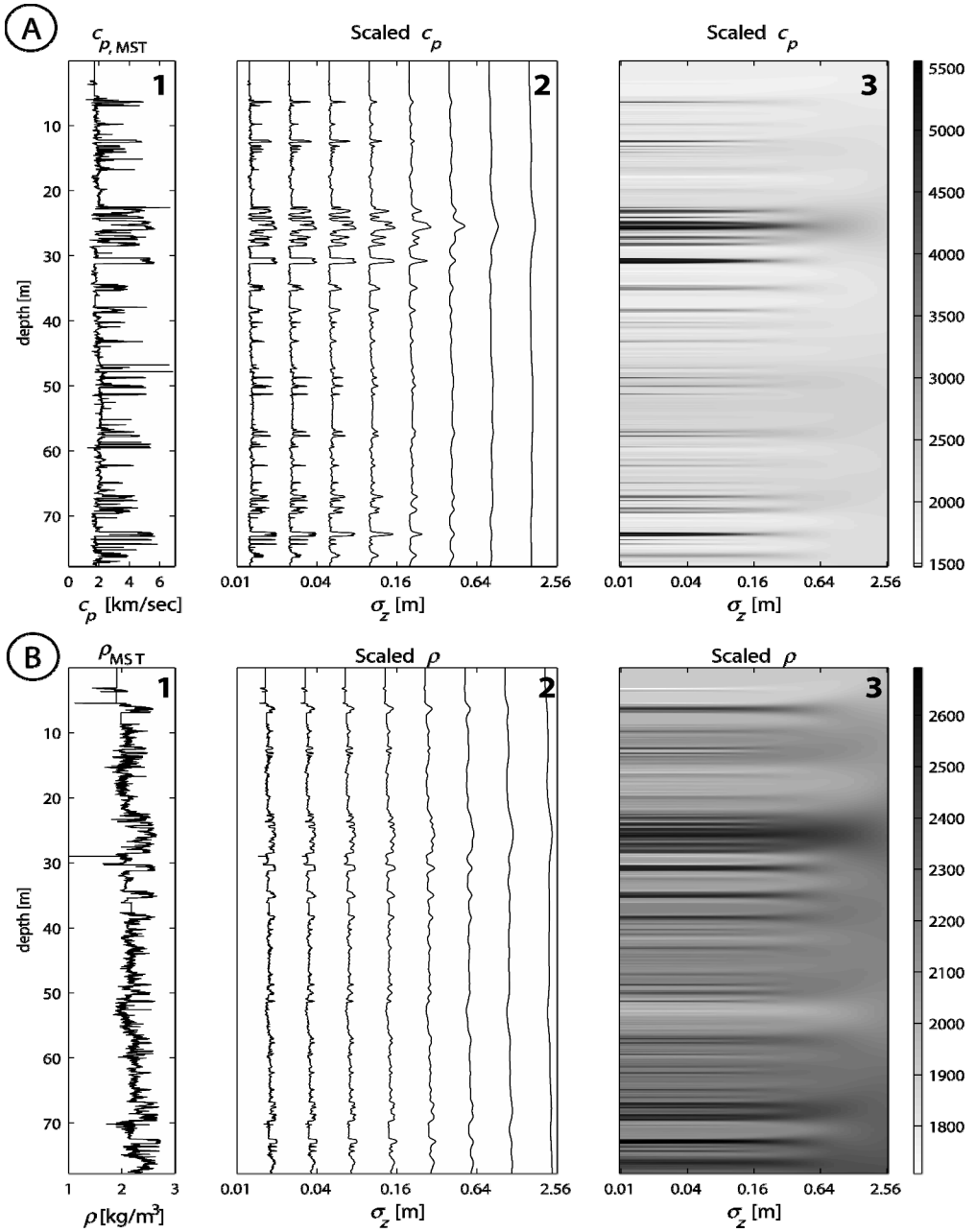

Figure 4.13. Velocity (A-1) and density MST logs (B-1) and the regularization for few distinct scales σ_z (2) and for a range of scales (80 regularised velocity profiles plotted closely spaced) in a greyscale plot (3). The greyscale denotes the density and velocity values.

(Chapter 3). From the real and imaginary parts, attenuation, $1/Q_{sc}(\omega)$, and dispersion, $\tau(\omega)$, are estimated (Figure 4.15). It can be seen that as the scale increases both dispersion and attenuation decrease. The medium properties become smoother with increasing scale, impedance contrasts become weaker, and therefore the strength of internal multiples is reduced. The energy spent in wavefront redirection due to internal multiples decrease with increasing scale. Consequently, the attenuation is less. The wave propagating through the upscaled medium becomes less dispersed compared to the wave propagating through a medium described by the initial MST velocity and density logs.

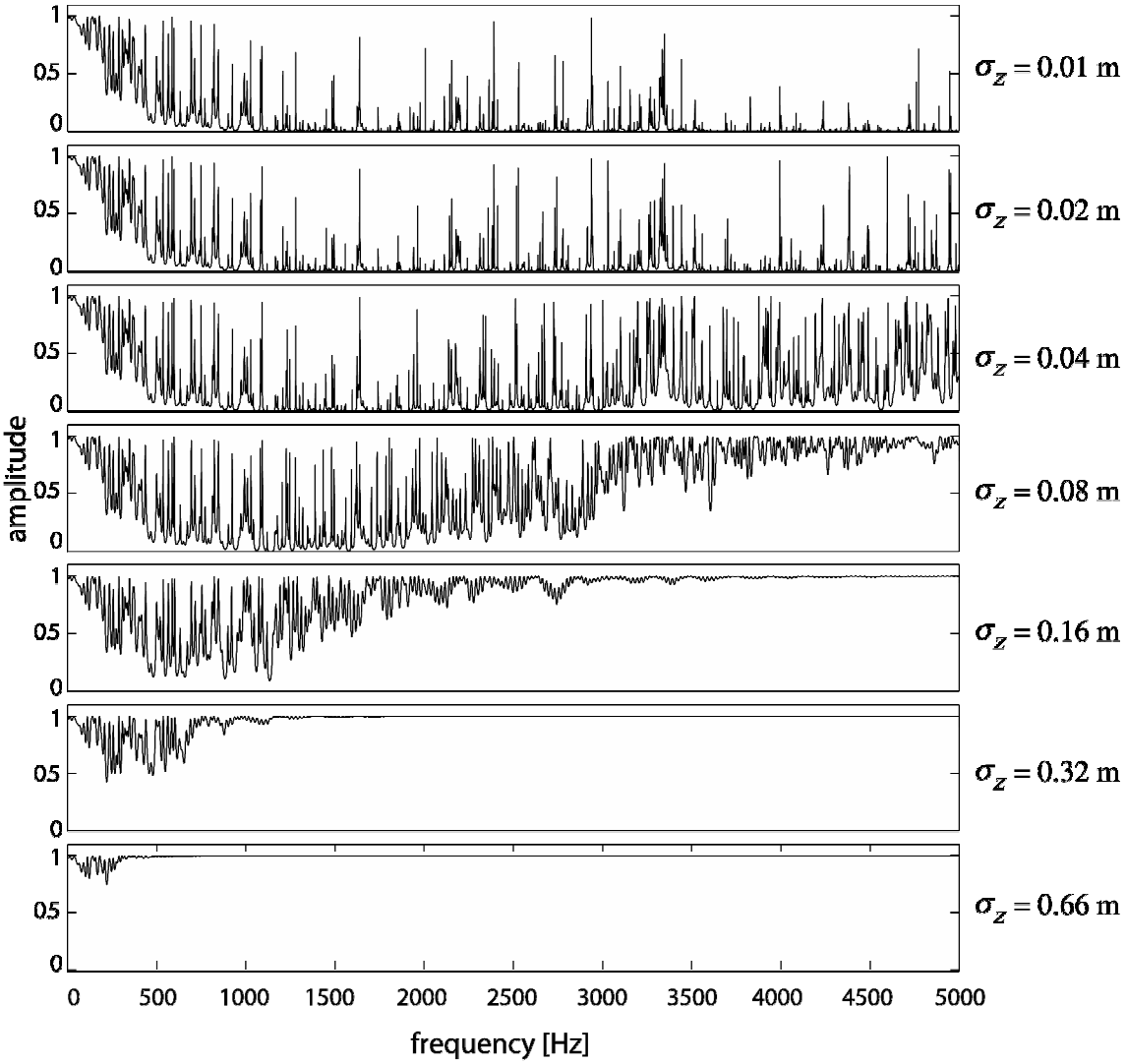

Figure 4.14. Transmission impulse responses for the c_p and density, ρ, measured on cores (MST) for the different scales shown in the middle panel of Figure 4.13.

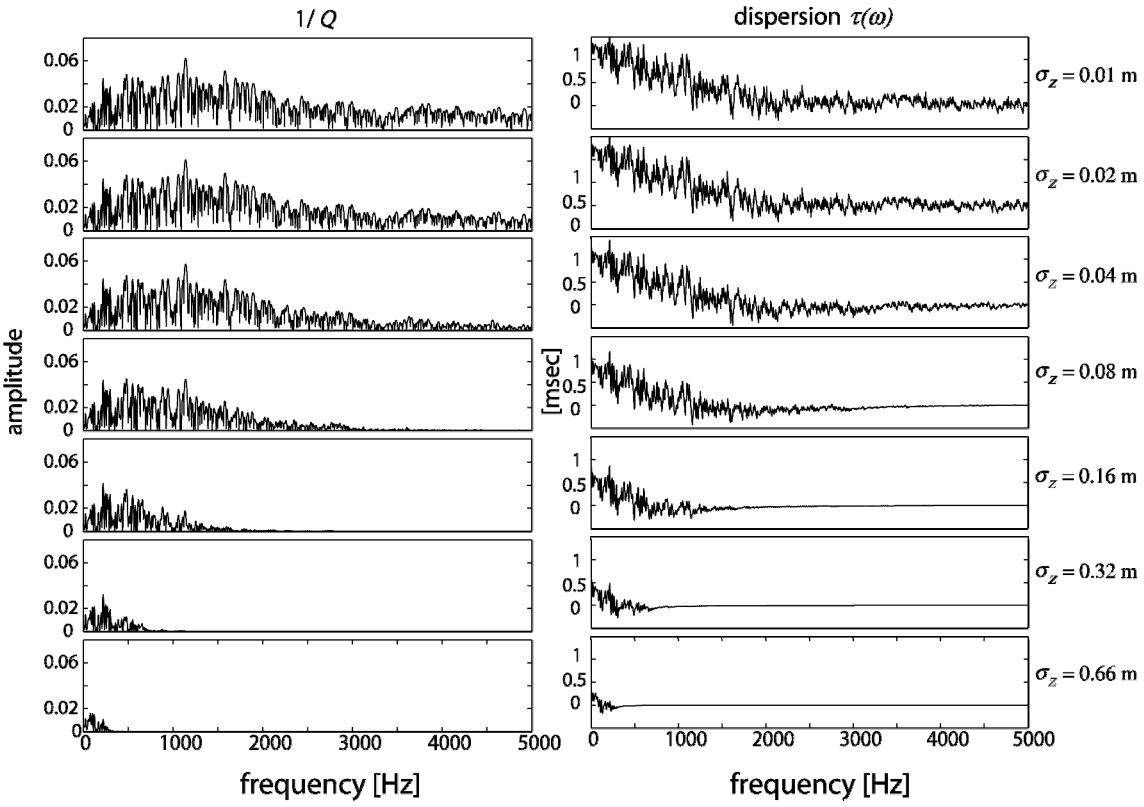

Figure 4.15. $1/Q_{sc}(\omega)$ (left) and dispersion $\tau(\omega)$ (right) as calculated from the coda term constructed from the full waveform transmission response, for different scales (0.01m, 0.02m,0.04m,0.08m, 0.16m 0.32m, 0.66m, 1.3m from top to bottom).

4.5.2. Macroscopic properties at different scales

Using the solution given for a driven damped oscillator, theoretical curves can be fitted to dispersion $\tau(\omega)$ and attenuation $1/Q_{sc}(\omega)$ as shown in Figure 4.15. This helps in characterizing the trend and the medium on basis of eigenfrequency (ω_0), and coefficients ***a*** and ***b***. For curve fitting, we use the synthetic data and solutions of the equation describing a driven damped oscillator with unknown coefficients.

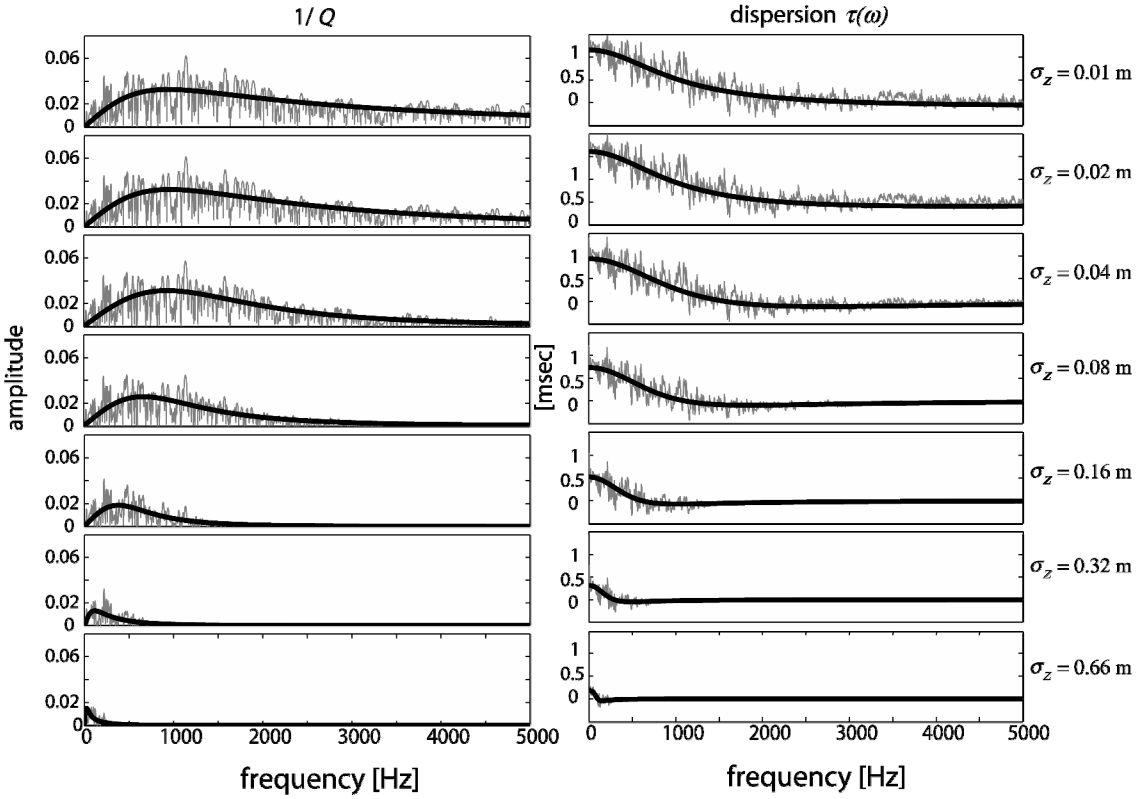

Figure 4.16. Fitted curves with the proposed macro-model for different scales.

Curves are fitted both to real and imaginary parts of $A(\omega)$ for all scales (Figure 4.16). For the real part, all coefficients were determined using the iterative optimization method described in Chapter 3. For the imaginary part, the eigenfrequency ω_0 as determined from the real part was input. Then the other two parameters, the coefficients ***a*** and ***b***, were fitted. In this way, the consistency of the fitting was ensured; the two parts (real and imaginary), even though fitted independently, yielded similar results. It is interesting that all coefficients decrease at a nearly exponential rate with increasing the scale (Figure 4.17).

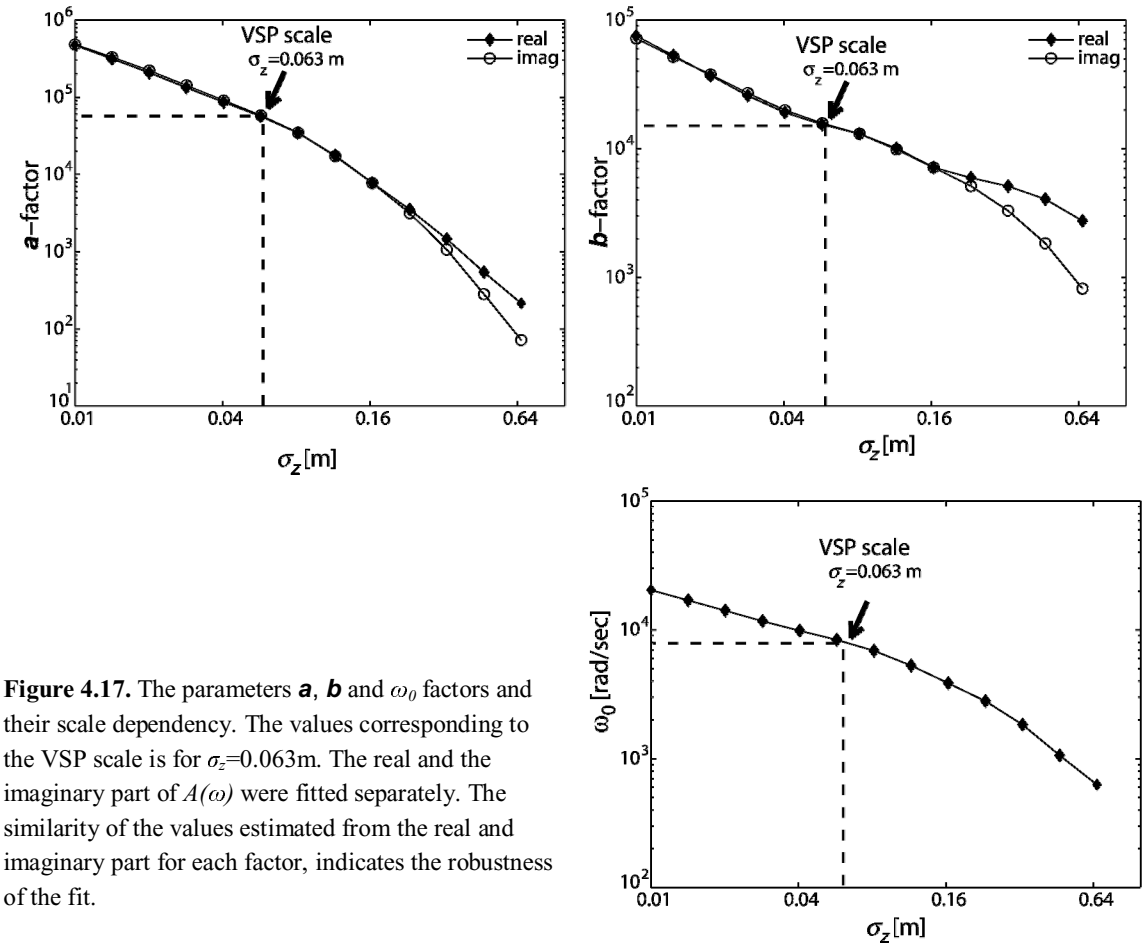

Figure 4.17. The parameters ***a***, ***b*** and ω_0 factors and their scale dependency. The values corresponding to the VSP scale is for σ_z=0.063m. The real and the imaginary part of $A(\omega)$ were fitted separately. The similarity of the values estimated from the real and imaginary part for each factor, indicates the robustness of the fit.

With the information from Figure 4.17 a macro-model representation of the coda term of the transmission response of the medium can be made at any scale. If the arrival time information is known *a priori*, full transmission and reflection responses can then be accurately reconstructed. The agreement of the values obtained fitting independently real and imaginary part of $A(\omega)$ demonstrates the robustness of the fit. The agreement decreases with increasing scale due to the reduced frequency range of transmission information (refer to Figure 4.14 and Figure 4.15). However, this has a negligible effect in our application. As explained in Chapter 3, the accuracy of the reconstructed response depends on the number of resonant frequencies considered. Hence, if more resonant frequencies are implemented, the reconstruction of the transmission response will improve both in amplitude and in timing and shape of the later arrivals.

Full-waveform seismograms allow for estimation of the dispersion of the wave propagating through a medium. Dispersion has time units; recall that the time delay $\tau(\omega)$ is frequency-dependent. However, *sensus stricto*, time is not commonly regarded as a

frequency-dependent property. When this extra time delay is added to the direct arrival time, it gives the arrival time obtained from the envelope of the propagated wave. This is associated with the group velocity resulting from wave propagating through a dispersive medium. In Chapter 3, the velocity regularization method as a means to account for the small scale variability in a fine-layered medium has been explained. The second step of this approach involves the usage of ray theory to calculate the time of the direct arrival. It is then evaluated by calculating the *drift*, which is the difference between the direct arrival-time (ray-theory time) of the regularized velocity profile and the direct arrival time at the original scale. When the drift is small, the result was found to "*compare well"* with the time predicted by the full waveform synthetic seismograms for the corresponding scales [Verhelst, 2000].

For the MST data at the Boulogne site, dispersion modelled at different scales using the regularized velocity profiles is shown in Figure 4.15. The most accurate way of determining the first-arrival time would be to estimate it from the full transmission response. That will essentially entail adding the direct arrival time (ray-theory) and the component due to dispersion. The drift (dotted line) is compared against the drift corrected for the dispersion (solid line) in Figure 4.18. The dispersion is calculated from the full wave seismogram. The drift corrected for dispersion, as estimated by the fitting process for the macroscopic properties is also plotted (full-circle marked line). The relative discrepancy between the drift and the drift corrected for dispersion using the full waveform modelling is more than 200% for small scales, and decreases with increasing scale. On the contrary, the proposed fitting method not only describes more accurately the amplitude, but also the first-arrival time when compared with the full waveform seismogram. We can conclude that the regularization method proposed by *Sams and Williamson* (1994) is sufficient for traveltime issues (the absolute maximum discrepancy between drift values is 1msec in Figure 4.18), but this time information cannot be used to estimate attenuation.

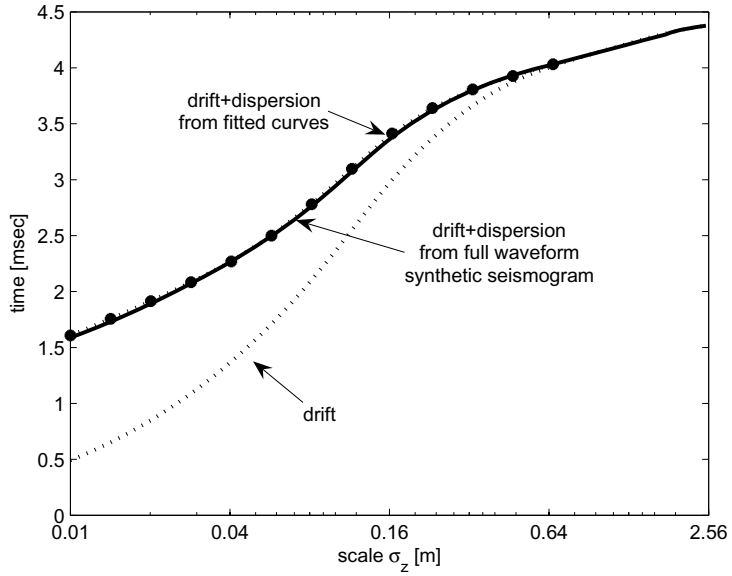

Figure 4.18. Drift determined from the MST of Boulogne via 3 different ways. Plotted in solid line is the drift corrected for the extra time delay introduced by dispersion, calculated from the full waveform seismogram. In full-circle marked line is the drift corrected for the extra time delay introduced by dispersion as calculated using the fitting process of the solution of a single driven damped oscillator. In dotted line is the drift calculated from the regularised MST velocity.

4.6. Apparent attenuation at the VSP scale

In order to compare the findings described above with the attenuation estimate obtained from the VSP experiment, the medium as observed through the MST measurements is upscaled to the same scale of observation. An MST-resolution is never reached in normal field applications. The highest resolute quantification of layering usually comes from sonic and density logs. Since a well log is always measured with a finite resolution, the true nature of the finely layered Earth remains unrevealed and hence a multitude of Earth models are possible [*Wapenaar* (1996)]. *Wapenaar* (1996) investigated the sensitivity of the seismic response in the time domain for different types of Earth models. In that study, a discretised fractal-like layered medium, similar to the one presented in Chapter 3, was considered to be the "true medium". Its seismic response was compared with the seismic response of various scaled versions of the same medium. The match was, in their words, not exact but acceptable. The conclusion drawn from the modelling experiments in *Wapenaar* (1996), for the transmission and reflection response of the "true" medium" and the different "smoothed logs" is that they *"yield responses that are hardly distinguishable, provided that the bandwidth of*

the continuous model is sufficiently large in comparison with the bandwidth of the source function". It was observed that the primary transmission and reflection response was not affected significantly by the smoothing, result that agrees with the findings of *Verhelst* [2000]. It also agrees with the results presented in this thesis as shown by the drift (Figure 4.16) the absolute value of change on the drift is not more than 3 msec for the scales shown.

Even though in the time domain the discrepancy between the response of the "true medium" and the smoothed ones is small, it can be seen in the figures with the transmission response at different scales (Figure 4.14) that the coda related with high frequencies are significantly affected by the smoothing the scaling process. The high-frequency content is important because the coda waves contribute in the dispersion and attenuation calculated even below the $\lambda/4$ or the $\lambda/8$ [Widess, 1973] resolution. *Hall* (2006) discussed about the resolution of bed thickness and found that a bed with thickness of 70-25% of the interpreted thickness can actually be resolved in the Fourier domain using cepstral decomposition. Internal multiples in layers of such thicknesses affect the attenuation and dispersion estimation, hence the importance of including the high frequency content.

As discussed in previous paragraphs when a frequency range is chosen solely relying on the effective wavelengths corresponding to the VSP experiment frequency range, it would drastically reduce the effect that the internal multiples may have on attenuation and dispersion. It has been shown in Chapter 3 that due to the smoothing effect of the wavelet transform the overall statistics of the medium change. On the other hand, using the information directly from the MST and preserving all the high frequency information, would imply that we discard the smoothing effect that the VSP input signal have. This would result in overestimation of the attenuation due to scattering. Therefore, it is necessary to introduce a criterion to establish the frequency range and smoothing scale needed to accurately model the impulse response of the medium. The frequency range is bounded by our measurement and in the case of the Boulogne data, the frequency content is taken with a maximum of 600Hz.

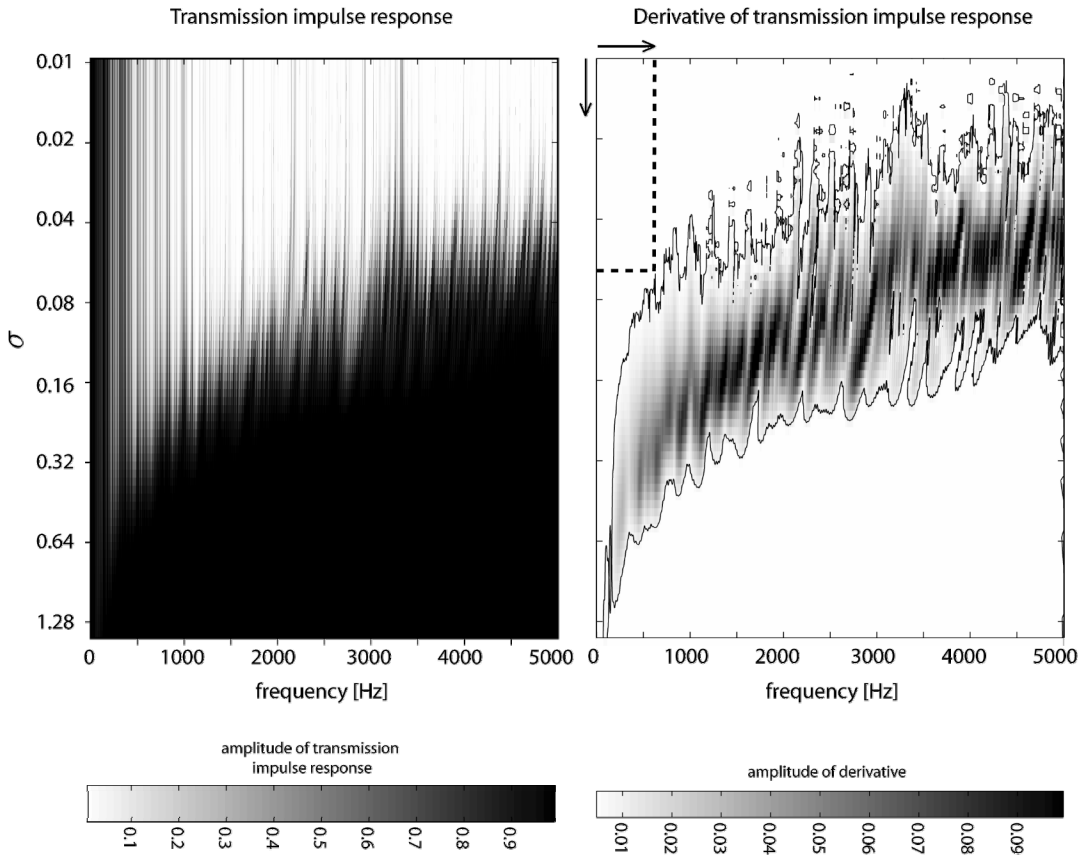

Figure 4.19. Left: Look-up table of transmission impulse responses for the scaled media. Right: The differential of the left panel along the y-axis ($\partial A/\partial \sigma_z$).

Figure 4.19-left depicts a look-up table where the amplitude of the transmission impulse response is plotted for different scales. In order to quantify the rate of changes in the amplitude of the impulse response due to the scaling process (wavelet transform), the derivative of the amplitude $\partial A/\partial \sigma_z$ is taken for every frequency and is shown in Figure 4.19-right. It can be observed that for each frequency there is a band of scales in which most of the changes occur. We would like to avoid using information in this rapidly changing area for our analysis in order to obtain stable results. In order to provide the maximum bandwidth to include the coda waves we will use the following criterion: The scale to be used for estimating the attenuation and dispersion was determined by the maximum of the frequency of the received signal (600Hz) and a certain minimum of the threshold value of the differential. The minimum is taken to be 0.5% (contour line in Figure 4.19 right). Following this criterion, the scale at which the MST should be regularized for comparing with the VSP

measurement is σ_z=0.063m in the present case. In order to obtain a smooth version of the $1/Q_{sc}$ profile, the coefficients ω, ***a*** and ***b*** are found as described in paragraph 4.5.2.

4.7. Conclusions

The approach used in this Chapter, for linking the VSP and core measurements in terms of attenuation is to estimate a frequency dependent average Q_{eff} from the VSP data. The attenuation due to internal multiples (Q_{int}) is determined by modelling the transmission response through a lossless medium comprising a stack of layers, upscaled in the VSP observation scale. The maximum resolution achieved, given by the finest scale of observation, corresponds to the core measurements and is 0.01m. Below this limit it is assumed that the layers are homogeneous. Although this assumption may not correspond to reality, it is deemed acceptable for the purpose of this thesis.

In a homogeneously absorbing medium, anelasticity (intrinsic absorption) and scattering contribute cumulatively to the effective attenuation, because it is assumed that arrivals of equal traveltimes have suffered the same amount of absorption regardless of their trajectory. Therefore it can be written that:

$$S_{eff} = S_{int} + S_{sc} \tag{4.5}$$

where S_{eff}, S_{int} and S_{sc} are the slopes related to effective attenuation measured from the data, attenuation due to intrinsic properties and attenuation due to scattering respectively. Separation of scattering and intrinsic contribution can be based on the additive relation [*Dainty* (1981), *Rovelli* (1982), *Spencer et al.* (1982), *Richards and Menke* (1983), *Menke and Dubendorff* (1985), *Mayeda et al.* (1992), *Kang and McMechan* (1994)].Therefore, it can also be written that:

$$\frac{1}{Q_{eff}} = \frac{1}{Q_{int}} + \frac{1}{Q_{sc}}. \tag{4.6}$$

Based on equation (4.6), the intrinsic attenuation can be calculated (Figure 4.20). The apparent attenuation due to scattering generally decreases as the frequency increases, due to the fact that the corresponding wavelength is smaller. The propagation regime approaches the

short wavelength limit, where reflections arrive at later times and do not to cause dispersion (or equivalently, attenuation). The maximum values occur in the high-frequency range. The values for intrinsic attenuation are lower than that for attenuation due to scattering for frequencies above 320Hz; internal scattering is responsible for apparent attenuation at this frequency range. The apparent attenuation due to internal multiples was found to be less than the intrinsic attenuation for frequencies smaller than 320Hz.

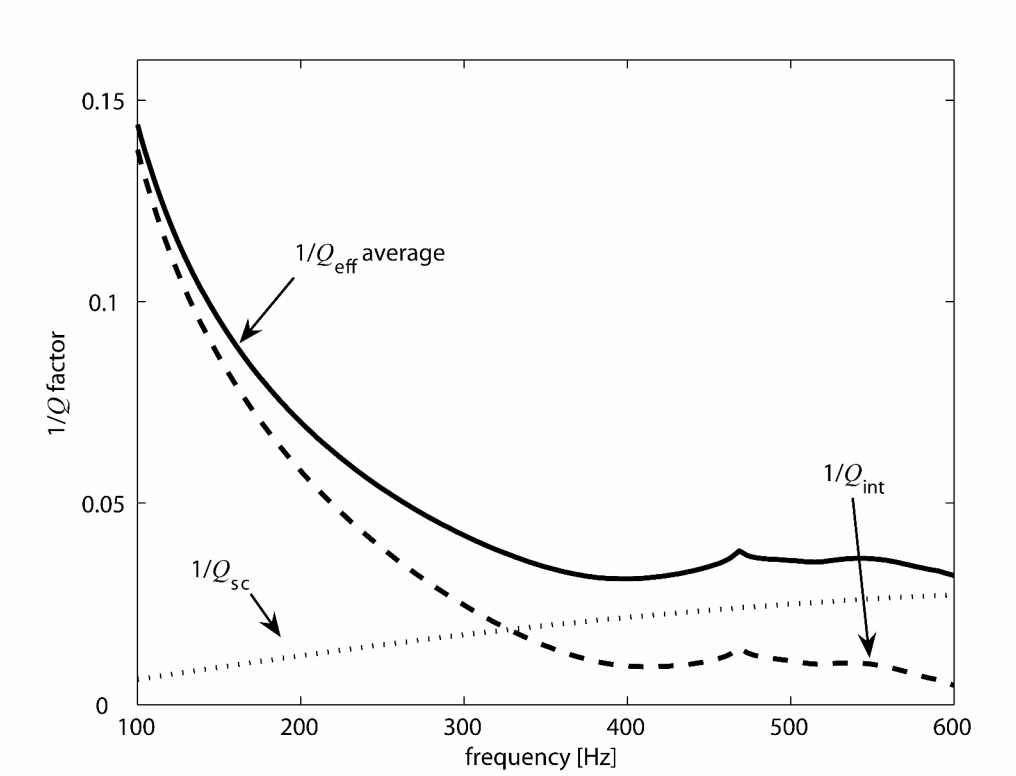

Figure 4.20. Estimated $1/Q_{eff}$ from the VSP data with the spectral ratio technique , $1/Q_{sc}$ estimated from the upscaled MST velocity and density and calculated $1/Q_{int}$ assuming cumulative properties in the inverse of the quality factor.

The siliciclastic sequence under study is located in the intertidal zone, therefore it is water saturated and comprises mostly of unconsolidated to partly consolidated sediments. Grain-to-grain interactions [*Hamilton* (1972), *Stainsby and Worthington* (1985), *Buckingham* (1997, (1999, (2000)] and squirt-flow [*Mavko and Kjartansson* (1979), *Mavko and Jizba* (1991), *Dvorkin et al.* (1995)] in water saturated sediments have been found to be responsible for large values of attenuation (thus small values of Q_{eff}).

In our study the finest layer thickness for the numerical experiments is determined to be the depth resolution of the MST logs. Below that the layers are considered homogeneous. Therefore only a macroscopic effect of grain-to-grain interactions could be speculated in the velocity and density measurements. The concept of grain-to-grain interaction and wave energy attenuation due to friction of granular surfaces initiated a series of numerical experiments using a lattice solid model to investigate the influence of friction in wave propagation. A detailed overview of the numerical experiments and the resulted observations are to be found in Appendix B. With these experiments, it was shown that increase of friction has a non-linear effect in the amplitude of a wave propagating through single size particles; for small values of friction coefficient the amplitude generally decreased. However, increasing value of coefficient of friction resulted in increasing stiffness of the lattice; this in turn facilitated wave propagation and minimized attenuation.

Mistakes are almost always of a sacred nature. Never try to correct them.
On the contrary: rationalize them, understand them thoroughly.
After that, it will be possible for you to sublimate them.
Salvador Dali

Chapter 5

Scale-dependent attenuation and dispersion in a Miocene Carbonate Reef Platform

5.1. Introduction

Some of the largest oil fields in the world are in carbonate environments (Middle East, Malaysia, etc). The analysis of the stratigraphic sequence is very important in such an environment. Imaging using seismic waves is probably the most efficient non-invasive approach to unravel the structure of the subsurface. Understanding the differences of stratal architecture, and hence in seismic impedance contrast between siliciclastic sequences and carbonate systems, is of great economic interest. Distinction of lithological boundaries becomes particularly significant in hydrocarbon exploration in order to interpret accurately the facies architecture and to create appropriate model for reservoir development [*Loucks* (1996)].

Complementary to the siliciclastic sequence at Boulogne (Chapter 4) the next target is a carbonate sequence: the prograding rimmed-reef platform located in Mallorca (Spain). This second natural observatory used in this research is an outcrop analogue of carbonate reservoirs. Apart from the economic value associated with hydrocarbon potential, reef platforms like the Llucmajor Platform (Mallorca) are closely linked to sea-level changes. These fluctuations are captured in the evolution of the reef and are associated with climate changes. Therefore, they are an invaluable tool for palaeoclimatic reconstruction. They can facilitate the monitoring of contemporary climate changes. Our particular interest has been

focused on resolving the seismic imaging in such a complex geology. The scale-dependent attenuation and dispersion in the seismic data are quantified in this chapter. A multidisciplinary set of experiments took place in the area of Cap Blanc (Figure 5.1), which is part of the Llucmajor Platform, in Mallorca. One 3D multi-component surface seismic reflection dataset was acquired, along with vertical seismic profiles (VSP), various logs, core data and samples of the cliff facies. The VSP experiments and core measurements are used for the attenuation and dispersion studies. The geological description of the area is considered crucial at this point, as it can establish the geophysical challenge faced through the emerging stratigraphic complexity.

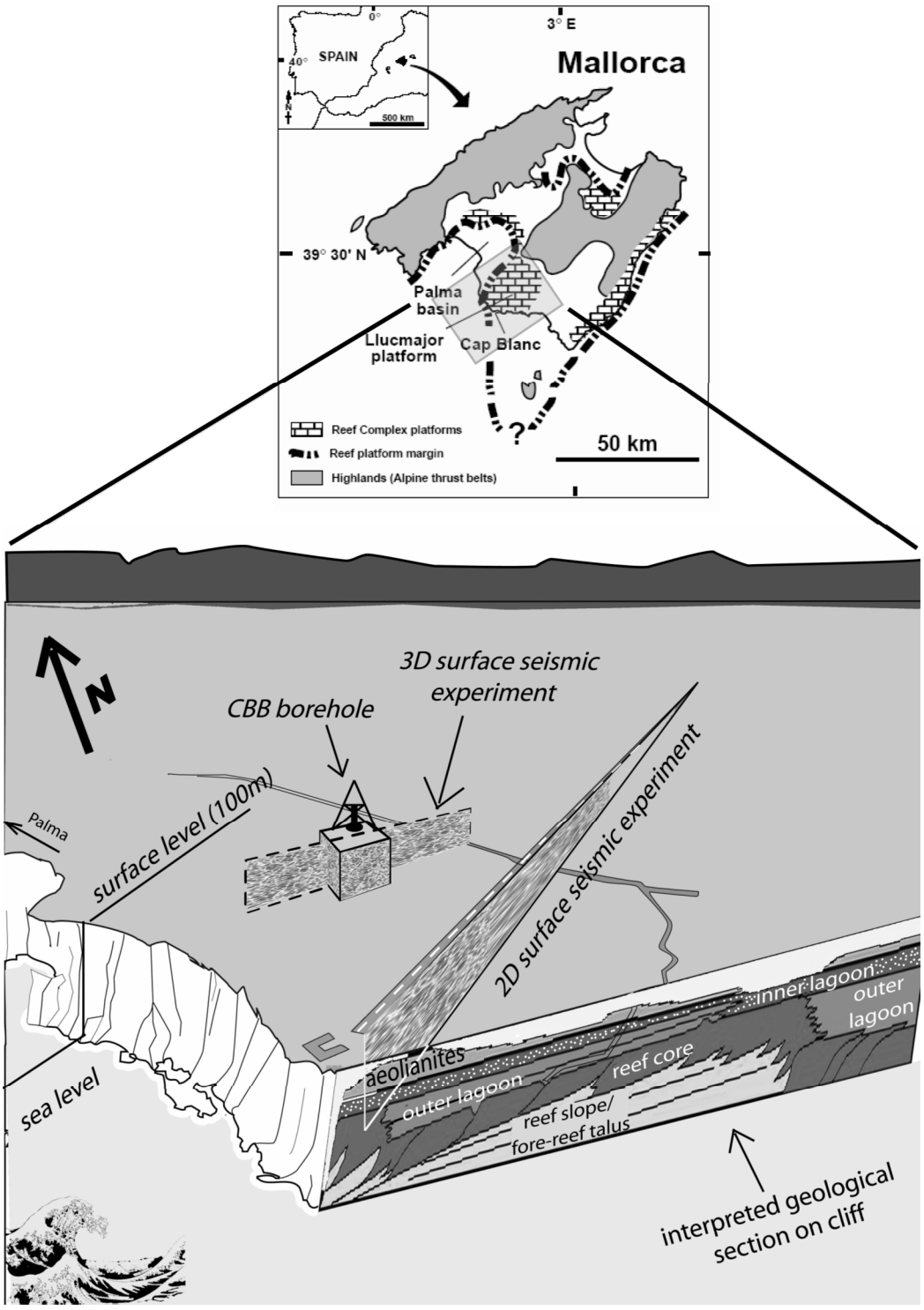

Figure 5.1. Location of the Llucmajor platform on the central-southern part of Mallorca island in the western Mediterranean Sea.

5.2. Lithological setting and geological history

The second natural observatory used in this research is the carbonate sequence of the prograding rimmed-reef of the Llucmajor Platform, located in Mallorca, Spain (Figure 5.1, Figure 5.2). This carbonate system is controlled by high frequency changes in accommodation and sediment supply [*Pomar and Ward* (1994)].

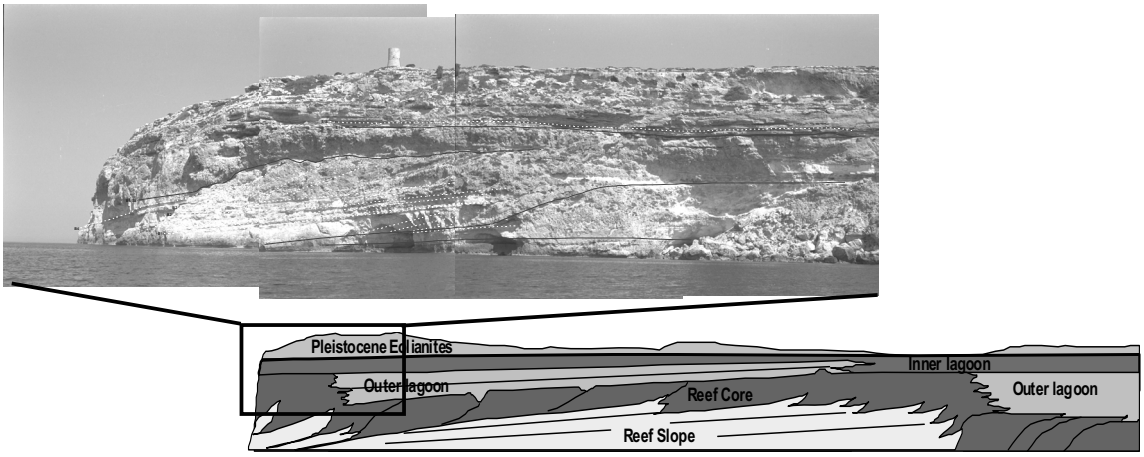

Figure 5.2. Photomosaic of the south cliff of Cap Blanc with the interpreted geology complementing Figure 5.1. (*courtesy K. Verwer*).

Reef-rimmed progradational platforms were widespread in the western Mediterranean during the late Miocene [*Esteban* (1979),*Pomar* (2001b), *Pomar et al.* (2004)]. Following the major overthrusting of the middle Miocene Alpine orogeny, several carbonate ramps and platforms developed and overlie the deformed Early and Middle Miocene, Palaeogene and Mesozoic rocks of Mallorca and the other Balearic Islands, [*Pomar et al.* (1983)].

The Upper Miocene rocks of the Balearic archipelago (Mallorca, Menorca, Ibiza, Formentera and smaller islands) are commonly flat-lying limestone and dolostones, with slight tilting and flexure, probably caused by normal and strike slip faulting in the Late Neogene to Middle Pleistocene. They are composed of three third-order depositional sequences:

1) The lower sequence, attributed to the Early Tortonian, corresponding to a carbonate ramp with extensive rhodalgal lithofacies and no coral reefs.

2) The middle sequence, attributed to the Late Tortonian-Early Messinian, corresponding to well-developed progradational reefal platforms, including the Llucmajor Platform reef complex.

3) The upper sequence, assigned to the Messinian, consists of a variety of lithologies including oolites and stromatolites.

The experiments are focused on the Llucmajor Platform reef complex, and thus we are mainly interested in the middle sequence. This is a package 100-150 m thick and in south-western Mallorca has prograded laterally over more than 20 km. Near Cap Blanc in southwest Mallorca it is exceptionally well exposed along both depositional strike and dip directions in vertical sea cliffs and is only slightly deformed by Pliocene–Pleistocene uplift, faulting, and gentle flexure. Below we are discussing the facies and stratal geometries of the Llucmajor Platform reef complex outcropping around Cap Blanc.

The Miocene Reef Complex of the Llucmajor Platform crops out in high, vertical sea cliffs along 20km. This complete exposure allows accurate stratigraphic description of the platform and the construction of a depositional model of the facies architecture. Four main lithofacies can be distinguished [*Pomar and Ward* (1994)]:

1) *Lagoon (back reef) lithofacies* are exemplified by horizontal beds bounded by erosional surfaces. Inner and outer lagoonal deposits can be distinguished, with the former composed of mudstones and wackestone (with stromatolites and muddy sediments for the innermost part) and the latter mainly of grainstone/packstone. The biota varies slightly, with coral patches found in the outer lagoon.

2) *Reef-core lithofacies* have characteristic sigmoidal bedding (Figure 5.3) and consist of skeletal graystone/packstone within the coral framework. Coral morphology zonation is well visible with dish corals in the lower part, branching corals in the middle and massive corals in the upper. The coral zonation due to the depth-controlled growth of the corals, when combined with palaeobathymetry leads to the conclusion of high frequency sea-level change. The reef lithofacies characteristic accretional unit is the sigmoidal packages that interfinger basinwards with the fore-reef slope lithofacies and landward with lagoonal deposits. The sigmoids are bounded by subaerial and submarine erosion surfaces. The sigmoids comprise the basic building block of the reef, and significantly add to the complexity of the subsurface.

3) Clinobeds of *reef slope (fore-reef lithofacies)* range from coarse skeletal packstones in proximal settings to fine-grain packstones on the distal - slope to open-shelf settings. The proximal fore-reef slopes demonstrate a gradual lateral increase of grain size from the deeper slope facies upward to the reef. This trend for coarsening and thickening upwards accompanied the progadation of the platform.

4) *Open shelf (shallow basin) lithofacies* consist of bioturbated fine-grained packstones. Due to bioturbation and progradation these beds may be interbedded with biostromes of coarse-grained red-algae packstone and laminar corals.

Figure 5.3B and C give an impression of the accretional units in comparison with the size of the surface seismic experiments discussed at a later section. All these accretional units represent high-frequency depositional sequences (seventh to fourth order). They all have similar characteristics in stratal geometries, bounding surfaces and facies architecture.

Figure 5.3B and C are drafted from photo-mosaic along the cliff at Cap Blanc (sb= sequence boundary, dls=downlap surface, ci=condensed interval). The reef-crest line is defined by the successive positions of the reef crest in relation to progradation and it reflects the amplitudes of sea-level fluctuations. The Llucmajor platform is flat-lying with a slight tilting related to basin subsidence and strike-slip faulting during Pliocene and early Pleistocene. Possibly, gentle uplift on the depositional patterns could have occurred, slightly influencing the current picture, but in general tectonic stability during the depositional times is suggested. The platform has been buried only a few hundreds of meters at most, therefore primary and secondary porosity remains intact.

Observed porosity in the outcrop is the result of both deposition and diagenesis. Primary porosity is related to distribution and proportion of lithofacies, which vary with systems tracts. For example, framework mega-pores of the reef lithofacies are preserved in the aggrading system tracts of fifth-order sequences because the framework is better preserved during increases in accommodation. Intergranular primary porosity is best in grainstones of the outer and middle lagoon and in some upper-slope layers. Original porosity and permeability, which were closely related to depositional facies, were altered mostly by dolomitisation of much of the complex and dissolution of aragonitic components resulting to large secondary porosity. Moldic porosity is the predominant porosity type in nearly all the rocks.

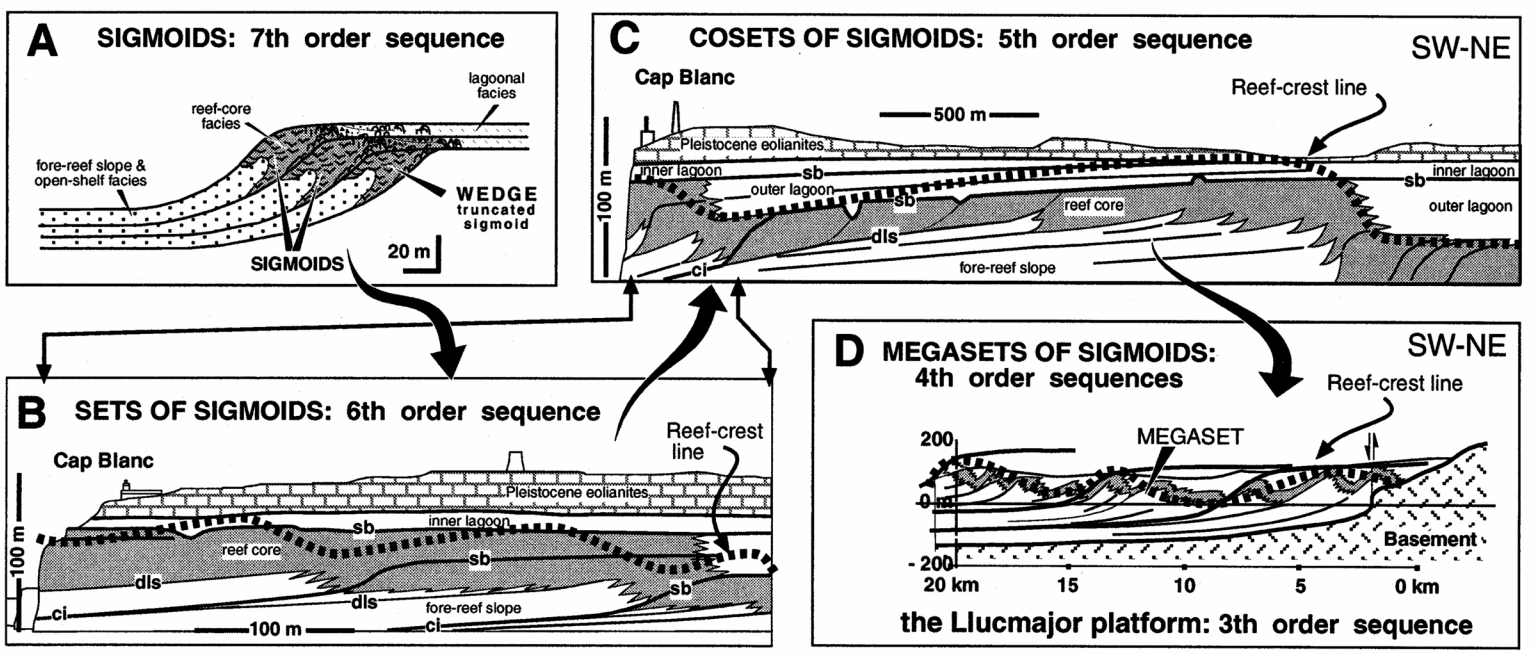

Figure 5.3. Accretional units defined in Upper Miocene Reef Complex of Mallorca [*Pomar and Ward* (1999)]. (A) The basic accretional unit or building block is the `sigmoid'. Sigmoids stack into progressively larger-scale accretional units of sets (B), co-sets (C), and mega-sets of sigmoids, which reflect hierarchical orders of sea-level cycles.

In both dolomitic and non-dolomitic rocks there generally are only thin crusts of cement in the moldic pores or in intergranular pores. Coarse, later-stage calcite is abundant in some pores in reef rock and in a few lagoon rocks, but rarely is porosity totally occluded; therefore, nearly all the rocks of this upper Miocene reef complex are highly porous. Because secondary porosity is characteristic of these rocks, total porosity and pore size is a function of original mineralogy, as well as of original grain size and sorting. For the most part, lithofacies that had abundant aragonitic components have the most secondary porosity. Lithofacies that included large aragonitic constituents, such as in reef and proximal-slope rocks, were left with mega-pores lined with only thin crusts of dolomite or calcite cement. Secondary porosity is less abundant in many inner and outer lagoon rocks. Many dolomitised distal-slope rocks have high porosity because both aragonitic and calcitic fossils are leached out [*Pomar and Ward* (1999)].

5.3. Seismic setting

The progradational reef at Mallorca is a popular destination for geophysicists, geologists, seismic stratigraphers and reservoir engineers mainly due to its analogy with carbonate reservoirs. Its modest scale also adds to the advantage of observing this reef in situ. Despite drawing such attention, little effort is been made to acquire high-resolution seismic images of the subsurface here.

A large part of our project resources were invested in developing this test site. Multiple surface and offshore seismic experiments were conducted. A number of 2D lines have been acquired, both parallel and perpendicular to the progradation. A 2.5km 2D line was shot in order to capture a full cycle of a fifth-order sigmoidal sequence. A 3D surface experiment was designed and seismic data acquired with three component receivers spaced at 2 m, covering an area of 300 m x 36 m and 38 m x 36 m respectively. Finite-difference modelling was performed prior to the acquisition to determine the acquisition parameters; the maximum depth investigated was 80 m. Initial seismic tests showed that 2D seismic experiments would not provide a good-quality image. The subsurface was well-known for its high lateral variability. Vertical and horizontal portable vibrators were used as seismic sources. Offshore seismic experiments were conducted in cooperation with the University of Gent, Belgium; a sparker was used as marine seismic source.

Expected reflector patterns for a simplified version of the structure of the reef have been predicted [*Pomar* (1993)]. These patterns are based on the assumption that the lithological boundaries here exhibit high reflectivity. This is justified by the high impedance contrast across physical surfaces describing distinctive lithologies [*Vail and Mitchum* (1977)]. The alternation between weak and strong reflectors will yield a seismic image of alternating high and low amplitude discontinuous reflectors (Figure 5.4). In this observatory, the significant impedance contrasts would be mainly the aeolian sediments with the inner lagoonal deposits, the reef crest curve and the boundary between reef slope and open shelf.

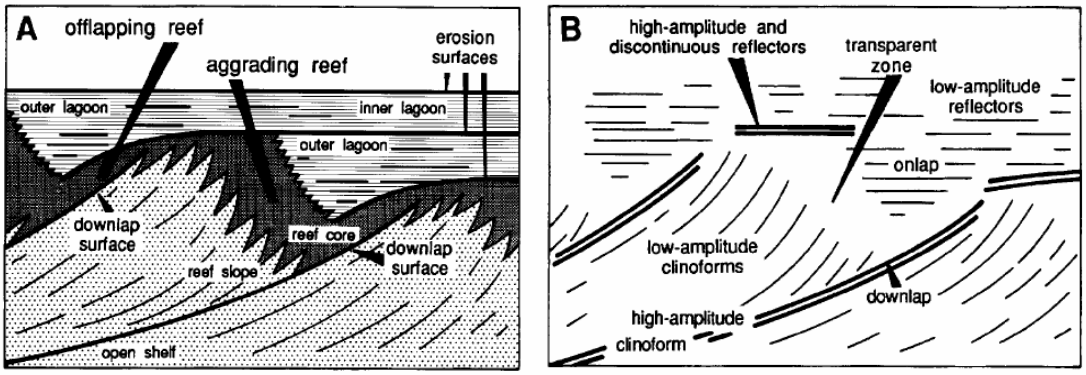

Figure 5.4. Expected seismic reflection patterns of the Cap Blanc high-frequency accretional units [*Pomar* (2001a)].

Even though the surface seismic experiments, and in particular the 3D, are of high resolution, they yielded poor imaging results. Figure 5.5 shows a time migrated seismic image from the horizontal component of the 3D surface seismic experiment, using the horizontal vibrator (SH component). On the right the processing scheme is summarised. Contrary to the VSP experiments, the S-wave surface experiments showed better data quality on specific gathers than the S-wave surface seismic data. However, the high-fold (330 traces) 3D seismic image returned a rather discontinuous pattern of reflectors, in contradiction with the predicted seismic stratigraphy of the area. We could interpret two possible reflections, the reef crest and the water table. The interpretation is possible only on few gathers, whether is the shot gather or the receiver domain. The reef crest is the only reflector that could be coupled with the VSP data. Any further attempt for interpretation of the surface seismic reflection section and well-tying was considered futile. Various processing tools have been used for processing the 3D data, with good results on the shot domain, on few gathers. Unfortunately, this did not yield a good stacked image.

Since the primary and secondary porosities remain intact, an air-filled chaotic environment of scatterers and diffractors is present. This contributes to the complexity of the sigmoidal accretional units. It is quite obvious that this high resolution surface-seismic experiment, in the Mallorca site, yielded a not satisfactory image. Hence, the observed wave attenuation here is believed to be predominantly due to scattering effects. The effective attenuation is measured from the P-wave VSP data. The core velocity measurements provide a model for the apparent attenuation due to internal multiples. The results presented in this chapter are obtained from application of the methodologies described in Chapter 3 and 4.

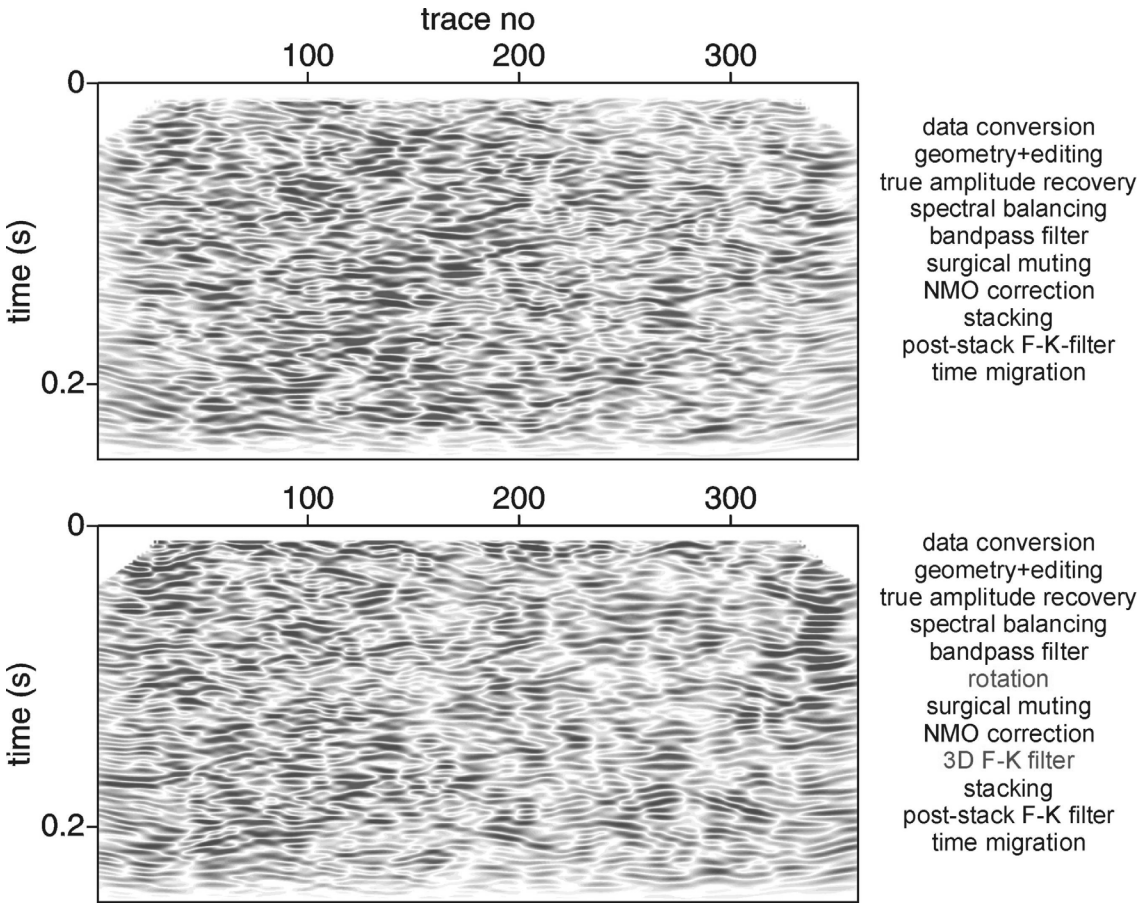

Figure 5.5. Time migrated SH-wave seismic section of the middle line of the setup. Top section is result of "standard" processing flow; lower section includes rotation of horizontal components and 3D F-K filtering. The processing flow for each image is given on the right.

5.4. Estimation of effective attenuation from VSP data

5.4.1. Acquisition and processing of VSP data

In August 2003, a borehole 80 m deep was drilled at the centre of the 3D seismic grid (Figure 5.1, CBB hole). Similarly to the Boulogne experiment, it was fully logged and cored. The VSP measurements took place soon after the 3D surface seismic reflection experiment (Figure 5.6). The seismic sources used were the vertical and the horizontal vibrators. The frequency sweep was in the same frequency range for both VSP and surface seismic reflection experiments. The seismic source was positioned at an offset of 3.10 m. At each depth level, the horizontal vibrator was positioned perpendicular and parallel to the borehole-source line. Walk-away measurements were made to determine the orientation of the horizontal components of the receivers. We used a 6-level three-component receiver tool for the VSP. The depth interval of sampling was 0.25 m, and the maximum depth reached was 72.75 m. The tool was clamped against the borehole wall by inflating a hose to a predetermined air pressure next to the receiver tool.

Figure 5.6. Preparation of the VSP experiment in Mallorca, Cap Blanc. A: Borehole location, B:6-level three-component receiver tool.

A standard processing scheme was used for the P-wave VSP dataset. After trace editing, a band-pass filter (100-400Hz) was applied to reduce the high-frequency cross-talk noise. The remaining cross-talk noise at lower frequencies could not be easily distinguished from the data. A surgical mute was applied to remove it and preserve the small arrival times. The ground force was estimated for every shot separately, using measured base plate and reaction mass accelerations. Source signature deconvolution was performed following the same procedure described in chapter 4; this corrected for source-to-source amplitude variation. Correction for the geometrical spreading was then applied. The data was resampled 8 times finer and a linear move-out correction was applied to enhance the alignment of the first arrivals. The pseudo-offset was treated as static; therefore the time shift was calculated and removed from the data. A velocity of 2000 m/sec was used for this correction.. The first arrival was crisp (Figure 5.7). The first arrival was time windowed and carefully tapered so that the tapering would not bias the frequency content used for attenuation estimation.

5.4.2. Coupling issues

Factors that may bias the spectral amplitude are mentioned in chapter 4. The Boulogne borehole was cased because of the unstable shale formations. The coupling of the VSP tool to the PVC casing was assumed constant and of good quality. In Mallorca, the borehole was uncased. A caliper log describes the changes in the borehole diameter (Figure 5.8A). Changes in the borehole diameter are related to well construction and to fracturing or caving along the borehole wall. Since the borehole at Mallorca was shallow (80 m deep), a constant diameter drill-bit was used. Therefore, the changes in the caliper are considered to be purely lithological and can be related to the secondary porosity. In many cases, changes in the diameter of the borehole affect directly the coupling of the VSP tool and may bias the recorded signal.

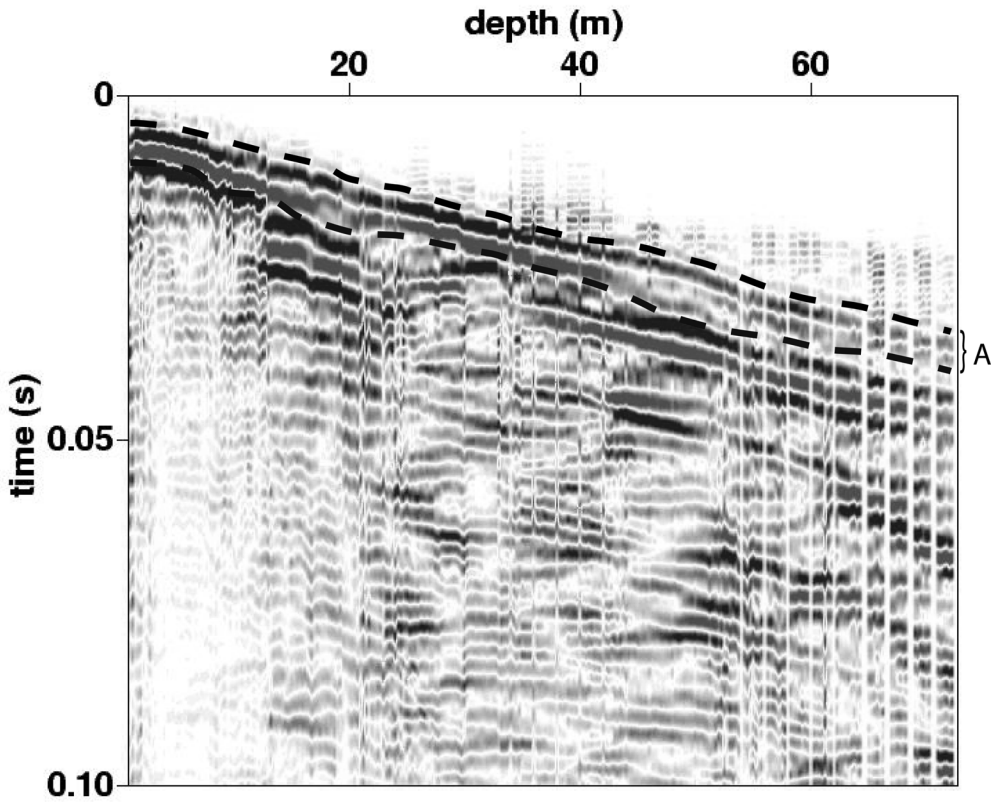

Figure 5.7. P-wave VSP data after processing. Missing depths were not interpolated. (A) The windowed first arrival is indicated with dotted lines.

The caliper log (Figure 5.8A) is compared with the amplitude spectra of the windowed first arrival and the amplitude spectra of the total processed recorded signal (Figure 5.7). Note that the grey scales in Figure 5.8(B) and (C) are not the same. The interpreted geology based on core examination is displayed alongside in the same figure. It is clear that there is a good agreement between the sudden changes in caliper values and the lithological boundaries. These changes are also reflected very well in the amplitude spectra, for both the first arrival and the total signal. Possibly the total signal offers more details, such as splitting of frequencies (leaking modes) at around 20 m. This is possibly due to bad coupling of the VSP tool, effect which is, in turn, a function of lithology (washout taking place at the lower Pleistocene Aeolianites). A thin layer of tight sand with doubtful lateral continuity, is observed in cores at 14.60 m - 15.60 m depth [*Clemmensen et al.* (1997)]. Below this thin layer, the frequency content and amplitude of the recorded signal changes significantly. The frequency content of the windowed first arrival shifts characteristically to lower frequencies at 25.09 m, where the boundary of aeolianiates-lagoonal deposits is located. No significant

changes are noticeable till the lower part of the reef core (approximately 47 m depth) and in the depth range where major changes in coral population occur and dish corals appear and dominate (50.89 m - 58.65 m). The cores in this interval show a fairly chaotic pattern generated by alternating rubble and in situ coral growth with different generations of sediment fills. The chaotic patterns are also reflected in the highly irregular caliper logs. Below this interval, the fore-slope and the distal slope sediments start at 68.54 m depth. The VSP experiment covered the upper 72.75 m of the 84.86 m deep borehole.

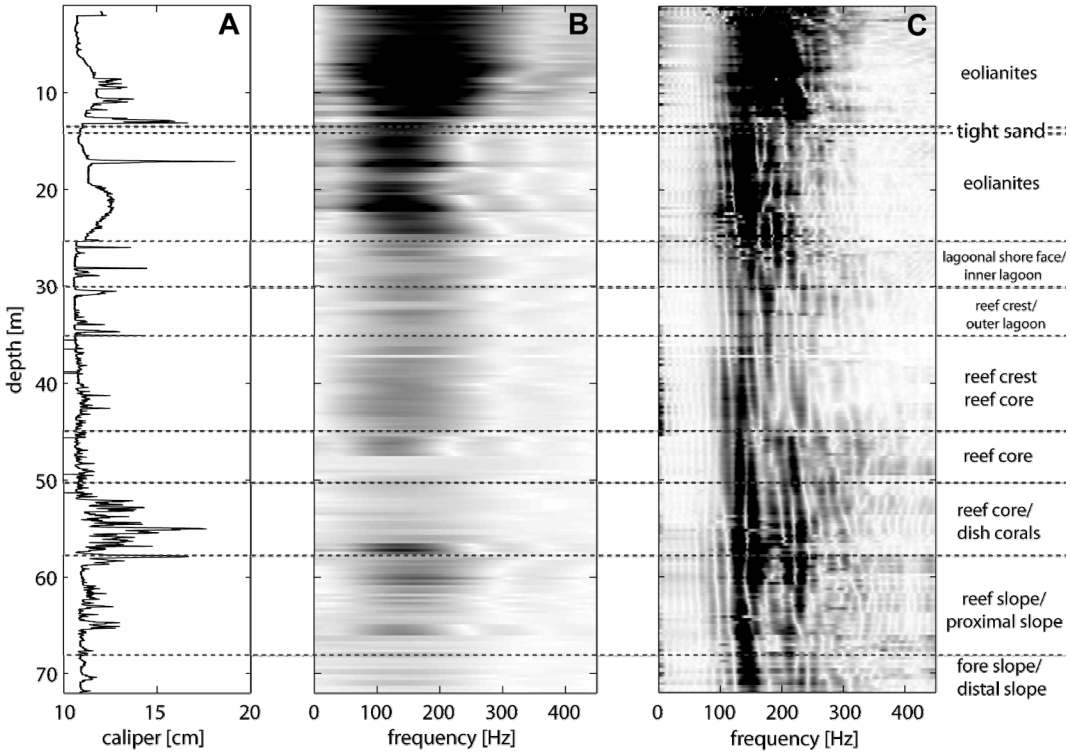

Figure 5.8. A) Caliper log in the CBB hole. B) Amplitude spectra of the windowed first arrival in the VSP data. C) Amplitude spectra of the total length of the recorded signal. The geology obtained from core examination is given on the right side.

5.4.3. Estimation of the quality factor, Q_{eff}

The receiver pairs for the spectral ratio method were chosen as described in chapter 4. A top and a bottom reference receiver were selected and 246 pairs were constructed. Even though different geological formations can be identified and grouped (e.g. aeolianites, lagoonal deposits, reef, slope), a choice was made for estimating the effective attenuation from the total VSP depth. The VSP experiment in Mallorca is characterised by lower

frequencies than its French counterpart. The frequency range used for the spectral ratio analysis was found to be limited to 80-250 Hz. The attenuation factor Q_{eff} was calculated. The difference between the Q_{eff} estimated with the top receiver as the reference and that using lower one instead is greater than the difference found in the Boulogne experiment. This is mainly due to the sudden change of spectral amplitude between the aeolianites (top 25 m) and the rest of the formations. Nevertheless, both Q-factor profiles are close enough to allow for a meaningful averaging. The unstable Q_{eff} values observed around 210-240 Hz with the top receiver as the reference is attributed to an increase of the amplitude spectra at specific depth intervals. These frequencies are, in turn, associated with noisy caliper values indicating poor coupling, mainly in the reef core part of the borehole.

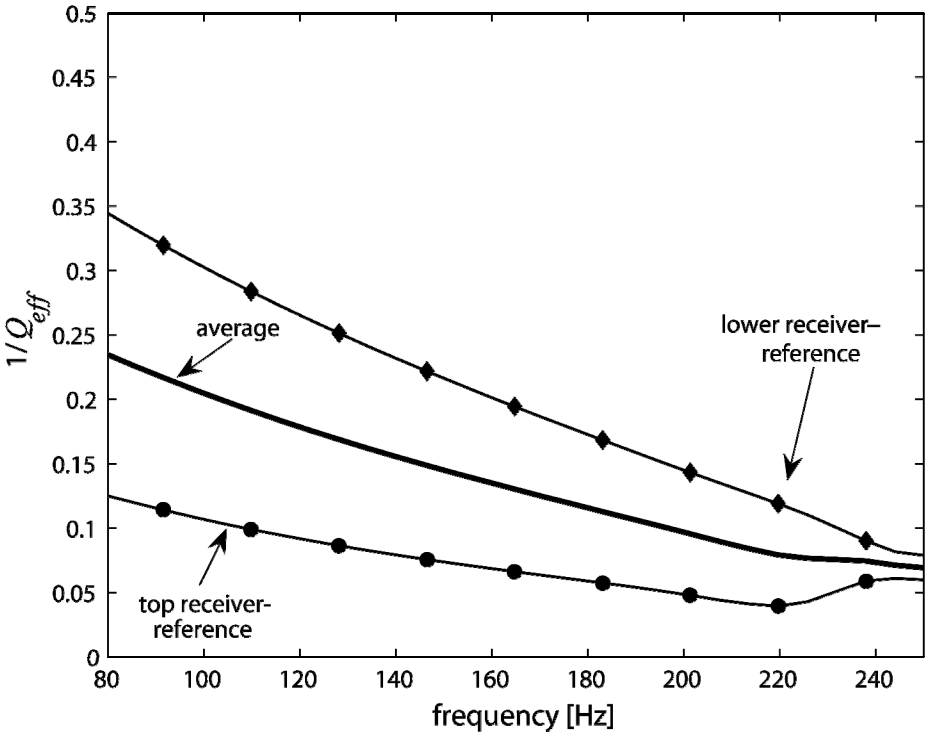

Figure 5.9. Q_{eff} versus frequency calculated from the VSP data.

5.5. Estimation of apparent attenuation, Q_{sc}, and dispersion

MST was used to measure acoustic velocity and bulk density. The depth sampling was 0.005 cm. Core recovery from the CBB hole was nearly continuous. Due to extremely high primary and secondary porosities, the core was brittle and not fully recovered at few short intervals. These gaps were interpolated and constant velocity was assumed.

5.5.1. Apparent attenuation and dispersion at different scales

The acoustic velocity and density logs measured on the core (MST) are regularised for different scales using the wavelet transform (Figure 5.10). A Gaussian was used as analysing wavelet, following the procedure described in chapter 3. The values of both logs fluctuate substantially, with the high velocity contrasts in the depth range 25 m - 55 m, which coincide with the lagoonal deposits and the reef formation. The highest density-contrast coincides with the reef part.

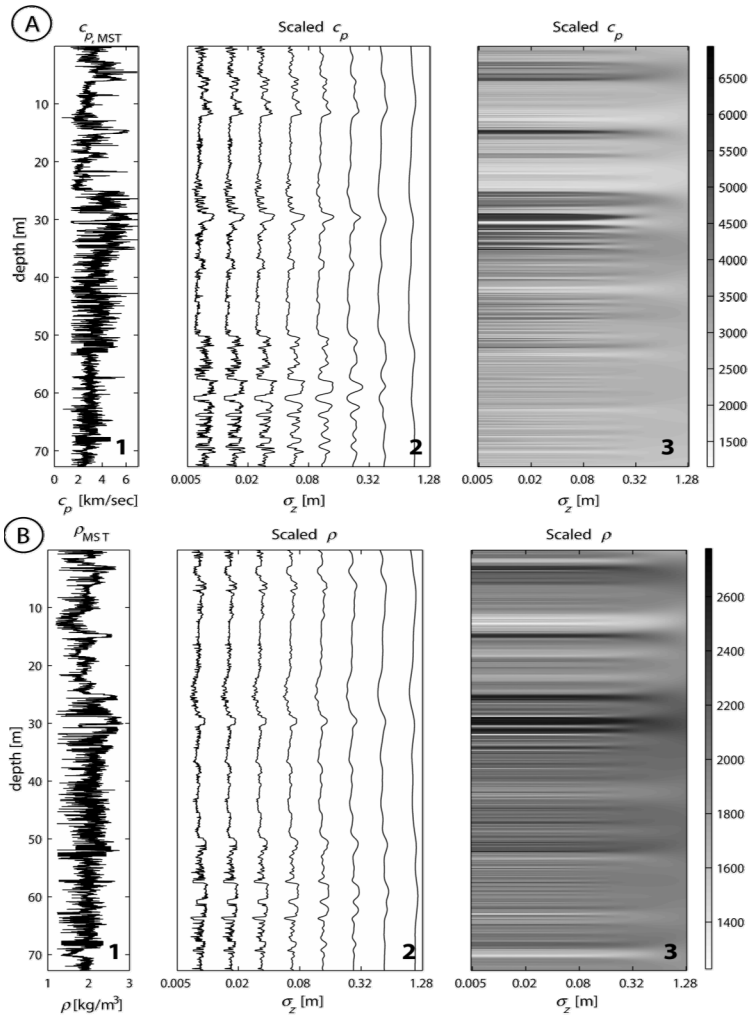

Figure 5.10. Velocity (A) and density (B) regularisation of the core-measured P-wave velocity log (left) for few distinct scales σ_z (middle) and for a range of scales (120 regularised velocity profiles plotted), closely spaced in a grayscale plot (right). The grayscale denotes the velocity values.

The upscaled velocity and density values are subsequently used to provide scale-dependent impedance logs. The transmission and reflection response of the medium at different scales are calculated using the full waveform reflectivity model (Figure 5.11). The

transmission impulse response is modelled on the assumption that the medium is finely-layered and non-dissipative, and that apparent attenuation is entirely a result of scattering due to internal multiples.

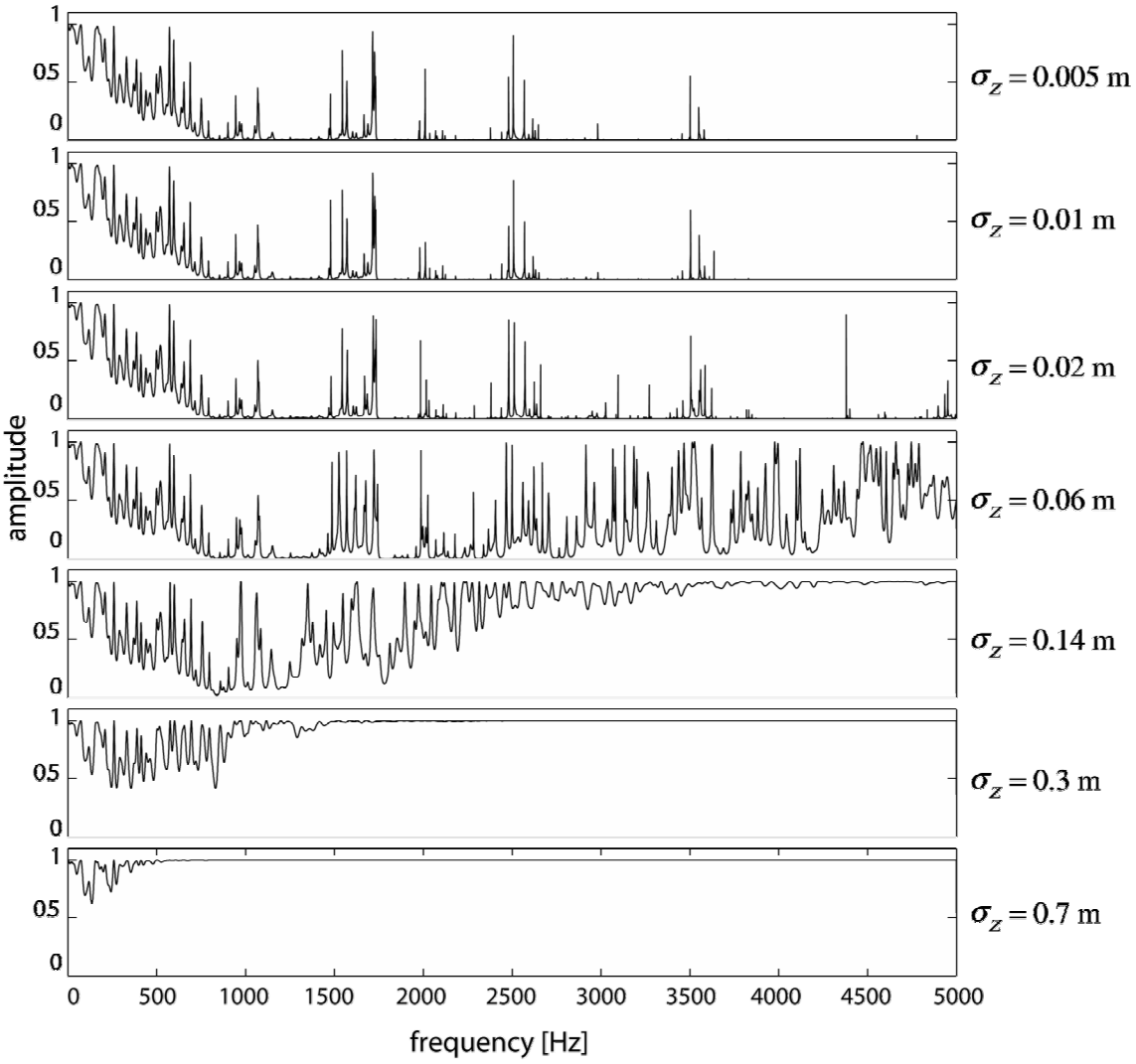

Figure 5.11 Transmission impulse responses for the c_p measured on cores for different scales, as shown in Figure 5.9.

It is interesting to observe that for scales smaller than σ_z=0.02 m there is no substantial change in the amplitudes of the transmission response. At scale σ_z=0.02 m, even though the amplitudes look very similar, a high peak appears at approximately 4400Hz. This is a direct result of the regularization, and thus of the change of velocity and density values. The statistics of the medium at this scale change in such a way that the constructive and destructive interference pattern changes accordingly. In a similar way we can observe how

this pattern changes as the scale increases. Transmission at high frequencies is at later scales again possible. Such observations can be linked with the inherent scale of heterogeneities of the medium described by the log values. It can also be seen that the pattern of the amplitude of the transmission response does not change until a comparatively large scale (in Figure 5.11 σ_z=0.14 m). A look-up table as in Figure 5.10C can be constructed and the relative changes in amplitude can be studied.

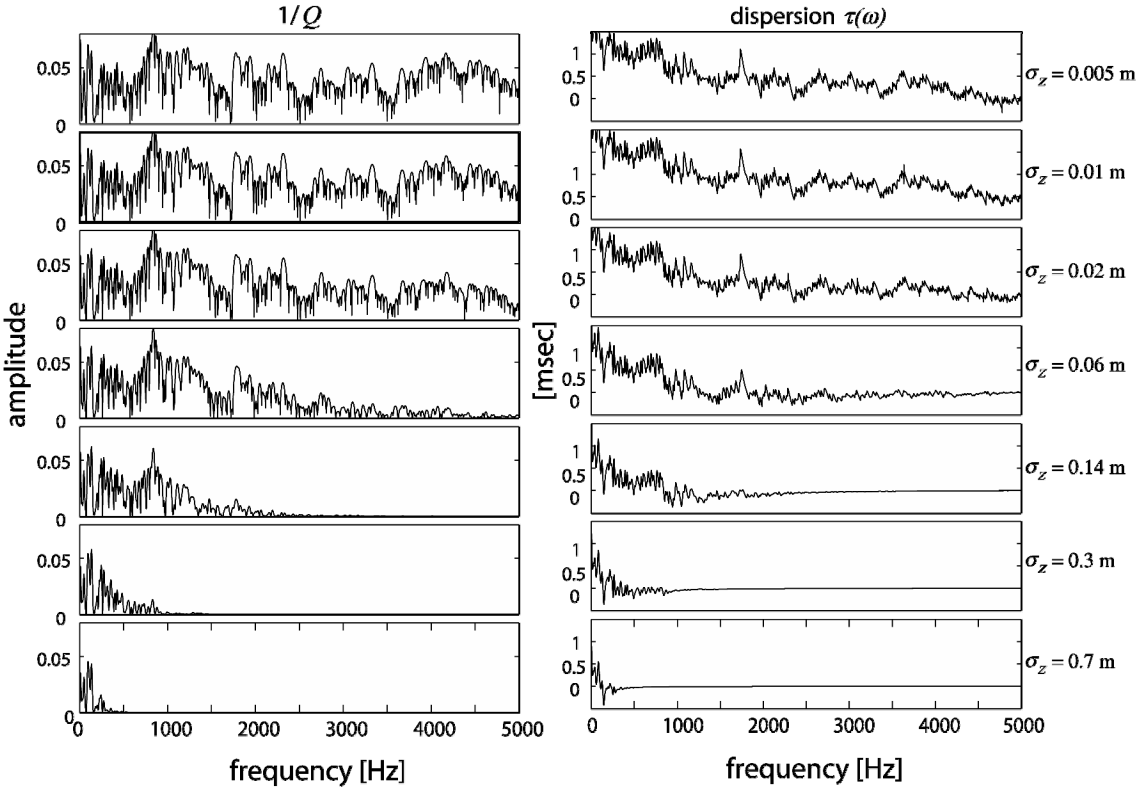

Figure 5.12. Attenuation $1/Q$ (left) and dispersion as calculated from the coda term constructed from the full waveform transmission response, for different scales (from upper to lower plot: 0.005m, 0.01m, 0.02m, 0.06m, 0.14m, 0.3m and 0.7m)

The attenuation and dispersion at different scales is calculated from the transmission response (Figure 5.12). There is a decrease of high frequencies with scale as an effect of the regularization of velocity and density. The scattering effect related to the finest scale measured properties can be quantified for the scale of the VSP. From the simulated transmission response, the coda term was constructed and the apparent attenuation and dispersion effect were determined (Figure 5.12).

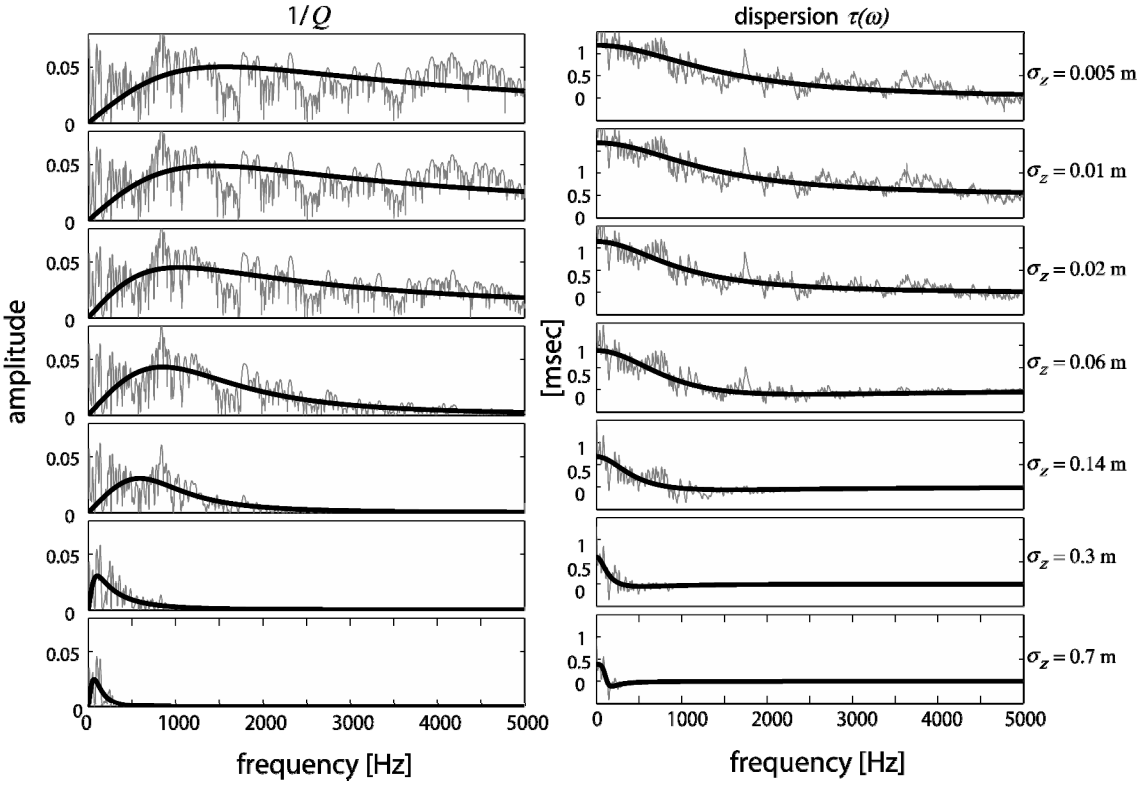

Figure 5.13. Fitted curves with the proposed macro-model for different scales.

5.5.2. Macroscopic properties at different scales

It has already been established that scale-dependent macro-model properties can be obtained deterministically from the simulated dispersion and attenuation terms (Chapter 3). The attenuation and dispersion curves are fitted using a non-linear least square fitting algorithm. The results are shown in Figure 5.13. From the attenuation and dispersion curves – at least- three regions can be distinguished in the lower part of the frequency range shown: 0-500 Hz, 500-1500 Hz and larger. As the scale increases, the amplitude of the real and the imaginary part of $A(\omega)$ decrease progressively towards lower frequencies (Figure 5.12). Lower frequencies correspond to large variability of the medium properties. The parameters of eigenfrequency, ω_0, ***a*** and ***b*** are shown in Figure 5.15. In general, the values decrease exponentially with scale; the larger the scale the smaller the values and the frequency range for term $A(\omega)$. Similarly, three regions can be identified for the three different scale ranges: 0.005 m -0.03 m, 0.03 m - 0.1 m and larger than 0.1 m. For all parameters, deviation from an exponential trend is noted at these scale-ranges. The fit is therefore biased by the shift from one regime to the other, denoting the limits of three-grouped variability. That implies that

even though a single term model is good enough, a higher order would be necessary to fit better the attenuation and dispersion curves. The ranges of frequencies mentioned above, are related with the characteristic ranges of scales in the medium.

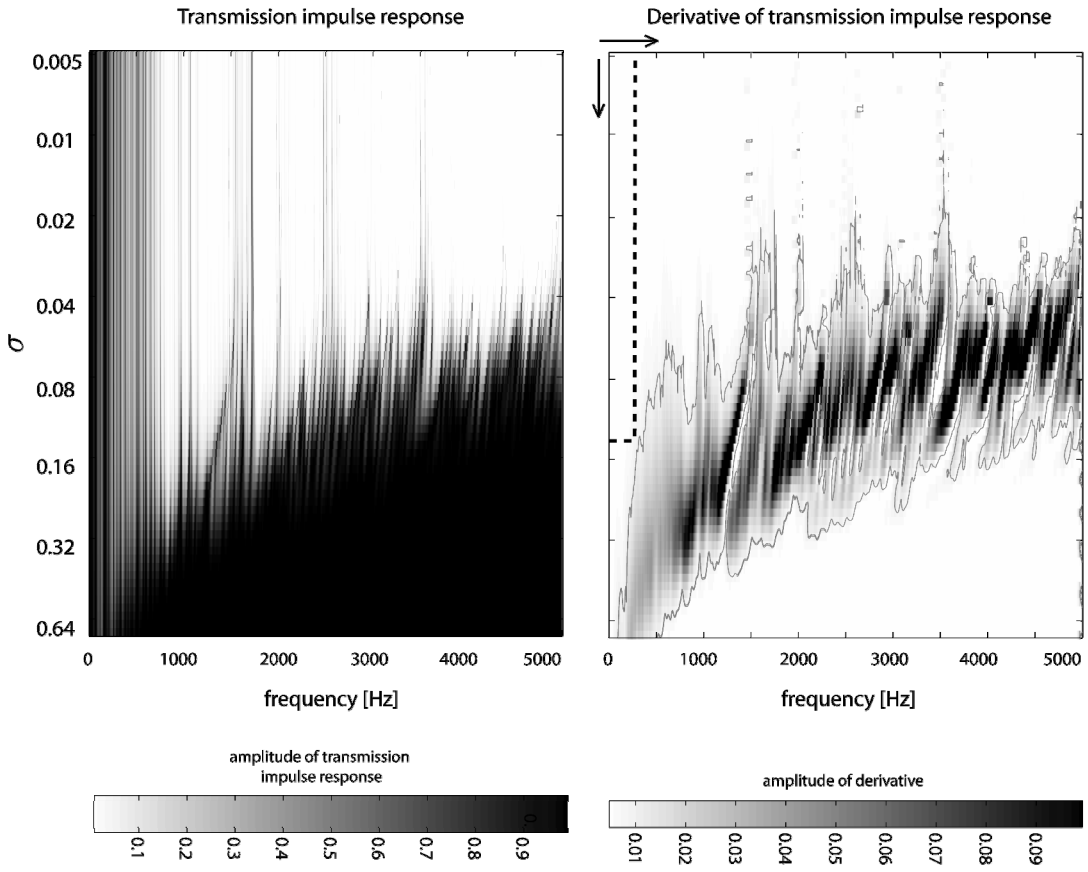

Figure 5.14. Left: transmission impulse response for different scales, plotted in greyscale. Right: the derivative of the transmission impulse response. The scale at which the MST should be upscale is determined to be σ_z=0.14m.

We have used the same criterion as in section 4.6, for estimating the scale at which the MST observations should be upscaled to be linked with the VSP. The amplitude of the transmission response was plotted for different scales and the rate of change $\partial A/\partial\sigma_z$ was calculated. Following the method described in 4.6, the scale at which the MST measurements need to be upscaled to be compared with the VSP is σ_z=0.14m for the Mallorca case. In order to obtain a smooth version of the attenuation profile the coefficients ω, ***a*** and ***b*** as described in 4.5.2.

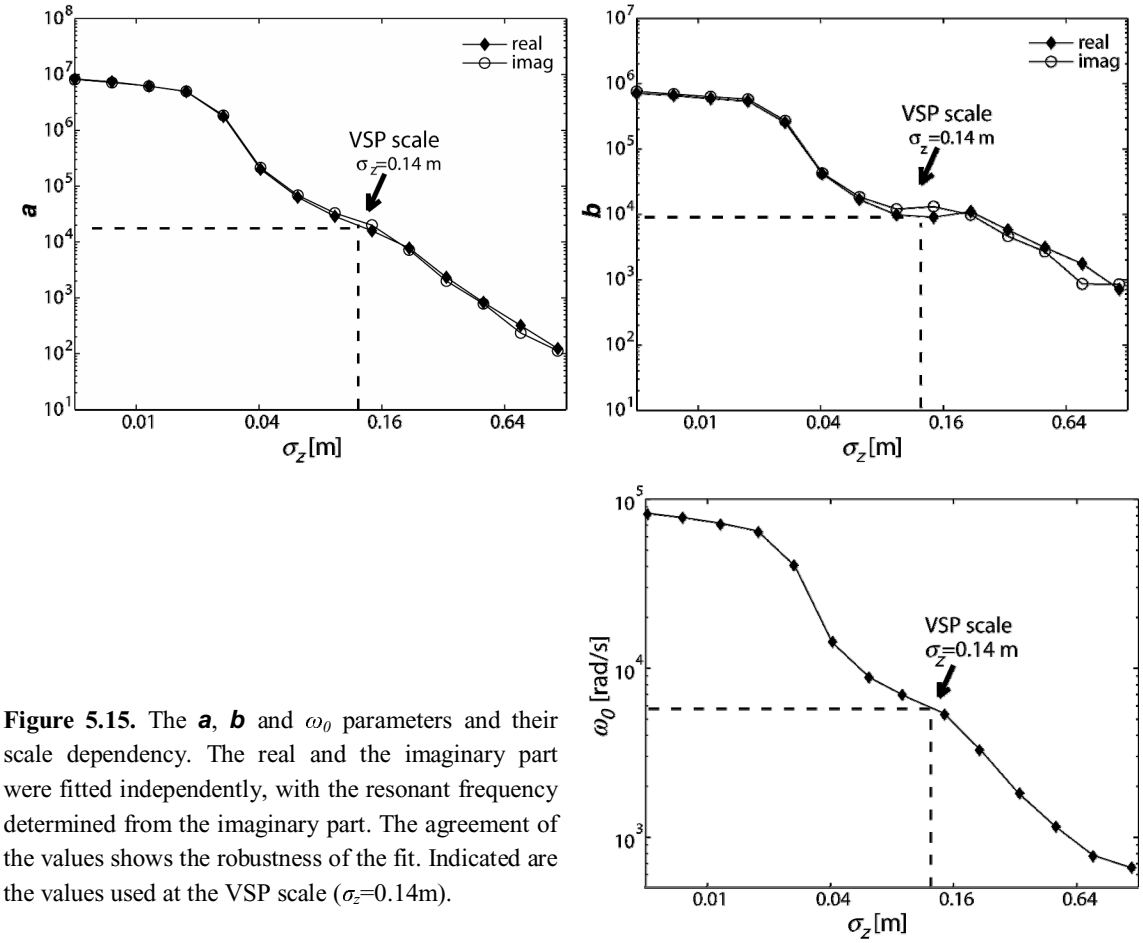

Figure 5.15. The ***a***, ***b*** and ω_0 parameters and their scale dependency. The real and the imaginary part were fitted independently, with the resonant frequency determined from the imaginary part. The agreement of the values shows the robustness of the fit. Indicated are the values used at the VSP scale (σ_z=0.14m).

The apparent attenuation derived from the curves fitted to the macro-model is used as a quantitative measure of the multiple energy contribution in wave propagation. Similarly, the dispersion term is used to demonstrate the deviation (drift) of the direct propagation travel time of the regularized velocity as proposed by *Sams et al.* (1997). This has been compared with the drift obtained by correcting for the extra time delay (dispersion). The extra time delay is calculated using the macro-model properties and the full waveform synthetic model for the VSP frequencies (Figure 5.16).

It can be seen that the time predicted using the macro-model parameters, has captured correctly the trend and the average value of the dispersion term as derived from the full waveform synthetic seismogram. Therefore, it validates the use of the macro-model for describing the total attenuation and dispersion.

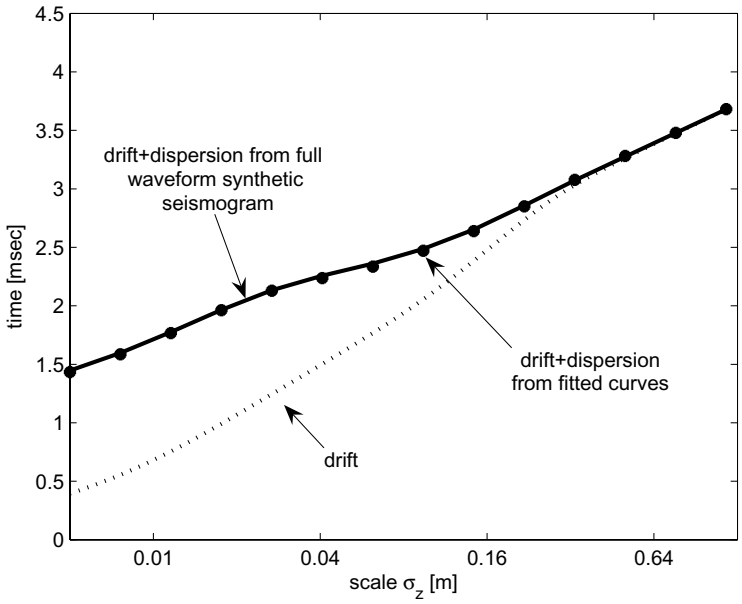

Figure 5.16. Integration of scale dependent arrival time of a wave.

5.6. Conclusions

The Llucmajor Platform site with all its complexity offered a unique opportunity to test the high-resolution experimental setup, with multiple surface-seismic experiments and vertical seismic profiles. High-resolution experiments had proven previously successful given the imaging results obtained from the siliciclastic sequence in Boulogne. The poor imaging results in the Mallorca outcrop demonstrate clearly the complexity of the site. A *"previously unattained high-resolution"* image was indeed achieved in the Mallorca experiment. However, this does not mean that we are satisfied with this image or that we are able to better interpret it. High-frequency broadband waves are more subjective to fine-scale scattering than their low frequency counterparts. The fact that the desired seismic image was not achieved in a site like Mallorca, should not discourage us. On the contrary, it corroborates the –yet unabridged– link between scale of observation and scale of heterogeneity. Processing techniques like band-pass filtering or other similar tools can not improve the image substantially. With this experiment it has become evident the importance of scale that is inherent in every geological or geophysical target. One important conclusion is derived by

these experiments: high-resolution surface seismic experiments are not a seismic imaging panacea that will yield detailed and wishful results at any geological environment.

Similar remarks addressing the scaling issues using different source frequencies were obtained from the results of an experiment that was performed using a georadar at the Department of Geotechnology, at the TUDelft. Three different source-frequencies (antennas) were used to scan over the same area. This experiment revealed that with different frequencies of the source signal, completely different images of the subsurface can be obtained (processed data shown in Figure 5.17). We cannot use the highest frequency image and filter it to obtain the lowest frequency image due to the frequency dependent convolution of the source signal with the medium. A proper scaling should reflect the physical processes taking place during the phenomenon under study. Similar to seismic experiments, propagation of the electromagnetic waves is scale-dependent. Therefore, supposing that a broadband electromagnetic source of i.e. f=100-450 MHz could be used, the three different images of the subsurface (Figure 5.17), could not be obtained with simple filtering.

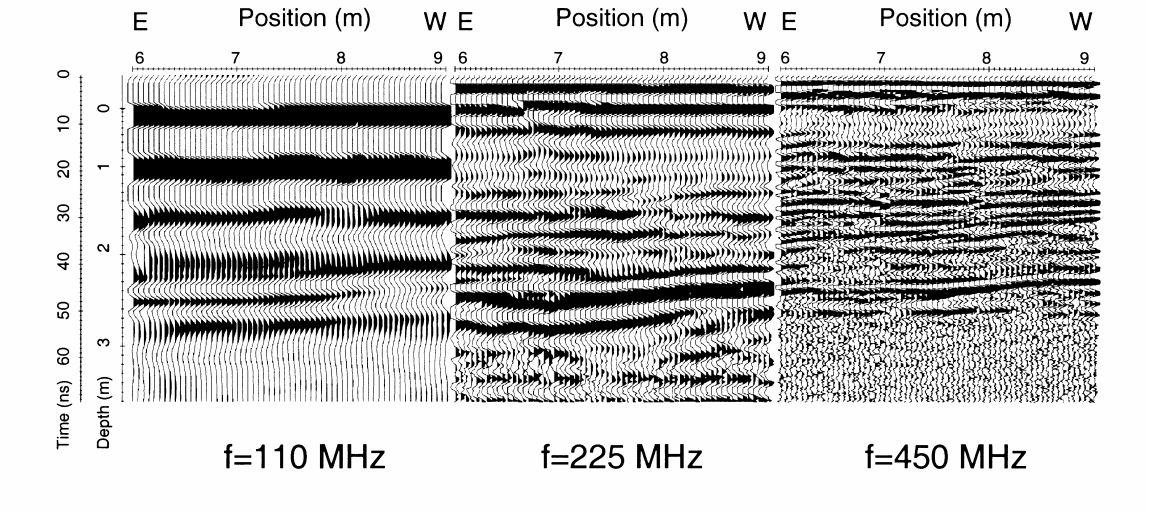

Figure 5.17. GPR measurements using three different source frequencies (110MHZ, 225MHZ and 450MHZ) revealing a different image for the same subsurface.

The high-resolution surface seismic experiment conducted at the Mallorca site, did not resolve satisfactorily any of the expected reflectors, let alone internal patterns of the reef. Consequently, using a lower-frequency source could possibly offer an alternative in revealing a seismic image of the subsurface at a coarser scale.

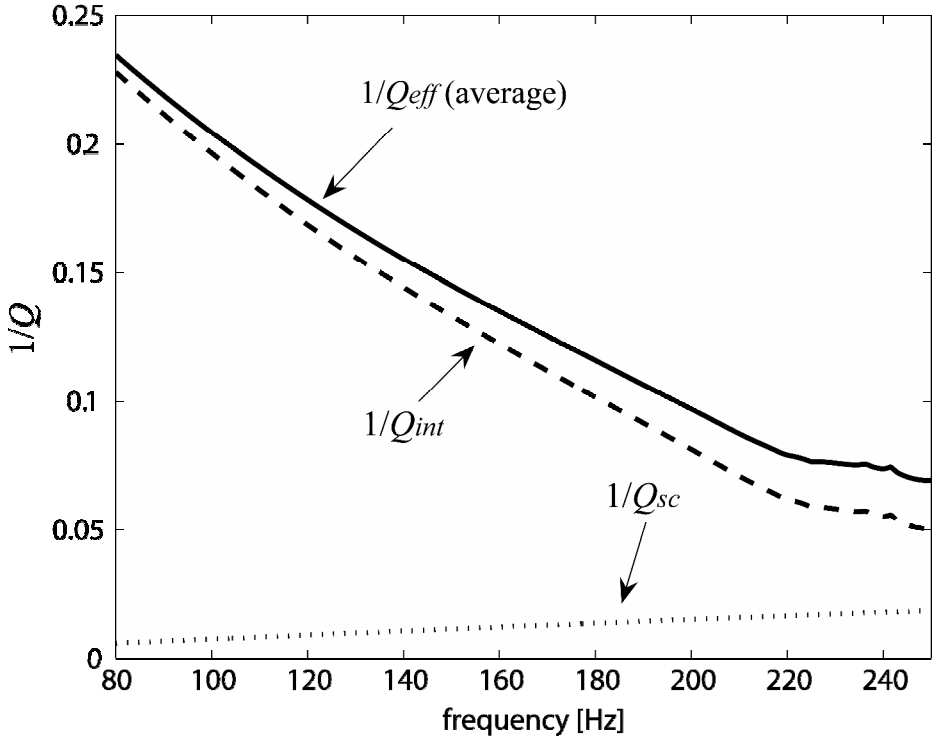

Figure 5.18. Estimated $1/Q_{eff}$ from the VSP data with the spectral ratio technique, $1/Q_{sc}$ estimated from modelling the wave propagation in a lossless finely-layered upscaled medium derived from the MST measurement and the calculated $1/Q_{int}$.

In this chapter, we have treated the subject of attenuation and dispersion using the same method as for the Boulogne dataset. The lateral invariability of Boulogne is an assumption that does not necessarily apply to the Mallorca site. Nevertheless, given the small lateral extent of the experiments used (VSP and core measurements) it is considered valid to use the same approach. However, we should be extremely cautious when thinking outside the area of our measurements.

Adopting the cumulative effect of attenuation model, described as:

$$\frac{1}{Q_{eff}} = \frac{1}{Q_{int}} + \frac{1}{Q_{sc}}, \tag{5.1}$$

we can estimate the intrinsic attenuation (Figure 5.18). It can be seen that for the frequency range for the VSP experiment the attenuation due to scattering is almost constant. That result agrees with the observations on the modelled scale-dependent transmission responses (Figure 5.11). It was shown that the amplitudes of the transmission response for the low-frequency range do not change until a substantially large scale, well above the scale of the VSP

experiment. However, taking into consideration the 3D effects, the water-saturation and the large porosity values, such a model could essentially underestimate the effect of wave attenuation due to scattering. As to which extent this would affect the $1/Q_{int}$ depends on the model used. The model described by (5.1) would imply that underestimation of the scattering component would lead to an overestimation of the intrinsic attenuation. This can very well be the case. If we manage to measure accurate amplitudes of both the transmission and reflection response we would be able to combine this information and get a more accurate estimation for the intrinsic attenuation.

A promising modelling method for studying attenuation and dispersion effects in formations with large porosity values could stem from discrete particle models. Such a model is the so-called Lattice Solid Model (LSM), presented in Appendix B. Even though experiments with variable porosities or voids simulating micro-karsts were not performed during our experiments, there are possibilities for developing realistic 3D models of dry rock structures at different scales.

I don't have *to know an answer. I don't feel frightened by not knowing things;*
by being lost in a mysterious universe without any purpose
which is the way it really is, as far as I can tell, possibly.
It doesn't frighten me.
Richard P. Feynman

Chapter 6

A tale of two sites: Synthesis

6.1. Introduction

We studied the effective attenuation and modelled the apparent attenuation due to internal multiples from data of two field sites. This offered us means to better understand wave propagation through the heterogeneities observed in the outcrops. In this chapter we compare and synthesize the different results we obtained for the two experiment locations: Boulogne and Mallorca.

An overview of the methodology used in the thesis is schematically presented in Figure 6.1. The framework of this project has combined multiple disciplines within geosciences, namely geology, petrophysics and geophysics. Different scales of geological heterogeneities are addressed and described. Laboratory measurements convert quantitative and macroscopical observations to acoustic properties. The acoustic properties are mapped by our reflection and transmission field experiments. In this research, the results of the experiments are presented in terms of attenuation and dispersion using transmission measurements only.

Surface seismic experiments in both sites were performed. In the Boulogne site a very good high-resolution seismic image of the subsurface was the final product. On the

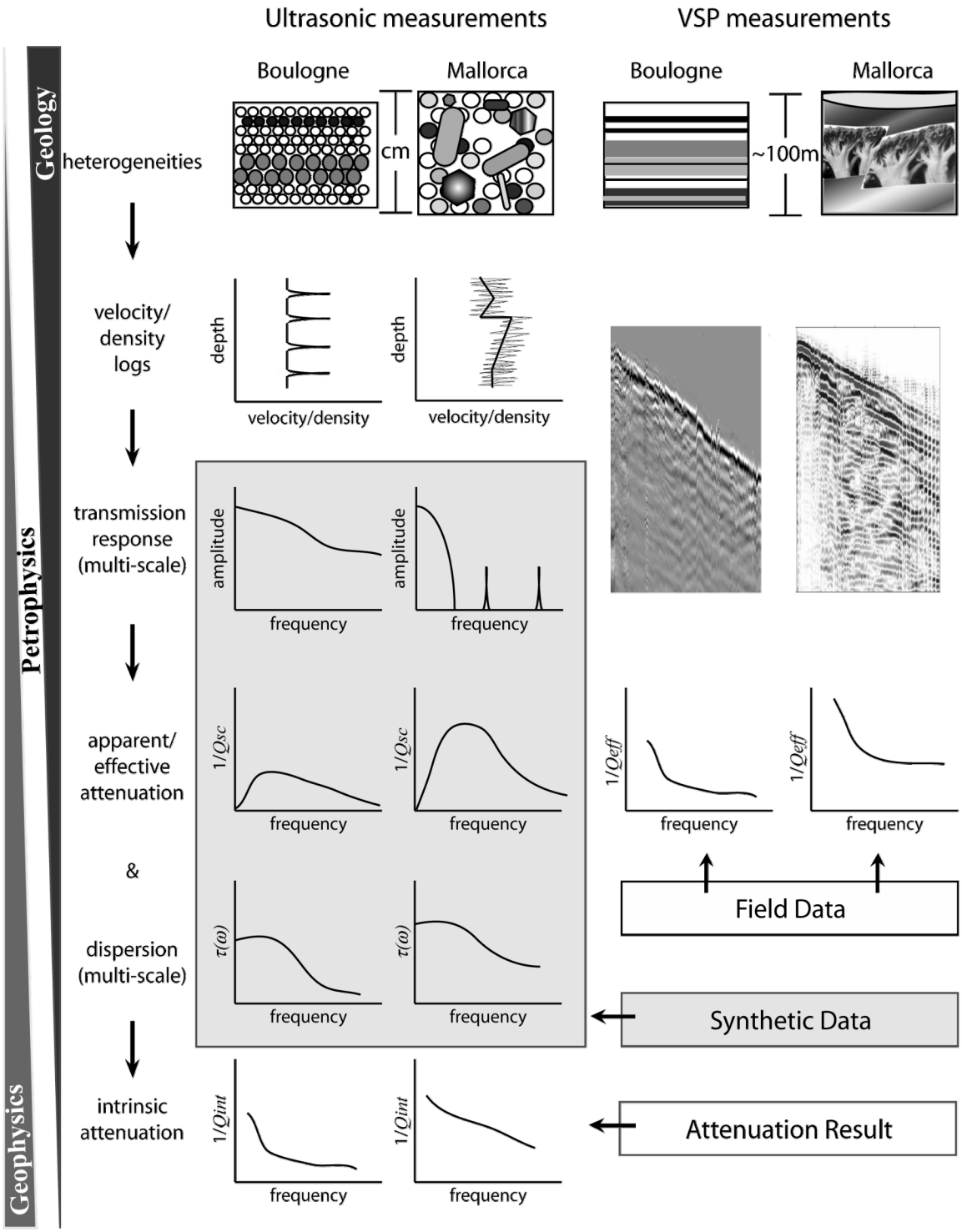

Figure 6.1. Schematic summary of the methods and results presented in this thesis.

contrary, the surface seismic experiment in Mallorca did not return a clear image of distinctive seismic reflectors. Nevertheless, the frequency content of the recorded signal of the VSP measurements showed very good agreement with the geological description in both outcrops. The two VSP datasets were used to estimate the effective attenuation, using a modified spectral ratio method.

Ultrasonic measurements of velocity and density were performed on cores from the boreholes in which the VSP experiments were performed. We used these measured acoustic properties to create a 1D finely layered medium. We modelled the transmission impulse response of the layered medium using the full waveform synthetic seismogram. From the modelled transmission response we estimated the dispersion and apparent attenuation due to internal multiples. We used the wavelet transform to scale the 1D finely layered medium to the VSP scale. In this way we could estimate the dispersion and apparent attenuation at the VSP scale. We used the cumulative model for the total attenuation in order to estimate the intrinsic attenuation, combining the field measurements and the modelling results.

6.2. Geology and petrophysics on the two sites

There are some significant differences on the genetic factors that control the development of depositional sequences in carbonates and clastics [*Haq et al.* (1987), *Handford and Loucks* (1991), *Schlager* (1991), *Hunt and Tucker* (1992), *Schlager* (1993)]. Clastic sequences are governed by lateral input of physically eroded sediment from the continent into the basin. Usually the sediments are well sorted and well organised. Carbonates, on the other hand, are quite often biological systems that are built up in-situ. Carbonate production is closely related to the sea level, changes which affect both accommodation and production. As a consequence, sea-level fluctuation can be inferred from the facies architecture.

6.2.1. Control of heterogeneities on acoustic properties

Microphotographs from the Boulogne and Mallorca outcrop clearly demonstrate the difference between the two outcrops. Boulogne shows good grain sorting and organisation. Examples of well ordered and compacted grains can be seen (Figure 6.2 (A)-(B)). Mallorca is characterised by chaotic material organisation with large porosities. The reef platform at Cap Blanc retains almost intact its primary and secondary porosity. Dissolution of shells (moldic porosity) adds to the chaotic nature of the outcrop. Mallorca (Figure 6.2 (C)-(D)) samples show various sizes and shapes of grains (aeolianites and inner lagoon), large porosities (reef, slope) and in particular high moldic porosity. From the thin sections in Figure 6.2 is obvious that in Mallorca occur larger velocity contrasts than in Boulogne in the same microscopic scale due to higher alternation of sediment and air-filled pores. Extreme values of acoustic properties would comprise of velocity/density of air for the low end and velocity/density of carbonate material as a high-end member, for the Mallorca experiment. In the case of Boulogne, the lower and higher values would be much closer; biased by velocity/density of water content in the pores and the acoustic properties of limestone.

6.2.2. Acoustic properties and impedance contrasts

The surface seismic experiment and in situ geological observations revealed that the formations in the Boulogne outcrop are laterally highly continuous and minimally variable. Therefore a simple 1D model is representative of the structure.

On the other hand, high lateral discontinuity was observed in Mallorca. Even though a 1D model can give insight on the wave propagation in the particular outcrop it will be still very limited. The interpretation of the findings has to be considered under the prism of the limitations of the 1D model. Moreover the laboratory velocity and bulk density measurements were performed on water saturated cores. This means that because the porosity is very high, the laboratory acoustic measurements were definitely

influenced by the presence of water. Let us recall that the in-situ Mallorca outcrop is dry. Should measurements on dry rocks be performed, the impedance contrasts would be much larger. This would return much higher apparent attenuation estimation. Essentially, the scattering effects observed in Mallorca have been underestimated in the 1D model. A more accurate estimation of the scattering effects could be obtained by a more detailed 2D and 3D experiment in both modelling and field experiments. We believe that further modelling using discrete particle models (like the LSM, presented in Appendix B) would facilitate such detailed and more realistic description.

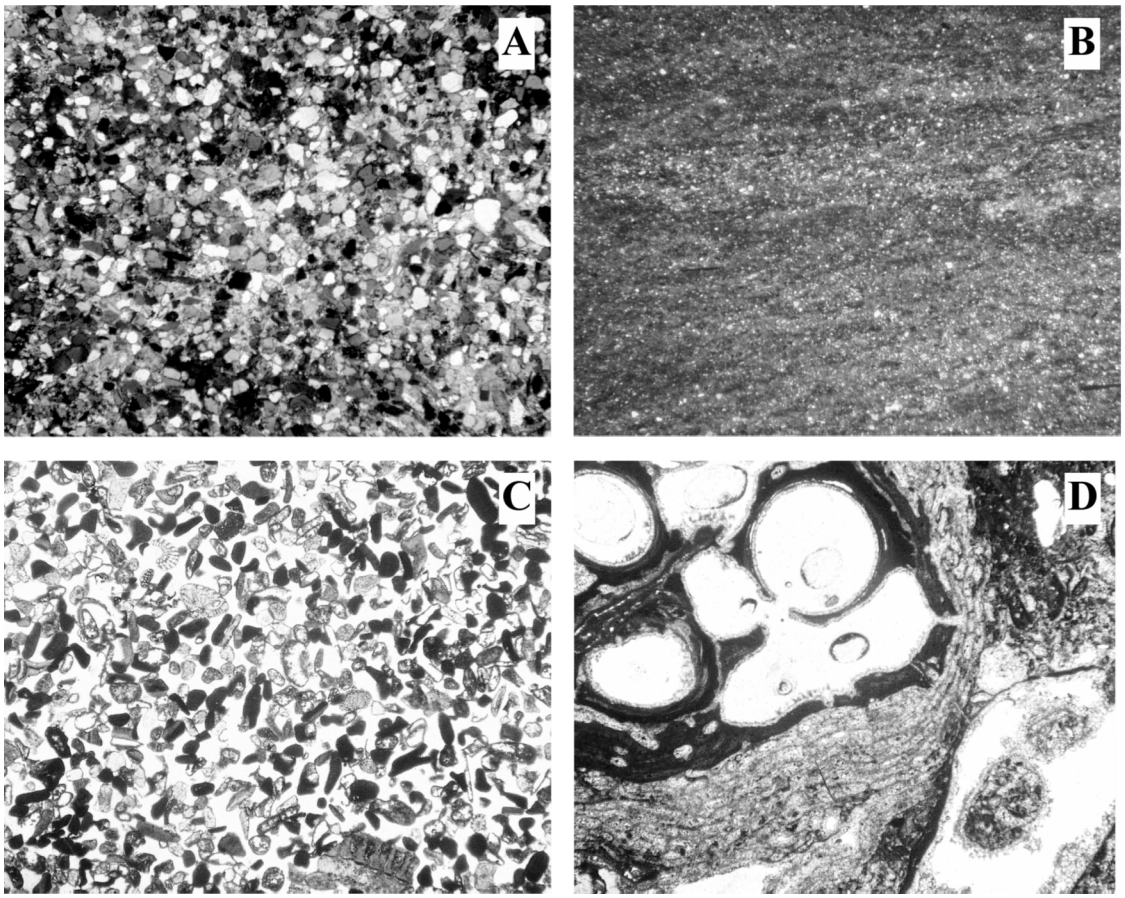

Figure 6.2. Photomicrographs of typical sediment fabrics in Boulogne (A and B) [*Braaksma* (2005)] and Mallorca: (C and D) [*Verwer et al.* (2006)].

The distribution of velocities and densities are completely different for the two fields as observed in the laboratory (MST) measurements. In the Boulogne case, there are clearly two regions of velocity-density pairs (Figure 6.3). The most populated region is of

low velocities-low densities and is well bounded between velocities that range from 1700m/s to 2400m/s and densities up to 2400kg/m^3. This group is related with clay/sand with low carbonate content. The second group, characterised by high velocities and high densities, is associated with high carbonate content, low clay and low to medium sand content [*Braaksma et al.* (2003)]. High velocities are scattered through all formations in the Boulogne. Therefore, high impedance contrasts are to be found at various depths.

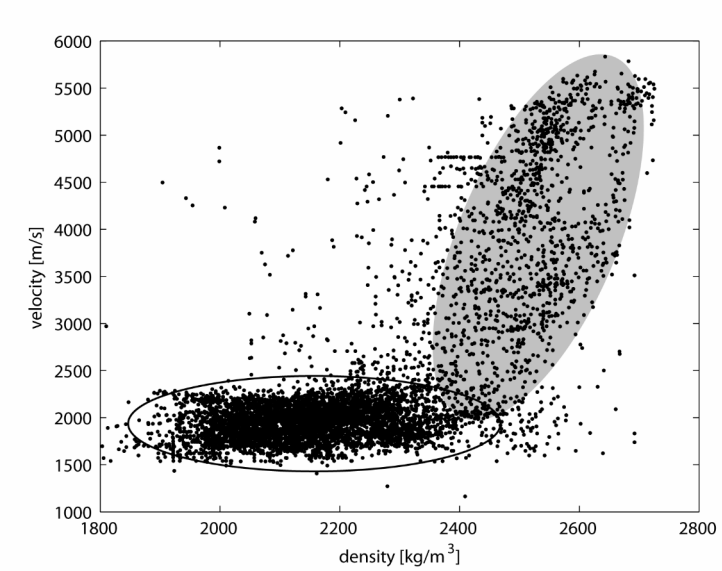

Figure 6.3. Velocity versus density plot from the Boulogne MST measurements.

In the Mallorca MST dataset (Figure 6.4), the distribution of velocity-density pairs is much more scattered in a wider region of velocities and densities than in Boulogne. The velocity-density pairs have been plotted for the main lithological packages discerned from the core description: aeolianites, lagoonal deposits, coral reef and dish coral zone and reef slope sediments.

Starting from the deepest formation (E), the reef slope, we see a dense group at the lowest values of density and velocity. The material of the reef slope was transferred from behind the reef and the reef itself. The reef could have acted as a sieve and only the lighter components may have been transferred through. Moreover, lighter material travels

further than heavier grains, which would be deposited in the lagoonal area. This could result in low densities and low velocities.

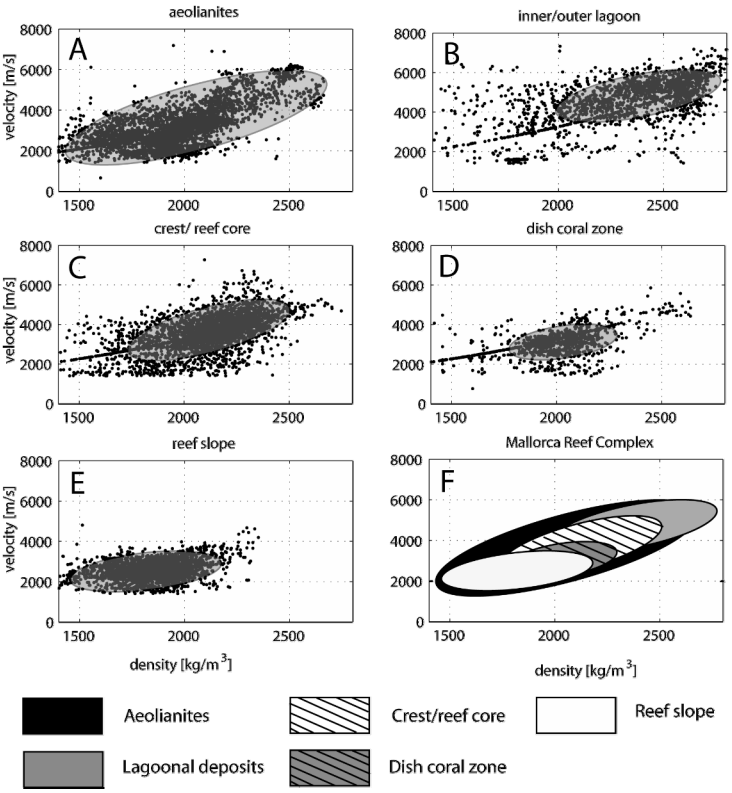

Figure 6.4. Velocity-density plots of the MST data from the Mallorca cores. For each geological formation, the highest population density is marked (ellipses)

The coral dish zone (D) has velocity-density pairs in the same region as the rest of the reef, only more concentrated, making it to stand out. The main reef and the reef crest (C) exhibit medium to high velocities with average density values. This can be explained by the fact that carbonate material has in general high velocities, but the reef region has very high primary and secondary porosity, which lowers the density.

The lagoonal sediments (B) depict high velocity-high density pairs. The top part of the sequence, the aeolianites (A), exhibit velocity and density values in all the spectrum of values available in the lower formations. The aeolianites are sediments deposited by the wind. Erosion of pre-existing formations provided the necessary material. The pre-existing formations in the area were exposed parts of the total reef complex. Hence,

densities and velocities of the material of the aeolianites coincide with the values observed in the lower formations (F). From the schematic representation of the grouping of velocity-density values per formation (F), it can be seen that there is a trend of decreasing velocity-density values with increasing depth.

In contrast with Boulogne, the wide distribution of velocity-density per formation does not happen gradually. Rather, these values are distributed in a "random" or "chaotic" way. Similarly, high impedance contrasts result from the "chaotic" fluctuations of velocity and densities.

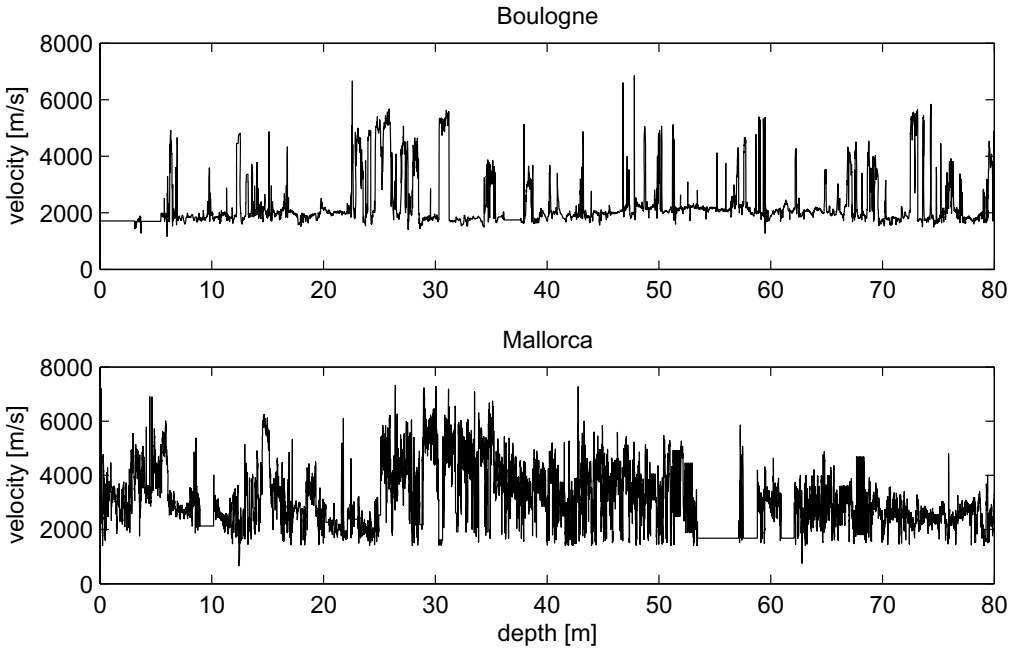

Figure 6.5. Velocity profiles from MST measurements on cores for Boulogne (a) and Mallorca (b).

Comparison of the MST velocity logs from the two fields depicts the description of the distribution of velocity values with depth. Density values generally agree with velocity values in both fields. For the Boulogne velocity log an almost constant base velocity of approximately 2000 m/sec is interrupted by few intervals with high velocities. These intervals correspond to high impedance contrasts. On the contrary, the velocity profile from MST measurements on cores from Mallorca lacks a constant base velocity.

Rather a velocity trend can be observed that generally follows the geological formations. Within the geological units, numerous high velocity contrasts are observed. These result in numerous high impedance contrasts.

6.2.3. Control of impedance contrasts on attenuation and dispersion

The calculated transmission responses using the MST acoustic properties for the Boulogne and Mallorca outcrop were shown in Chapters 4 and 5, respectively. We showed that increase in the number of high impedance contrasts in the medium affects the transmission response.

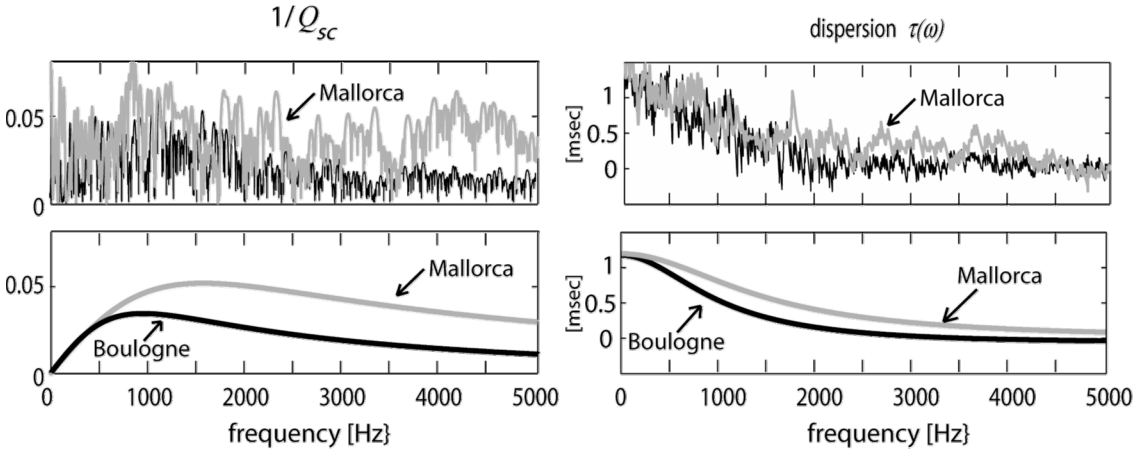

Figure 6.6. Apparent attenuation, $1/Q_{sc}$ estimated from the MST measurements for Boulogne (black) and Mallorca (gray). The smooth curves are the result of the fit with the damped harmonic oscillator model.

In Section 3.4, a damped harmonic oscillator model for constructing the coda term of the full waveform synthetic seismogram was presented that allowed us to observe the average trend in the coda term. It was demonstrated that with this model the first arrival can be modelled accurately both in timing and amplitude. The model approximates the general trend of the coda term, when a single oscillation is used. We have used this model to estimate the average frequency-dependent $1/Q_{sc}$ (Figure 6.6). In this figure, the results from the original (unscaled) MST values are shown. Comparing the two datasets, attenuation due to scattering estimated from modelling verifies that the effect of internal multiples is higher in the Mallorca dataset. Frequent high impedance contrasts cause

more scattering than fewer or smaller impedance contrasts. Higher scattering means higher $1/Q_{sc}$ values. This is also reflected on the dispersion values; dispersion is higher for Mallorca. It can also be seen that for high frequencies (>200Hz) the difference in values for both dispersion and attenuation between Mallorca and Boulogne increases. This is a direct result of the difference between the two media and consequently of the difference between the calculated transmission impulse responses.

The effective attenuation as estimated using the modified spectral ratio technique is also larger in Mallorca (Figure 6.7). This is an additional reason for the poor imaging results obtained by the surface seismic experiment in Mallorca. In reflection seismic, the signal is recorded on the surface and more energy is dissipated due to larger travelled paths.

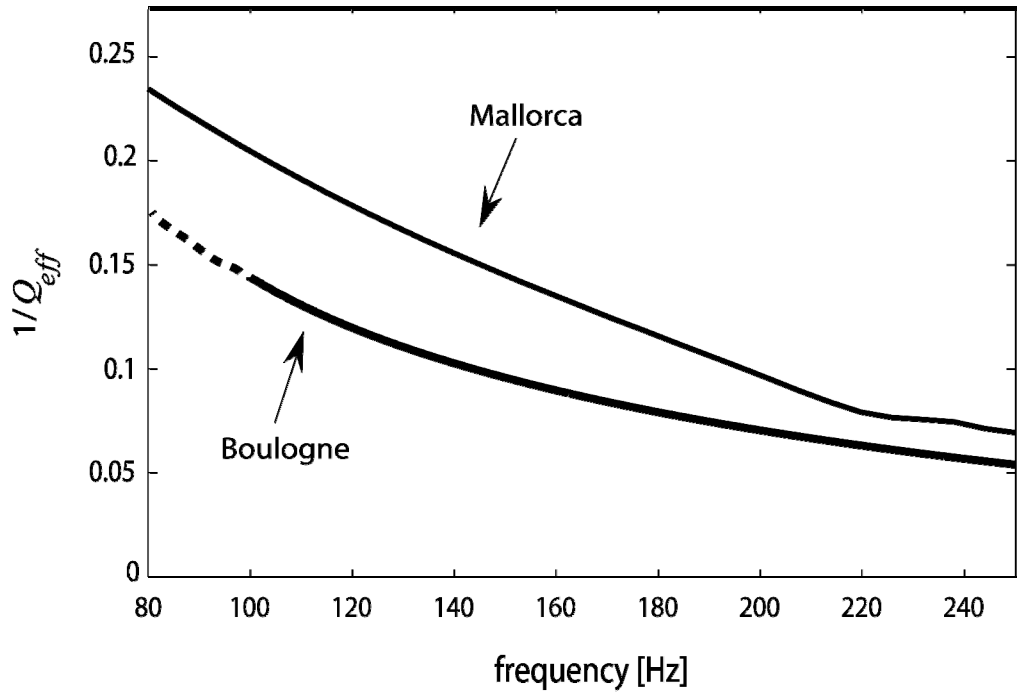

Figure 6.7. Effective attenuation, $1/Q_{eff}$, estimated from the VSP data, for Boulogne and Mallorca. Only the common frequency range is shown here.

In Figure 6.6 the $1/Q_{sc}$ is approximated by a general smooth trend. However, in detailed studies we are interested in understanding the finer structure of the formations studied. Let us observe the amplitude spectra of the transmission impulse responses

calculated from the full waveform synthetic seismogram (Figure 6.8). The main transmitted information is located in low frequencies (0-1000Hz for Boulogne, 0-700Hz for Mallorca) and decreases in higher frequencies. Borrowing terms from optics, most of the transmitted energy is located in the "red" part of the amplitude spectrum. This agrees with well-log studies establishing that the earths reflectivity is "blue", i.e., its the amplitude spectrum increases with frequency over the seismic frequency band [*Walden and Hosken* (1985), *Saggaf and Robinson* (2000)]. This general trend is found by the proposed differential effective model.

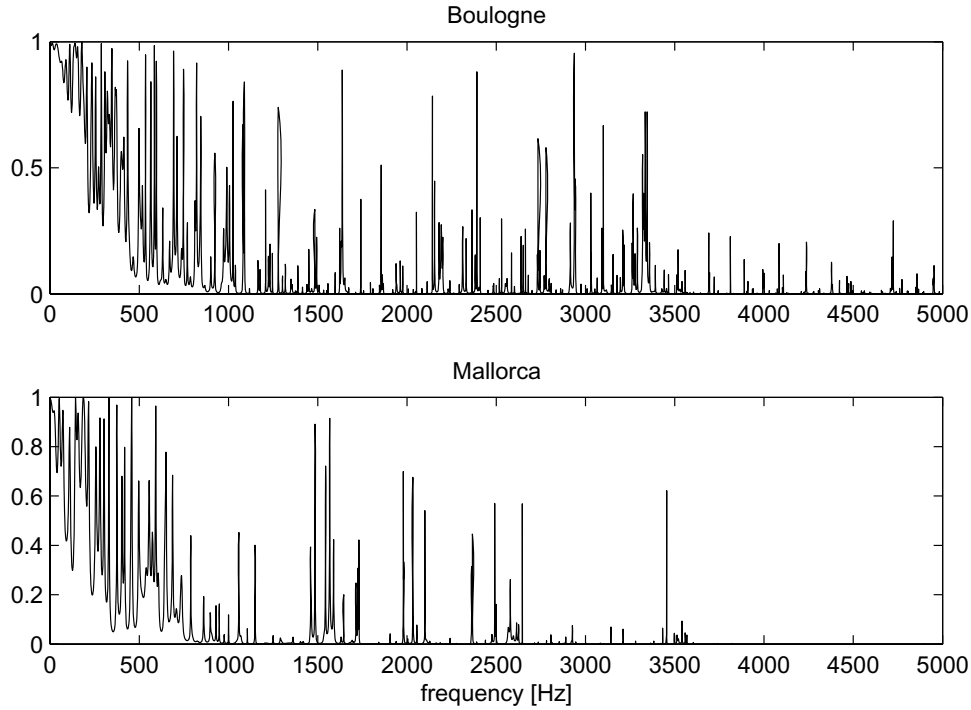

Figure 6.8. Transmission response amplitude spectra calculated from the MST acoustic measurements for Boulogne and Mallorca.

For higher frequencies, we notice that there are frequency bands with almost zero amplitude interrupted by narrow frequency bands (peaks) with high amplitudes. These bands have been identified as "spectral gaps" and are related to the statistical properties of the media. We notice that the amplitude spectrum of the transmission response for Boulogne (Figure 6.8), shows a great number of peaks, with very narrow spectral gaps,

implying that energy will be transmitted until frequencies as high as 3500Hz. On the contrary, the transmission response for Mallorca shows fewer peaks and much wider spectral gaps. The spectral gaps are a result of constructive and destructive interference. Constructive and destructive interference is of particular interest for periodically layered media, because the spectral gaps can then be predicted and tuned [*Figotin* (1993), *Figotin and Kuchment* (1994), *Hovem* (1995), *Figotin and Kuchment* (1996a, 1996b), *Griffiths and Steinke* (2001), *Wang et al.* (2001), *Haus and Soon* (2002)].

When it comes to geological structures we do not find geological sequences with purely periodic acoustic properties. Sedimentary sequences can be described as periodic with reference to their cyclicity, but strictly mathematical periodicity is not observed. Nevertheless, for illustrative purposes and qualitative interpretations we could assume periodicity. In this context, we could allow periodicity to be defined as the "almost-periodic" repetition of the acoustic properties. A simple numerical example is presented to illustrate the effect of periodicity in a layered medium on the transmission response.

6.2.4. Transmission in periodic media

In this section we model the transmission impulse response in finely layered media using the full waveform synthetic seismogram as in the previous chapters. We want to show the different characteristics that can arise depending on the statistics of the medium. Therefore, three velocity models are constructed, described by three specific velocity profiles.

The first velocity profile has the same statistics as the one used in Chapter 3. It is based on fractal Brownian motion around a base velocity of 2000m/sec (Figure 6.9 (a)). The second velocity profile is a periodic medium with a basic pattern of a shifted version of the function $|z|^{-0.4}$. The third velocity profile is a combination of the previous two: the fractal medium subtracting the base velocity and adding it to the periodic one. The three

velocity models consist of 8040 layers, with 0.005m thickness. Density was constant at 1000kg/m^3.

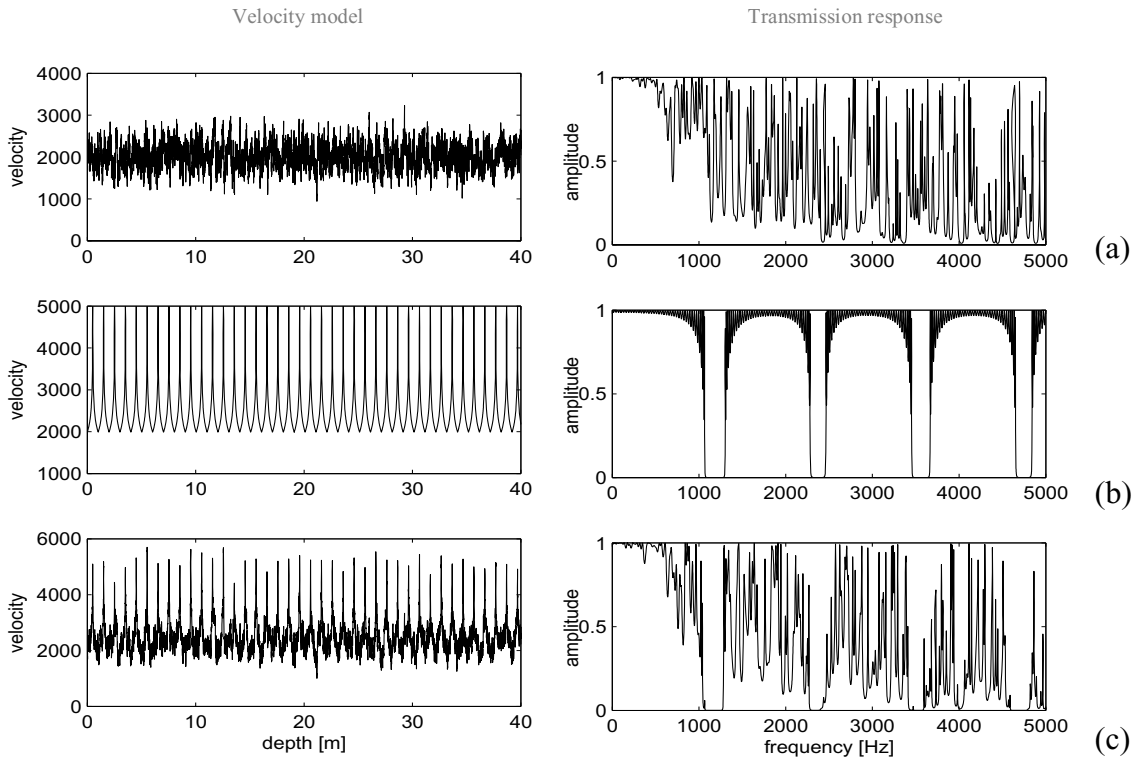

Figure 6.9. Amplitude spectra of transmission response of a fractal medium (a), periodic medium (b) and a combination (c) of the periodic medium with the fractal medium superimposed (the average 2000m/s velocity of the fractal medium is removed).

The amplitude spectrum of the calculated transmission impulse response for the three models is shown in Figure 6.9. For the first model, Figure 6.9 (a), it is shown that for low frequencies the amplitude spectrum is almost unity and decreases with increasing frequency. The "chaotically" distributed peaks are a result of internal multiples. The transmission response of the second model is shown at Figure 6.9 (b). Characteristic periodic bands of alternating high and low transmission can be seen. These spectral gaps are related to the periodicity of the medium properties and the impedance contrasts. Tuning these spectral gaps can be achieved, i.e. by changing the thickness of the layers and/or the velocities [*Griffiths and Steinke* (2001), *Wang et al.* (2001)]. The amplitude of

the transmission impulse response of the third medium can be seen in (Figure 6.9 (c)). Notice that the third model is no longer strictly periodic, but an underlying periodicity is maintained. The peaks originally observed in the fractal medium have changed because the internal-multiple pattern has changed as well. However spectral gaps are observed at the same location as in the purely periodic medium. Depending on the average impedance contrasts the spectral gaps may shift from the original position in different non-periodical locations.

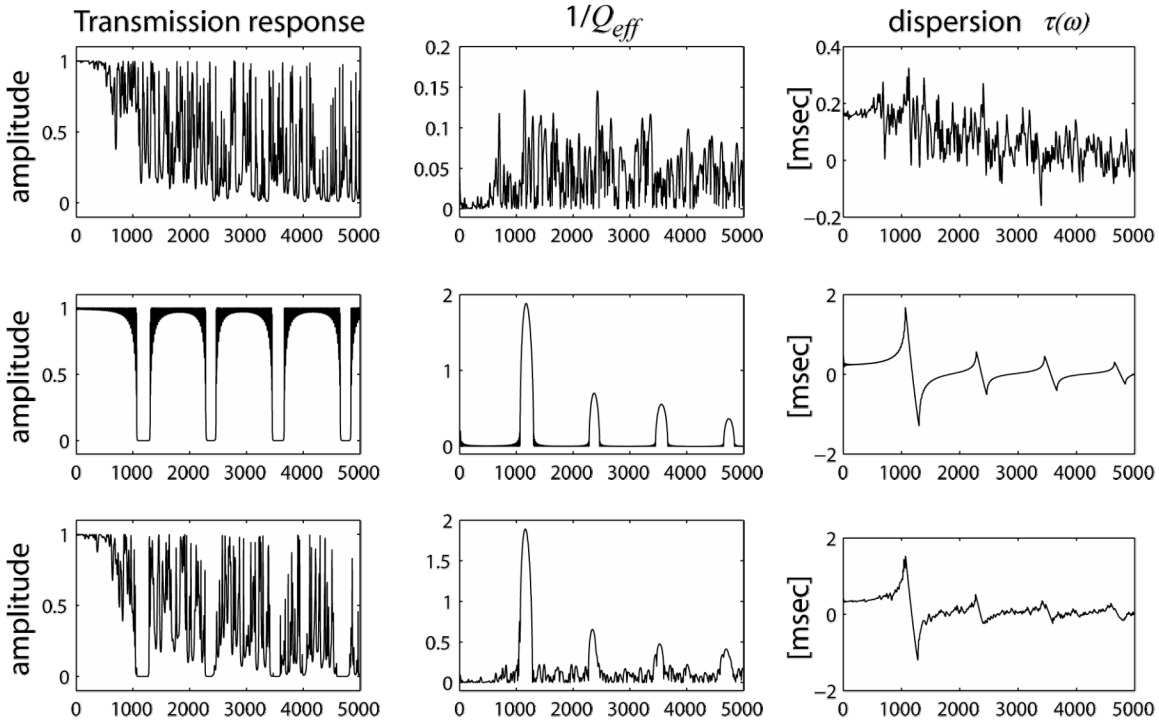

Figure 6.10. Calculated attenuation due to internal multiples, $1/Q_{eff}$, and dispersion for three models with particular velocity profiles: a Brownian fractal-motion based one, a periodic and a combination of the two.

Using the transmission response to infer the statistics of the medium without additional information (e.g. multi-angle, broad-band frequency information) can not return a unique medium structure. Nevertheless, useful conclusions can be derived by comparison of the distribution of the amplitude peaks, which can be associated with the distribution of the acoustic properties of the medium. Figure 6.10 depicts this idea. The transmission response calculated from the fractal medium (top row), shows many amplitude peaks distributed throughout the frequency range. The low peak at 500Hz,

corresponds to a high value of $1/Q_{eff}$ as expected. Low transmission, which can be a result of destructive interference, implies high attenuation. High attenuation implies high dispersion, and indeed an increase in the dispersion values can be seen around 500Hz. The effect of low transmission-high attenuation-high dispersion diminishes in higher frequencies. The peaks in attenuation and dispersion for the fractal medium are distributed in the same "disordered" way as in the modelled transmission response.

Similarly, the same association of peaks in transmission response and attenuation and dispersion is observed in the case of the periodic medium (Figure 6.10-middle row). In this case though, the high and low values are of periodic nature. Notice the resonating behaviour in the dispersion curve at the location where the minimum transmission and locally high attenuation occurs. The frequency range between the local maximum and the local minimum correspond to the width of spectral gap.

In the case of the "combined" medium (Figure 6.10-bottom row) the transmission response shows both the spectral gaps induced by the periodicity and the disordered peaks as a result of the superimposed fractal medium. Similar behaviour is observed, only the added velocity perturbations make all curves to deviate from the ones for the strictly periodic medium Notice also that the attenuation and dispersion values for the fractal medium are one order magnitude lower than for the periodic and combined media.

The above simple numerical experiment shows the effect of the statistical properties of the medium in attenuation due to internal multiples and dispersion. In the previous chapters we noticed that regularisation changes the statistics of the medium by averaging the velocity and density profiles. Essentially, the impedance contrasts are smoothened. This facilitates transmission, therefore attenuation due to scattering and dispersion decrease globally. However, there can be noticed sudden increase or decrease of amplitude peaks, mainly at higher frequencies, which is a result of the change in the patter of interference (Figure 6.11). A decrease (A) and an increase (B) in amplitude can be observed when compared with previous scales. The highlighted equidistant frequency

regions in Figure 6.11 are used for guidance. Observation of such changes can reveal information about how different scales behave in specific frequency ranges. Combined with the observation that at specific scales and frequency ranges an increase (or decrease) in the transmission response occurs, we can conclude about scale-dependent attenuation and dispersion. In this way, we might notice at which combination of scales and frequency range the attenuation and dispersion are particularly high or low. This could lead to understanding if and how apparent attenuation can be separated from intrinsic attenuation.

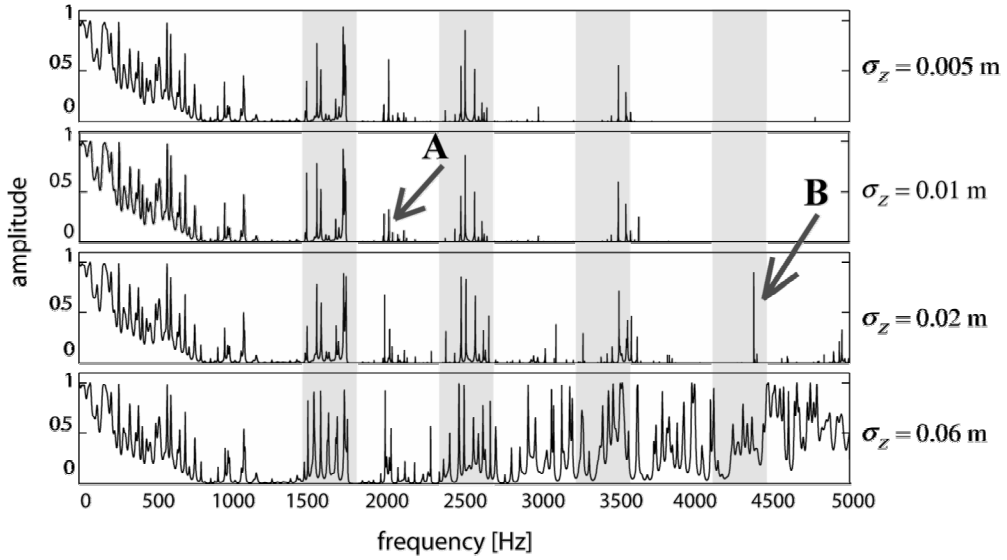

Figure 6.11. Part of figure 5.9 with highlighted equidistant regions to facilitate observation of the changes of the amplitude peaks. A decrease (A) and an increase (B) is observed compared to the previous scales.

6.3. Multilayer reflectors: the French silverfish and the Spanish butterfly

In this thesis, we focused our interest in understanding wave propagation in two outcrops. The acoustic properties of these media were measured both in the field and in the laboratory. We have assumed that the geological structure of these outcrops can be represented by finely layered media. Non-dissipative finely layered models were

constructed from the laboratory measured acoustic properties to estimate the attenuation and dispersion due to internal multiples (scattering).

Studying the transmission and reflection response is not a subject pertaining uniquely to geophysics. Multilayer reflectors are also studied in biology; the concept is very attractive for the layman due to its phenomenological simplicity; colour. The studied subjects are readily available for anyone to ponder upon and enjoy. Interesting studies on structural colour on animals should attract the attention of anyone studying wave propagation phenomena. The scale of these phenomena i.e. the wavelength and the thickness of the layers, as well as the type of wave (light) used, are far from the wavelengths and geological targets probed in geophysics. Nevertheless, the concepts are similar.

In biology, some material exhibits so-called structural colour, which is the result of selective reflection or iridescence. This is done with natural multilayer structures and not due to pigmentation. Structural colour may vary depending on the viewing angle. The selective reflection (or transmission) leads to a selective reinforcement of a particular portion of the light spectrum because of nano-scale spatial-periodicity in variation of the refractive index. Depending on the organisation of the refractive index of the multilayer reflector, the resulted structural colour can be due to coherent or incoherent scattering. Separation between the two is done by observation of the periodicity of the variations in the refractive index.

Structural colour is responsible for i.e., iridescent blue plants [*Lee* (1997)], the blues and greens of butterfly wings [*McPhedran and Nicorovici* (2001), *Prum et al.* (2006)], beetle elytra [*Neville* (1977), *Parker et al.* (1998)], silverfish colour [*Large et al.* (2001)] etc. Green beetles were found to have multilayer elytra with periodical optical properties [*Parker et al.* (1998)]. Scattering through this multilayer composite reflector results in a bright green colour, giving them the necessary camouflage over tree foliage. Similarly, it may return bright golden colours in other species. Butterflies have multilayer

wings with scales attached on them; scattering also results in structural colouring and iridescence [*Prum et al.* (2006)]. Studies on fish skin revealed a remarkable combination of periodicity and chaotic patterns in its multilayered composite skin. The reflected light would reflect in a broad spectrum yielding in grey colour, that could be maintained even when the fish is swimming and essentially the thickness of the layers change, hence angle-independent reflectivity [*McKenzie et al.* (1995)]. The silverfish, a small nocturnal wingless insect, also exhibits broadband reflectance due to its multilayer-reflector exoskeleton [*Large et al.* (2001)]. The similarities in the concepts of wave propagation in these examples with the applications in lithological targets are worth rediscovering.

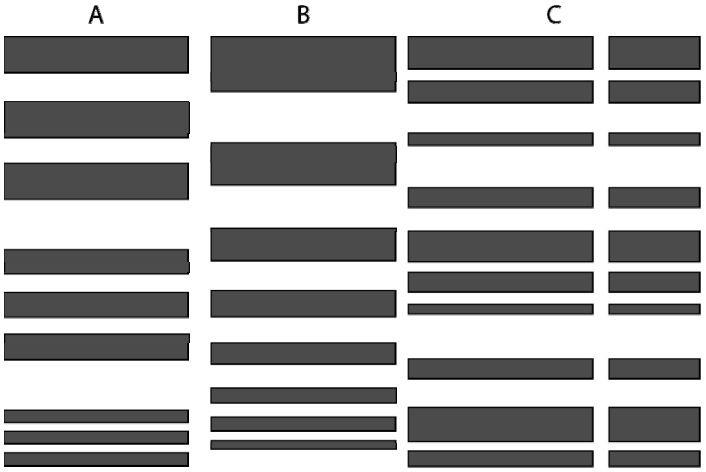

Figure 6.12. Three ways of achieving a broadband reflectance in a multilayer stack. High refractive index material is shown shaded. (A) Three regular multilayer stacks, each tuned to a different wavelength. (B) A 'chirped' stack. (C) A 'chaotic' stack [*Parker et al.* (1998)].

If we could characterise the two outcrops studied in this thesis, borrowing the concept of the spectrum of the visible light for the modelled transmission responses then we could say that Boulogne is more "grey" compared to the "red" Mallorca, due to more broadband transmission response. The transmission response calculated from the Boulogne MST showed that due to internal scattering, many amplitude peaks occur in all frequency range modelled. In experimental biology [*Parker et al.* (1998)], a broad band reflectance (or transmission) appearing silver to human eye, *"can be achieved in a multilayer stack in at least three ways* (Figure 6.12)*:* (A) *a composite of regular*

multilayer stacks each tuned to a specific wavelength, (B) *a stack with systematically changing optical thicknesses, termed a "chirped" stack* [*Ouellette et al. (1995)*]*; and* (C) *a disordered arrangement of layer thicknesses about a mean value".*

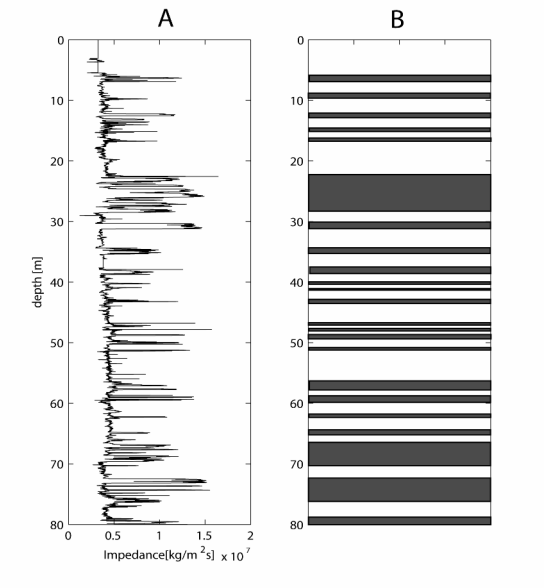

Figure 6.13. (A) Impedance log from the Boulogne MST measurements. A simplification of high (black) and low (white) impedance layers (B). This demonstrates the almost locally-periodic to chaotic succession of stack of layers in this composite "multilayered reflector".

In Figure 6.12 a binary system of high and low refractive indexes is shown. The idea of disordered arrangement allows space for incorporating geological models. A stack of layers with disordered arrangement is not really far different than a stack of layers with locally periodic or chirped distribution. The refractive index can be substituted by parameters used in acoustic wave propagation through layered media: reflection coefficients and impedance contrasts. Similarly, we could construct a binary multilayered reflector for the Boulogne case (Figure 6.13). This is valid through acknowledged simplification and with the assumption that there is little lateral variability. Observing the structure and the assumed "grey" colour of the Boulogne layered model, it is impossible to resist the comparison of seismic images with thin sections of layered media encountered, for instance, on insects. Figure 6.14 beautifully bridges the concepts of different scales. On the top figure we see an off-shore sparker-line acquired at Boulogne. The almost parallel layers of sediments can be seen with a succession of high and low amplitudes. The vertical scale is approximately 40m (1μsec equals approx.1m), while the

length of the seismic line is almost 1500m. The figure in the middle is a thin section of the exoskeleton of the common silverfish (*Ctenolepisma sp.*). The dimensions of this figure is a few hundreds μm [*Large et al.* (2001)]. A remarkable layering with high and low amplitudes denoting the different refractive material is observed. A seismic section from the 3D surface-seismic experiment shot on the beach of Boulogne is shown in the lower-left figure. The vertical scale is 50m and the horizontal is approximately 200m. Next to it, in an interesting comparison, is a cross section of the cuticle of a gold beetle (*Aspidomorfa tecta*) [*Neville* (1977)].

The amplitude spectrum of the transmission response of Mallorca is mainly located in the low frequencies, or in the "red" part of the spectrum. Large and chaotically distributed primary and secondary porosity limits the assumption for lateral continuity in a very local sense. Taking into consideration the chaotic patterns observed at all geological scales in the reef part, we should be even more cautious about generalising our results in a lateral sense. Bringing a similar analogue as for the Boulogne case, changes in the observed amplitudes (transmitted and reflected) due to different angle of incidence is observed in many butterflies. The wings of butterflies also comprise composite multilayered reflectors. Interference of the reflected light results in bright iridescent blue and green colours, while the transmitted light is of red-brown colour. Scales are attached on the wings. A cross section of a scale reveals that the multilayer reflector is laterally inhomogeneous. Air-bubbles are embedded in the scales creating "impedance" contrasts. The structural colour of butterflies is a very complicated issue, yet another characteristic example of interference, high and low reflection and transmission of light. Here we give a very gross simplification to accommodate the concept of air-filled multilayered structures and intrigue our imagination to visualise the scattering that occurs during wave propagation experiments in a field observatory like Mallorca.

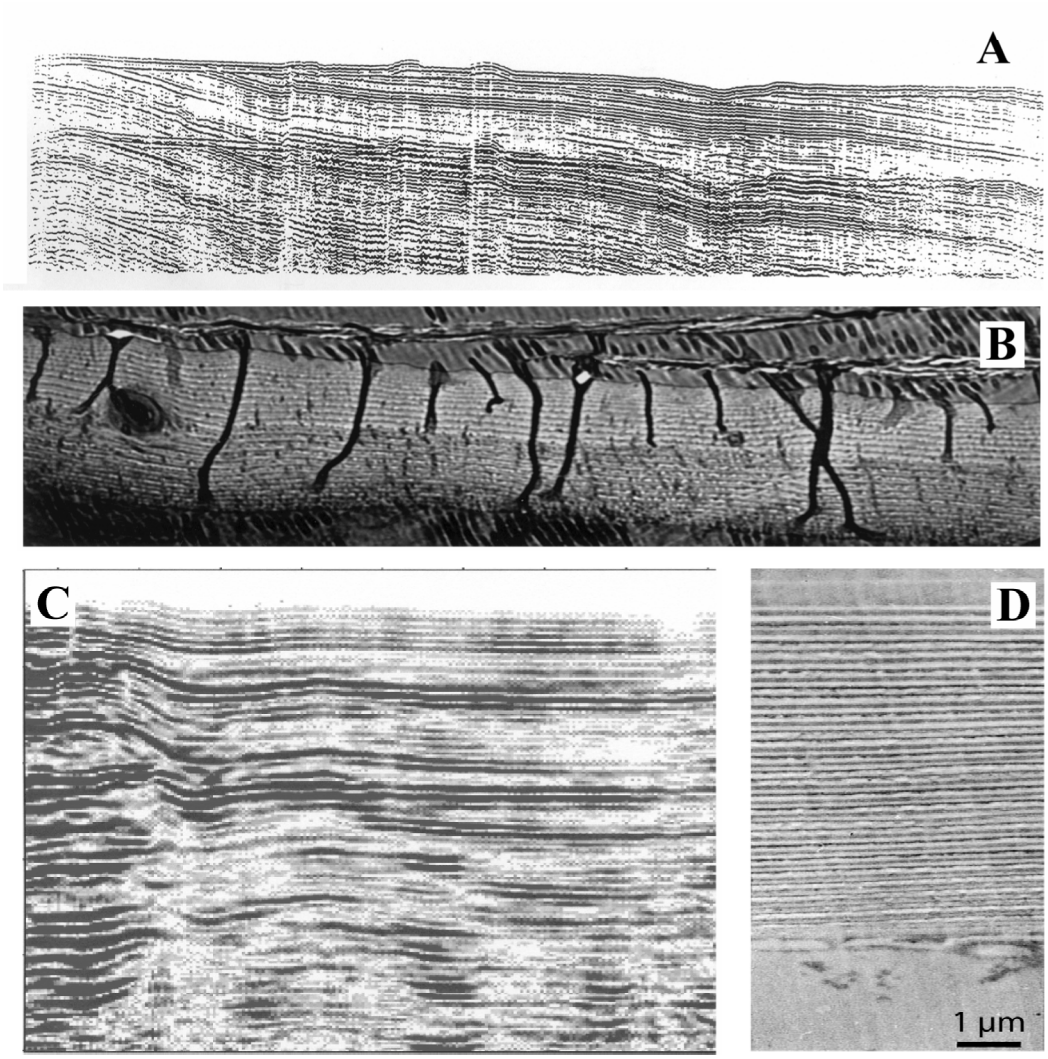

Figure 6.14. Microscopic multilayered reflectors, or finely layered geological media? Scales different, yet, so similar. (A) offshore 2-D sparker line of the Boulogne observatory [*Mahieux et al.* (1988)]. Vertical scale 1msec approx 1m, horizontal 1500m. (B) cross sectional TEM of the exoskeleton of the common silverfish (*Ctenolepisma sp.*). Dimensions: a few hundeds µm [*Large et al.* (2001)]. (C) Seismic section from the 3D surface-seismic survey in Boulogne, horizontal scale 200m. (D) TEM of a vertical section of a cuticle of a gold beetle *Aspidomorpha tecta*. [*Neville* (1977)].

6.4. Discussion and conclusions

The versatile seismic experiments conducted for this projected involved a multidisciplinary group of geoscientists brought together to combine their expertise. This productive interaction confirmed one of the main ideas inspiring this thesis: progress occurs at the edges of disciplines. In this section we borrowed some notions and examples outside geosciences. It is demonstrated that layered media can have selective "colouring" in their reflected and transmitted responses due to coherent and incoherent interference. We have seen that wave propagation is studied on other than geophysical targets. The physical concepts, models and experiment-setups used are essentially the same, despite the fact that the scales of observation and heterogeneities vary significantly. In this way, it becomes apparent that even for geophysical-based projects, multi-disciplinarity should not be pursued only within the group of geosciences but even further; in unexpectedly common fields of e.g. experimental biology and zoology. Their experiments, methods and observations can probably help us, geophysicists, to understand better wave propagation in layered media -for instance. Perhaps then we will start perceiving our recorded seismic responses not as a complicated series of numbers to filter and deconvolve but as what they truly are: the revealed "colour" of the interior of the Earth.

(Ctenolepisma sp.)

Appendix A

Transformations

A.1. Introduction

Time-varying signals can be converted in other domains than time, using the appropriate transform and facilitate further processing and analysis. In Geophysics, the most common one is the Fourier transform, relating the total time signal to its total frequency content.

In Digital Signal Processing we often need to look at relationships between real and imaginary parts of a complex signal. These relationships are generally described by Hilbert transforms. Hilbert transform not only helps us relate the real ($\Re$) and imaginary ($\Im$) components but it is also used to create a special class of causal signals called analytic which are especially important in simulation. Analytic signals help us to represent bandpass signals as complex signals which have specially attractive properties for signal processing.

As mentioned earlier, Fourier basis functions are localised in frequency but not in time. Small frequency changes in the Fourier transform will produce changes everywhere in the time domain. The usage of wavelet transforms has been proposed for localised analysis and processing. Wavelets (also referred to as *basis* or *base functions*) are local both in frequency/scale, via dilations, and in time, via translations. This type of transformations, especially when referred to their discrete counterpart are advantageous in temporal/spatial locality of the base function compared to, for instance, short-time

Fourier transform. Wavelet transforms are intrinsically less complicated compared to fast Fourier transform (FFT) and may therefore require less computational time for achieving better results.

In this appendix, these three types of transformation, their definitions and application (where necessary) are discussed. Basic knowledge and applications of the Fourier and Hilbert transformation is considered and applications are therefore skipped. The greatest part of this appendix is dedicated to the wavelet transform and its applications related to this thesis.

A.2. The Fourier Transform

In this thesis we will use the following definition for the Fourier transformation:

$$F\left\{f\left(t\right)\right\} = \hat{f}\left(\omega\right) = \int_{-\infty}^{+\infty} f\left(t\right) e^{-i\omega t} \mathrm{d}t\,, \tag{A.1}$$

where ω is the angular frequency, t is time, $j$is the imaginary unit and $f(t)$ is the time domain function that is transformed to the frequency domain function $\hat{f}\left(\omega\right)$. The inverse temporal Fourier transformation is:

$$F^{-1}\left\{\hat{f}\left(\omega\right)\right\} = f\left(t\right) = \frac{1}{\pi}\Re\int_{0}^{+\infty} \chi(\omega)\hat{f}\left(\omega\right)\exp(i\omega t)\mathrm{d}\omega\,, \tag{A.2}$$

when $f(t)$ is real valued, where $\chi(\omega)$ is the function:

$$\begin{aligned} \chi(\omega) &= 0 \quad \omega < 0 \\ \chi(\omega) &= \frac{1}{2} \quad \omega = 0\,. \\ \chi(\omega) &= 1 \quad \omega > 0 \end{aligned} \tag{A.3}$$

Expression (A.2) transforms the signal from the frequency domain back to the time domain. The symbol $\Re$ denotes that the real part is taken.

A.3. The Hilbert transform

A complex signal $z(t)$ that relates to the real valued $f(t)$ can be defined as:

$$\begin{aligned} z(t) &= f(t) + ig(t) \\ &= a(t)\exp\left[i\theta(t)\right] \\ &= a(t)\cos\theta(t) + ia(t)\sin\theta(t) \end{aligned} \tag{A.4}$$

In the above representation, there are infinite ways to define a complex signal $z(t)$ for which $a(t)\cos\theta(t) = f(t)$. Gabor introduced the analytical signal $f_a(t)$. The analytical signal $f_a(t)$ is a complex signal which has spectral the spectrum of $f(t)$ for the positive frequencies and zero for the negative. It can also be described by:

$$f_a(t) = \frac{1}{\pi}\int_{-\infty}^{+\infty} \chi(\omega)F(\omega)e^{j\omega t}\mathrm{d}\omega\,, \tag{A.5}$$

The Hilbert transform **F**(τ) of the function *f(t)* is defined by:

$$\mathbf{F}(\tau) = \mathcal{H}\left[f(t)\right] = \frac{1}{\pi}PV\int_{-\infty}^{+\infty}\frac{f(t)}{\tau - t}\mathrm{d}t\,. \tag{A.6}$$

Because of the possible singularity at $\tau=t$, the integral is to be considered as a Cauchy principal value (noted as *PV*) integral. The integration in principal value corresponds to the limit:

$$\lim_{\varepsilon\to 0}\left[\int_{-\infty}^{\tau-\varepsilon}\frac{f(t)}{\tau - t}\mathrm{d}t + \int_{\tau+\varepsilon}^{+\infty}\frac{f(t)}{\tau - t}\mathrm{d}t\right]. \tag{A.7}$$

In order to distinguish between the Fourier and Hilbert transformed quantites, the first is denoted with capital italic (*F(ω)*)and the latter with capital bold (**F**(τ)) fonts.

In the frequency domain, the Hilbert transform is defined by:

$$\boldsymbol{F}(\omega) = FT\left[\mathbf{F}(t)\right] = -sign(\omega)F(\omega)\,, \tag{A.8}$$

where $F(\omega)$ is the Fourier transform of *f(t)* in the frequency domain and

$$sign(\omega) = \begin{cases} -1 & \text{for } \omega<0 \\ 0 & \text{for } \omega=0 \\ 1 & \text{for } \omega>0 \end{cases}. \tag{A.9}$$

$\boldsymbol{F}(\omega)$ shows that the Fourier transform of $\mathbf{F}(t)$ only differs from $F(\omega)$ only by the phase. Thus , the Hilbert transform can be seen as a type of filtering that passes the amplitudes of the spectral components of the signal unaltered, but it introduces a phase of $-\pi/2$ (-90°) for the positive frequencies and $\pi/2\,(90^{\circ})$ for the negative frequencies. The Hilbert transformation is better known for its applications in complex signal analysis. In this thesis, the Hilbert transform is use to obtain the imaginary part from the real part of a causal function.

A.4. The Wavelet Transform

The wavelet transform is a different representation of the signal itself. Wavelets are not a very new idea (Haar wavelet, named after Alber Haar was established in 1909) but the wavelet transformation and its application has been widely investigated in the 90s including the Grossmann and Mallat group [*Grossmann and Morlet* (1985), *Grossmann et al.* (1989), *Mallat* (1989), *Meyer* (1990), *Mallat and Hwang* (1992), *Mallat and Zhong* (1992)] who investigated the continuous wavelet transforms, [*Meyer* (1990) referring to multiresolution analysis and *Daubechies* (1988, (1990, (1996) with her work on construction of wavelets among other authors.

There many types of wavelet transforms and the most important include the continuous wavelet transform (CWT), the discrete wavelet transform (DWT), the fast wavelet transform (FWT), wavelet packets or filter banks and the complex wavelet transform. Usually CWT is used for signal analysis while DWT for signal processing in various and extremely diverse subjects (finance, medical investigations, coastal engineering and geography etc). In the present work, the continuous wavelet transform is

used as a tool for calculating windowed equivalent media as suggested by *Sams and Williamson* (1994) and *Rio et al.* (1996).

A.4.1. The Continuous Wavelet Transform

The continuous wavelet transform has been used to address, among other applications, the regularization of time-varying signals [*Sams and Williamson* (1994), *Herrmann* (1997), *Verhelst* (2000)], similarly to noise reduction techniques, and lithology interfacial characterisation [*Goudswaard* (2001), *Goudswaard and Wapenaar* (2001), *Ghose and Goudswaard* (2004), *Wapenaar et al.* (2005)] corresponding to edge detection techniques. The definition of the continuous wavelet transform for a signal varying in depth (z)[1] is an expansion of the signal *f(z)* on the transformation basis, $\vartheta_{\sigma,z}(z')$:

$$\vartheta_{\sigma,z}(z') = \frac{1}{\sigma^{\mu}}\vartheta\left(\frac{z'-z}{\sigma}\right), \text{ with } \sigma > 0, \tag{A.10}$$

where $\frac{1}{\sigma^{\mu}}$ normalises the wavelet basis. The function $\vartheta(z)$ is also called the *mother wavelet* from which the analysing wavelets $\vartheta_{\sigma,z}(z')$ will be derived. The continuous wavelet transform, $\overset{\vee}{f}(\sigma,z)$ is given by:

$$\overset{\vee}{f}(\sigma,z) = \frac{1}{\sigma^{\mu}}\int_{-\infty}^{+\infty} f(z')\vartheta^{*}\left(\frac{z'-z}{\sigma}\right)\mathrm{d}z'. \tag{A.11}$$

Following *Herrmann* (1997), the L_1-normed Gaussian function is used for mother wavelet in this thesis, defined as:

$$\vartheta(z) = \frac{1}{\sigma_z}\exp\left[-\pi(z/\sigma_z)^2\right]. \tag{A.12}$$

[1] Usually the expressions are stated for time-varying signals; nevertheless in this study we will be referring to velocity profiles, thus signals varying in depth.

The Gaussian function is preferred for its C^{∞} regularity, meaning that all its derivatives are continuous. Strictly speaking, the Gaussian is not a wavelet sicen it has non-zero mean value. Here it is essentially used as a smoothing function.

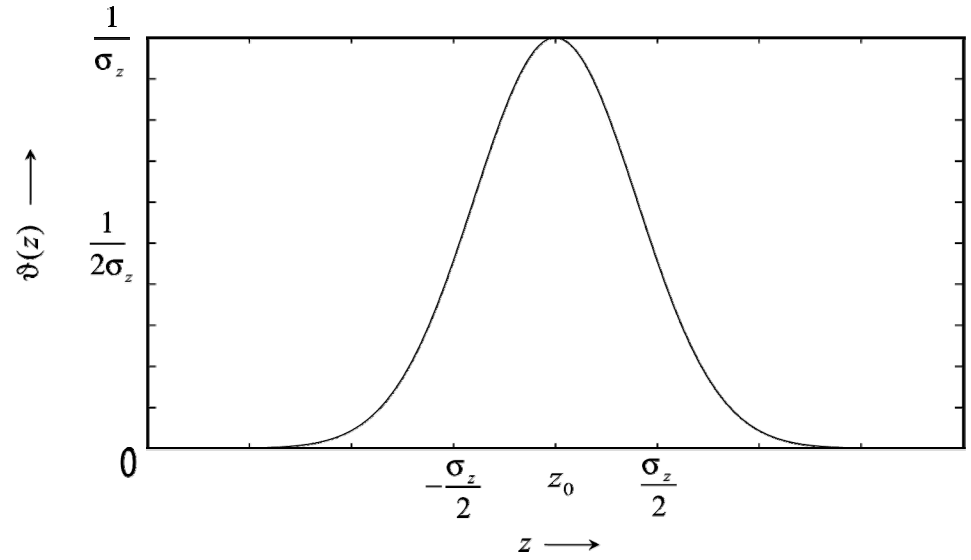

Figure A.1. The Gaussian, in this thesis used as analysing wavelet for regularizing velocity profiles.

In order to investigate the scaling behaviour of the regularised velocity the Gaussian wavelet is used (Figure A.1). Figure A.2 shows the effect of the wavelet transform on function with three different isolated singular points is shown on the left panel. They are shifted versions of $|z|^{-0.4}$ (top), a stepfunction (middle) and $|z|^{0.2}$ (bottom). The first panel shows the function to be regularized. The second panel shows the regularized function in distinct scales. It can be seen the smoothing effect that increases with scale. The third panel shows 120 profiles as in the second panel, plotted next to each other. The grayscale denotes the values. The effect of the regularisation of the function using the Gaussian as analysing wavelet can be seen as a windowed effective medium averaging technique. The larger the scale the smoother the function contrasts. Its application is discussed in Chapters 3, 4 and 5.

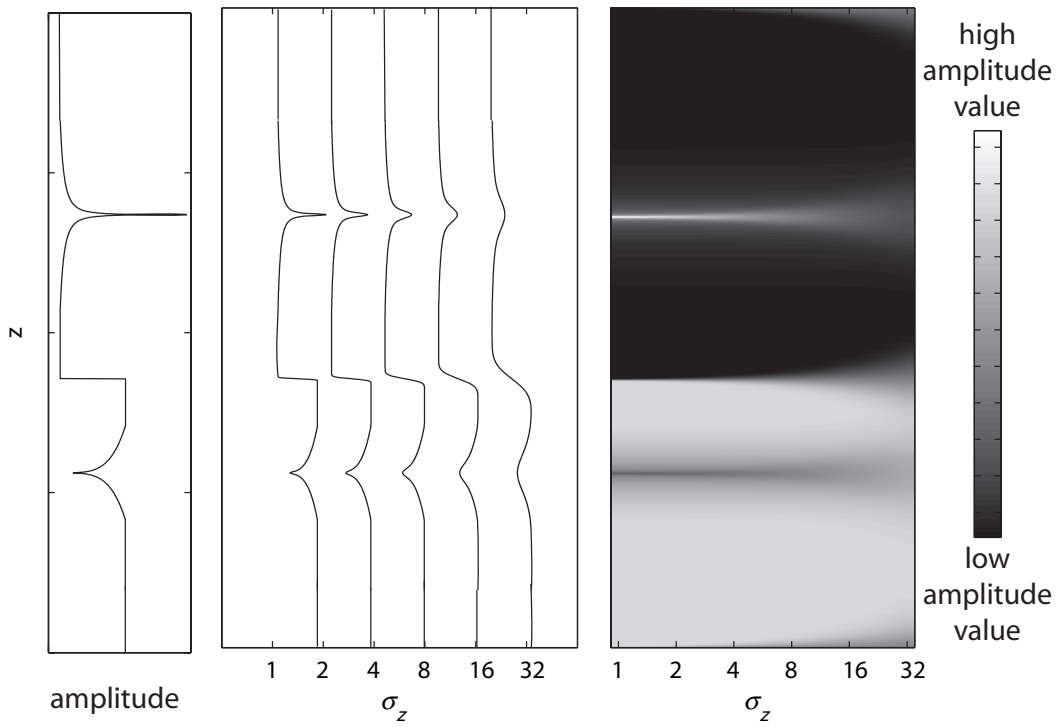

Figure A.2. Example of regularization of a function constructed with shifted versions of $|z|^{-0.4}$ (top), a stepfunction (middle) and $|z|^{0.2}$ (bottom).

Appendix B

Intrinsic attenuation in a discrete particle model

Abstract[*].

We present a study on energy dissipation of wave propagation in a discrete particle model due to intrinsic friction, which is an intrinsic property of rocks and especially of unconsolidated sediments. We support that grain-to-grain interactions in sediments can macroscopically account for energy loss due to frictional forces. In our approach the dissipation is described as function of different values of coefficient of friction. The amplitude attenuation as a function of frequency is presented for both vertical and horizontal motion (P and S waves) using separately a vertical-force source and a horizontal-force source. In general, the increase of friction coefficient gives rise to an increase of the stiffness of the medium facilitating the wave propagation. The dissipation of amplitude generally increases exponentially with frequency, even though results derived for the vertical component using a horizontal-force source demonstrate a more complicated behaviour. Amplitude dependence on the friction coefficient is also more complex. For a vertical-force source, the dependence of amplitude (P-wave) versus

---

[*] The contents and results of this Appendix have been presented in:

1. **Modelling Vertical Seismic Profiles using a Lattice Solid Model,** N. Filippidou**,** S. Abe, G.G. Drijkoningen, H. Braaksma, (2003) SEG, Dallas, USA
2. **Using a Lattice Solid Model for Vertical Seismic Profiles**, N. Filippidou, S. Abe, G. G. Drijkoningen, (2003) EEGS, Prague
3. **Seismic Wave Attenuation in a Particle Based Model**, N. Filippidou, S. Abe, G,G. Drijkoningen, P. Mora, EGU, (2004) Nice, France
4. **Numerical experiments investigating frictional losses in wave propagation through a Lattice Solid Model.** N. Filippidou, S. Abe, G.G. Drijkoningen, P. Mora (2004) EAGE, Paris, France

the coefficient of friction is non-linear up to friction coefficient values of 0.6. For a horizontal source, the amplitudes of the horizontal component (S-wave) generally increase as coefficient of friction increases. The range of coefficient of friction 0.4 and 0.6 exhibits a higher slope than the range above 0.6, resembling the equivalent range observed from the vertical component using the vertical-force source (P-wave). Finally, in the cases of same-direction source and receiver component (P-and S-waves), a linear trend is observed for the values of the coefficient of friction higher than 0.6.

B.1. Introduction

Seismic wave energy attenuation has been widely observed in seismic data and laboratory experiments. A great effort is being undertaken to better understanding the mechanisms that can explain this phenomenon, both in the theoretical and the experimental direction; a good command of attenuation characteristics can reveal valuable and unique information about lithology and rock properties. Attenuation has been investigated as a function of saturation, pressure, matrix anelasticity with implementation of intrinsic friction, viscosity and flow of fluids, gas pockets, temperature and others [*Connell and Budiansky* (1977), *Johnston et al.* (1979)] and is generally described as the loss of energy per cycle [*Johnston and Toksöz* (1981)]. In the previous chapters, the notion of attenuation due to internal multiples (scattering) was discussed. In this appendix some numerical experiments of wave energy attenuation due to friction in a discrete particle lattice will be presented.

Seismic experiments in soils and shallow, unconsolidated formations have proven to involve certain challenges concerning the transmission of seismic energy, namely: geometric spreading of the wavefront, especially high scattering of waves, coupling problems at both the receiver and source site [*Jeng et al.* (1999)]. Energy attenuation is much higher in shallow sediments than in rocks, which may result in slight broadening of the seismic pulse, an effect which can be employed for the quantification of dissipation [*Liu* (1988)] and in a more pronounced amplitude decay with offset, the method used in this study.

One of the numerous mechanisms that has been proposed for wave energy dissipation refers to viscoelastic losses [*Johnston et al.* (1979)], which are due to the macroscopically observed viscous behaviour of some materials, especially those with fluid content (i.e., sands or soft rocks). Theories explaining attenuation due to viscosity are generally categorised according to the frequency dependence of the observations [*Mavko and Nur* (1975)] and to other pertinent factors such as pore-shapes and fluid flow within the material [*Walsh* (1966), *Kuster and Toksöz* (1974)]. Viscoelastic losses could account for a part of this energy dissipation, even though viscosity itself does not seem to be the real physical process involved since we are not dealing only with a fluid; however, it can be introduced as a parameter to control the physical damping. Many authors have argued that both in fluid saturated unconsolidated sediments and in dry sands, unlike in rock, grains are unbonded and they are relatively mobile; thus, the energy dissipation is mainly due to grain-to-grain interactions with viscoelastic losses being negligible [*Hamilton* (1972), *Stoll* (1989), *Buckingham* (1997)]. Therefore, we are particularly interested in understanding and quantifying the effect of intrinsic friction in partly consolidated sediments. Relative motion at the grain boundaries caused by a wave propagating through a medium that can allow such motions to take place, which has been long proposed is one of the mechanisms for energy dissipation [*Walsh* (1966)]. The medium extracts energy from the wave due to intrinsic friction. From a physical point of view, this mechanism seems to be more evident in unconsolidated or partly consolidated mediums like soils and other soft sedimentary formations.

In this appendix, we demonstrate our approach in numerically investigating frictional losses using a discrete particle model: the Lattice Solid Model (LSM) [*Mora* (1991)]. It is shown that wave attenuation is, in general, exponentially dependent on the frequency for the employed friction coefficient values. Moreover, it is shown that friction eventually results in increasing the stiffness of the medium, as has been previously described by Buckingham (1997), which consequently raises the wave velocity slightly and which certainly facilitates the wave propagation, especially for the S-wave. For convenience we have chosen a configuration where observations are made in the medium: in seismic exploration this configuration is commonly called a Vertical

Seismic Profile (VSP). In the seismic wave propagation for the VSP configuration that we model, the main focus lies on the transmission response. Such experiments are not unique and the presented approach could be employed for better understanding and interpretation of frictional losses.

The LSM was originally derived by short-range molecular dynamics concepts and combined with numerical methods for modelling wave propagation in granular assemblies [*Cundall and Strack* (1979)]. It was further developed to study earthquake processes and has not until today been used for studying wave propagation, as proposed in this study.A 2D setup of circular particles is created in triangular packing, whereby these particles can be either connected or not. Basic laws of physics are directly implemented to govern the wave propagation, intrinsic friction and viscosity, as well as the properties of the matrix and the individual particles. The model can also include particles of arbitrary sizes, namely creating a various size particle lattice, which simulates more complex structures, with a wide range of grain distribution within the same formation. This approach can potentially explain the energy dissipation due to scattering effects, but it is beyond the scope of this study. In this appendix, particles can represent units of the formation, thus representing a macroscopic effect of the grain-to-grain interaction through intrinsic friction. The models described can be used in multidisciplinary studies; a fundamental feature of LSM is the flexibility of its use in geophysical, geomechanical and engineering applications.

We have performed a series of numerical experiments that range from a single-size-bonded-particle setup with no viscosity and no friction included, to more complicated (but still fundamentally and conceptually simple) ones that include both viscosity and friction.

B.2. Theory of Lattice Solid Model

Cundall & Strack (1979) presented a numerical method for simulating wave propagation in granular assemblies. This method is based on the microstructural

definition of rocks, and is capable of describing the mechanical behaviour of distinct particles comprising the rock under study. The immediate advantage of a numerical model versus an analytical or a physical model is that data can be retrieved any time during the simulation and from any position in the volume of the model.

In 1991, Mora presented a Boltzmann Lattice gas-like approach for modelling P-waves in a homogeneous medium, an idea derived by short-range molecular dynamics concepts of atomic solid-state physics. Afterwards, the implementation of wave propagation equations through complex viscoelastic media with friction effects followed, namely using what is called the Lattice Solid Model (LSM). This algorithm enables non-linear processes such as intrinsic friction to be modelled. Such an approach leads to more realistic simulation capabilities of the physics of unconsolidated sediments rather than the commonly used (viscoelastic) finite-difference approaches.

The model is based on a lattice constituted of particles that may represent unit blocks of soils or rocks with specified interactions. Initially the model could represent only single size particles, but it has been extended to model random sizes of particles. The particles can be either bonded together or not: the bonds determine the elastic behaviour of the lattice and are regarded as massless springs. The forces of interaction are governed by Hooke's law.

The equation of motion for the LSM has been accurately described in previous papers [*Donzé and Mora* (1991), *Mora* (1991)] and is given essentially as:

$$m_i \frac{d^2 \vec{\mathbf{u}}_i(\vec{\mathbf{x}},t)}{dt^2} = \sum_j \vec{\mathbf{F}}_{ij}^{bonded}(\vec{\mathbf{x}},t) + \sum_j \vec{\mathbf{F}}_{ij}^{unbonded}(\vec{\mathbf{x}},t) + \vec{\mathbf{S}}_i(\vec{\mathbf{x}},t)\,, \qquad \text{(B.1)}$$

where m_i is the mass of particle i; u_i the displacement at time t; $\vec{\mathbf{F}}_{ij}^{bonded}$ is the sum of the interaction forces from particles j bonded to i; $\vec{\mathbf{F}}_{ij}^{unbonded}$ accounts for interaction forces among unbonded particles that come into contact; and $\vec{\mathbf{S}}_i$ is the external force applied to the particles, representing the seismic source.

In the current study, particle bonds are considered to be elastic and the associated bonds do not break; therefore, energy is not spent on fracture creation. The normal force exerted between two bonded particles is:

$$\vec{\mathbf{F}}_{ij} = k(r_{ij} - r_0)\vec{\mathbf{e}}_{ij} - \nu\frac{d\vec{\mathbf{u}}_i}{dt}, \tag{B.2}$$

where k is the spring constant; r_{ij} is the distance between the centres of two bonded particles after displacement from the initial equilibrium distance r_0; $\vec{\mathbf{e}}_{ij}$ is the unit vector pointing from particle i to j; ν is the viscosity coefficient; and $\vec{\mathbf{u}}_i$ the particle velocity of particle i. The viscosity term has been implemented to account for damping energy [*Place and Mora* (1999)]. For unbonded particles $\vec{\mathbf{F}}_{ij} = 0$ as long as they do not collide, in which case, they transfer impulse.

A term of friction between unbonded particles has been added [*Place and Mora* (1999)]. This frictional force is opposite to the direction of displacement and the magnitude is given by:

$$\vec{\mathbf{F}}_{ij}^{friction} = \mu\left|\vec{\mathbf{F}}_{ij}\right|, \tag{B.3}$$

where μ is the friction coefficient. The frictional force is calculated only between unbonded particles.

For the numerical implementation of the model, a finite-difference modified velocity Verlat-scheme has been used; the new positions of the particles are calculated immediately after all the interactions have taken place. This implementation provides better time integration than other widely used particle codes. The time step depends on the radius of the smallest particle to ensure numerical stability.

B.3. Modelling with no frictional losses

The evolution of our numerical experiments regarding wave attenuation in the discrete particle model is described in detail in this section. The model consists of particles that are set in triangular packing: each particle can be connected with its six

neighbouring particles. As for configuration of source and receivers, we use a VSP configuration: namely, the receivers are set in the middle column of the model (positioned every second row) and the source is placed on the surface; i.e., the first row of the model. Figure B.1 shows a schematic of a single-size particle lattice where all particles are bonded, with the darkest particles representing the source particles and the dashed particles the monitoring/receiver particles.

The simplest case is when all particles are of the same size and there is no viscosity term allowed. In terms of source, we simulate a plane wave; thus, all particles of the top row move in one direction at the same time. This motion is described in the form of a negative polarity Gaussian wavelet:

$$S_{f_p}^{\tau}(t) = -\exp(-\pi f_p (t-\tau)^2) \,, \tag{B.4}$$

where τ is the delay and f_p the central frequency of the wavelet. The frequencies (f_p) chosen in the numerical experiments in this appendix range from 0.01 to 0.20, representing various dominant wavelengths, ranging from 100 to 5 particles respectively.

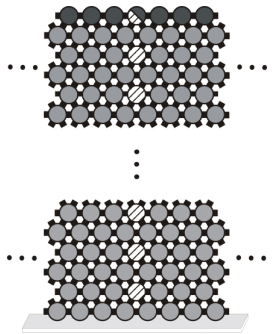

Figure B.1. Example of lattice comprising single-size all-bonded particles in VSP configuration. Darker particles on the top row and dashed particles of the centre column represent source and receivers respectively.

We used a lattice of 401x200 (horizontal and vertical direction respectively) particles, as a reference model. The particles have the same size and density, all bonded together. The dimensions were chosen so that reflections from the side boundaries of the model will reach the receivers with sufficient delay, so that they will not interfere with the direct arrival. The model is placed on a rigid wall, the top of the model is a free surface and the side boundaries are circular (periodic).

The simulation is stopped once the transmitted wave reaches the bottom of the model. The component of the velocity field of interest is plotted as seismic data (Figure B.2) for its component. For the vertical-force source, the vertical component is depicted in Figure B.2a, where the direct P-wave and the reflection from the bottom are visible. The shear motion is cancelled by each neighbouring particle: only the shear motion from the circular boundaries can be detected (Figure B.2b). In the case of the horizontal-force source, vertical motion is generated along with the shear input, which is obviously detected in the vertical component (Figure B.2c). The S-wave as detected at the horizontal component, can be seen in Figure B.2d. The first arrival of the wave under study is windowed and the absolute maximum is determined. Afterwards, maximum amplitude of the envelope is normalised and plotted versus the model parameters, which in this study are depth, frequency and coefficient of friction. For the last two parameters, a representative depth level is chosen.

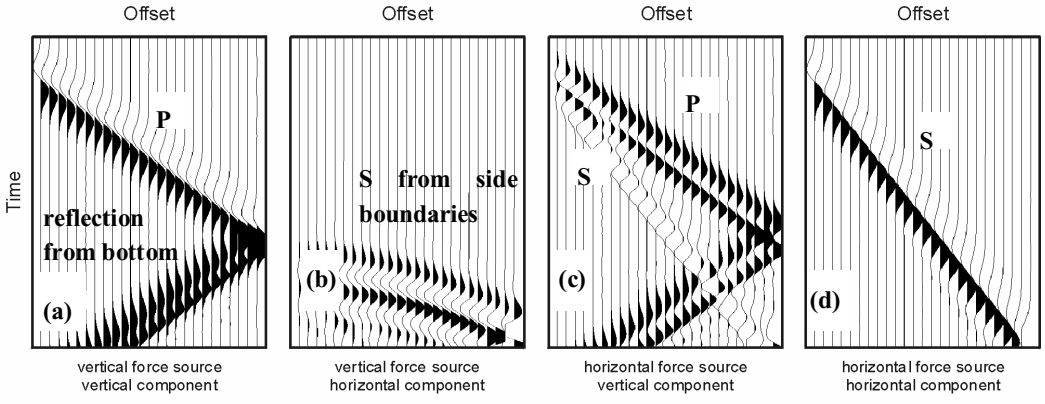

Figure B.2. Simulations of seismic recordings from transmission through loss-free single-size particles lattice of the vertical component depicting the generated wave modes. (a) vertical source force–vertical component, (b) vertical force source–horizontal component, (c) horizontal force source–vertical component, (d) horizontal force source–horizontal component.

Firstly, modelling with no viscosity (ν=0.0) has been performed. The source function (eq. 4) is applied solely in the vertical direction, simulating a vertical-force source. At this point, we introduce a set of values of viscosity coefficient. After the maximum amplitudes have been determined, they are normalised by the first maximum value of the amplitude of the first receiver. The normalised amplitude decreases slightly

with increasing frequency, an effect that is attributed to numerical discrepancies and is subsequently corrected for so that comparisons among models with different parameters that can affect wave attenuation are valid.

We have modelled the attenuation in amplitudes for viscosity coefficient values ranging between 0.1 and 0.5, for an input wavelet with central frequency f_p=0.07. The amplitude of the first arrival is compared with ν=0.0 amplitudes. The dissipation of the amplitudes with the implementation of viscosity is trivially predictable. As expected, increase of the viscosity coefficient results in decrease of amplitudes with distance of propagation (Figure B.3). The method can be used for a quick estimation of a value of a viscosity term that can be associated with an observed amplitude attenuation trend in real data.

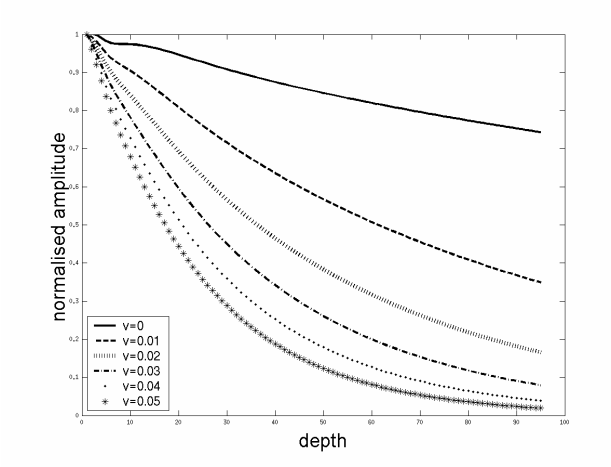

Figure B.3. Normalised amplitudes for single-size particles lattice, for f_p=0.07 with increasing values of viscosity coefficient.

B.4. Modelling with frictional losses

Viscoelastic losses seem unlikely to be the actual physical mechanism determining the damping of amplitudes in unconsolidated or partly consolidated mediums like soils and other soft sedimentary formations; as such viscosity is only a phenomenological description. A more likely physical explanation seems to be particles moving in relation

to each other. In this section, our efforts are focused on investigating wave energy attenuation due to friction.

Friction can occur at the grain boundaries of an unconsolidated formation when they move against each other: motion that can be generated by a wave propagating through. The part of the seismic energy lost through friction is converted into heat energy, which usually is not measured while recording a seismic survey. Nevertheless, it has been proposed by many authors as an energy dissipation factor to be taken into account.

In our implementation, friction can occur among unbonded particles. In order to introduce areas of unbonded particles, we keep the initial particle distribution and setup the same (i.e., single size), but we use the central part as the area of study, which is partly unbonded in the vertical direction. The top and the bottom of the model comprises fully bonded-together particles, while the middle part comprises rows of particles bonded in the horizontal direction and unbonded in the vertical direction every two rows (see Figure B.4). We use a 401x200 model with single size particles, in which the first 20 rows are fully bonded to avoid near field effects. At the first interface (between row 20 and 21), there is a clear reflection occurring, caused by the unbonded contrast. Therefore, the amplitudes are normalised to the first receiver of the unbonded area.

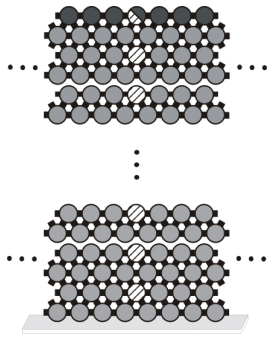

Figure B.4. Example of lattice comprising single-size particles. Every two rows in the vertical direction are unbonded in the central part. In these regions friction is allowed.

In the next section, we separate the discussion into two parts: a vertical-force generating mainly P-waves and a horizontal-force source, generating mainly S-waves but also P-waves.

B.5. Vertical-force source (P-waves)

The values of the coefficient of friction studied range from 0.0 (representing a "reference case") to 1.0. We generate vertical motion on the top row and study the vertical component at the receiving end. We chose the first-arrival P-wave and picked its envelope of amplitude. The trend of the attenuation of amplitudes depending on frequency and friction coefficient is more complicated than the viscosity case. Even though the amplitude versus depth behaviour is still exponential (see Figure B.5), one can notice that for high values of coefficient of friction (μ>=0.6), there is a local fluctuation of amplitude. Such behaviour is known as creep and relaxation, and is present in unconsolidated sediments as a result of intergranular friction (*Buckingham* (1997)).

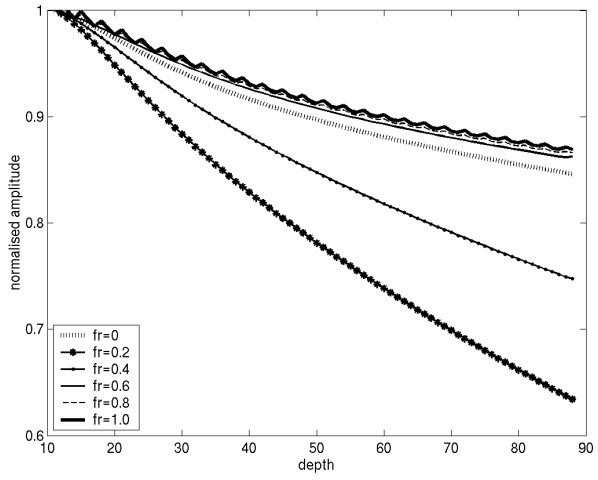

Figure B.5. Normalised amplitudes of P-wave for different values of coefficient of friction (vertical-force source–vertical component, f_p=0.07).

However, the trend of amplitude damping versus friction is not that straightforward (see Figure B.6). For a chosen depth, the amplitude has an initial value at μ=0 and initially decreases with increasing friction up to a minimum point, after which the

amplitude increases again (Figure B.6.). We suggest that even though two different values of friction coefficient may indeed provide the same amplitude value, the character of the medium is different. As the friction coefficient increases beyond the minimum, the medium becomes stiffer and the amplitudes increase. This can be verified by direct observation of the resulting seismic response, of the velocity of the propagating wave. Two different values of friction coefficient may result in the same normalised amplitude for a specific depth, but the velocity will be different: this observation has led us to the verification of the increase of stiffness (Figure B.7). In the example described, observing Figure B.6, we can see that normalised amplitudes for μ=0 and μ=0.6 are almost equal. In the latter case, the P-wave propagates faster (for a time difference Δt). An estimate of the change of stiffness in terms of change in the velocity of the propagating wave resulting from two different coefficients of friction can be given as:

$$\Delta V_p = \frac{\Delta x}{\Delta t}, \tag{B.5}$$

where ΔV_p is the velocity change due to introduced stiffness (resulting from increasing friction); Δx is the distance traveled; and Δt the difference in time as shown in Figure B.7.

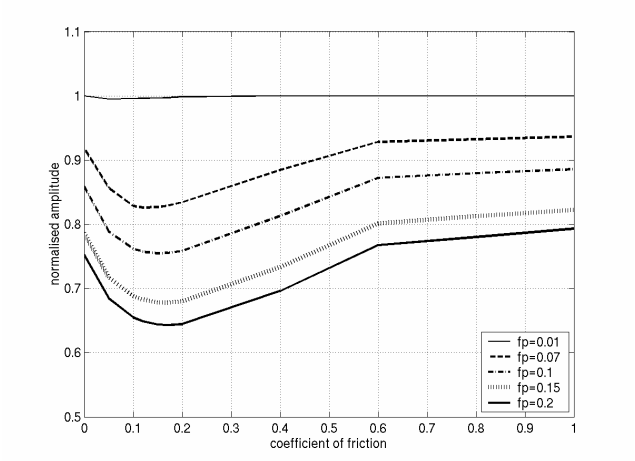

Figure B.6. Friction dependence of normalised amplitudes of P-wave for different center-frequencies of input wavelet (depth is 80th row in the model–vertical component).

All amplitude-versus-friction curves in Figure B.6 show frequency dependence with clearly distinguished amplitudes and a similar overall non-linear trend. In fact, we can identify three areas: for values of friction coefficient until the global minimum (ranging for 0.1-0.2, depending on the frequency), for values of friction coefficient from the global minimum until approximately 0.6, and for values of friction coefficient larger than 0.6 (where the dependence appears to be linear). The resulted dependence of amplitude attenuation with frequency for different values of friction coefficient as shown Figure B.8, demonstrates increasing attenuation that scales exponentially with frequency.

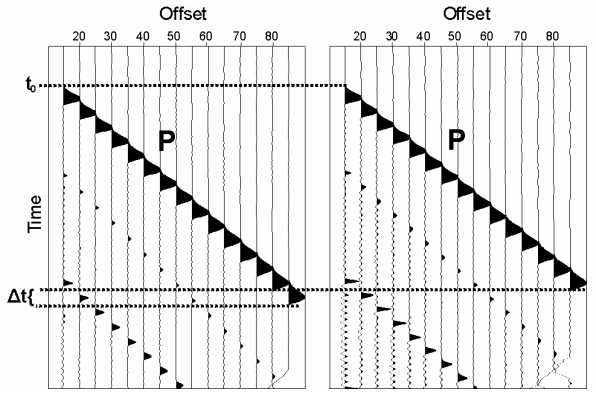

Figure B.7. Vertical-force source-vertical component, P-wave, with friction coefficient μ=0 (left) and μ=0.6 (right), windowed at the area of interest (fp=0.07). Observe reduced time delay *Δt* due to stiffening of medium.

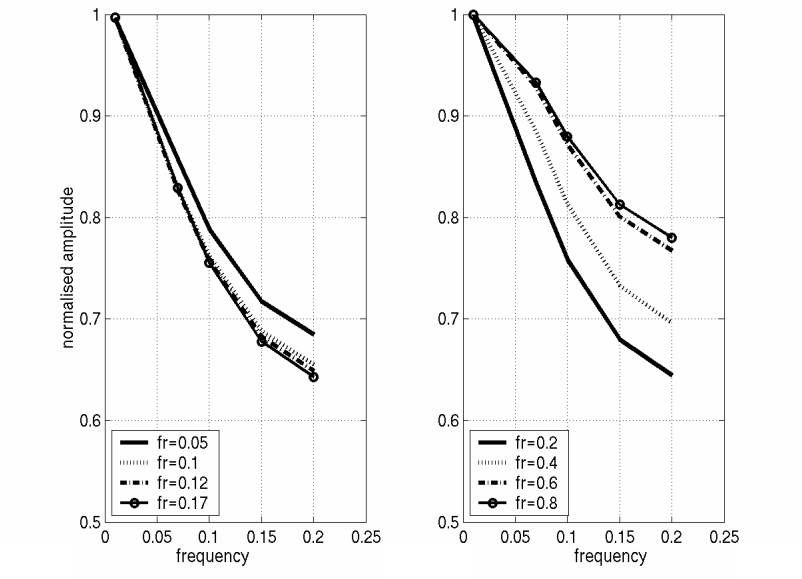

Figure B.8. Amplitude attenuation dependence over frequency (P-wave from vertical-force source–vertical component, depth is 80th row in the model).

B.6. Horizontal-force source (S- and P-waves)

In order to simulate a shear source, the top row moves solely in the horizontal direction. The parameters have been kept the same as for the respective numerical experiments for the vertical force. We use both the horizontal and the vertical component data from the receivers. The shear motion of the source gives rise to a vertical component. In the following paragraphs, we present results for both shear and compressional mode from the horizontal and vertical component respectively. Contrary to what has been shown from the numerical experiments with vertical source, the dependence of the normalised amplitudes with coefficient of friction is more complex. The first arrival of the shear wave cannot be resolved for the entire depth of the model for all cases: when the value of friction coefficient is low, the coda waves of the faster P-wave interfere destructively with the first arrival of the shear wave. Nevertheless, as discussed above, the higher the friction coefficient, the stiffer the medium becomes; thus for higher friction values, the shear waves propagate crisply and clearly all the way to the last row of the model (Figure B.9). While the coefficient of friction takes low values (μ<0.4), the coda waves following the faster P-wave (identified in the vertical

component, not shown here) disturb the resolution of the highly attenuated shear motion; thus, the interpretation of the shear component throughout the model is not possible. As the coefficient of friction increases and the medium becomes stiffer, the interpretation of the shear wave is easier. Due to this effect, we use shallower depth to investigate the amplitude attenuation; nevertheless, this still returns valuable results.

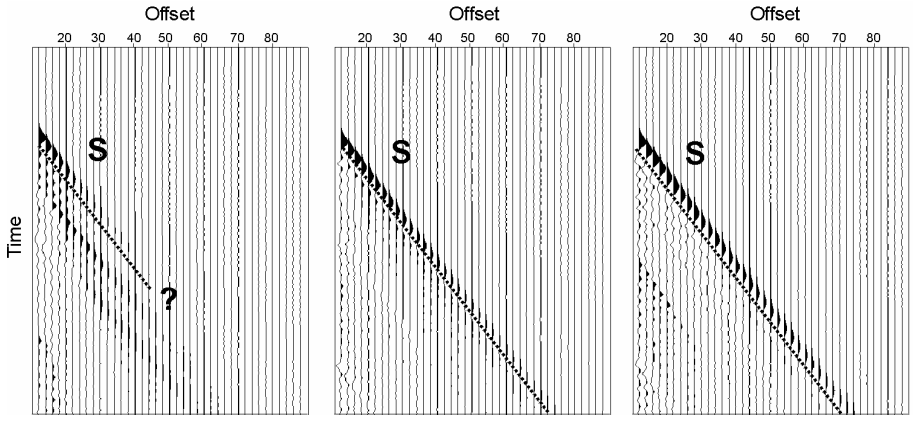

Figure B.9. Horizontal source-horizontal component and with friction coefficient μ=0.2 (left), μ=0.6 (centre) and μ=1.0 (right), windowed at the area of interest (f_p=0.07). Notice high attenuation of first-arrival S-wave in first case while fully propagating through in the second and third case (dotted line used as guide).

Based on the seismograms of Figure B.9, the maxima can be picked and set out as a function of friction. It can be seen (Figure B.10) that the normalised amplitudes from the horizontal component increase with increasing coefficient of friction.

Unless we accept a rough linear trend (that is, normalised amplitude scales linearly with the coefficient of friction), we can indeed distinguish three areas for $0<\mu<0.4$, $0.4<\mu<0.6$ and $\mu>0.6$. For the first range of values of friction coefficient, the trend is less linear than the latter two. The second range ($0.4<\mu<0.6$) exhibits a higher slope than the last part, resembling the equivalent range of values of coefficient of friction for the normalised amplitudes observed from the vertical component using the vertical source. Finally, a linear trend is observed in both cases of co-polar source and receiver, for values of coefficient of friction higher than 0.6.

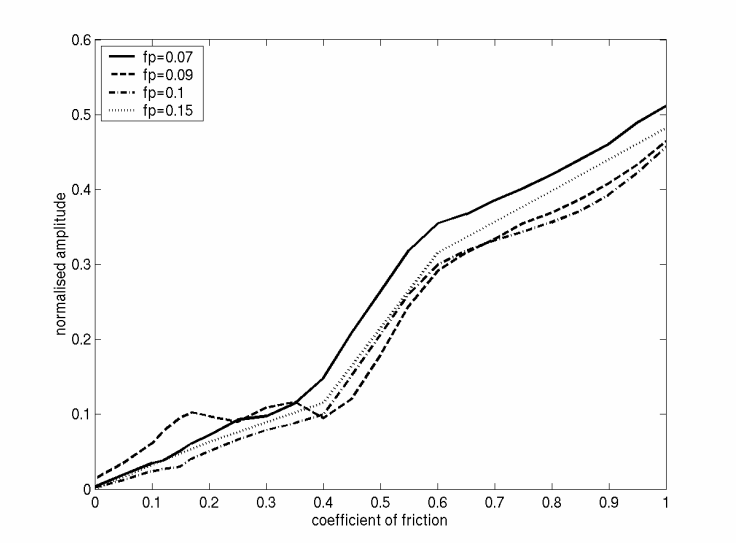

Figure B.10. Normalised amplitudes of S-wave from horizontal force–horizontal component. Notice general trend of increasing amplitudes with increasing coefficient of friction.

In the case of the vertical component where the P-wave has been picked and studied, the trend of the normalised amplitudes versus the coefficient of friction is still non-linear; however, it does not present a general trend among different frequencies (Figure B.11). Generally the normalised amplitude decreases as the coefficient of friction increases. An explanation of this is that while the medium stiffens, more energy is guided to the shear motion.

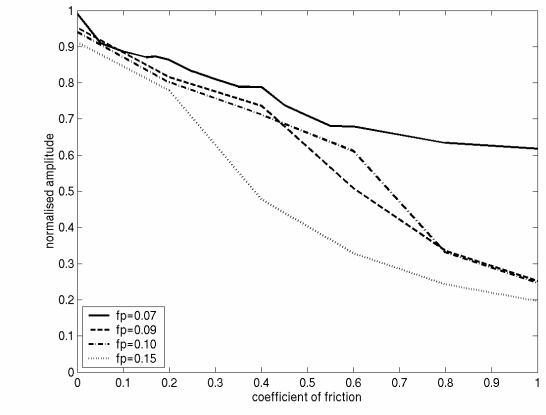

Figure B.11. Normalised amplitudes of P-wave from horizontal-force source–vertical component. Notice a general decreasing trend with increasing coefficient of friction, but no clear similarity for this dependence through different frequencies.

The amplitude dependence on frequency is generally exponential for both S- and P-wave (as calculated from the horizontal and vertical components, respectively); however, the coupling between the P and the S wave can slightly bias the definition of the local maximum amplitude. For this reason there is a decrease of amplitude with frequency but not as clear as in the case of the vertical force (Figure B.12). The S-wave exhibits a more obvious exponential trend than does its P-wave counterpart, as shown comparatively in Figure B.12(left for S-wave and right for P-wave). In order to better perceive the exponential scaling of the vertical component data, the results for the μ=0.6 have been fitted with an exponential curve: (*normalised_amplitude*=0.8497*exp(-5.6745 *f*)), where *f* is the mean frequency with regression value R^2=0.96). (Figure B.11b, black exponential curve).

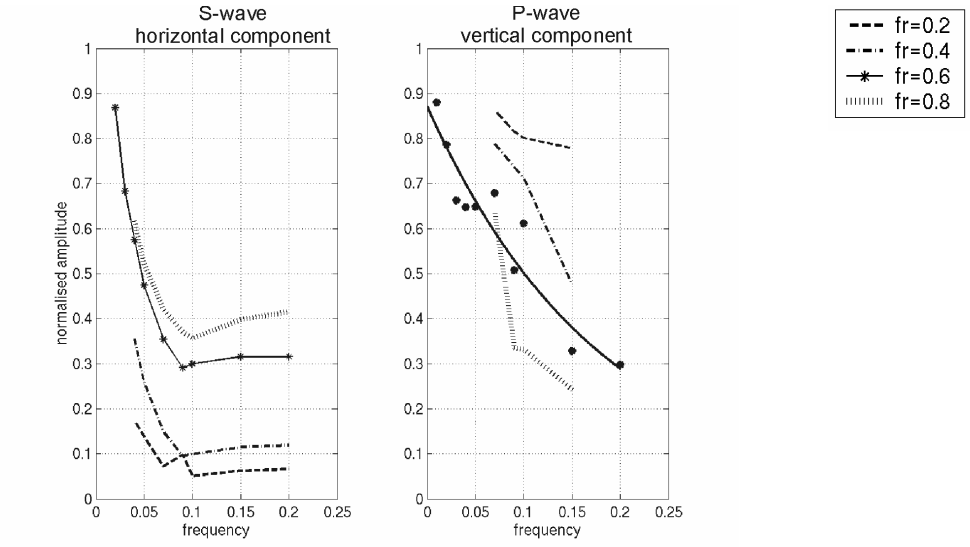

Figure B.12. Normalised amplitudes of S-waves (left) and P-waves (right) plotted against frequency for the horizontal force-source for vertical (left) and horizontal (right) component.

B.7. Conclusions

We have presented results from numerical experiments concerning seismic attenuation due to intrinsic friction. The method presented contributes substantially to our understanding of energy dissipation in unconsolidated sediments due to viscous and frictional effects (a primarily intrinsic soil property). It shows increasing propagation

velocities with increasing frictional forces, which are explained by increased stiffening of the medium with increasing friction coefficient values.

For the P-wave (first arrival) for the vertical source force, we observed a nonlinear trend for low values of friction coefficient (μ<0.6), above which the amplitudes scale linearly with μ. For the S-wave in the horizontal-force source for the horizontal component, the range of 0.4<μ<0.6 exhibited a higher slope than did the range μ>0.6, resembling the equivalent range of values of the coefficient of friction compared to what is observed from the vertical component using the vertical source. Finally, in both cases of co-polar source and receiver, a linear trend has been observed for values of coefficient of friction higher than 0.6.

Independently of the source used (vertical or horizontal), the medium became stiffer with an increase of coefficient of friction. Coefficient of friction is related to the frictional force applied to the particles and has been shown that above a certain value (μ=0.6) the motion of the particles change, resulting to creep-relaxation behaviour as response to an instantaneous stress. The range of values generally agrees with the experimental results regarding maximum friction for a wide variety of rocks as proposed by *Byerlee* (1979). The frequency dependence of frictional losses in LSM shows that as the frequency increases the losses are higher, in most cases generally in an exponential sense, as expected both from theory and experience on field experiments.

B.8. Future work

Discrete particle models such the LSM can provide usefull insight in the rock behaviour under any stress-strain environment, or as used in this work for wave propagation. Quite representative detailed modelled can be created and attenuation and scattering of the wavefront can be observed in the numerical simulations. More complex geometries and geologies such voids (Figure B.13A), grains of different size (Figure B.13B)or different material, dipping layers etc can be implemented and wave propagation numerical experiments should be conducted.

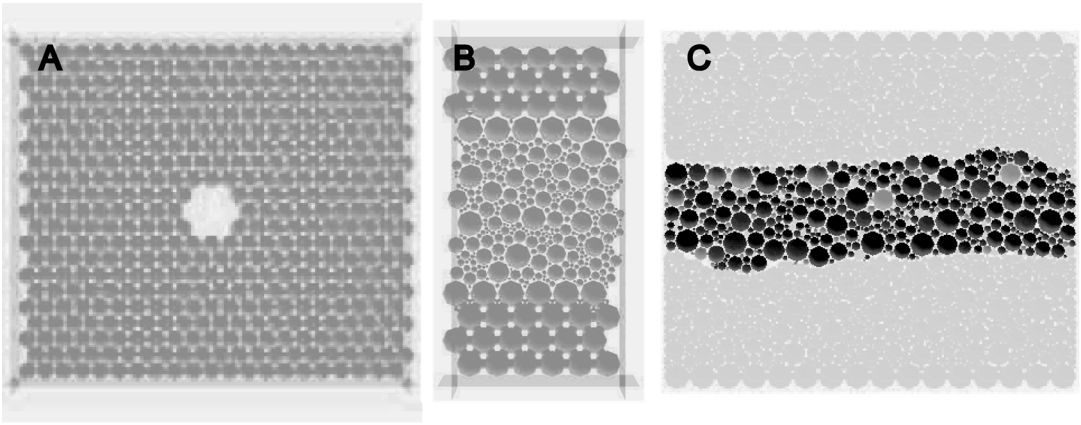

Figure B.13 Discrete particles setups created with LSM: lattice containing a void (A), various sizes of grains (B) and inclusion of different material in a non-horizontal layering (C).

Bibliography

Abramowitz, M., and I. A. Stegun (1972), *Handbook of Mathematical Functions with Formulas, Graphs, and Mathematical Tables*, 9th printing ed., 940-943 pp., New York: Dover.

Aki, K. R., P.G. (1980), *Quantitative Seismology, Theory and Methods*, W.H. Freeman, San Francisco.

Albani, A. E., J. F. Deconinck, J. P. Herbin, and J. N. Proust (1993), Charact´erisation g´eochimique de la mati`ere organique et mineralogie des argiles du Kimm´edridgien du Boulonnais, *Ann. Soc. Geol. Nord.*, *2*, 113-120.

Amundsen, L., and R. Mittet (1994), Estimation of phase velocites and Q-factors from zero-offset, vertical seismic profile data, *Geophysics*, *59*, 500-517.

Bacri, J. C., and D. Salin (1986), Sound-Velocity of a Sandstone Saturated with Oil and Brine at Different Concentrations, *Geophys. Res. Lett.*, *13*, 326-328.

Banik, N. C., I. Lerche, and R. T. Shuey (1985), Stratigraphic Filtering .1. Derivation of the Odoherty-Anstey Formula, *Geophysics*, *50*, 2768-2774.

Barra, F., and P. Gaspard (1999), Scattering in periodic systems: from resonances to band structure, *J. Phys. A-Math. Gen.*, *32*, 3357-3375.

Berkhout, A. J. (Ed.) (1982), *Seismic migration:imaging of acoustic energy by wave field extrapolation: Volume A: Theoretical aspects*, Elsevier Science Publ. Co. Inc.

Berkhout, A. J. (Ed.) (1984), *Seismic migration:imaging of acoustic energy by wave field extrapolation: Volume B: Practical aspects*, Elsevier Science Publ. Co. Inc.

Biot, M. A. (1956a), Theory of Propagation of elastic waves in a fluid saturated porous solid, I: Low frequency range, *J. Acoust. Soc. Am.*, *28*, 168-178.

Biot, M. A. (1956b), Theory of propagation of elastic waves in a fluid saturated porous solid, II: High frequency range, *J. Acoust. Soc. Am.*, *28*, 179-191.

Bourbier, T., O. Coussy, and B. Zinzner (1986), *Acoustique des milieux poreux*, Technip, Paris.

Braaksma, H. (2005), Geological and Petrophysical Calibration of Seismic Stratigraphy (Upper Jurassic Siliciclastics, Northern France), PhD Thesis, Vrije Universiteit, Amsterdam.

Braaksma, H., G. G. Drijkoningen, N. Filippidou, J. A. M. Kenter, and J. N. Proust (2006), The origin and nature of seismic reflections of sharp-based shoreface deposits (Upper Jurassic Siliciclastics, northern France), *Geophys. Prospect.*

Braaksma, H., J. A. M. Kenter, J. N. Proust, V. Dijkmans, T. v. Hoek, G. Mahieux, and G. G. Drijkoningen (2003), Controls on acoustic properties of late Jurassic Siliciclastic rocks (Boulonnais, northern France), *Geophysics*, *68*, 58-69.

Braaksma, H., J. N. Proust, J. A. M. Kenter, G. G. Drijkoningen, and N. Filippidou (2005), Sedimental, petrophysical and seismic characterization of an upper Jurassic shoreface-

dominated shelf-margin (The Boulonnais, Northern France), *Journal of Sedimentary Research*.

Buckingham, M. J. (1997b), Theory of acoustic attenuation, dispersion, and pulse propagation in unconsolidated granular materials including marine sediments, *Journal of the Acoustical Society of America*, *102*, 2579-2596.

Buckingham, M. J. (1999), On the phase speed and attenuation of an interface wave in an unconsolidated marine sediment, *Journal of the Acoustical Society of America*, *106*, 1694-1703.

Buckingham, M. J. (2000), Wave propagation, stress relaxation, and grain-to-grain shearing in saturated, unconsolidated marine sediments, *Journal of the Acoustical Society of America*, *108*, 2796-2815.

Burchette, T., and V. Wright (1992), Carbonate ramp depositional systems, *Sedimentary Geology*, *79*, 3-57.

Byerlee, J. D. (1979), Friction of rocks, *Pure & Applied Geophysics*, *116*, 615-626.

Cadoret, C., D. Marion, and B. E. Zinszner (1992), 1kHz elastic wave velocities in partially saturated limestones; evidence of fluid distribution effect, in *SEG Annual Meeting*, edited.

Castagna, J. P., M. L. Batzle, and R. L. Eastwood (1985), Relationships between compressional wave and shear wave velocities, *Geophysics*, *50*, 571-581.

Causse, E., and B. Ursin (2000), Viscoacoustic reverse time migration, *J. Seism. Explor.*, *9*, 165-184.

Clemmensen, L. B., J. J. Fornos, and A. Rodriguez-Perea (1997), Morphology and architecture of a late Pleistocene cliff-front dune, Mallorca, western Mediterranean, *Terra Nova*, *9*, 251-254.

Connell, R. J. O., and B. Budiansky (1977), Viscoelastic properties of fluid-saturated cracked solid, *J. Geophys. Res.,*, *82*, 5719-5735.

Cope, J. C. W., J. K. Ingham, and F. Rawson (1992), Atlas of Palaeogeography and Lithofacies, *Geol. Soc. London Memoir*, *13*, 1-152.

Cundall, P. A., and O. D. L. Strack (1979), A discrete numerical model for granular assemblies, *Geotechnique*, *29*, 47-65.

Dainty, A. M. (1981), A Scattering Model to Explain Seismic-Q Observations in the Lithosphere between 1 and 30 Hz, *Geophys. Res. Lett.*, *8*, 1126-1128.

Daubechies, I. (1988a), Orthonormal Bases of Compactly Supported Wavelets, *Commun. Pure Appl. Math.*, *41*, 909-996.

Daubechies, I. (1988b), Time Frequency Localization Operators - a Geometric Phase-Space Approach, *IEEE Trans. Inf. Theory*, *34*, 605-612.

Daubechies, I. (1990), The Wavelet Transform, Time-Frequency Localization and Signal Analysis, *IEEE Trans. Inf. Theory*, *36*, 961-1005.

Daubechies, I. (1996), Where do wavelets come from? - A personal point of view, *Proc. IEEE*, *84*, 510-513.

Dellinger, J., and L. Vernik (1994), Do traveltimes in pulse transmission experiments yield anisotropic group or phase velocities?, *Geophysics*, *59*, 1774-1779.

Donzé, F., and P. Mora (1991), Numerical simulations for the Lattice Solid Model, IPG, Paris.

Draganov, D., G. G. Drijkoningen, H. v. d. Meer, A. Volker, and A. K. T. Wever (2001), A very shallow (0-100m) 3-D land seismic survey near Boulogne-sur-Mer (N-France), paper presented at 63rd meeting of the European Association of Geoscientists & Engineers (EAGE), Amsterdam.

Dvorkin, J., G. Mavko, and A. Nur (1995), Squirt Flow in Fully Saturated Rocks, *Geophysics*, *60*, 97-107.

Erdos, P., E. Liviotti, and R. C. Herndon (1997), Wave transmission through lattices, superlattices and layered media, *J. Phys. D-Appl. Phys.*, *30*, 338-345.

Esteban, M. (1979), Significance Of The Upper Miocene Coral Reefs Of The Western Mediterranean, *Paleogeogr. Paleoclimatol. Paleoecol.*, *29*, 169-188.

Feynman, R. P. (2001), *The Pleasure of Finding Things Out : The Best Short Works of Richard Feynman*, Gardners Books

Figotin, A. (1993), Existence of gaps in the spectrum of periodic dielectric structures on a lattice, *Journal of Statistical Physics*, 3/4.

Figotin, A., and P. Kuchment (1994), Band-gap structure of the spectrum of periodic maxwell operators, *Journal of Statistical Physics*, *74*.

Figotin, A., and P. Kuchment (1996a), Band-gap structure of spectra of periodic dielectric and acoustic media: I.Scalar model, *SIAM Journal of Applied Mathematics*, *56*, 68-88.

Figotin, A., and P. Kuchment (1996b), Band-gap structure of spectra of periodic dielectric and acoustic media: II.Two-dimensional photonic crystals, *SIAM Journal of Applied Mathematics*, *56*, 1561-1620.

Filippidou, N., G. G. Drijkoningen, R. Romijn, and G. Mahieux (2001), An AVO analysis on very shallow 3-D seismic data, *Proceedings of the 7th Meeting of the Environmental and Engineering Geophysics Society*.

Futterman, W. I. (1962), Dispersive body waves, *J. Geophys. Res.*, *67*, 5279-5291.

Ghose, R., and J. Goudswaard (2004), Integrating S-wave seismic-reflection data and cone-penetration-test data using a multiangle multiscale approach, *Geophysics*, *69*, 440-459.

Ghose, R., V. Nijhof, J. Brouwer, Y. Matsubara, Y. Kaida, and T. Takahashi (1998), Shallow to very shallow, high-resolution reflection seismic using a portable vibrator system, *Geophysics*, *63*, 1295-1309

Ghose, R., and E. C. Slob (2006), Quantitative integration of seismic and GPR reflections to derive unique estimates for water saturation and porosity in subsoil, *Geophys. Res. Lett.*, *33*.

Gill, P. R., W. Murray, and M. H. Wright (1981), *The Levenberg-Marquardt Method, §4.7.3 in Practical Optimization*, 136-137 pp., Academic Press, London.

Goff, J. A., and K. Holliger (2003), *Heterogeneity in the crust and upper mantle, Nature, Scaling and Seismic Properties* Kluwer Academic/Plenum Publishers, New York.

Goudswaard, J. (2001), Multiangle Multiscale Characterisation of Seismic Reflection Data, 173 pp, Delft University of Technology, Delft.

Goudswaard, J., and K. Wapenaar (2001), Scale and angle dependent reflection properties of self-similar interfaces, *J. Comput. Acoust.*, *9*, 1015-1023.

Gregory, A. R. (1976), Fluid Saturation Effects on Dynamic Elastic Properties of Sedimentary-Rocks, *Geophysics*, *41*, 895-921.

Griffiths, D. J., and C. A. Steinke (2001), Waves in locally periodic media, *Am. J. Phys.*, *69*, 137-154.

Grossmann, A., R. Kronland-Martinet, and J. Morlet (1989), Reading and understanding continuous wavelet transforms, in *Wavelets: time-frequency methods and phase space*, edited by J. M. Combes, et al., pp. 2-20, Springer-Verlag, Berlin.

Grossmann, A., and J. Morlet (1985), Decomposition of functions into wavelets of constant shape and related transforms, in *Mathematics and Physics, lectures on recent results*, edited by L. Streit, World Scientific Publisher, Singapore.

Haase, A. B., and R. R. Stewart (2004), Attenuation (Q) from VSP and log data: Ross Lake, Saskatchewan, paper presented at CSEG National Convention, Calgary.

Hall, M. (2006), Predicting bed thickness with cepstral decomposition, *TLE*.

Hamilton, E. L. (1972), Compressional-wave attenuation in marine sediments, *Geophysics*, *37*, 620-646.

Handford, C. R., and R. G. Loucks (1991), Unique Signature Of Carbonate Strata And The Development Of Depositional Sequence And Systems Tract Models For Ramps, Rimmed Shelves, And Detached Platforms, *Aapg Bulletin-American Association Of Petroleum Geologists*, *75*, 588-588.

Haq, B. U., J. Hardenbol, and P. R. Vail (1987), Chronology Of Fluctuating Sea Levels Since The Triassic, *Science*, *235*, 1156-1167.

Hauge, P. S. (1981), Measurements of attenuation from vertical seismic profiles, *Geophysics*, *46*, 892-903.

Haus, J. W., and B. Y. Soon (2002), Spatio-temporal instabilities for counter-propagating waves in periodic media, *Optics Express*, *10*.

Hearst, J. R., and P. H. Nelson (1985), *Well Logging for Physical Properties*, McGraw-Hill, New York.

Herrmann, F. (1997), A scaling medium representation, a discussion on well-logs, fractals and waves, 298 pp, Delft University of Technology, Delft.

Herrmann, F. J. (2001), Singularity characterization by monoscale analysis: Application to seismic imaging, *Appl. Comput. Harmon. Anal.*, *11*, 64-88.

Hovem, J. M. (1995), Acoustic waves in finely layered media, *Geophysics*, *60*, 1217-1221.

Hunt, D., and M. E. Tucker (1992), Stranded Parasequences And The Forced Regressive Wedge Systems Tract - Deposition During Base-Level Fall, *Sedimentary Geology*, *81*, 1-9.

Hyun, Y., S. P. Neuman, V. V. Vesselinov, W. A. Illman, D. M. Tartakovsky, and V. Di Federico (2002), Theoretical interpretation of a pronounced permeability scale effect in unsaturated fractured tuff, *Water Resources Research*, *38*.

Jeng, Y., J. Y. Tsai, and S. H. Chen (1999), An improved method of determining near-surface Q, *Geophysics*, *64*, 1608-1617.

Johnston, D. H., and M. N. Toksöz (1981), Chapter 1: Definitions and terminology, in *Seismic wave attenuation*, edited by M. N. Toksöz and D. H. Johnston, pp. 1-12, SEG.

Johnston, D. H., M. N. Toksöz, and A. Timur (1979), Attenuation of seismic waves in dry and saturated rocks, II: Mechanisms, *Geophysics*, *44*, 691-711.

Jones, J. W. (1995), Scale-Dependent Resistivity Measurements of Oracle Granite, *Geophys. Res. Lett.*, *22*, 1453-1456.

Kang, I. B., and G. A. McMechan (1994), Separation of Intrinsic and Scattering Q-Based on Frequency-Dependent Amplitude Ratios of Transmitted Waves, *J. Geophys. Res.-Solid Earth*, *99*, 23875-23885.

Karrenbach, M. (1995), Elastic Tensor Field, Stanford University.

Kennett, B. L. N. (1974), Reflections, Rays, and Reverberations, *Bull. Seismol. Soc. Amer.*, *64*, 1685-1696.

Kjartansson, E. (1979), Constant Q-wave propagation and attenuation, *J. Geophys. Res.*, *84*, 4737-4748.

Klimentos, T., and C. McCann (1990), Relationships among Compressional Wave Attenuation, Porosity, Clay Content, and Permeability in Sandstones, *Geophysics*, *55*, 998-1014.

Kolsky, H. (1956), The propagation of stress pulses in viscoelastic solids, *Phil. Mag.*, *1*, 693-710.

Kopf, M. (1977), Fortschritte der Petrophysik, in *Physik der Erdkruste*, edited by R. Lauterbach, Akademie-Verlag, Berlin.

Kuster, G. T., and M. N. Toksöz (1974), Velocity and attenuation of seismic waves in two-phase media. Part I. Theoretical formulations, *Geophysics*, *39*, 587-606.

Lake, L. W., and S. Srinivasan (2004), Statistical scale-up of reservoir properties: concepts and applications, *J. Pet. Sci. Eng.*, *44*, 27-39.

Landau, L. D., and E. M. Lifschitz (1984), *Electrodynamics of Continuous Media,*, 2nd ed., pp. 280-283 pp., England: Pergamon Press, Oxford.

Large, M. C. J., D. R. McKenzie, A. R. Parker, B. C. Steel, K. Ho, S. G. Bosi, N. Nicorovici, and R. C. McPhedran (2001b), The mechanism of light reflectance in silverfish, *Proceedings of the Royal Society of London Series a-Mathematical Physical and Engineering Sciences*, *457*, 511-518.

Lee, D. W. (1997), Iridescent blue plants, *American Scientist*, *85*, 56-63.

Levenberg, K. (1944), A Method for the Solution of Certain Problems in Least Squares, *Quart. Appl. Math.*, *2*, 164-168.

Levin, F. K. (1979), Seismic velocities in transversely isotropic media, *Geophysics*, *44*, 918-936.

Lhomme, T. P. Y. (2005), Initiation of Hydraulic Fractures in Natural Sandstones, Delft University of Technology, Delft.

Liu, H. (1988), Effects of source spectrum on seismic attenuation measurements using the pulse-broadening method, *Geophysics*, *53*, 1520-1526.

Liu, H. H., and G. S. Bodvarsson (2003), Upscaling of constitutive relations in unsaturated heterogeneous tuff matrix, *J. Hydrol.*, *276*, 198-209.

Loucks, R. G. M., R.T. ; Bellis, J.K.; Brown A.A. (1996), Regional depositional setting and pore netwerk of the El Garia Fm. (Metlaoui Group, Lower Eocene), Offshore Tunisia, *Abstracts of the Fifth Tunisian Petroleum Exploration Conference*, 146-171.

Lu, S. L., F. J. Molz, G. E. Fogg, and J. W. Castle (2002), Combining stochastic facies and fractal models for representing natural heterogeneity, *Hydrogeology Journal*, *10*, 475-482.

Mahieux, G., J. N. Proust, B. Tessier, M. D. Batist, and H. Chamley (1999), Stratigraphie sismique et sequentiell haute resolution des formations du Jurassique sueprieur du Boulonnais (Nord de la France), *C.R. Acad. Sci. Paris*, *328*, 341-346.

Mahieux, G., J. N. Proust, B. Tessier, and M. Debatist (1988), High resolution seismic and sequence stratigraphy: raletionships between the seismic record and the sequence stratigraphic picture, *Marine Petrol. Geol.*, *15*, 329-342.

Mallat, S., and W. L. Hwang (1992), Singularity Detection and Processing with Wavelets, *IEEE Trans. Inf. Theory*, *38*, 617-643.

Mallat, S., and S. Zhong (1992), Characterization of Signals from Multiscale Edges, *IEEE Trans. Pattern Anal. Mach. Intell.*, *14*, 710-732.

Mallat, S. G. (1989a), Multifrequency Channel Decompositions of Images and Wavelet Models, *Ieee Transactions on Acoustics Speech and Signal Processing*, *37*, 2091-2110.

Mallat, S. G. (1989b), A Theory for Multiresolution Signal Decomposition - the Wavelet Representation, *IEEE Trans. Pattern Anal. Mach. Intell.*, *11*, 674-693.

Marchand, P., and L. Marmet (1983), Binomial Smoothing Filter - a Way to Avoid Some Pitfalls of Least-Squares Polynomial Smoothing, *Review of Scientific Instruments*, *54*, 1034-1041.

Marion, D., T. Mukerji, and G. Mavko (1994), Scale Effects on Velocity Dispersion - from Ray to Effective-Medium Theories in Stratified Media, *Geophysics*, *59*, 1613-1619.

Marquardt, D. (1963), An Algorithm for Least-Squares Estimation of Nonlinear Parameters, *SIAM J. Appl. Math.*, *11*, 431-441.

Marsan, D., and C. J. Bean (1999), Multiscaling nature of sonic velocities and lithology in the upper crystalline crust: evidence from the KTB Main Borehole, *Geophys. Res. Lett.*, *26*, 275-278.

Mavko, G., and D. Jizba (1991), Estimating Grain-Scale Fluid Effects on Velocity Dispersion in Rocks, *Geophysics*, *56*, 1940-1949.

Mavko, G., and E. Kjartansson (1979), Effect of Friction on Velocity and Attenuation, *Geophysics*, *44*, 333-333.

Mavko, G., E. Kjartansson, and K. Winkler (1979), Seismic-Wave Attenuation in Rocks, *Rev. Geophys.*, *17*, 1155-1164.

Mavko, G., and T. Mukerji (1998), Bounds on low-frequency seismic velocities in partially saturated rocks, *Geophysics*, *63*, 918-924.

Mavko, G., and A. Nur (1975), Melt squirt in the aesthenosphere, *J. Geophys. Res.*, *80*, 1444-1448.

Mavko, G. M. (1979), Frictional Attenuation - Inherent Amplitude Dependence, *Journal of Geophysical Research*, *84*, 4769-4775.

Mavko, G. M., and A. Nur (1979), Wave Attenuation in Partially Saturated Rocks, *Geophysics*, *44*, 161-178.

Mayeda, K., S. Koyanagi, M. Hoshiba, K. Aki, and Y. H. Zeng (1992), A Comparative-Study of Scattering, Intrinsic, and Coda Q(-1) for Hawaii, Long Valley, and Central California between 1.5-Hz and 15.0-Hz, *J. Geophys. Res.-Solid Earth*, *97*, 6643-6659.

McKenzie, D. R., Y. Yin, and W. D. McFall (1995), Silvery fish skin as an example of a chaotic reflector, *Proceedings of the Royal Society of London Series a-Mathematical Physical and Engineering Sciences*, *8*, 579-584.

McPhedran, R. C., and N. A. Nicorovici (2001), Learning Optics in nature's school, *Australian Optical Society*, *15*, 7-9.

Menke, W., and B. Dubendorff (1985), Discriminating Intrinsic and Apparent Attenuation in Layered Rock, *Geophys. Res. Lett.*, *12*, 721-724.

Meyer, Y. (1990), *Ondelettes et operateurs I:ondelettes, II:operateurs de Calderon-Zygmund,III:(withR. Coifman) operatuers multilineaires*, english translation of first volume is published by Cambridge University Press, Paris.

Mora, P. (1991), The lattice gas Boltzmann, IPG, Paris.

Morgan, N. A. (1969), Physical Properties of Marine Sediments as Related to Seismic Velocities, *Geophysics*, *34*, 529-&.

Mukerji, T., G. Mavko, D. Mujica, and N. Lucet (1995), Scale-Dependent Seismic Velocity in Heterogeneous Media, *Geophysics*, *60*, 1222-1233.

Murphy, W., A. Reischer, and K. Hsu (1993), Modulus Decomposition of Compressional and Shear Velocities in Sand Bodies, *Geophysics*, *58*, 227-239.

Murphy, W. F., K. W. Winkler, and R. L. Kleinberg (1986), Acoustic Relaxation in Sedimentary-Rocks - Dependence on Grain Contacts and Fluid Saturation, *Geophysics*, *51*, 757-766.

Nastev, M., M. M. Savard, P. Lapcevic, R. Lefebvre, and R. Martel (2004), Hydraulic properties and scale effects investigation in regional rock aquifers, south-western Quebec, Canada, *Hydrogeology Journal*, *12*, 257-269.

Neuman, S. P. (1990), Universal Scaling of Hydraulic Conductivities and Dispersivities in Geologic Media, *Water Resources Research*, *26*, 1749-1758.

Neuman, S. P. (1994), Generalized Scaling of Permeabilities - Validation and Effect of Support Scale, *Geophys. Res. Lett.*, *21*, 349-352.

Neuman, S. P., and V. Di Federico (2003), Multifaceted nature of hydrogeologic scaling and its interpretation, *Rev. Geophys.*, *41*.

Neville, A. C. (1977), Metallic gold and silver colours in some insect cuticles, *J. Insect Physiol*, *23*, 1267-1274.

O'Connell, R. J., and B. Budiansky (1977), Viscoelastic properties of fluid saturated cracked solids, *Journal of Geophysical Research*, *82*, 5719-5736.

O'Doherty, R. F., and N. A. Anstey (1970), Reflections on Amplitudes, *Geophysics*, *35*, 1151-&.

Odling, N. E., S. D. Harris, and R. Knipe (2004), Permeability scaling properties of fault damage zones in siliclastic rocks, *J. Struct. Geol.*, *26*, 1727-1747.

Ouellette, F., P. A. Krug, T. Stephens, G. Dhosi, and B. J. Eggleton (1995), Dispersion compensation using chirped sampled fibre Bragg gratings, *Electronics Letters*, *31*, 899-901.

Pachepsky, Y., D. Benson, and W. Rawls (2000), Simulating scale-dependent solute transport in soils with the fractional advective-dispersive equation, *Soil Science Society of America Journal*, *64*, 1234-1243.

Paillet, F. L., and C. H. Cheng (1986), A numerical investigation of head waves and leaky modes in fluid-filled boreholes, *Geophysics*, *51*, 1438-1449.

Painter, S. (1995), Random Fractal Models of Heterogeneity - the Levy-Stable Approach, *Mathematical Geology*, *27*, 813-830.

Painter, S. (1996), Evidence for non-Gaussian scaling behavior in heterogeneous sedimentary formations, *Water Resources Research*, *32*, 1183-1195.

Parker, A. R., D. McKenzie, and M. C. Large (1998), Multilayer reflectors in animals using green and gold beetles as contrasting examplesq, *The Journal of Experimental Biology*, *201*, 1307-1313.

Place, D., and P. Mora (1999), The lattice solid model to simulate the physics of rocks and earthquakes: incorporation of intrinsic friction, *J. Comp. Phys.*, *150*, 1-41.

Poggiagliolmi, E., and R. D. Allred (1994), Detailed reservoir definition by integration of well and 3-D seismic data using space adaptive wavelet processing, *The Leading Edge*, *13*, 749-754.

Pomar, L. (1993), High-resolution Sequence Stratigraphy in Prograding Carbonates: Application to Seismic Interpretation. , in *Carbonate Sequence Stratigraphy: Recent Advances and Applications*, edited by B. Louks and R. J. Sarg, p. 545

Pomar, L. (2001a), Ecological control of sedimentary accommodation: evolution from a carbonate ramp to rimmed shelf, Upper Miocene, Balearic Islands, *Palaeogeography Palaeoclimatology Palaeoecology*, *175*, 249-272.

Pomar, L. (2001b), Types of carbonate platforms: a genetic approach, *Basin Research*, *13*, 313-334.

Pomar, L., M. Brandano, and H. Westphal (2004), Environmental factors influencing skeletal grain sediment associations: a critical review of Miocene examples from the western Mediterranean, *SEDIMENTOLOGY*, *51*, 627-651.

Pomar, L., A. Rodriguez, and P. Santanach (1983), Thrust And Vertical Faulting Tectonics, And Gravity Slips In The Serra De Tramuntana (Mallorca, Spain), *Comptes Rendus De L Academie Des Sciences Serie Ii*, *297*, 607-&.

Pomar, L., and W. C. Ward (1994), Response Of A Late Miocene Mediterranean Reef Platform To High-Frequency Eustasy, *Geology*, *22*, 131-134.

Pomar, L., and W. C. Ward (1999), Reservoir-scale heterogeneity in depositional packages and diagenetic patterns on a reef-rimmed platform, upper Miocene, Mallorca, Spain, *Aapg Bulletin-American Association of Petroleum Geologists*, *83*, 1759-1773.

Portsmouth, I. R., M. H. Worthington, and C. C. Kerner (1993), A Field-Study of Seismic Attenuation in Layered Sedimentary-Rocks .1. Vsp Data, *Geophysical Journal International*, *113*, 124-134.

Proust, J. N., G. Mahieux, and B. Tessier (2001), Field and seismic images of sharp-based shoreface deposits: Implications of sequence stratigraphic analysis, *Journal of Sedimentary Research*, *71*, 944-957.

Prum, R. O., T. Quinn, and R. H. Torres (2006), Anatomically diverse butterfly scales all produce strustural colour by coherent scattering, *Journal of experimental biology*, *209*, 748-765.

Redheffer, R. M. (1962), Relation of Transmission-Line Theory to Scattering and Transfer, *Journal of Mathematics and Physics*, *41*, 1-&.

Richards, P. G., and W. Menke (1983), The Apparent Attenuation of a Scattering Medium, *Bull. Seismol. Soc. Amer.*, *73*, 1005-1021.

Riesz, A. D. (1981), Seismic absorption due to induced fluid motions, *Journal of Geophysical Research*, *86*.

Rio, P., T. Mukerji, G. Mavko, and D. Marion (1996), Velocity dispersion and upscaling in a laboratory-simulated VSP, *Geophysics*, *61*, 584-593.

Rovelli, A. (1982), On the Frequency-Dependence of Q in Friuli from Short-Period Digital Records, *Bull. Seismol. Soc. Amer.*, *72*, 2369-2372.

Rozman, M. G., P. Reineker, and R. Tehver (1994), Scattering by Locally Periodic One-Dimensional Potentials, *Phys. Lett. A*, *187*, 127-131.

Saggaf, M. M., and E. A. Robinson (2000), A united framework for deconvolution of traces on nonwhite reflectivity, *Geophysics*, *65*, 1660-1676.

Sahimi, M., and S. E. Tajer (2005), Self-affine fractal distributions of the bulk density, elastic moduli, and seismic wave velocities of rock, *Phys. Rev. E*, *71*.

Salo, E. L., and G. T. Schuster (1989), Traveltime Inversion of Both Direct and Reflected Arrivals in Vertical Seismic Profile Data, *Geophysics*, *54*, 49-56.

Sams, M. S., J. P. Neep, M. H. Worthington, and M. S. King (1997), The measurement of velocity dispersion and frequency-dependent intrinsic attenuation in sedimentary rocks, *Geophysics*, *62*, 1456-1464.

Sams, M. S., and P. R. Williamson (1994), Backus Averaging, Scattering and Drift, *Geophysical Prospecting*, *42*, 541-564.

Schlager, W. (1991), Depositional Bias And Environmental-Change Important Factors In Sequence Stratigraphy, *Sedimentary Geology*, *70*, 109-130.

Schlager, W. (1993), Accommodation And Supply - A Dual Control On Stratigraphic Sequences, *Sedimentary Geology*, *86*, 111-136.

Schön, J. H. (1996), *Physical Properties of Rocks, Fundamentals and principles of petrophysics*, Elsevier Science Ltd.

Solomon, S. C. (1973), Shear wave attenuation and melting beneath the mid-Atlantic range, *Journal of Geophysical Research*, *78*, 6044-6059.

Spencer, W. T., J. R. Sonnad, and T. M. Butler (1982), Seismic Q-Stratigraphy or dissipation, *Geophysics*, *47*, 16-24.

Spetzler, H., and D. L. Anderson (1968), The effect of temperature and partial melting on velocity and attenuation in a simple binary system, *Journal of Geophysical Research*, *73*, 6051-6060.

Stainsby, S. D., and M. H. Worthington (1985), Q-Estimation from Vertical Seismic Profile Data and Anomalous Variations in the Central North-Sea, *Geophysics*, *50*, 615-626.

Stoll, R. D. (1989), Sediment Acoustics, in *Lecture Notes in Earth Sciences*, edited, Springer-Verlag, Berlin.

Stoll, R. D., and G. M. Bryan (1970), Wave attenuation in saturated sediments, *J. Acoust. Soc. Am.*, *47*, 1440-1447.

Su, N. H., G. C. Sander, F. W. Liu, V. Anh, and D. A. Barry (2005), Similarity solutions for solute transport in fractal porous media using a time- and scale-dependent dispersivity, *Applied Mathematical Modelling*, *29*, 852-870.

Szipocs, R., K. Ferencz, C. Spielmann, and F. Krausz (1994), Chirped multilayer coatings for broadband dispersion control in femtosecond lasers, *Opt. Lett.*, *19*.

Taniguchi, N. (1974), On the Basic Concept of 'Nano-Technology', paper presented at Intl. Conf. Prod. Eng. Tokyo, Japan Society of Precision Engineering, Japan.

Tankard, A. J., and H. R. Balkwill (1989), Extensional Tectonics and stratigraphy of the North Atlantic margins: an introduction, in *Extensional Tectonics and stratigraphy of the North Atlantic margins*, edited by A. J. Tankard and H. R. Balkwill, pp. 1-6, Amer. Assoc. Petrol. Geol. Mem.

Tittmann, B. R., V. A. Clark, J. Richardson, and T. W. Spencer (1980), Possible mechanism for seismic attenuation in rocks containing small amounts of volatiles, *Journal of Geophysical Research*, *85*, 5199-5208.

Tonn, R. (1991), The determination of the seismic quality factor Q from VSP data: a comparison of different computational methods, *Geophysical Prospecting*, *39*, 1-27.

Ursin, B., and T. Toverud (2002), Comparison of seismic dispersion and attenuation models, *Studia geophysica geodaetica*, *46* 293−320.

Vail, P. R., and R. M. Mitchum (1977), Seismic stratigraphy and global changes of sea level, Part 1, in *Seismic Stratigraphy - Applications to Hudrocarbon Exploration*, edited by C. E. Payton, AAPG Memoir 26, p.51-52.

Verhelst, F. (2000), Integration of seismic data with well-log data, Delft University of Technology, Delft.

Vernik, L., and A. Nur (1992), Petrophysical classification in sliciclastics for lithology and porosity predictions from seismic velocities, *AApg Bulletin*, *76*, 1295-1309.

Verwer, K. (2004), Macro-porosity using digital photos on in situ observations on the cliff of Cap Blanc, Mallorca personal communication

Verwer, K., J. Kenter, G. G. Drijkoningen, H. Braaksma, and N. Filippidou (2006), Natural laboratories linking geology, petrophysics, and geophysics: Prograding coralgal reefs (Mallorca, Spain) paper presented at AAPG Regional Conference, Palma de Mallorca, 30 April -3 May.

Volker, A. W. F. (2002), Assessment of 3-D seismic acquisition geometries by focal beam analysis, Delft University of Technology, Delft.

Walden, A. T., and J. W. J. Hosken (1985), An investigation of the spectral properties of primary reflection coefficients, *Geophysical Prospecting*, *33*, 400-435.

Walsh, J. B. (1966a), Seismic wave attenuation in rock due to friction, *Journal of Geophysical Research*, *71*, 2591-2599.

Walsh, J. B. (1968), Attenuation in partially melted material, *Journal of Geophysical Research*, *73*, 2209-2216.

Walsh, J. B. (1969), New analysis of attenuation in partially melted rock, *Journal of Geophysical Research*, *74*, 4333-4337.

Wang, X. F., M. S. Kushwaha, and P. Vasilopoulos (2001), Tunability of acoustic spectral gaps and transmission in periodically stubbed waveguides, *Physical Review Letters B*, *65*.

Wapenaar, C. P. A., and A. J. Berkhout (Eds.) (1989), *Elastic Wave Extrapolation: redatuming of single- and multi-component seismic data*, Elsevier Science Publ. Co. Inc.

Wapenaar, C. P. A., D. Draganov, and J. W. Thorbecke (2003), Relations between codas in reflection and transmission data and their applications in seismic imaging., paper presented at 6th SEGJ international symposium - imaging technology, Tokyo, Japan.

Wapenaar, C. P. A., and J. L. T. Grimbergen (1996), Reciprocity theorems for one-way wave fields, *Geophysical Journal International*, *127*, 169-177.

Wapenaar, K., R. Ghose, G. Toxopeus, and J. Fokkema (2005), The wavelet transform as a tool for geophysical data integration, *Integr. Comput.-Aided Eng.*, *12*, 5-23.

Wautelet, M. (2001), Scaling laws in the macro- micro- and nanoworlds, *Eur. J. Phys.*, *22* 601-611.

White, J. E. (1975), Computed seismic speeds and attenuation in rocks with partial gas saturation, *Geophysics*, *40*, 224-232.

White, J. E., N. G. Mikhaylova, and F. M. Lyakhovitskiy (1976), Low-frequency seismic waves in fluid saturated layered rocks, *Phys. Solid Earth*, *11*.

Wikipedia, C. (2006), Levenberg-Marquardt algorithm.

Winter, C. L., and D. M. Tartakovsky (2001), Theoretical foundation for conductivity scaling, *Geophys. Res. Lett.*, *28*, 4367-4369.

Yariv, A., and P. Yeh (2002), *Optical Waves in Crystals: Propagation and Control of Laser Radiation* 608 pp., Willey.

Zhang, D. X., R. Y. Zhang, S. Y. Chen, and V. E. Soll (2000), Pore scale study of flow in porous media: Scale dependency, REV, and statistical REV, *Geophys. Res. Lett.*, *27*, 1195-1198.

Ziegler, P. A., and V. v. Hoorn (1989), Evolution of North Sea rift system, in *Extensional Tectonics and stratigraphy of the North Atlantic margins*, edited by A. J. Tankard and H. R. Balkwill, pp. 471-500, Amer. Assoc. Petrol. Geol. Mem.

Ziolkowski, A., J. R. Underhill, and R. G. K. Johnston (1998), Wavelets, well ties, and the search for subtle stratigraphic traps, *Geophysics*, *63*, 297-313.

We'll meet again, don't know where, don't know when
But I know we'll meet again some sunny day

Acknowledgements

Most people involved with writing a PhD Thesis are aware of the Sisyphean effort compiling and finishing a book like the one you are holding. Needless to say, this process is by far not a one-woman show. Words are but a meagre way to express my feelings about the people that supported me one the way I hope that I have demonstrated my appreciation with actions in the course of time.

I would like to thank my promotor, prof. Jacob T. Fokkema, for taking me under his aegis especially the last months. I am grateful to Guy G. Drijkoningen, my supervisor, for helping me grow up during this didactic process and the fantastic time on the field, which I'll certainly miss. My appreciation goes to prof. Kees Wapenaar for his stoic patience and ideas during dry periods. Had I been smarter to ask for his advice earlier, I would have certainly learnt much more from him. Field experiments are ruled by Murphy's Law, but Albér Hemstede taught me that "all work and no play, makes Jack a dull boy". Down at the dungeons, he makes sure that our receivers and vibrators give us maximum fieldwork pleasure. Dik Delforterie and the numerous students from Spain, Italy, Netherlands and Greece are thanked for the good time at the Mallorca acquisition. Remco Romijn is thanked for trying to make good songs out of bad Mallorcan tunes. I am grateful to Ranajit Ghose, for he was the first to get wounded from this manuscript while I was still curving it on stone. Rick Donselaar is thanked for the geodiscussions. I "owe" chapter 6 to Dr. Large, Dr. Montilla and Dr. Galisteo ho improved my vision in the field of optics. I learned deadly stories about the local flora and fauna, lunching with the group of P. Mora and S. Abe among ibis, possums and lizards while in University of Queensland, Down Under, shaking discrete particle lattices. Guus Lohlefink made sure we get the same "shaken-not stirred" results here at TUD compiling the LSM code a hundred times. The VU Amsterdam group is thanked for the co-operation: Jeroen, Hendrik, Klaas, Michele.

Even though I avoided group lunches, mainly due to the insulting cantina-food (and the early hours), I have certainly enjoyed the company of the group all these years, and I

was fortunate to have peers who knew a lot of things about a lot of things: Jeroen G., Menno D., Rutger, Rob, Gerdje, Lourens, Dennis, Gerrit, Daria, Ali, Daniela, Dirk, Sebastien, Jan T. and Jan vdK. I also want to thank my favourite slaves –ehmm…I mean students: Guus, Chris, Joost, Jona and Elmer. Special thanks to my roommates: Martijn, Sevgi, Antonio, Deyan and Petar for succumbing to my unusual ideas on dilbertean activities in the working environment.

Colleague or pal, Evert Slob has a very special place in my heart. Without him motivating me, I doubt whether this book would have ever taken shape, even though himself might not think this way. He has been there for me all the way: friend, tutor, inspiration, supervisor, with endless ideas, a smile and a cup of good coffee. He has seen me in good, bad and very bad moments and I consider myself very lucky to have met such an intelligent and generous person.

My thankful bytes have been travelling through my virtual refuges, www.gourmet.gr and www.hungry.gr, to friends that cherish the joy of fine dining and not only: evris, Tina Stavrou, hero, Dimitris Rous, ankan, K.Mp., K.P., Stef, Frantzeska, Annax2, A. Gavris, Kallie, Penelope, Juanita, Ch.Zachariadis, kxan, to mention a few.

I have been travelling days and nights on both hemispheres thanks to Stathis+Vibi, Kostas, kiwi-Vasso, Christos, Eleni, Vitke, Pyrrhos the Great, Sotiris, Lena, Roula+Marco and the Spanish Mafia (Alfonso+Alejandra, Alberto, Manu, Ramon, Vanesa, Casper etc.), who were among the friends who kept me unreasonably sane (or was it reasonably insane?). A. Tzanis (Errik) is thanked for Schrödinger's cat and for firmly insisting I should get out of UoA.

The most beautiful Janna in the world and Marijana (Dr. Evil to you) have been such an explosive mixture that the latter had to flee to Groningen. Ferdi, Motormuis II, thank you for the full throttle travels in space, infinity and beyond, with spaceships and motorcycles.

For my family from Mars (Shellgi, Iknowa, Mr. Shaw, Lomo Ze-Man, Cas), Ici and Dani, I swirl my uttermost corpo-vocabulary, proactively shearing the very same fabric of time and space in an urban lobotomistic approach. Ladiez, gentz, thanks a brazillion, for the hard-core absurdity, intense surrealism, incoherent discussions, high-level freakiness, anti-(anti-)nerdism, solidarity and vestibules while munching by the automatic vendor, at gazebos and BBQs or at the Piriscope. Lomo, thanks for Dordrecht.

Inspired teaching and love, is what makes a Teacher worthy of the title and I want to thank: Tsagkarousianou, Kalouda, Vlissidis and Tsampiras (9^{th} High School, Nikaia) and X. Sideris (Dept of Geology, Univ. of Athens) for that spark in their eyes.

I want to thank my extended family: grandmas, aunts, uncles and cousins for creating the necessary turbulence that transported me from "*there*" to "*here*". My infinite respect goes to my cousin, Marios, for showing me how life should be lived.

My parents have always believed in me and have been giving me their love already for 30 years. Although they have been obeying Heisenberg's principle of uncertainty, they were always sometimes somewhere somehow definitely around to provide support.

Jorge, thanks for standing (by) me, for the genuine love and endurance dealing with my mood swings, weird hobbies, cooking experiments, Greek-word-etymology mania and for dragging me to the colourful side of life. Thanks for teaching me the craft; I will definitely be able to get a job in house refurbishing.

There is this one person who despite being seven years late, has been taking care of me, bringing some good laughs in bad moments and immensely pissing me off at others, supporting me and loving me unconditionally ever since. For real, I don't dare to imagine my life without my brother.

About the author

Nikoletta (Aletta) Filippidou was born in Krefeld, Germany, on the 4th of March 1976 but grew up and studied in Pireas, Greece. She always wanted to be an astronomer, but shifting her observation target 180º, she studied at the Faculty of Geology, University of Athens (1993-1998). After 3 months at the University of Oslo, she started her M.Sc. studies at the University of Athens, specialising in Geophysics-Seismology. Thanks to a Norwegian Research Council scholarship, she wrote her M.Sc. thesis on AVO under the supervision of Prof. dr. M. Landrø at the Institute of Petroleum Technology, at Trondheim University of Technology (NTNU), in 1999-2000. She conducted her Ph.D. research at Delft University of Technology, Faculty of Civil Engineering and Geosciences (CiTG), department of Geotechnology, under the tutelage of Prof. dr. ir. J.T. Fokkema and dr. G.G. Drijkoningen. Her project involved experiments in rainy France, warm Spain and down-under Australia. She has joined a company that originally dealt with antiques, curios and oriental seashells, among others scallops.

Aletta is nearly convinced that the answer to Life, Universe and Everything is 42. She prefers to devote her time in attenuation of pessimism and dispersion of negativity in the Garden of Desires with good friends, good food and good discussions.

This is the first book she writes more or less by herself.

ITHACA

Konstantinos Kavafis, Alexandria,1911

As you set out for Ithaka
hope your road is a long one,
full of adventure, full of discovery.
The Laestrygonians, the Cyclops,
fierce Poseidon-don't be afraid of them:
you'll never find things like that on your way
if you keep your thoughts raised high, if rare
excitement stirs your spirit and your body.
The Laestrygonians, the Cyclops,
wild Poseidon-you won't encounter them
unless you bring them along inside your soul,
unless your soul sets them up in front of you.

Hope your road is a long one.
May there be many summer mornings when,
with what pleasure, what joy,
you enter harbors you're seeing for the first time;
may you stop at Phoenician trading stations
to buy fine things,
mother of pearl and coral, amber and ebony,
sensual perfume of every kind-
as many sensual perfumes as you can;
and may you visit many Egyptian cities
to learn and go on learning from their scholars.

Keep Ithaca always in your mind.
Arriving there is what you're destined for.
But don't hurry the journey at all.
Better if it lasts for years,
so that you're old by the time you reach the island,
wealthy with all you've gained on the way,
not expecting Ithaca to make you rich.

Ithaca gave you the marvelous journey.
Without her you wouldn't have set out.
She has nothing left to give you now.

And if you find her poor, Ithaca won't have fooled you.
Wise as you will have become, so full of experience,
you will have understood by then what these Ithacas
mean.

ΙΘΑΚΗ

Κωνσταντίνος Καβάφης, Αλεξάνδρεια 1911

Σα βγεις στον πηγαιμό για την Ιθάκη,
να εύχεσαι νάναι μακρύς ο δρόμος,
γεμάτος περιπέτειες, γεμάτος γνώσεις.
Τους Λαιστρυγόνας και τους Κύκλωπας,
τον θυμωμένο Ποσειδώνα μη φοβάσαι,
τέτοια στον δρόμο σου ποτέ σου δεν θα βρείς,
αν μέν' η σκέψις σου υψηλή, αν εκλεκτή
συγκίνησις το πνεύμα και το σώμα σου αγγίζει.
Τους Λαιστρυγόνας και τους Κύκλωπας,
τον άγριο Ποσειδώνα δεν θα συναντήσεις,
αν δεν τους κουβανείς μες στην ψυχή σου,
αν η ψυχή σου δεν τους στήνει εμπρός σου.

Να εύχεσαι νάναι μακρύς ο δρόμος.
Πολλά τα καλοκαιρινά πρωϊά να είναι
που με τι ευχαρίστησι, με τι χαρά
θα μπαίνεις σε λιμένας πρωτοειδωμένους·
να σταματήσεις σ' εμπορεία Φοινικικά,
και τες καλές πραγμάτειες ν' αποκτήσεις,
σεντέφια και κοράλλια, κεχριμπάρια κ' έβενους,
και ηδονικά μυρωδικά κάθε λογής,
όσο μπορείς πιο άφθονα ηδονικά μυρωδικά·
σε πόλεις Αιγυπτιακές πολλές να πας,
να μάθεις και να μάθεις απ' τους σπουδασμένους.

Πάντα στον νου σου νάχεις την Ιθάκη.
Το φθάσιμον εκεί είν' ο προορισμός σου.
Αλλά μη βιάζεις το ταξίδι διόλου.
Καλλίτερα χρόνια πολλά να διαρκέσει·
και γέρος πια ν' αράξεις στο νησί,
πλούσιος με όσα κέρδισες στον δρόμο,
μη προσδοκώντας πλούτη να σε δώσει η Ιθάκη.

Η Ιθάκη σ' έδωσε το ωραίο ταξίδι.
Χωρίς αυτήν δεν θάβγαινες στον δρόμο.
Αλλο δεν έχει να σε δώσει πια.

Κι αν πτωχική την βρεις, η Ιθάκη δεν σε γέλασε.
Ετσι σοφός που έγινες, με τόση πείρα,
ήδη θα το κατάλαβες η Ιθάκες τι σημαίνουν.

Propositions

Belonging to the thesis:

"Multi-scale attenuation and dispersion in seismic transmission data"

Nikoletta Filippidou

October, 19, 2006

1. Natural Laboratories provide both the complexity of the natural features and the controlled conditions required for the development of new field-experiment techniques. (*Chapter 1, this thesis*)

2. The scale of the observable should determine the scale of the experiment. (*Chapter 2, this thesis*)

3. As long as we cannot measure the seismic wave energy propagating in all possible directions we will never be able to separate intrinsic attenuation from scattering. (*Chapter 3, this thesis*)

4. High resolution surface seismic experiments are not a seismic imaging panacea given the current acquisition techniques and seismic sources. (*Chapter 5, this thesis*)

5. What geophysicists cannot image, geologists can imagine.

6. Memories can be seen as the wavelet transform of one's past life; the choice of mother wavelet and scaling factor depends on the physical, emotional and mental condition of the person.

7. The misconception that science is something cryptic and painfully difficult is a result of poor and uninspired teaching; in turn it feeds nothing but a combustible mixture of ignorance and power.

8. The colloquial usage of a foreign word (*allochtoon*) to negatively address foreigners in dutch, is yet another oxymoron depicting the absurdity of xenophobia.

9. Even in a democratic society, a repeatable combination of an abstract threat and denouncement of pacifists for lack of patriotism is enough to bring the people to the bidding of greedy warmonger leaders.

10. Aid should reflect the culture of the benefited and not the image of the benefactor.

11. Should parenting license be established the human race could become extinct.

These propositions are considered opposable and defendable and as such have been approved by the supervisor Prof. dr. ir. J.T. Fokkema.

Stellingen

behorende bij het profschrift:

"Multi-scale attenuation and dispersion in seismic transmission data"

Nikoletta Filippidou

Oktober, 19, 2006

1. Natuurlijke laboratoria voorzien zowel in de complexiteit van natuurlijke kenmerken alswel de gecontroleerde omstandigheden welke nodig zijn voor de ontwikkeling van nieuwe veldexperiment technieken. (*Hoofdstuk 2, dit proefschrift*)

2. De schaal van het observeerbare hoort de schaal van het experiment te bepalen. (*Hoofdstuk 2, dit proefschrift*)

3. Zolang wij niet in staat zijn om de energievoortplanting van seismische golven in alle mogelijke richtingen te meten, kunnen wij de intrinsieke demping niet scheiden van de verstrooiingsdemping. (*Hoofdstuk 3, dit proefschrift*)

4. Hoogresolutie seismische oppervlakte experimenten zijn geen wondermiddelen van seismische beeldverwerking, gezien de huidige acquisitiemethoden en seismische bronnen. (*Hoofdstuk 5, dit proefschrift*)

5. Wat geofysici niet in beeld kunnen brengen, kunnen geologen zich verbeelden.

6. Herinneringen kunnen worden gezien als de wavelet transformatie van iemands verleden; de keuze voor de moederwavelet en schaalfaktor hangt af van de fysieke, emotionele en mentale toestand van de persoon.

7. De misvatting dat wetenschap cryptisch en pijnlijk ingewikkeld is, is het resultaat van matig en inspiratieloos onderwijs; op haar beurt voedt het niets anders dan een explosief mengsel van onwetendheid en macht.

8. Het alledaags gebruik van een buitenlands woord (*allochtoon*) om buitenlanders in negatieve zin aan te duiden in het Nederlands, is weer zo een oxymoron welke de absurditeit van xenofobie weergeeft.

9. Zelfs in een democratische samenleving is een herhaalde combinatie van een abstracte dreiging en het hekelen van pacifisten voor gebrek aan vaderlandsgezindheid voldoende om de bevolking over te leveren aan hebzuchtige oorlogsstokende leiders.

10. Hulp hoort de cultuur van de ontvanger te weerspiegelen, niet het beeld van de aanbieder.

11. Wanneer ouderschapsvergunningen zouden worden ingesteld zou het menselijk ras uit kunnen sterven.

Deze stellingen worden opponeerbaar en verdedigbaar geacht en zijn als zodanig goedgekeurd door de promotor Prof. dr. ir. J.T. Fokkema.